A DISLOCATION APPROACH TO PLATE INTERACTION

by

RAYMON LEE BROWN, JR.

B.S., University of Texas
(1967)

M.S., University of Hawaii
(1969)

SUBMITTED IN

PARTIAL FULFILLMENT

OF THE REQUIREMENTS FOR THE

DEGREE OF DOCTOR OF PHILOSOPHY

at the

MASSACHUSETTS INSTITUTE OF TECHNOLOGY

August, 1975

Signature of Author.....
Department of Earth and Planetary Sciences,

Certified by.....
Thesis Supervisor

Accepted by.....
Chairman, Departmental Committee on Graduate Students

Abstract

A Dislocation Approach to Plate Interaction

by

Raymon Lee Brown, Jr.

Submitted to the Department of
Earth and Planetary Sciences on
August 25, 1975 in partial
fulfillment of the requirements
for the degree of Doctor of Philosophy

A dislocation can be described in terms of a surface of discontinuity or the line which circumscribes this surface. We have applied the solutions of Yoffe (1960) and Comninou (1973) for an angular dislocation line to the problem of calculating the fields due to general polygonal dislocations.

Next, a numerical method has been developed explicitly for finite sources (Finite Source Method or FSM) which allows the computation of fields from a dislocation that penetrates several layers of a layered half-space. The speed of the FSM allows the calculation of many models which are not economically possible by other means. It is used here to model

earthquakes in layered media and plate bottom effects due to the interaction of lithospheric plates.

Finally, the problem of the mutual interaction of lithospheric plates in relative motion has been posed in terms of dislocation theory (anti-dislocations). Dislocation models of various portions of the San Andreas fault in California are proposed and evaluated by comparing them with seismic and geodetic data. We find, for example, that fault creep near Hollister acts to obscure any locking at depth and that as much as 70% of the fault could be locked (down to 20 km) and still be consistent with the geodetic data.

The models also suggest that the depth of locking (or non-slipping portion of the fault) varies from 10 to 80 km along the San Andreas. Under San Francisco the depth of locking appears to be 20 to 40 km while just north and south of this region the locking is from 10 to 15 km deep. Our models are also indicative of a more northerly component of motion for the Pacific with respect to the American plate than would be expected if the San Andreas were a simple strike-slip fault. South of Cholame the depth of locking begins a rapid increase and appears to lock to 80 km in the Tejon bend portion of the San Andreas. We are not able, however, to distinguish between an actual locking of the fault, capable of taking high stresses, or simply a low stress state.

Thesis Supervisor: M. Nafi Toksöz

Title: Professor of Geophysics

ACKNOWLEDGEMENTS

This thesis represents the work of the author, but is, to a large extent, a reflection of the author's environment during the time in which the thesis was developed.

I was encouraged to study the general subject of tectonic stresses in California by Professor M. Nafi Toksöz. Professor Keiiti Aki is responsible for teaching me philosophy and the fundamentals of dislocation theory (and introducing me to Maria Comninou). Don Weidner made me prove mathematically that dislocations could be used to model plate interaction. I miss the interaction I had with Don. Maria Comninou got me started with angular dislocations and helped considerably when I was programming her thesis.

At one point in time the author wanted to eliminate the chapter on the numerical method for finite sources. This chapter would not have been completed had it not been for the firm encouragement of Professor M. Nafi Toksöz. I am appreciative of his help. Norm Brenner was instrumental in getting the author over the FFT hump at this stage of the thesis.

Discussions with Raul Madariaga led to many of the results in Chapter II. Raul's availability for detailed discussions of complex problems make him an integral part of my M.I.T. experience.

Writing a west coast thesis on the east coast was made easier by the author's discussions with several west coast informants. Bill Ellsworth, Dave Hadley, and Gordon Stewart gave the author fault plane solutions (published and unpublished) and their opinions of the tectonics of California. Bob Nason (U.S.G.S.) was extremely helpful with discussions on fault creep data and his impressions of what is driving the fault creep. Peter Molnar suggested some changes in Chapter IV and furnished additional insight into the tectonic history of California. Jim Savage (U.S.G.S.) read the whole thesis (and even checked some of the calculations). His interest in my thesis is deeply appreciated.

Several people read my thesis in a rough form and helped me clarify certain points. I wish to thank Ken Anderson, Mike Chinnery, Mike Fehler, Tony Shakal, and Seth Stein for wading through a rough draft of the work presented. Seth Stein spent several hours going through the thesis and reviewing it with me. Donald Paul and I had several useful discussions on the discrete Fourier transform and Ken Anderson was always available (except on weekends) for programming assistance. During the initial stages of Chapter III Richard Buck helped with the drafting.

The typing of this thesis was done by Dorothy Frank. Her patience and even temper made our association a pleasure. I cannot thank her enough for a job well done.

Moral support during the writing of the thesis came from Shamita Das.

Although I have sacrificed a great deal for this thesis I feel that my wife, Merri, and our two daughters, Jennifer and Deborah, have given up far more. I hope that I can make it up to them.

The research has been supported by the Advanced Research Projects Agency, monitored by the Air Force Office of Scientific Research under contracts F44620-71-C-0049 and F44620-75-C-0064, and by the Air Force Cambridge Research Laboratories, Air Force Systems Command under contract F19628-74-C-0072.

TABLE OF CONTENTS

CHAPTER I

INTRODUCTION

1.1 Purpose and Scope of Thesis

For at least 5-25 million years the portion of land seaward of the San Andreas fault zone in California has been drifting northwestward with respect to the North American continent at an approximate rate of 3-5 cm/year. As the two land masses slide past one another, portions of their interface lock and internal stress builds up around these locked sections of the fault. The stress build up results eventually in the occurrence of an earthquake. The problem to be considered here is the quantitative description of the above mentioned stress accumulation and release. In particular, the main objectives of this thesis are: 1) the development and application of numerical techniques for computing the static fields of finite dislocations distributed throughout layered media; 2) the representation of the problem of plate interaction in terms of dislocation theory, and; 3) the application of the dislocation theory of plate interaction to specific regions of California.

The computation of the stress accumulation due to lithospheric plate interaction is of importance because it yields (1) a quantitative discussion of the amount of locking and earthquake potential for various sections of the fault,

(2) a direct test of complex fault models and their effects upon local strain fields (rather than guessing, as is often the case), and (3) a more realistic model of earthquake pre-stress than the usually assumed constant stress (and therefore stress drop). In order to handle the complexity of the dislocations and/or structures required to study the problem of plate interaction, two computational methods for dislocation fields are introduced which considerably facilitate the study of many models. The first of these methods allows for the quick computation of the exact solutions for arbitrary polygonal dislocations in an infinite medium or a homogeneous half-space. The second method allows a fast numerical solution to the problem of an arbitrary, finite dislocation in a layered medium. The speed, convenience, and general applicability of this second numerical method should make it a useful tool for other areas of geophysics. Because of its generality, the numerical method for finite sources may be the most significant contribution of the thesis.

Since the dislocation approach to the problem of plate interaction represents a new use for dislocations it is important to place this new application in perspective. For this reason a short history of static dislocation theory and its applications is presented in the second portion of the introductory chapter.

In Chapters II and III, the new computational methods utilized in this thesis for the dislocations and for the San Andreas fault are described. Chapter II introduces a computational scheme which is new to geophysics but is well established in the physics of solids (Yoffe, 1960). The scheme involves the addition and subtraction of angular dislocations in order to form general polygonal dislocations. The primary contributions made by the author in this chapter are (1) the introduction of a new and more useful multi-valued term into the solutions of Yoffe (1960) and Comninou (1973) and (2) the first computation (computations discussed in Chapter IV) of the fields due to complex dislocations in a homogeneous half-space using the solutions for an angular dislocation in a half-space (Comninou, 1973).

Chapter III applies the methods described in Chapter II in order to calculate primary fields (fields due to a finite dislocation in an infinite medium). These primary fields are then used in a new numerical approach (Finite Source Method or FSM) to compute the secondary fields due to layering. The FSM requires computation times of a few minutes for problems which require a few hours using standard techniques. The secret to the speed of the FSM lies in the elimination of integration over the fault plane. We apply the FSM to the study of (1) the effects of realistic crustal structures upon finite earthquake fields and (2) the effects of soft underlying layers upon plate

interaction fields. Of particular importance in the conclusions of this chapter are the circumstances under which the effects due to the bottom of the plate may be neglected. Under these conditions the models may be constructed from dislocations in a homogeneous half-space thus allowing faster exact solutions to be used.

In Chapter IV the problem of plate interaction is posed in terms of anti-dislocations. By a simple subtraction of relative rigid body motion the anti-dislocation models can then be computed via equivalent dislocations. The equivalent dislocations may be constructed using the methods described in Chapters II and III.

The anti-dislocation models will be used to study two specific regions of the San Andreas fault in California. The first region includes a small bend in the San Andreas which occurs in the vicinity of San Juan Bautista, California and includes the Hayward and Calaveras faults. The second region of interest encloses a large bend ("the big bend", Hofmann, 1968) in the San Andreas which extends from Ft. Tejon to Cajon Pass. The question posed by this chapter concerns the importance of these features. Are these bends representative of the interface between the Pacific and North American plates or are they simply very near surface features which have little tectonic significance? The answer will be found by comparing predictions from tectonic models of these regions to the

seismic and geodetic data available.

Finally, in Chapter V, the fields due to the large earthquakes ($M \geq 6$) in California will be added to the fields of a tectonic model of California in order to study the present stress state of California. This addition will yield zones of high strain accumulation and therefore zones of probable future earthquake activity. Such calculations will also allow us to gain a more realistic picture of the tectonic pre-stress that exists in a region before an earthquake occurs. Thus statements of probable earthquake magnitude, radiation, and slip could be estimated from theoretical studies (e.g. Andrews, 1975). There will of course be a number of uncertainties in these calculations but the results should allow us to point to regions which deserve further study and instrumentation.

1.2 History of Dislocation Theory and its Application

The conceptual beginning of dislocation theory occurred during the 1800's when most scientists thought that space (the aether) had elastic properties resembling in some respects those of a solid. In order to explain the motion of material bodies through space, C.V. Burton (1892) proposed that matter was made up of modifications (effectively dislocations) of the aether. In an attempt to do away with the "Weberian" concept of action at a distance, Larmor (1897) proposed that electrons are made up of dislocations ("point

singularities of intrinsic strain") in the aether. However, the mathematical foundations of dislocation theory began in the development of elastic theory.

According to Love (1927), J.H. Mitchell (1900) was the first to examine the analytical possibility that certain stress functions may be many-valued (under the condition that the displacements be expressed by single-valued functions); however the association of many-valued displacements with multi-valued displacements was first made by G. Weingarten in 1901. During the years 1900-1920, the theory of dislocations in an elastic continuum was developed by the Italian school and by A. Timpe (Nabarro, 1967). V. Volterra (1907) developed a more general theory of dislocations with some improvements by E. Cesaro and described what is known today as the Volterra type of dislocation (Love, 1927). Volterra referred to dislocations as "distorsioni". The name "dislocation" was first used by Love (1927).

When G.I. Taylor (1934) brought these Volterra dislocations into the explanation of the work hardening in aluminum crystals many people began to devote their efforts to the fundamental theory of dislocations (Mura, 1968). The most successful of these was Burgers (1939) who extended Taylor's (1934) two-dimensional analysis to three dimensions and introduced the concept of the dislocation line. Taylor (1934) is credited with the solution of what is known as an

edge-dislocation and Burgers (1939) found the solution to the screw dislocation.

While the above work on dislocation theory and its application to the theory of solids was in progress, geophysicists began asking fundamental questions about the nature of the earthquake mechanism and the system of forces causing earthquakes. In a study of geodetic data taken before and after the 1906 San Francisco earthquake, Reid (1910) proposed a theory of elastic rebound for earthquakes which is conceptually similar to dislocations in elastic media. He suggested that "...external forces must have produced an elastic strain in the region about the fault line, and the stresses thus induced were the forces which caused the sudden displacements, or elastic rebounds, when the rupture occurred. The only way in which the indicated strains could have been set up is by a relative displacement of the land on opposite sides of the fault and at at some distance from it." Reid's (1910) proposal is of considerable importance in this thesis and will later be posed in terms of dislocation theory.

One of the first attempts to study the static fields of an earthquake mathematically was made by K. Sezawa (1929). He proposed a point of dilatation and higher order derivatives of this source as a model of the earthquake. Although his study was prompted by the availability of geodetic data which measured the distortion of the land associated with earthquakes,

he made no attempt to compare his theory with the data to see which, if any, of his special nuclei of strain applied to earthquakes.

Whipple (1936), in an effort to extend the work of Honda and Miura (1935), appears to have been the first to suggest a point dislocation (strain nucleus) model of the earthquake. His model did not become generally popular at this time because of the lack of data to support any strain nucleus as being the source of earthquakes and because of the general debate over which nuclei were really applicable (Honda, 1957).

In the meantime the first crack models of earthquakes were published in the late 1950's (Kasahara, 1957; 1959; Knopoff, 1958; Keilis-Borok, 1959) and represented modified versions of the cracks studied by Griffith (1921) and Starr (1928). More recently people have begun to study crack models with friction (Orowan, 1960; Savage and Wood, 1971; Walsh, 1968).

The current application of static dislocation theory to the study of earthquakes began with the published work of Housner (1955), Rochester (1956) and Vvendenskaya (1956). However, the major emphasis upon the static theory of dislocations began when Steketee (1958a,b) suggested the dislocation as a model of the earthquake and derived one set of the six sets of Green's function necessary to calculate the displacement fields for a dislocation in a homogeneous half-space.

In addition, he was able to show that the solutions for the Griffith (1921) crack (and therefore other cracks, e.g. Starr, 1928) could be reduced to those of a Somigliana dislocation. T. Maruyama (1964) extended Steketee's (1958b) work by solving for the other five sets of Green's functions. Chinnery (1961) made a detailed study of the displacements associated with surface faults using Steketee's (1958b) results and later used the theory to calculate the stress drops associated with earthquakes (Chinnery, 1963, 1964). Since the introduction of dislocations to geophysics the primary application has been to the change in fields associated with earthquakes (e.g. Savage and Hastie, 1966; Savage and Hastie, 1969; Plafker and Savage, 1970; Fitch and Scholz, 1971; Canitez and Toksöz, 1972; Jungels and Frazier, 1973; Alewine and Jungels, 1974).

Other applications of static dislocation theory include models of fault creep (Stewart, et al., 1973), rock bursts (McGarr, 1971), secondary faulting (Chinnery, 1966a, 1966b), and tectonic stress (Droste and Teisseyre, 1960). When Press (1965) demonstrated that permanent earthquake strains could be detected at teleseismic distances and Wideman and Major (1967) observed the "strain steps" associated with certain earthquakes many investigators began to study the effects of a realistic earth model upon the observed strains. These effects include those of a spherical earth (e.g. Ben-Menahem,

et al., 1969), layering (e.g. Sato, 1971), and the combination of these with gravitational effects (Smylie and Mansinha, 1971).

The present state-of-the-art of the application of static dislocation theory to the description of earthquake fields consists of putting finite dislocations in more realistic earth models. This has been done in two dimensions by Jungels and Frazier (1973) and Alewine and Jungels (1973) using the finite element technique and in three dimensions by Sato (1971), Javanovich et al. (1975), and Sato and Matsu'ura (1973) using a numerical integration scheme on their resultant integrals. A more detailed description of the work done in this area will be given in the third chapter. For a review of the application of dislocation theory in other areas the reader is referred to the work of Mura (1968).

Chapter II

Construction of Finite Dislocation Loops Via Angular Dislocations

2.1 Introduction

In this chapter we present a method for the calculation of a very general class of Volterra (1907) dislocations. The dislocations will be built from a fundamental unit, an angular dislocation. The procedure to be used will allow for the simple computation of the fields of an n-sided polygonal dislocation with an arbitrary Burgers' vector. The method to be presented represents a building block for the rest of the thesis. In Chapter III it will be used in the calculation of fields from dislocations in layered media. In Chapter IV the problem of plate interaction will be posed in terms of complex dislocations which can be easily handled by the methods described here.

In addition to the problems considered in this thesis, the method described should be applicable to other areas in geophysics. With the introduction of improved geodetic data and other means of measuring the displacements and strains of the earth has come a need for a more sophisticated model of earthquakes. Greater complexity can be added to the model of either the source or the media (e.g. the layered media discussed in Chapter III). Greater source complexity can be

added by allowing for variable slip over the fault surface and/or allowing the fault surface to have more character than a flat rectangle. Since the technique described here is not restricted to planar dislocations nor to simple rectangles it offers a powerful tool for the study of source complexity via static near-fields. The idea behind the method is well established in solid state physics (Yoffe, 1960) but this chapter represents, as far as the author is aware, a first application of the method to obtain the displacement fields associated with a fixed surface of discontinuity (solid state physicists are concerned more with strain energies and interaction energies which depend upon the dislocation strains).

2.2 Volterra Dislocations

A dislocation is often defined in terms of a cut in an elastic material. If the two sides of the cut are moved relative to one another in such a way that neither side of the cut experiences any distortion (relative rigid body motion), the dislocation is referred to as a Volterra (1907) or discrete dislocation. The Somigliana dislocation Steketee,(1958) is the most general form of a dislocation and only requires that the final dislocation configuration be in equilibrium. Of particular interest to us here is the Volterra dislocation in a half-space.

The computation of the fields of a dislocation has usually been accomplished by a numerical (e.g. Canitez and Toksöz, 1972) or exact (Press, 1965) integration of the Green's function (Whipple, 1936; Vvendenskaya, 1956; Steketee, 1958 (a,b); Maruyama, 1964). Recently the exact solutions for finite, oblique, shear dislocations of the Volterra type (Mansinha and Smylie, 1971) and of particular forms of the Somigliana type (Converse, 1974) have been presented. However, these solutions are restricted to plane surfaces with the Burgers' vector in the plane of the surface.

A method will now be presented which will allow us to calculate the exact solution for a general polygonal shaped Volterra (1907) dislocation (not restricted to being planar) with an arbitrary Burgers' vector. The need for such solutions in geophysics will become apparent in Chapter IV.

2.3 Angular Dislocations

The dislocation has been reviewed as a displacement discontinuity across a surface, since this represents the popular concept of a shallow earthquake. However, specification of the dislocation by means of a surface does not yield the most general representation of the dislocation. It is the dislocation line, the line that follows the edge of all possible surfaces of discontinuity, which allows the most general representation of the dislocation (Maruyama,

1964; Mura, 1968). Burgers (1939) initiated the use of the dislocation line and this approach to dislocations has found considerable popularity in the physics of solids.

Because of the recent work of Maria Comninou (1973) it will be to our advantage to revert to the use of the dislocation line in our description of dislocations. She has solved the problem of an angular dislocation in a half-space. The term angular describes the configuration of the dislocation lines. As can be seen in Figure 2.1 (a), the angular dislocation consists of two semi-infinite dislocation lines which meet at the point A. Her work extends the work of Yoffe (1960) who solved the angular dislocation in an infinite medium. The solutions given by Comninou and Yoffe allow us to construct the exact solutions for arbitrary polygonal dislocations (Yoffe, 1960). The angular dislocations are used as the primary building blocks. Figure 2.1 (b) shows the construction of a π dislocation (Comninou, 1973) using two angular dislocations. The π dislocations may then be added to yield an arbitrary polygonal dislocation (Figure 2.1 (c)). The actual addition requires that the π's be translated and rotated to the correct coordinate system. Since there are no restrictions on the polygon being in a plane, the above method of calculation allows us to calculate the fields for a very general class of dislocations. There is, however, a caveat which will be described in the

following section.

2.4 Dislocation Surfaces and Multi-valuedness

In approaching the problem of constructing a general polygonal dislocation by means of angular dislocations one must use care in evaluating the displacement fields. If a dislocation is described via the dislocation line, the associated surface can be anywhere as long as its edges end on the dislocation line. The solution given by Burgers (1939) for a line dislocation is

$$2.1 \qquad \vec{u} = \frac{1}{4\pi} \vec{b}\,\Omega + \frac{1}{4\pi} \vec{b} \times \int \frac{1}{r}\, d\vec{l} + \frac{\alpha}{4\pi} \vec{\nabla} \int \frac{1}{r} (\vec{b} \times \vec{r}).d\vec{l}$$

where $\alpha = \frac{\lambda + \mu}{\lambda + 2\mu}$, $\vec{r}$ is the vector from the line to the observation point, $\vec{b}$ is the Burgers' vector, dl the line element describing the dislocation line and

$$\Omega = \frac{1}{4\pi} \iint \hat{n} \cdot \vec{\nabla}\left(\frac{1}{r}\right) d\Sigma$$

where $\hat{n}$ is the normal to the dislocation surface.

The function Ω is the multi-valued term associated with dislocation fields and is proportional to the solid angle subtended by the dislocation from the point of observation (figure 2.2a). It is the only portion of the solution which allows a discontinuity of values across a surface. Thus, the multi-valued terms in the solution of a

line dislocation determine where the effective dislocation surface is with respect to the line. If the multi-valued terms in the solution should consist of a series of arc-tangents of various functions it becomes important to know the principal values over which the arctangents are to be evaluated. The particular choice we make will determine the dislocation surface.

An example of this multi-valuedness may be found in the solution of the angular dislocation in an infinite medium shown in Figure 2.2 (b). The solution for the displacement in the x direction with a Burgers' vector in the x-direction is (Yoffe, 1960):

$$2.2 \qquad u_1 = b\phi + \frac{b}{8\pi(1-\nu)}\left[\frac{xy}{r(r-z)} - \frac{\eta x}{r(r-L)}\right]$$

where b is the Burgers' vector in the x-direction

$$r^2 = x^2 + y^2 + z^2$$

$$L = y \sin \alpha + z \cos \alpha$$

and

$$\eta = y \cos \alpha - z \sin \alpha$$

The multi-valued term is

$$2.3 \quad \phi = \frac{1}{4\pi}\left[\tan^{-1}\frac{Y}{x} - \tan^{-1}\frac{\eta}{x} + \tan^{-1}\frac{xr\sin\alpha}{x^2\cos\alpha + y\eta}\right]$$

Yoffe (1960) claims that ϕ as defined in equation 2.3 "remains single-valued on circling the negative z and ζ axes, but increases by unity when its circuit passes once into the paper between the positive axes". She further indicates that this discontinuity may occur across the shaded area in Figure 2.2 (b). However, she does not describe which principal values should be used for the arctangents in order to make the multi-valued term behave as described. In fact, for conventional limits on the arctangent (either $-\pi$ to π or 0 to 2π) the function ϕ as described by Yoffe (1960) does not have a single surface of discontinuity (the shaded region in figure 2.2 (b)). This can be more easily understood by following Yoffe's decomposition of this term into the multi-valued terms of simpler dislocations.

The term $\tan^{-1}$ (y/x) corresponds to one half of the multi-valued term of an infinite straight line dislocation along the z axis. By defining the arctangent from $-\pi$ to π we see that this dislocation has a plane of discontinuity extending through the z axis along the negative x axis

(figure 2.3a). Thus the plane of discontinuity is perpendicular to the shaded plane in figure 2.2(b). Similarly, the term $\tan^{-1}(\eta/x)$ represents one half the solid angle that would be subtended (at the observation point x,y,z) by the half-plane which cuts through the η axis and the negative x-axis (figure 2.3 (b)). The third term in equation 2.3 represents the junction of two angular dislocations with opposite senses. The plane of discontinuity in this case occurs in the $x = 0$ plane (figure 2.3 (c)). The sum of these three terms yields a rather pathological dislocation surface consisting of two angular wedges extending to $x = -\infty$ which are capped with surfaces of discontinuity in the $x = 0$ plane (figure 2.3 (c)). The dislocations in the third quadrant cancel yielding zero strain and a rigid body displacement of the wedge. The wedge in the first quadrant yields the same strains as the angular dislocations shown in figure 2.2 (b). However the displacements differ by rigid body terms from those of an angular dislocation with the discontinuity in the $x = 0$ plane.

If we were only concerned with strains it would not be necessary to discuss these surfaces of discontinuity. However, in constructing a polygonal dislocation loop via angular dislocations the construction will be facilitated if the angular dislocations are discontinuous in the plane of the angle. We therefore wish to find a ϕ which has the same

derivatives as the ϕ given in equation 2.3 but which has a single surface of discontinuity in the x = 0 plane. This can be accomplished by adding together straight line dislocations with surfaces of discontinuity in the proper plane. Thus if we add $\tan^{-1}(x/-y)$ and $\tan^{-1}(x/\eta)$ to the multi-valued term of a junction dislocation with surfaces of discontinuity complementary to those shown in figure 2.3 (d) we obtain

$$2.4 \quad \phi = \frac{1}{4\pi}\left[\tan^{-1}\left(\frac{x}{-y}\right) + \tan^{-1}\left(\frac{x}{\eta}\right) - \tan\left(\frac{xr\sin\alpha}{-x^2\cos\alpha - y\eta}\right)\right]$$

Figure 2.4 shows a schematic diagram of the dislocation decomposition of equation 2.4. The ϕ given in equation 2.4 behaves exactly as Yoffe (1960) claims it should if we evaluate the arctangents from $-\pi$ to π (figure 2.4).

In order to use these results with the results obtained by Comninou (1973) we need only use equation 2.4 for the dislocation in the half space added to the multi-valued term for the image dislocation

$$\phi = \frac{1}{4\pi}\left[\tan^{-1}\left(\frac{x}{-y}\right) + \tan^{-1}\left(\frac{x}{-\eta}\right) - \tan^{-1}\left(\frac{xr\cos\alpha}{x^2\cos\alpha + yn}\right)\right]$$

Figure 2.5 illustrates the respective positions for the surfaces of discontinuity obtained by using the above expressions in Comninou's (1973) solutions.

Now that the surface of discontinuity is in the plane of the angular dislocation, it becomes a simple matter to construct a vertical, polygonal dislocation loop in either an infinite medium (Yoffe, 1960) or a half-space (Comninou, 1973) in which the plane of discontinuity is in the plane of the loop (figures 2.6 (a), 2.6 (b)). However, for the loop oblique to the surface, the use of π dislocations arranges the surfaces of discontinuity in a manner which is not very useful for the description of earthquakes (figure 2.6 (c)). Since Comninou (1973) has simplified her solutions by requiring that one leg of the angular dislocation remain perpendicular to the free surface we must make a slight modification to the results calculated for the dislocation shown in figure 2.6 (c). The problem consists of converting the displacement field from the dislocation given in figure 2.6 (c) to one with any other surface which ends on the same dislocation line (e.g. figure 2.6 (d)). Conceptually, it is easy to see that all that is necessary is a simple addition and/or subtraction of rigid body motions to the solution for the dislocation shown in figure 2.6 (c). For the sake of completeness we present here a short proof of this relation between the

dislocations in figure 2.6 (c) and 2.6 (d) which has been given to the author by Comninou (personal communication).

The integral solution for the dislocation in figure 2.6 (c) is (Mura, 1968)

$$2.5 \quad U_m(\vec{r}) = b_i \iint_{S'} C_{ijkl} \bar{U}_{km,l} (\vec{r},\vec{r}') \, ds_j'$$

where the C_{ijkl} are the elastic constants for a generalized Hooke's law. The $U_{km}(\vec{r},\vec{r}')$ satisfy the equation of equilibrium

$$2.6 \quad C_{ijkl} U_{km,lj} (\vec{r},\vec{r}') + \delta_{im} \delta(\vec{r}-\vec{r}^1) = 0$$

and the free surface boundary conditions if we are solving the half-space problem. We shall use the convention shown in figure 2.7 throughout the thesis, of defining the + surface as that surface on which the linking circuit ends (Mura, 1968). With this convention the integral in equation 2.5 is taken over the S^- surface and the Burgers' vector is

$$b_i = U_i^+ - U_i^-$$

If we specify the components of the Burgers' vector to be b_i on the surface composed of the surfaces $S_L = S_1^+ + S_2^+ + S_3^+ + \ldots S_n^+ + S_B^-$ then we have the solution (with b_i defined on the S_i^+ surface).

2.7

$$U_m(r) = -b_i \iint_{S_1^+ + S_2^+ + \ldots S_n^+} C_{ijkl} U_{km,l}(r,r')\, ds' - b_i \iint_{S_b^-} C_{ijkl} U_{km,l}(\vec{r},\vec{r}')\, ds'$$

where the sense of S_L is out of the volume enclosed by all of the surfaces. An alternative to equation 2.7 may be obtained by using the divergence theorem in equation 2.5 and exchanging the derivative over the source coordinate to one over the observation coordinate to obtain

2.8 $$U_m(\vec{r}) = -b_i \iint_V C_{ijkl}\, U_{km,l}(\vec{r},\vec{r}^1)\, dV'$$

where V is the volume enclosed by the surfaces. Using equation 2.6 in 2.8 we obtain

2.9 $$U_m(\vec{r}) = b_i\, \delta_{im}\, \delta(\vec{r}-\vec{r}')$$

or finally

2.10 $$U_m(\vec{r}) = \begin{cases} 0 & \vec{r}\ \varepsilon V \\ b_m & \vec{r}\ \varepsilon V \end{cases}$$

Now the integral in 2.7 can be written in the form

2.11 $$U_m(\vec{r}) = +b_i \iint_{S_1^- + S_2^- + S_3^- \ldots S_n^-} C_{ijkl} U_{km,l}(\vec{r},\vec{r}')\, ds' - b_i \iint_{S_b^-} C_{ijkl} U_{km,l}(\vec{r},\vec{r}')\, ds'$$

where we have changed the first integral to one over the S_i^- surfaces (i=1,2,...n).

Thus, equating 2.10 and 2.11 we find

$$b_i \iint_{S_b^-} C_{ijkl}\, U_{km,l}(\vec{r},\vec{r}')ds' = b_i \iint_{S_1^- + S_2^- + S_3^- + \ldots S_n^-} C_{ijkl} U_{km,l}(\vec{r},\vec{r}')ds'$$

2.12 $$-\left\langle \begin{matrix} 0 \\ b_m \end{matrix} \right\rangle \begin{matrix} r \notin V \\ r \in V \end{matrix}$$

Equation 2.12 shows that the difference between the dislocations in figures 2.6 (c) and 2.6 (d) is a rigid body displacement determined by the Burgers' vector.

2.5 Summary

The ideas presented in this chapter allow us to construct the fields of a general, polygonal, Volterra (1907) dislocation in either an infinite medium (Yoffe, 1960) or a half-space (Comninou, 1973). In applying these ideas it

is especially convenient to use π dislocations (Comninou, 1973) as the basic building blocks for polygonal dislocations in a half-space (figure 2.8). In chapter IV we shall use the π dislocations to construct complex tectonic models of the San Andreas fault in California. We will describe the models by giving the coordinates of the corners of the dislocations and the Burgers' vector for the models.

In order to compute the displacement fields for the general dislocations discussed, we have had to modify the displacement solutions. This was necessary since the multi-valued terms given by Yoffe (1960) and Comninou(1973) do not allow a simple representation of earthquake displacements. In particular, the multi-valued terms were changed so that one surface of discontinuity would be associated with each angular dislocation. In our case, we have fixed the surface of discontinuity to be in the plane of the angular dislocation and between the acute angle formed by the dislocation lines.

Although the dislocations described in the rest of the thesis could have been calculated by a numerical integration of the Green's function for a point dislocation, the speed and agility of angular dislocation approach should make it the method most used by future workers in this area. In fact, we believe that many of the models considered in this thesis would not have even been approached had it not been for the power of the methods presented here.

Figure 2.1

(a) Dislocation line for an angular dislocation. The lines extend to infinity since a dislocation line cannot end in the medium without violating equilibrium.

(b) Construction of a π dislocation out of two angular dislocations.

(c) Construction of rectangular dislocation loop out of π dislocations.

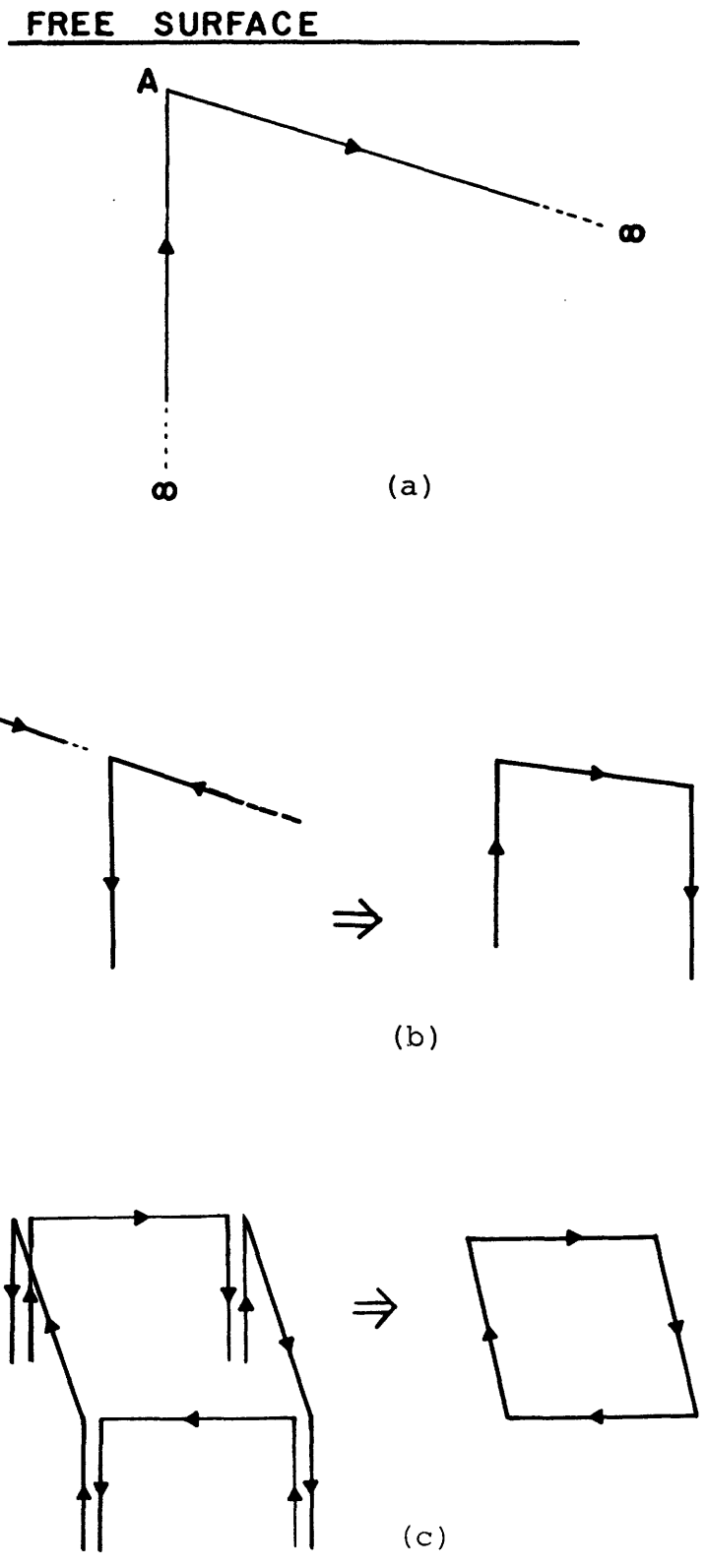

Figure 2.1

Figure 2.2

(a) Diagram of the solid angle Ω subtended by a dislocation circuit σ.

(b) Angular dislocation with angle α. Shaded region represents one of an infinite number of possible surfaces of discontinuity associated with the angular dislocation line shown.

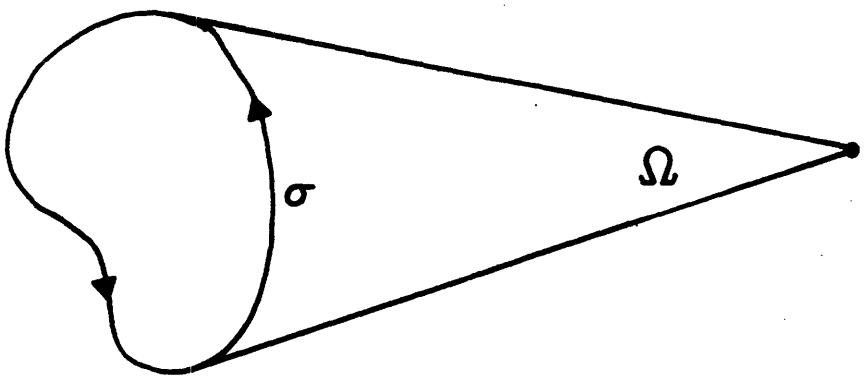

(a)

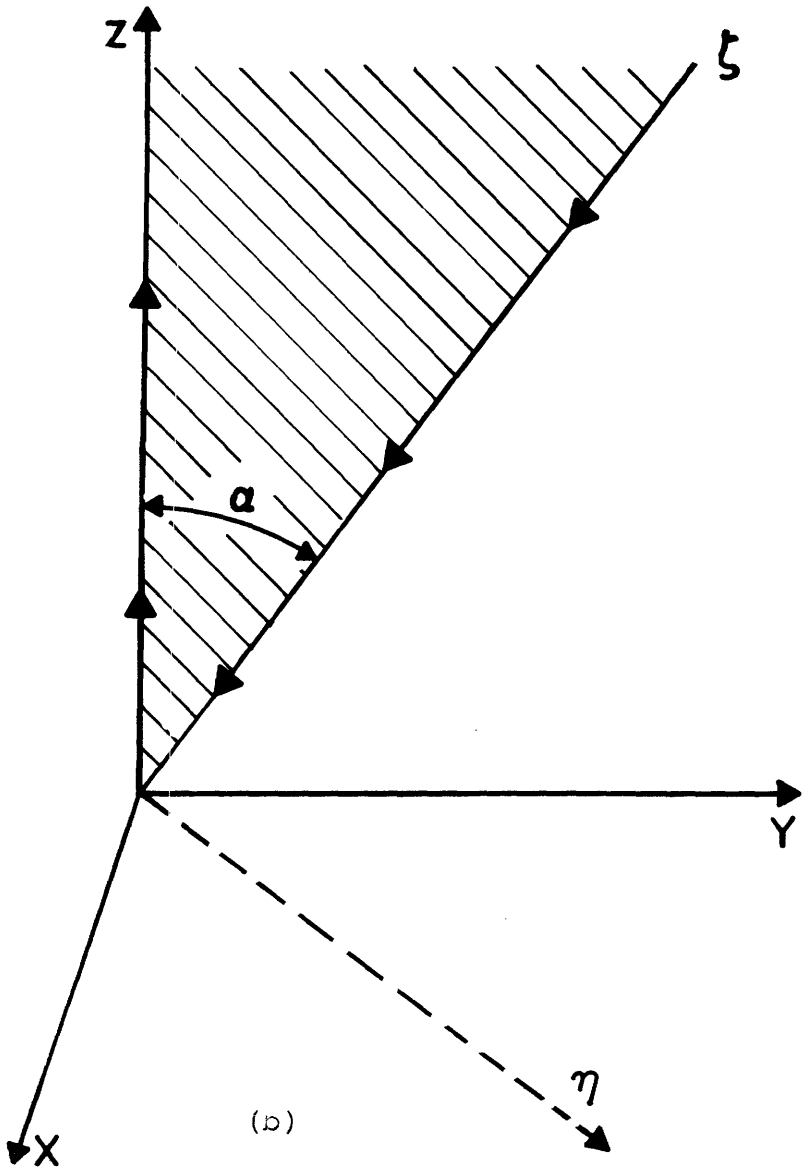

(b)

Figure 2.2

Figure 2.3

Surfaces of Discontinuity (shaded areas) associated with individual terms in equation 2.3. Arctangents are evaluated from $-\pi$ to π.

(a) dislocation line corresponding to term $\tan^{-1}(y/x)$

(b) dislocation line corresponding to term $\tan^{-1}(n/x)$

(c) dislocation line corresponding to term

$$\tan^{-1}\left(\frac{xr \sin \alpha}{x^2 \cos \alpha + yn}\right) .$$

(d) dislocation surfaces obtained by putting the expressions shown in (a), (b) and (c) into equation 2.3.

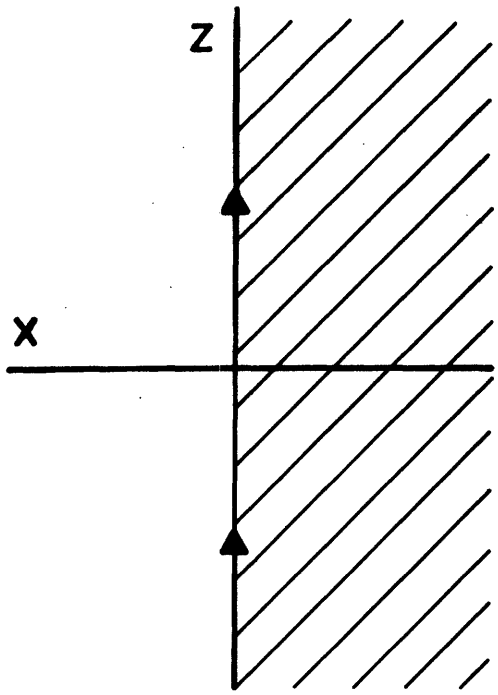

(a)

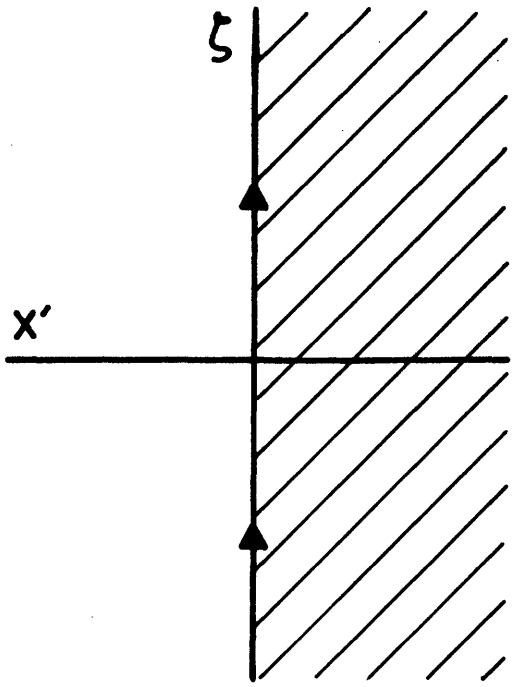

(b)

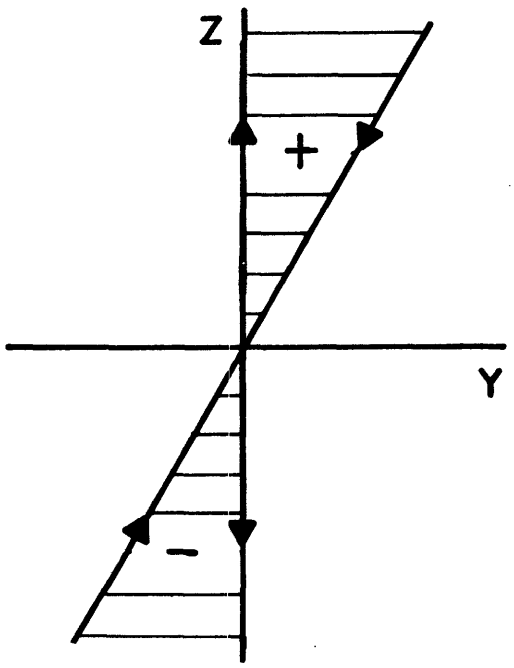

(c)

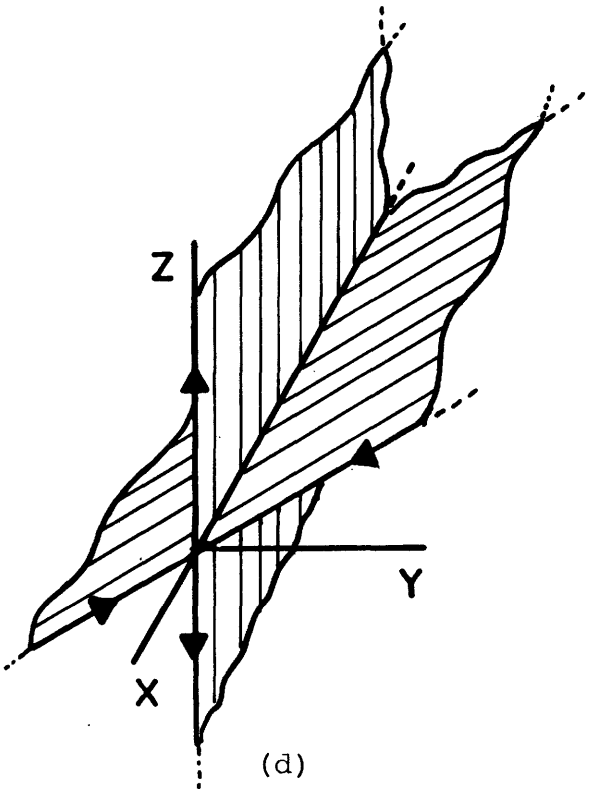

(d)

Figure 2.3

Figure 2.4

Surfaces of Discontinuity (shaded areas) associated with individual terms in equation 2.4 with $\alpha = 0$. Arctangents are evaluated from $-\pi$ to π.

(a) dislocation line corresponding to term $\tan^{-1}$ (x/-y)

(b) dislocation line corresponding to term $\tan^{-1}$ (x/-n)

(c) dislocation line corresponding to term

$$\tan^{-1}\left(\frac{xr\ \sin\alpha}{x^2\ \cos\alpha\ -yn}\right)$$

(note these surfaces are complimentary to those surfaces in Figure 2.3c)

(d) dislocation surface obtained by combining the terms in equation 2.4.

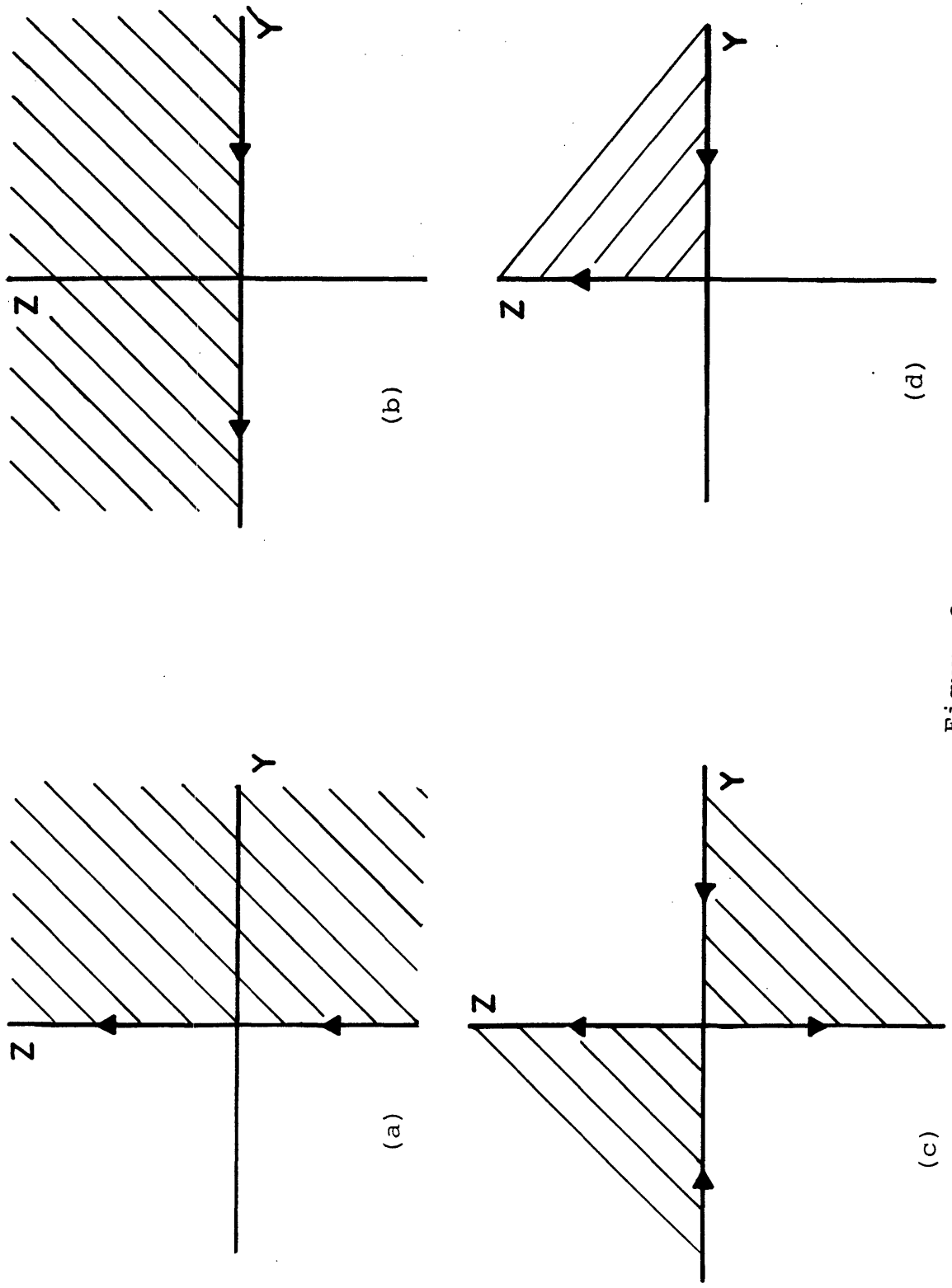

Figure 2.4

Figure 2.5

Surfaces of discontinuity (shaded regions) for the primary dislocation and its image using the multivalued terms given in the text.

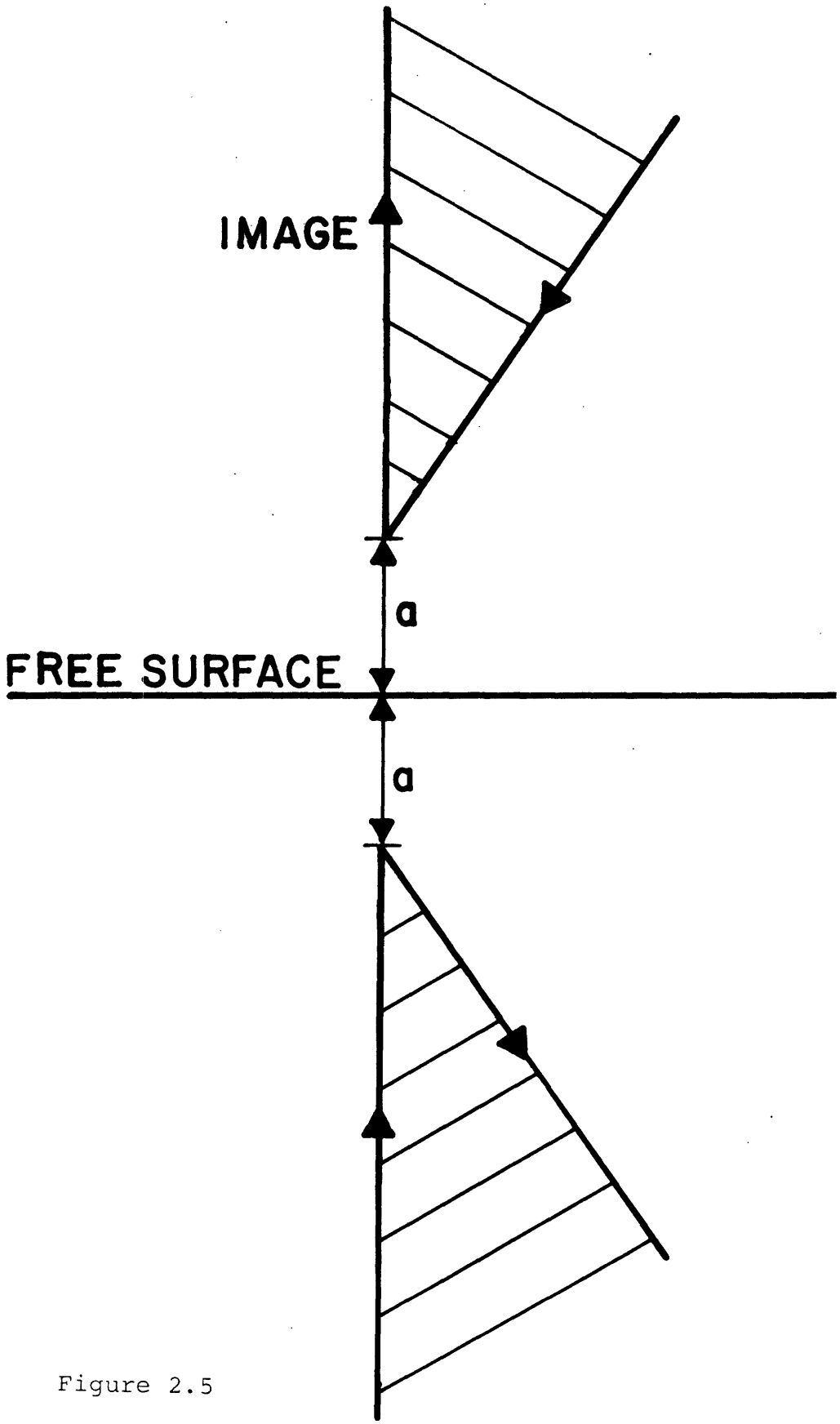

Figure 2.5

Figure 2.6

(a) Construction of a polygonal dislocation using angular dislocations. The surfaces of discontinuity (shaded regions) are in the plane of the dislocation circuit.

(b) Polygonal dislocation (planar)

(c) Construction of a polygonal dislocation in a half-space by means of dislocations. The surface of discontinuity consists of the sum of the surfaces $S_1, S_2 \ldots S_n$ for an n-sided polygonal dislocation.

(d) Same dislocation circuit as in (c) but with a different surface (S_B).

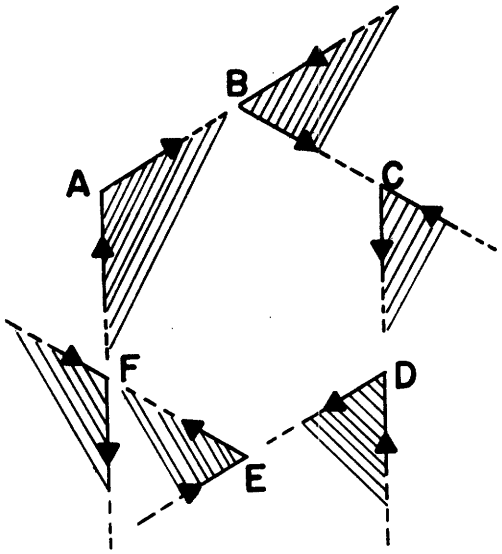

(a)

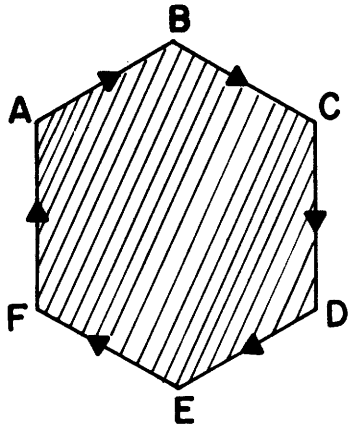

(b)

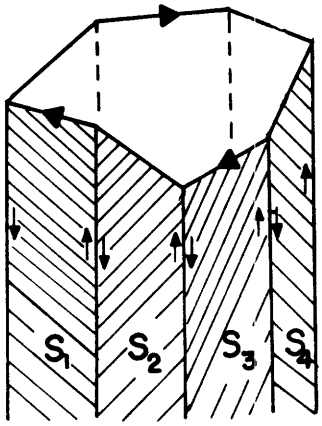

(c)

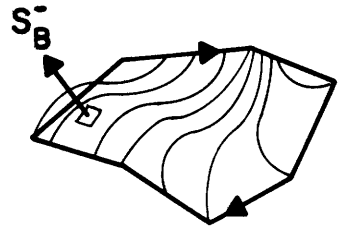

(d)

Figure 2.6

Figure 2.7

Sign convention for surfaces of discontinuity. Pointing the thumb of the right hand in the direction of the dislocation circuit and wrapping the fingers around the circuit places the finger tips on the positive side of the dislocation surface.

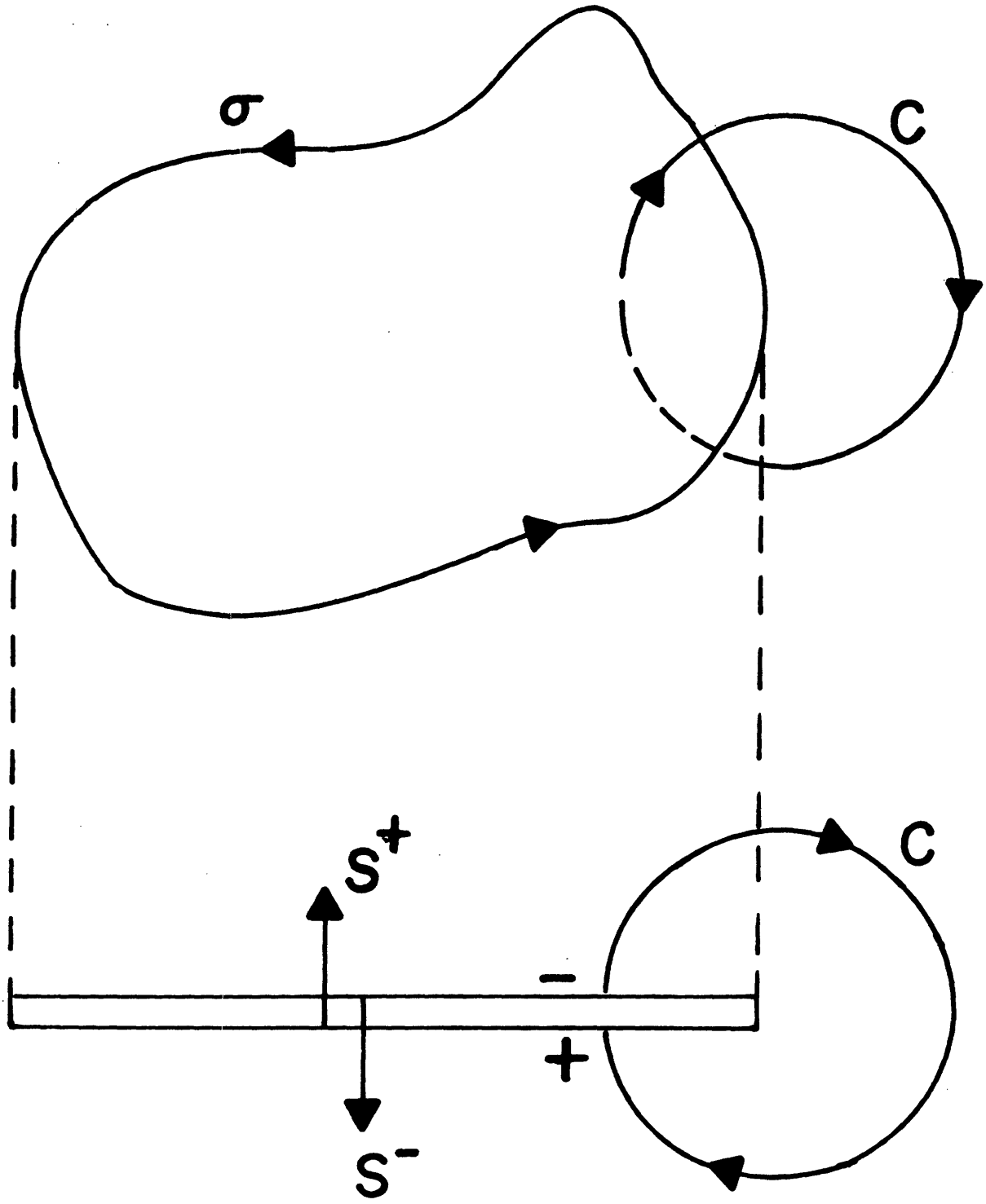

Figure 2.7

Figure 2.8

(a) Addition of the fields of two angular dislocations at the observation point (X°, Y°, Z°). The overlapping legs of the two angular dislocations cancel yielding a π dislocation (Comninou, 1973).

(b) π dislocations (with vertical legs) between the pairs of points (P_1, P_2), (P_2, P_3), (P_3, P_4), and (P_4, P_1) may be used to construct an arbitrary polygonal dislocation. The overlapping vertical legs cancel.

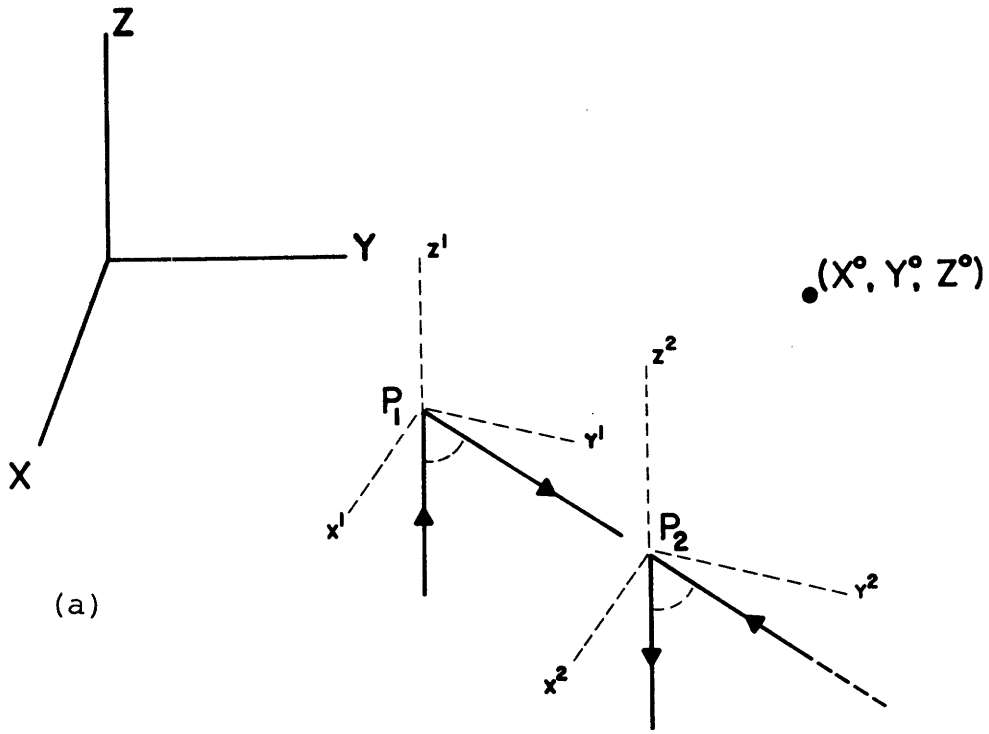

(a)

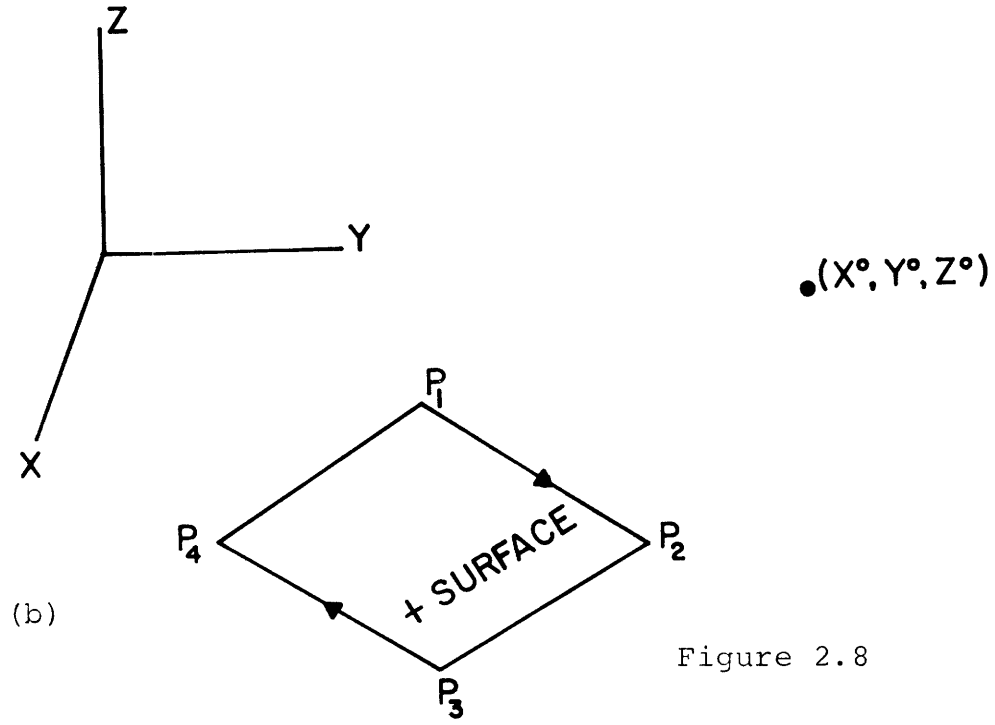

(b)

Figure 2.8

CHAPTER III

FINITE DISLOCATIONS IN FLAT LAYERED MEDIA

3.1 Introduction

In this chapter a numerical approach (Finite Source Method or FSM) to the problem of a finite dislocation in a layered half-space is presented. The ultimate goal of the chapter is the application of the FSM method to the study of dislocation fields in layered media. This problem is of interest because we wish to study: (1) the effects of layering upon static earthquake fields and (2) the effects of layering and/or a plate bottom upon the internal stress accumulation due to plate interaction. The plate bottom and its ability to modify the strain fields due to plate interaction will be of primary importance to us in Chapter IV.

One of the simplest approaches to the problem of a dislocation in a layered half-space is obtained if the problem is restricted to two dimensions. The resultant fields are quite simple and the method of images may be used to obtain the effects of layering. This method has been applied by Rybicki (1971) to study the 1966 Parkfield earthquake and by Chinnery and Javanovich (1972) to examine the effects of a buried soft layer.

Rybicki (1971) found that for a soft surface layer over a more rigid half-space that the displacements and strains

decay with distance from the fault much faster than those of the homogeneous half-space. He arrived at essentially the same results as Kasahara (1964) by concluding that application of half-space models to a realistic earth (where rigidity increases with depth in the lithosphere) yields an apparent depth which is shallower than the actual depth. On the other hand, Chinnery and Javanovich (1972) were interested primarily in buried zones of low rigidity and concluded that soft layers below the source leads to increased displacements with distance away from the fault in comparison to half-space models.

The first study of the three-dimensional problem of a point dislocation in a layered media was made by McGinley (1968). Braslau and Lieber (1968) also made a theoretical study of the problem but left their results in quadrature. McGinley's (1968) conclusions on the effects of layering were essentially the same as those of the later two dimensional studies mentioned above. Sato and Matsu'ura (1973) have recently studied in three dimensions the displacement fields for a finite dislocation in a layered half-space by numerically integrating the earlier work of Sato (1969). One of the important results from the three dimensional models is the sign reversal of certain fields for realistic earth models in comparison to half-space models (McGinley, 1968; Sato and Matsu'ura, 1973).

In order to extend the work described above this chapter

presents a study in three dimensions of finite Volterra (1907) dislocations in layered media. Of particular interest to us here are the fields within a few characteristic fault lengths away from the source. It is this region which allows geodetic measurement of displacement fields. At distances greater than this the fields approach those of a point source and the effect of the media becomes critical (McGinley, 1968; Sato, 1971; Sato and Matsu'ura,1971; Jovanovich and Chinnery, 1974a,b). Our goal then is to determine under what circumstances the effect of the media is important in the near-field region and/or when the effective media is that of a homogeneous half-space. The only previous calculation of this sort was made by Sato and Matsu'ura (1973). They calculated the vertical component of displacement for an oblique thrust fault. Their numerical procedure required considerable computation time (approximately one hour) on computers such as the IBM 360/195 (personal communication from M. Matsu'ura, 1973). This is approximately the time that would be required on the IBM 370/168 used by the author. The calculation is time consuming because it is first necessary to integrate the solution for a point source at a particular point. Next this result is used as one point in the integration over the fault plane. This process has to be repeated for the various components of the displacements and/or strains. The FSM method to be introduced here eliminates the time consuming integration over the fault

plane and simultaneously solves for all components of the field. The first portion of this chapter is devoted to a description of the theory and technique used in the FSM. The chapter concludes by applying the FSM to realistic earth models.

3.2 Finite Sources in Layered Media

3.2.1 A finite source numerical method in three dimensions

The summation of images for the two-dimensional plane-layered problem is perhaps the simplest of the numerical approaches. Jungels and Frazier (1973) and Alewine and Jungels (1973) have recently applied a two-dimensional finite element technique to solve for the combined effects of a complex source and media. Because of the assumption of two dimensionality these solutions are not especially useful at distances greater than a fault length away.

In three dimensions the problem becomes complicated. One numerical approach to the problem consists of making the calculations using three-dimensional finite elements. However, finite element node positions must be specified for each model making the task of studying various models extremely tedious. In addition, the matrices involved become too large to handle easily on most computers.

Another approach to the three-dimensional problem involves reducing the problem to quadrature in a cylindrical coordinate system. The resulting integrals contain Bessel functions and

can be integrated using a number of numerical techniques. One of the most popular approaches consists of fitting the integral kernels with exactly integrable functions and converting the integral to a series of exactly integrable integrals. This method has been applied by McGinley (1968), Ben-Menahem and Gillon (1970), Sato and Matsu'ura (1973), and others. We now wish to propose another approach to the study of dislocations in heterogeneous media which should allow for a convenient formulation of the problems in this thesis. The method is applied in cartesian coordinates and uses the discrete Fourier transform.

The prime advantage of our numerical scheme lies in the fast representation of the source (primary) fields in terms of the fields due to layering and/or a free surface (secondary fields). It is customary in geophysics to represent point sources in terms of a discontinuity in the secondary fields across the plane of the point source (e.g. Saito, 1967). We modify this approach and represent finite sources in terms of discontinuities in the secondary fields across the layer interfaces. Consider the problem of a finite dislocation embedded in the top layer of a layered medium (figure 3.1). Inside medium 1 we have primary fields and secondary fields. The primary fields will be constructed via the angular dislocations described in Chapter II (using the solutions of Yoffe (1960) and Hokanson (1963). Continuity of stress and

displacement across the interface between medium 1 and medium 2 yields the result

$$3.1 \qquad Y_1^P + Y_1^S = Y_2^S$$

or

$$3.2 \qquad Y_2^s - Y_1^s = Y_1^p$$

where superscripts p and s refer to primary and secondary and the Y's represent any of the displacements and/or stresses on the interface. Thus we may represent the source (finite or point source), in solving for the secondary fields, as a discontinuity in the secondary fields. In practice, the solutions will be formulated in k-space so that the Fourier transform of the source field at the interface will be needed. This will be accomplished with the fast Fourier transform (Cooley, and Tukey, 1965). This approach then allows us to use the matrix method for flat layered media (Haskell, 1963; Singh, 1970) and to solve the complex problem in which the source is distributed throughout several homogeneous layers.

Although in this thesis the term primary field will imply the field due to a finite source in an infinite medium it can be taken in a general sense to be that field for which a solution is already available. Thus, for example, if we have the solutions for a homogeneous half-space then the secondary field represents the effect of only the subsurface layers.

Under these circumstances, considerable computational efficiency (and even accuracy) can be obtained by the elimination of what is known from the computations.

In our case we have chosen the primary field to be the solutions due to a finite polygonal dislocation embedded in an infinite medium. These solutions are constructed using angular dislocations and the methods described in chapter II. The displacements and stresses for an angular dislocation in an infinite medium have been obtained by Yoffe (1960) and Hokanson (1963) respectively.

Once the primary fields are constructed, we may find the total solution to the problem of the finite source in a layered media by adding secondary fields to the primary solutions. The secondary fields must satisfy the static Navier's (homogeneous) equation and must be chosen so that the total field obeys all of the necessary boundary conditions. A solution to the homogeneous Navier's equation can be constructed from vector harmonics (Morse and Feshbach, 1953).

The construction of the secondary fields via vector harmonics will be described in the following section.

3.2.2 Homogeneous solutions

We now wish to set up the solutions to the homogeneous Navier's equation,

$$\nabla^2 \vec{u} + \frac{1}{1-2\sigma} \vec{\nabla}(\vec{\nabla}.\vec{u}) = 0 \qquad 3.3$$

where

$$\sigma = \frac{\lambda}{2(\lambda+\mu)}$$

in a form which can be used to find a matrix solution to the problem. We follow Morse and Feshbach (1953), McGinley (1968), and Ben-Menahem and Singh (1968) and use the three vector solutions

3.4
$$\vec{M} = \nabla\psi$$
$$\vec{N} = \nabla X(\hat{e}_z\psi)$$
$$\vec{F} = \vec{G} - 2\delta\nu z\vec{N}$$

where
$$\vec{G} = 2\psi\hat{e}_z - \vec{N}$$
$$\delta = \frac{1}{3-4\sigma}$$

and ψ is a solution to the Laplace equation $\nabla^2\psi = 0$. $\hat{e}_z$ is the unit vector in the z direction and ν is the wave vector in the z direction. If the z dependence of ψ is separated out and a transform taken over the transverse cylindrical (Singh, 1970) or cartesian components we may write the solutions in 3.4 in k-space. In order to take advantage of the FFT algorithm (Cooley and Tukey, 1965) we chose to use cartesian coordinates. Thus, our three solutions in k-space may be written in the form

3.5 $$\vec{N}^{\pm} = \{ik_x \psi^{\pm}\hat{e}_x + ik_y \psi^{\pm}\hat{e}_y \pm \nu\psi^{\pm}\hat{e}_z\}$$

3.6 $$\vec{M}^{\pm} = \{ik_y \psi^{\pm}\hat{e}_x - ik_x\psi^{\pm}\hat{e}_y\}$$

3.7 $$\begin{aligned}\vec{F}^{\pm} = &\{-(1\pm 2\delta\nu z)\ ik_x\psi^{\pm}\}\hat{e}_x \\ &+ \{-(1\pm 2\delta\nu z)\ ik_x\psi^{\pm}\}\hat{e}_y \\ &+ \{\pm\nu(1 \pm 2\delta\nu z)\}\hat{e}_z\end{aligned}$$

where $\nu^2 = k_x^2 + k_y^2$ and $\psi^{\pm} = A^{\pm}(k_x,k_y)e^{\pm\nu z}$

We may now write a general solution to the homogeneous Navier's equation in the form

$$\vec{u} = A^{+}\vec{N}^{+} + A^{-}\vec{N}^{-} + B^{+}\vec{M}^{+} + B^{-}\vec{M}^{-} + C^{+}\vec{F}^{+} + C^{-}\vec{F}^{-}$$

Thus the displacements are

3.8 $$\begin{aligned}u_1 = &\ ik_x e^{\nu z} A^{+} + ik_x e^{-\nu z} A^{-} \\ &+ \{ik_y e^{\nu z}\}B^{+} + \{ik_y e^{-\nu z}\}B^{-} \\ &+ \{-(1+2\delta\nu z)ik_x e^{\nu z}\}c^{+}\ \{-(1-2\delta\nu z)ik_x e^{-\nu z}\}C^{-} \\ u_2 = &\{ik_y e^{\nu z}\}A^{+} + \{ik_y e^{-\nu z}\}A^{-} \\ &\{-ik_x e^{\nu z}\}B^{+} + \{-ik_x e^{-\nu z}\}B^{-} \\ &\{-(1+2\delta\nu z)ik_y e^{\nu z}\}C^{+} + \{-(1-2\delta\nu z)ik_y e^{-\nu z}\}C^{-}\end{aligned}$$

$$u_3 = \{\nu e^{\nu z}\}A^+ + \{-\nu e^{-\nu z}\}A^-$$

$$+ \{0\}\ B^+ + \{0\}\ B^-$$

$$+ \{(\nu-2\delta\nu^2 z)e^{\nu z}\}C^+ + \{-(\nu+2\delta\nu^2 z)e^{-\nu z}\}C^-$$

and the stresses are

3.9 $$P_{13} = \{2\mu ik_x \nu e^{\nu z}\}A^+ + \{-2\mu ik_x \nu e^{-\nu z}\}A^-$$

$$+ \{i\mu\nu k_y e^{\nu z}\}B^+ + \{-i\mu\nu k_y e^{-\nu z}\}B^-$$

$$+ \{-2\mu\delta\nu[2\nu z+1]ik_x e^{\nu z}\}C^+ + \{-2\mu\delta\nu[2\nu z-1]ik_x e^{-\nu z}\}C^-$$

$$P_{23} = \{2\mu i\nu k_y e^{\nu z}\}A^+ + \{-2\mu i\nu k_y e^{-\nu z}\}A^-$$

$$+ \{-i\mu\nu k_x e^{\nu z}\}B^+ + \{i\mu\nu k_x e^{-\nu z}\}B^-$$

$$+ \{-2\mu\delta\nu[2\nu z+1]ik_y e^{\nu z}\}C^+ + (-2\mu\delta\nu[2\nu z-1]ik_y e^{-\nu z})C^-$$

$$P_{33} = \{2\mu\nu^2 e^{\nu z}\}A^+ + \{2\mu\nu^2 e^{-\nu z}\}A^- + \{0\}B^+ + \{0\}B^-$$

$$+ \{[2\lambda\nu^2(1-\delta) + 2\mu\nu^2(1-2\delta-2\delta\nu z)]e^{\nu z}\}C^+$$

$$+ \{[2\lambda\nu^2(1-\delta) + 2\mu\nu^2(1-2\delta + 2\delta\nu z)]e^{-\nu z}\}C^-$$

Equations 3.8 and 3.9 may be written in the form

$$\underset{\sim}{Y} = \underset{\sim}{E}'(z)\underset{\sim}{K}'$$

where

$$\underset{\sim}{Y} = \begin{pmatrix} u_1 \\ u_2 \\ u_3 \\ P_{13} \\ P_{23} \\ P_{33} \end{pmatrix}$$

and

$$\underset{\sim}{K}' = \begin{pmatrix} A^+ \\ A^- \\ B^+ \\ B^- \\ C^+ \\ C^- \end{pmatrix}$$

and $\underset{\sim}{E}'(z)$ is the matrix of coefficients obtained from equations 3.8 and 3.9. We may rearrange these equations into the form (Haskell, 1963)

3.10 $$\underset{\sim}{Y} = \underset{\sim}{E}(z)\ \underset{\sim}{K}$$

where

$$\underset{\sim}{K} = \begin{pmatrix} A^+ + A^- \\ A^+ - A^- \\ B^+ + B^- \\ B^+ - B^- \\ C^+ + C^- \\ C^+ - C^- \end{pmatrix}$$

The expressions for E'(z) and E(z) are given in the Appendix.

3.2.3 Matrix Approach to Layered Media

We may now use the vector solutions to the homogeneous Navier's equation to construct solutions to the problem of static fields in layered media. From equation 3.10 we have

$$\underset{\sim}{Y}_n^{(z_n)} = \underset{\sim}{E}_n^{(z_n)} \underset{\sim}{K}_n$$

where n is the layer number. Continuity of displacements and stresses on each interface requires

$$Y_n^{(z_n)} = Y_{n+1}^{(z_n)}$$

or

$$\underset{\sim}{E}_n(z_n)\underset{\sim}{K}_n = \underset{\sim}{E}_{n+1}(z_n)\underset{\sim}{K}_{n+1}$$

Solving for $\underset{\sim}{K}_n$ gives

3.11 $$\underset{\sim}{K}_n = \underset{\sim}{E}_n^{-1}(z_n)\underset{\sim}{E}_{n+1}(z_n)\underset{\sim}{K}_{n+1}$$

Equation 3.11 gives the relation between the constants in layer n and the constants in layer n+1. It is easy to find a similar relation for the $\underset{\sim}{Y}$'s since from equation 3.10 we have

$$\underset{\sim}{E}_n^{-1}(z_n)\underset{\sim}{Y}_n(z_n) = \underset{\sim}{K}_n$$

and

$$\underset{\sim}{E}_n^{-1}(z_{n+1})\ \underset{\sim}{Y}_n(z_{n+1}) = \underset{\sim}{K}_n$$

Thus equating the above expressions and using 3.18 we obtain

3.12 $$\underset{\sim}{Y}_n(z_n) = \underset{\sim}{E}_n(z_n)\underset{\sim}{E}_n^{-1}(z_{n+1})\underset{\sim}{Y}_{n+1}(z_{n+1})$$

Following Haskell (1963) we define the matrix

$$A_n = \underset{\sim}{E}_n(z_n)\underset{\sim}{E}^{-1}(z_{n+1})$$

so that

3.13 $$\underset{\sim}{Y}_n(z_n) = A_n\ \underset{\sim}{Y}_{n+1}(z_{n+1})$$

We may use 3.13 to propagate the $\underset{\sim}{Y}$ vector through many layers to the surface z=0 so that

$$Y_1(0) = A_1 A_2 \ldots\ldots A_n Y_n(z_n)$$

We may evaluate the A_n described by temporarily shifting the origin to $z=z_{n+1}$ so that

$$A_n = E_n(+d_n) E_n^{-1}(0)$$

where $E_n^{-1}(0)$ and $E_n(z)$ are given in the Appendix. We are now ready to put a source into an N-layered media.

3.2.4 A Finite Source Distributed Through Several Layers

Consider now the problem of a dislocation source distributed through several layers (figure 3.2a). We begin by examining the fields in the two adjacent layers shown in figure 3.2b. In each layer we have the primary fields (denoted by superscript p) which in this case are the fields which would be observed if no layering were present and the secondary fields (superscript s) which are a result of the layering. Continuity of displacements and stresses at $z = z_6$ yields

$$Y_5^P(z_6) + Y_5^S(z_6) = Y_6^P(z_6) + Y_6^S(z_6)$$

Solving for $Y_5^S(z_6)$ we obtain

3.14 $$Y_5^S(z_6) = D_6 + Y_6^S(z_6)$$

where

$$D_6(z_6) = Y_6^P(z_6) - Y_5^P(z_6)$$

However, from the previous section we have

3.15 $$Y_5^S(z_5) = A_5\ Y_5(z_6)$$

Thus, from 3.14 and 3.15 we obtain

$$Y_5^S(z_5) = A_5\{D_6(z_6) + Y_6^S(z_6)\}$$

or, in general

3.16 $$Y_n^S(z_n) = A_n\{D_{n+1}(z_{n+1}) + Y_{n+1}^S(z_{n+1})\}$$

Equation 3.16 allows us to relate the solution in one layer to the solution in an adjacent layer. Repeated application of equation 3.16 allows us to write the general solution of a source penetrating (m-1) layers of an n-layered medium in the form

3.17 $$Y_1^S(z_1) = G + HK_6'$$

where

3.18 $$G = D_1 + A_1D_2 + A_1A_2D_3 + \ldots A_1A_2A_3..A_{m-1}D_m$$

and

3.19 $$H = A_1A_2A_3\ldots.A_{n-1}E_n'(z_n)$$

In the last layer the boundary condition requiring that the solutions be finite at $z = -\infty$ (z being positive up) simplifies K_6' to

3.20 $$K_6' = \begin{pmatrix} A+ \\ 0 \\ B^+ \\ 0 \\ C^+ \\ 0 \end{pmatrix}$$

Substitution of equation 3.20 into 3.17 yields the following result for the stresses on the free surface

$$P_{13}(z_1) = G_4 + H_{41}\,A^+ + H_{43}\,B^+ + H_{45}\,C^+$$

$$P_{23}(z_1) = G_5 + H_{51}\,A^+ + H_{53}\,B^+ + H_{55}\,C^+$$

$$P_{33}(z_1) = G_6 + H_{61}\,A^+ + H_{63}\,B^+ + H_{65}\,C^+$$

where the subscripts on the G's and H's refer to the particular components of the respective matrices. Since the stresses must vanish on the free surface we have three equations which allow us to solve for the three unknowns A^+, B^+, and C^+. These values may then be substituted into the equations for the displacements which are found by substituting equation 3.20 into 3.17 to obtain

3.21
$$U_1(k_x,k_y,\ z = 0) = G_1 + H_{11}\,A^+ + H_{13}\,B^+ + H_{15}\,C^+$$

$$U_2(k_x,k_y,\ z = 0) = G_2 + H_{21}\,A^+ + H_{23}\,B^+ + H_{25}\,C^+$$

$$U_3(k_x,k_y,\ z = 0) = G_3 + H_{31}\,A^+ + H_{33}\,B^+ + H_{35}\,C^+$$

The inverse transform of equations 3.21 yield the desired solutions.

3.2.5 Discrete Fourier Transform

The formalism set up in the previous two sections allows us to find the displacements in k_x-k_y space for a particular depth z. The approach is based upon the discrete Fourier

Transform (Gold and Rader, 1967) which allows us to calculate the $\underset{\sim}{D}$ vector in equation 3.18. The $\underset{\sim}{D}$ vector represents the difference in displacements and tractions on the interface surface between the sources in the two media. The representation is in k-space so that the first term in the $\underset{\sim}{D}_{\ell}$ vector would be of the form

$$\Delta U_1 = U_1^{\ell+1}(k_x,k_y,z_\ell) - U_1^{\ell}(k_x,k_y,z_\ell)$$

where $U_1^{\ell+1}(k_x,k_y,z_\ell)$ is the displacement in the x1 direction at the $z = z_\ell$ interface due to the source in the $\ell+1$ medium and $U_1^{\ell}(k_x,k_y,z_\ell)$ is the same field due to a source in medium ℓ. The transforms are evaluated using the Fast Fourier Transform. Applying this approach to all the components of the $\underset{\sim}{D}$ vector and propagating our solutions to the surface allows us to construct the solutions $U_1(k_x,k_y,0)$, $U_2(k_x,k_y,0)$, $U_3(k_x,k_y,0)$. Our final solutions will be of the form

$$U_1(x^j,y^k,0) = \frac{1}{NM} \sum_{m=0}^{M-1} \sum_{n=0}^{N-1} U_1(k_x^n,k_y^m,0) e^{ik_x^n x^j} e^{ik_y^m y^k}$$

where

$$k_x^n = n\frac{2\pi}{N\Delta x}$$

$$k_y^m = m\frac{2\pi}{M\Delta y}$$

$$x^j = j\Delta x$$

$$y^k = k\Delta y$$

The sources of error involved in these calculations will be of the same nature as those encountered in conventional signal analysis problems. A detailed comparison of the discrete Fourier transform with the continuous Fourier transform and the errors involved may be found in the paper by Cooley et al. (1970).

3.3 Discussion and Application

We now turn to the actual application of the method described in section 3.2 to the solution of a dislocation in layered elastic media. In particular we shall discuss some of the details necessary to actually get numbers out of the equations presented in section 3.2 and then make a study of the effective differences between homogeneous half-space models and layered half-space models.

3.3.1 Big Numbers

One of the first problems to be faced is the selection of the sampling lengths Δx, Δy and the number of samples N_x and N_y to be used. Once this is accomplished a straight forward substitution in the equations given in 3.2 should allow us to compute the solutions. However the layer matrix A_n is made up

of cosh (νd_n) and sinh (νd_n) terms where d_n is the thickness of a particular layer. Since we expect the sample sizes Δx and Δy to be smaller than the layer thickness the terms (νd) will be of the order of $2\pi\frac{d}{\Delta x} >> 1$ which causes the elements of the A matrix to be very large. Thus in using the A matrices as they are set up in section 3.2 we end up manipulating very large numbers to find small numbers. This inevitably leads to round off errors and scaling problems. We may avoid this problem by rewriting the solution in the form (for n layers)

3.22 $$Y = D_1 + \cosh \nu d_1\, a_1\, D_2 + \cosh \nu d_1 \cosh \nu d_2\, a_1\, a_2\, D_3$$
$$+ \ldots$$
$$+ \cosh \nu d_1 \cosh \nu d_2 \ldots \cosh \nu d_{n-1}\, a_1 a_2 \ldots a_{n-1} e'_n e^{\nu d_n} K'_n$$

where the a_i's represent the layer matrices with the term cosh νd_i factored out and e'_n is the E'_n matrix with the factor $e^{\nu dn}$ taken out. We may now absorb these multiplicative constants into the constant vector K'_n without changing the problem. Thus 3.22 may be written as

3.23 $$Y = G + hK'_n$$

where $$h = a_1 a_2 a_3 \ldots a_{n-1} e'_n(d_n)$$

and $$G = D_1 + \cosh \nu d_1\, a_1 D_2 + \cosh \nu d_1 \cosh \nu d_2\, a_1 a_2 D_3$$
$$+ \ldots$$

The construction of the h vector in 3.23 may now be accomplished without the use of large numbers. However, for a fixed k_x and k_y, the G vector still has the terms which increase rapidly with the layer thicknesses. In the continuous problem these terms present no trouble since the continuous transform of the D vectors goes to zero beyond a finite limit. Thus the larger terms (higher frequencies or shorter wavelengths) are multiplied by the zeroes in the D vectors. In the discrete case the effects of aliasing and the finite window size tend to eliminate the possibility of cancellation. For layers which are thin in comparison to the total width of the Fourier window - the high frequency terms offer no problem. For thick layers the less accurate high k values are amplified out of proportion yielding considerable error in the solutions. We are therefore forced to eliminate these high k terms. The approach to this elimination may be accomplished by a review of the physics of the problem. The problematic terms in the G vector represent a layer matrix multiplied by a set of displacements and stresses applied at the bottom of the layer. If we consider the wavelength of a stress and/or a displacement on the surface as the effective area over which the boundary condition is applied then we may use St. Venant's theory (Fung, 1965) to argue that little contribution is made to our solution by those displacements and/or stresses in the D vector with wavelengths shorter than the thickness of the layer through which the solution is to be propagated.

In order to perform the effective filtering described we multiplied our D vector transforms by the following window

$$W(k_x,k_y) = \begin{cases} 1 \text{ when } \nu d_i \leq 2.0 \\ e^{3(\nu d_i - 2)^2} \quad \nu d_i > 2.0 \end{cases} \tag{3.24}$$

With the factor described in 3.24 we limit the source vectors at the bottom of the deep and/or thicker layers to long wavelength contributions while the source vectors at the bottom of thin near surface layers contribute at almost all (if not all) wavelengths to the solution. This filter has been checked by constructing a model with several identical layers (effectively a half-space) and comparing the results with exact half-space results. The comparison of the two results yields accuracies which are essentially those of the half-space models to be presented in the next section.

3.3.2 Comparison with half-space solutions

We now proceed to test the program by comparing the numerical results with the exact results for a dislocation in a homogeneous half-space. Such a comparison will allow a study of the errors involved in our numerical approach and will yield a stringent test of the program itself. Sato and Matsu'ura (1973) and Sato (1971) have contented themselves with a discussion of the fit of the integral kernel with a polynomial.

Such a discussion must represent indirectly the final error involved in the displacements but does not test in any way the correctness of the integral kernel. Similarly, Javanovich et al. (1974) apply different numerical techniques to the same integral kernel to obtain the relative error between the two methods. However, they do not discuss the accuracy of their numerical method with any closed solution (e.g. a homogeneous half-space). This again leaves open the question of the absolute error of the numerical procedure. We shall assume in this thesis that at least a comparison was made in the above mentioned papers in order to insure that their integral kernels are correct.

A straight-forward method of testing the errors involved in the Fourier transform of the primary fields is to simply Fourier transform the portion of the aliased primary field which was neglected (Cooley, Lewis and Welch, 1970). Thus, by summing up the contributions to the primary field from neighboring Fourier boxes and Fourier transforming, we may obtain a direct measure of the error involved in transforming the primary fields. Unfortunately, we have no means of calculating the aliasing when we return from the transform space to x, y space. For this reason we resort to simply comparing our results with the exact solutions for a homogeneous half-space (Comninou, 1973).

We begin by testing the simple model shown in Figure 3.3. It is a vertical dip-slip fault with a length and width of

4 km and a depth (top of the fault) of 4 km. The vertical fault offers the greatest challenge to the finite source method because of the rapid changes in some displacements as one goes from one side of the fault to the next. For this reason our choice of Δx and Δy must be small enough to sample the short wavelength changes in displacement near the fault.

In Figures 3.4, 3.5, and 3.6, we have plotted the displacements for the model in Figure 3.3 calculated by two methods. The solid line represents the numerical solution using a 64 x 64 grid and a sampling interval of 1 km. The exact solution (when different from the numerical solution) is shown by a dashed line. The U_1 displacement in Figure 3.4 has the general form of the second derivative of a Gaussian distribution while the U_2 and U_3 displacements shown in figures 3.5 and 3.6 behave like the first derivative of a Gaussian function. As can be seen by comparing figures 3.4-3.6, the 64 x 64 grid gives the best results for the lower frequency single derivative fields. Considerable improvement in the displacements may be obtained by decreasing the sample size and increasing the grid to 128 x 128 points (Figure 3.7). The changes in U_2 and U_3 would not be visible in figures 3.5 and 3.6. The improvement in the accuracy is shown in detail in figure 3.8. The choice of x and y is not optimum so that a small amount of aliasing exists near the edge of the Fourier

box used. In figure 3.8(a) we have plotted the difference between the exact solutions computed via Comninou's results (1973) and the numerical results obtained by the FSM. It should be pointed out that the program used to compute Comninou's results has been compared with (1) a program which numerically integrates Maruyama's (1964) Green's triad over the surface of the fault and (2) a program to compute the exact solutions for vertical faults given by Press (1965). All three programs agree to 5 places which is close to the numerical accuracy for single precision on the IBM 370/165 used. The interesting point to be made in figure 3.8(a) is that the difference between the numerical solution and the exact solution is essentially constant across the Fourier box. Thus, as can be seen in Figure 3.8(b) and 3.8(c), the relative error tends to be largest where the displacements are smallest. This behavior is quite similar to the % error of geodetic measurements and should allow us to use our results even near the edge of the Fourier box (assuming that the accuracy of the computation exceeds the accuracy of the data). For the 128 x 128 grid the % error for the single derivative fields remains less than 1% for at least 3 fault lengths away and is of the order of .1% for a distance of the order of 1-1/2 fault lengths. For the double derivative field (U_1 in this example) the error varies from 60% (due to the small exact solution near the origin) to 5% over the first 3 fault lengths away. The 64 x 64

grid is found to be quite adequate for the single derivative fields but it forces us to choose too large a sample for the double derivative fields. For the problems to be considered in this thesis we have chosen a 128 x 128 grid so that we may study all components of displacement with reasonable accuracy.

In applying the FSM it is important to remember that the errors are model dependent. The effects of source size and depth can easily be taken care of by choosing sample sizes several times smaller than the fault dimensions and less than or equal to the fault depth. This effectively pushes the Nyquist k to a high enough value to eliminate the effects of the neighboring Fourier boxes in k_x-k_y space. For a fixed number of points however we may have difficulty in the x-y space due to the finite size of the Fourier windows. For what we wish to call realistic earth models (increasing rigidity with depth) the fall-off with distance is much more rapid and the accuracy of such models is increased due to the fact that these solutions do not feel the edges of the Fourier box. For models in which the rigidity decreases with depth the fields extend to greater distances and the edge effects become more important. For a fixed number of points and well chosen sample sizes these models tend to be less accurate. Fortunately this problem can easily be spotted in the solutions when the solutions and/or their slopes are significantly different from zero at the edges of the Fourier box. It can be eliminated by increasing the number of points.

3.3.3 Soft surface layer

We now wish to apply the FSM to particular models in order to examine the effects of layering upon earthquake displacements. We shall begin with a problem of a soft (sedimentary) layer overlying a harder half-space (figure 3.10). The soft surface layer is important because it offers the largest contrast in elastic properties and is nearest to the surface (for a typical continental crust). We are especially interested in this problem because of its possible effects upon vertical displacements and tilts observed near strike-slip faults. Recent observations of anomalous tilts by Stuart and Johnston (1974) indicate that the moment of the precursory slip before a particular earthquake was approximately 10 times that of the subsequent event. We wish to examine here the possibility that this observation could be an effect of the media.

In figure 3.10 we show the tw. strike-slip models to be considered. Model VSTOP (vertical strike-slip in the top layer) shown in figure 3.10(a) represents a small (LENGTH (L) = .5 km, WIDTH (W) = .5 km) strike-slip event at a depth (D) of .5 km. It is embedded in the soft surface layer and is assumed to have a net slip of 1 meter. In figure 3.11 the U_1 displacement for VSTOP (perpendicular to the strike of the fault) is compared to the same component of motion for a half-space model with the elastic properties of the harder

high density of small ($M \leq 5$) earthquakes between the depths of 3-10 km and a few events outside of this depth range (Wesson et al., 1973). Thus, most of the events fall below the sediment layer in this area.

The fault parameters for the model shown in 3.10(b) are L = 2 km, W = 2 km, and D = 3 km. The net slip is one meter (this allows for easy scaling).

In figures 3.17-3.20 we have plotted a comparison of the displacements for VSBOT versus those of a half-space with the elastic constants of the lower half-space in VSBOT. The U_1 and U_2 displacements show a distinct amplification over the hard half-space model and a broadening of the peaks. For the U_2 displacement this is essentially the same result obtained by Rybicki(1971) for a finite two dimensional fault. In figures 3.19 and 3.20 we show two separate profiles of the U_3 displacement in order to point out the small differences (less than 10% at x_2 = .5 km and less than 20% at x_2 = 2 km) between VSBOT and the half-space model. We conclude from these results that the soft surface layer has an insignificant effect upon the vertical displacements (and therefore the tilts).

For VSBOT all the fields approach those of the hard half-space model at approximately eight fault widths (16 km) away from the fault. This result is expected since most of the far field energy should be transmitted via the harder half-space below the soft surface layer.

layer in VSTOP. The profile is taken at x_2 = .2 km. The fault extends from x_2 = +.25 km to x_2 = -.25 km. The net effect of the soft layer on this component is effectively a reduction in amplitude (by a factor of 5) in comparison to the hard half-space model. In figure 3.12 we compare the solution of VSTOP to a soft half-space (with elastic constants equal to those of the top layer). The agreement is excellent in this case and indicates that for small events in the top layer that the displacements in this layer are essentially those of the source in a soft half-space. The same conclusion may be reached for the other components by viewing figures 3.13 through 3.16. A small deviation from this interpretation may be seen in figure 3.14 in which the U_2 displacements for VSTOP have a slightly faster fall-off with distance than the soft half-space model.

As can be seen in figure 3.15 the wrong choice of elastic constants for the half-space can have a considerable effect upon the vertical displacements and tilts (factor of five for the case shown). This will be a point of discussion in our summary.

Now consider model VSBOT (figure 3.10b) in which the strike-slip fault is below the soft layer. The strike-slip event below a soft surface layer is of special importance on that portion of the San Andreas between Parkfield and San Juan Bautista, California. The region is characterized by a

In summary, we wish to make the following points about the effects of a soft surface layer upon strike-slip faults: (1) if the source is in the top layer the fields behave essentially like those of a half-space model with the elastic constants of the soft layer, (2) if the source is below the soft layer then U_1 (perpendicular to strike) and U_2 (parallel to strike) show a maximum amplification of approximately 40% over the hard half-space model while the U_3 displacement is essentially the same as the hard half-space model. As a corollary, these results suggest that one possible explanation of the results of Stuart and Johnston (1974) is that the precursory slip occurred mostly in the harder half-space while the earthquake occurred in the softer surface layers. If the models used to match the data were half-space models with a Poisson's ratio of .25 (typically used in modeling earthquake fields) then a good approximation of the precursory slip would be obtained via tilts while the earthquake slip would be grossly underestimated.

In conclusion we find that half-space models should be used with care and a special effort made to determine which layer(s) contain the source. This conclusion will be discussed further in the following sections.

3.3.4 Continental crustal models vertical faults

We now proceed to study several types of sources embedded in a typical continental crust in order to examine the effects of layering upon earthquake near-fields. In particular, this section compares a typical half-space model ($\sigma = 1/4$) to layered models in order to examine the errors involved when layering is neglected. The only previous study of a finite fault model of the sort presented here has been made by Sato and Matsu'ura (1973). They calculated the vertical component of displacement for a shallow dipping fault in a four layered half-space (four layers over a half-space). In figure 3.21 we show a four layered crust with elastic constants typical of continental crusts which will be used here to represent what we shall call a realistic crust (figure 3.21). The intermediate layer in this model does not appear to exist for certain areas of California (Eaton, 1963) but is a feature of the crust in Japan (Sato and Matsu'ura, 1973). The effect of leaving out this intermediate layer can be found approximately by comparing the results of this section to those of the preceding section on the soft surface layer.

The first models to be considered are vertical faults in realistic crustal structures. In figure 3.22(a) we show model RVSS (Realistic Earth, Vertical fault, strike-slip). This model is 16 km long, 8 km wide, and has a net slip of 1 meter.

The depth to the top edge of all realistic crustal models considered will be kept at 3 km. The displacements for RVSS are shown in figures 3.23-3.25.

The results are surprising since the U_1 and U_3 displacements are affected in the opposite sense to those for the simple soft layer over a half-space presented in the previous section. In figure 3.23 the U_1 displacements differ significantly (approximately 40%) from those of the half-space values when observed within two fault widths away (16 km). At distances of 2 to 3 1/2 fault widths away the displacements fall off at the same rate with the layered model behaving like a half-space with elastic constants equal to those of the second layer in the crustal model. At greater distances the half-space fields fall off faster than the layered model. The behavior described is expected from such layered models (McGinley, 1968). These are also the essential features visible in the U_3 displacements in figure 3.25.

The U_2 displacements (parallel to the strike of the fault) shown in figure 3.24 exhibit an amplification (approximately 10% at the peak) over the half-space model as was shown to be the case for the strike-slip fault beneath a soft surface layer. Otherwise the fall-off behavior is similar to the U_1 and U_2 fields. The fall-off in this case, however, is not as easily distinguished from the half-space due to the rapidity of the fall-off for both models.

We now examine the model RVDS (Realistic earth, vertical fault, dip-slip) which is a vertical dip-slip event. It spreads through the same layers as the strike-slip model considered above. In this case the U_1 and U_2 displacements show the greatest deviation from the half-space model (figures 3.26-3.28). The U_3 displacements (figure 3.29) are essentially undisturbed by the layering. The U_1 displacements of the layered model are greater than those of the half-space model at distances less than two fault widths (16 km) away but begin a more rapid fall-off with distance past this point than the half-space fields. This rapid fall-off occurs for all the components. The most dramatic change due to layering occurs in the U_2 displacement across the middle of the fault (figure 3.28). Here the fields differ not only in amplitude but in sign as well.

To summarize the results obtained for vertical faults we find that (1) displacements in the primary direction (i.e. parallel to the burgers vector) do not differ significantly from the half-space models while the other components show large changes (and even sign reversals), (2) the fall-off with distance for all displacements is faster for the realistic model than the half-space models for the dip-slip event and slower than the half-space model for the strike-slip case. We now study the effects of oblique faulting in a realistic crustal model.

3.3.5 Oblique faults

We now wish to examine the special case of a shallow dipping fault (dip = 30°) cutting through the realistic crust shown in figure 3.21. In figure 3.30(a) a schematic drawing of model ROSS (Realistic earth, Oblique fault, Strike-slip) is shown. Three profiles of the displacements are shown in figures 3.31-3.33. In figure 3.31 the U_1 displacements of the layered model show the greatest deviation from the half-space model when they are observed at a position which is not directly over the fault (negative values of distance). Over the fault the difference between the half-space and layered model is smaller. The U_2 displacements for model ROSS shown in figure 3.32 are greater than the half-space values (by approximately 20% at maximum) when observed over the fault. Away from the fault the fall-off with distance is faster for the layered model. However, the opposite is true for the fall-off of the U_3 displacements in figure 3.33. The primary point to be observed in figure 3.33 is that the half-space and layered models do not show any large differences (i.e. greater than 20%).

In figure 3.30(b) an oblique dip-slip fault model is shown. The displacements for model RODS (Realistic earth, Oblique fault, Dip-slip) are shown in figures 3.34-3.37. As for model ROSS described above the greatest deviations in the

general form of the displacement profiles occur just off the projection of the top and bottom edges of the fault onto the surface. Over the fault the fields differ in amplitude but the general shape of the profile is unchanged. For this particular model the vertical component (figures 3.36 and 3.37) shows the smallest change (especially over the fault) from the half-space values. The U_3 displacements for the layered model exhibit the reverse area pointed out by Sato and Matsu'ura (1973) in their study of this component for an oblique thrust fault. Thus our results agree (at least qualitatively) for this case.

In summary, we have used the FSM to study a few specific source models embedded in a layered crust. The size of the layers and the elastic constants involved are typical of continental crusts. Because of the variability of the results between the models it is difficult to point to any particular conclusions which encompass all of our results. Even if such conclusions could be drawn from the specific problems studied they could not be extended to those problems in which the source penetrates other layers.

We believe that if a detailed study of the source is to be made that layering cannot be neglected in a near-field study. If, however, one is able to live with a certain amount of error then half-space solutions may be used to model particular components of the field with varying degrees of success (from 10 to 40%). With the continuing improvement

in geodetic techniques, however, we feel that layered models are here to stay.

3.3.6 A hard layer over a soft half-space

In the last chapters of this thesis we shall be concerned with the computation of the fields due to the interaction of lithospheric plates. The problem will be posed in terms of dislocation theory. Because of the speed and ease with which dislocations in a homogeneous half-space can be computed it behooves us to examine the effects of neglecting the bottom of the plate. For the particular problem of a dislocation embedded in a hard layer (lithosphere) overlying a soft half-space (asthenosphere) we feel that if the layer thickness is much greater than the other characteristic dimensions of the problem (such as dislocation size or distance from the dislocation) that the effects of the soft underlying layer may be neglected. However, when all of these dimensions become comparable the soft layer could play a major role in our solutions. For this reason we now examine two dislocations of particular interest embedded in a hard layer which overlies a soft half-space.

In figure 3.38 we show a schematic of model VASS (Vertical fault, Asthenospheric model, Strike-slip). The displacements for this model are shown in figures 3.39-3.42. The U_2 component or primary field (displacement parallel to

the Burgers vector) plotted in figure 3.40 shows what we consider to be a negligible difference between the layered and half-space models. The effect of the soft layer is to amplify the U_2 displacements in the near-field (the amplification is more visible on other profiles not shown). As we move away from the fault, however, the fall-off with distance from the fault is less rapid than that for the half-space. This effectively extends the range of the shear strain component computed from U_2.

The components most affected by the soft layer are U_1 (figure 3.39) and U_3 (figures 3.41 and 3.42). The U_1 component is simply amplified but the U_3 component exhibits reversals in the sense of the motion.

These results indicate that we may use half-space models (to a good approximation) to get the physics (i.e. the sense) of the horizontal displacements and the strains computed from them. The same is not true for the vertical displacements.

Now consider the model described in figure 3.43. It represents a dislocation in which the two sides are being pulled away from one another. We shall show in the last chapter that such a model can be representative of lithospheric plate collision. Thus model VAC (Vertical fault, Asthenospheric model, Collision) in figure 3.43 represents (minus relative rigid body terms to be discussed in Chapter IV) two plates impinging upon one another across the dislocation interface.

The displacements for this model are shown in figures 3.44-3.48. In the case of model VAC the U_1 displacements shown in figure 3.44 represent the primary field. The effect of the soft layer upon U_1 in this example is a broadening of the peaks. This will practically double the effective fall-off distance of the compressive e_{11} strains for this model. However, the sense of the motion for the layered model is in agreement with the half-space models. This statement cannot be made, however, for the U_2 components shown in figures 3.45 and 3.46. The U_3 components shown in figures 3.47 and 3.48 exhibit a large amplification over the half-space values but no change in the sense of motion. Thus in this case we may obtain the sense of motion for model VAC by using half-space models for only the U_1 and U_3 displacements and not the U_2 displacement. This is unfortunate for it implies the possibility of obtaining the incorrect sense of the horizontal motion (U_1, U_2) and its derivatives (e_{11}, e_{22}, e_{12}) if we simply use half-space models.

The two models discussed above represent extreme cases in which the soft layer is unrealistically soft and the dislocation penetrates the hard surface layer. In the case of the San Andreas which has only shallow focus earthquakes (less than 20 km) a more appropriate model would be one in which the dislocation penetrates only the upper fraction of

the surface layer. Such a model is shown in figure 3.49 and the displacements for this model are compared with half-space displacements in figures 3.50-3.52. The underlying layer in this model is extremely soft (as for models VASS and VAC). However, the deviation of these results from those of a half-space is insignificant. The greatest difference is approximately 5% and occurs in the U_1 displacement shown in figure 3.50. If in addition to making the fault more realistic in size we also make the soft layer have elastic properties closer to those of the low velocity zone as determined seismically by Herrin (1972) then the results approach those of a homogeneous half-space (figures 3.53-3.55). These results imply that in the case of shallow faults in a more realistic structure that half-space models may be used without a significant loss of accuracy.

In summary, we have examined the problem of a hard elastic layer over a soft half-space. In the case of the extremely soft underlying layer we conclude that: (1) half-space models yield the correct sense of horizontal motion for a strike-slip fault penetrating the hard layer (with a significant difference in amplitude), (2) half-space models for collisional faults of the type shown in figure 3.43 can predict the wrong sense of motion (depending upon the component and the model), and (3) the vertical component is the most sensitive to the soft underlying half-space.

For those models more directly applicable to California (i.e. a shallow fault and a moderately soft underlying half-space), we find that the homogeneous half-space model differs insignificantly from the layered model. These conclusions are important and will be used throughout Chapter IV.

3.4 Conclusions

The problem of computing the fields of a finite source embedded in a layered media has often eluded computation in the past because of the necessity of summing many point sources in the representation of the finite source. We have developed a numerical technique (Finite Source Method or FSM) which eliminates the integration over the source and allows for the fast computation of solutions for a variety of problems. We have applied the FSM specifically to static dislocations but it should also be useful in dynamic problems and/or even electromagnetic prospecting problems.

In particular we have applied the FSM to the problem of static displacements due to dislocations embedded in layered media and compared the results to those of a half-space ($\sigma = 1/4$). Since an infinite number of models exist for study we have tried to limit our study (and therefore our conclusions) to a few particular models. We find that in many cases the half-space model produces results which are

significantly different from layered models. We have not attempted to generalize the results because we feel that the reader may easily apply the FSM to his own particular models. The layered models we have presented, however, have the general features present in previous studies (Rybicki, 1971; Chinnery and Javanovich, 1972; Sato, 1971; Sato and Matsu'ura, 1973; Javanovich et al., 1974a,b).

The conclusions which have the greatest effect upon our work in the following chapter concern the application of half-space models to the problem of plate interaction. Specificially, we find that when the dislocation penetrates the lithosphere that the half-space models can under certain circumstances be used to model the sense of the resultant displacements (and therefore strains). This statement is especially true for those models more specifically applicable to California. But we find in the case of an extremely soft asthenosphere that the results can differ in amplitude and even sense of motion. In all cases, however, we find that the component of motion parallel to the relative plate motion (Burger's vector) is of the same form as the half-space solution. For this reason we shall in Chapter IV consider the plate bottom as a second order effect in comparison to the interaction across the plate interface.

Figure 3.1

Schematic diagram of a finite dislocation in a layered media. $\vec{Y}$'s represent displacements and/or stresses. Superscript p is for primary fields and s for secondary fields. In this thesis primary fields for a particular layer are defined to be the displacements and stresses due to a finite dislocation (constructed by means of angular dislocations) in an infinite medium whose elastic constants equal those of the layer. The secondary fields represent the effects of the layering and free surface. Matching of boundary conditions across the interface between medium 1 and medium 2 yields a discontinuity in the secondary fields which is equal to the primary field in medium 1.

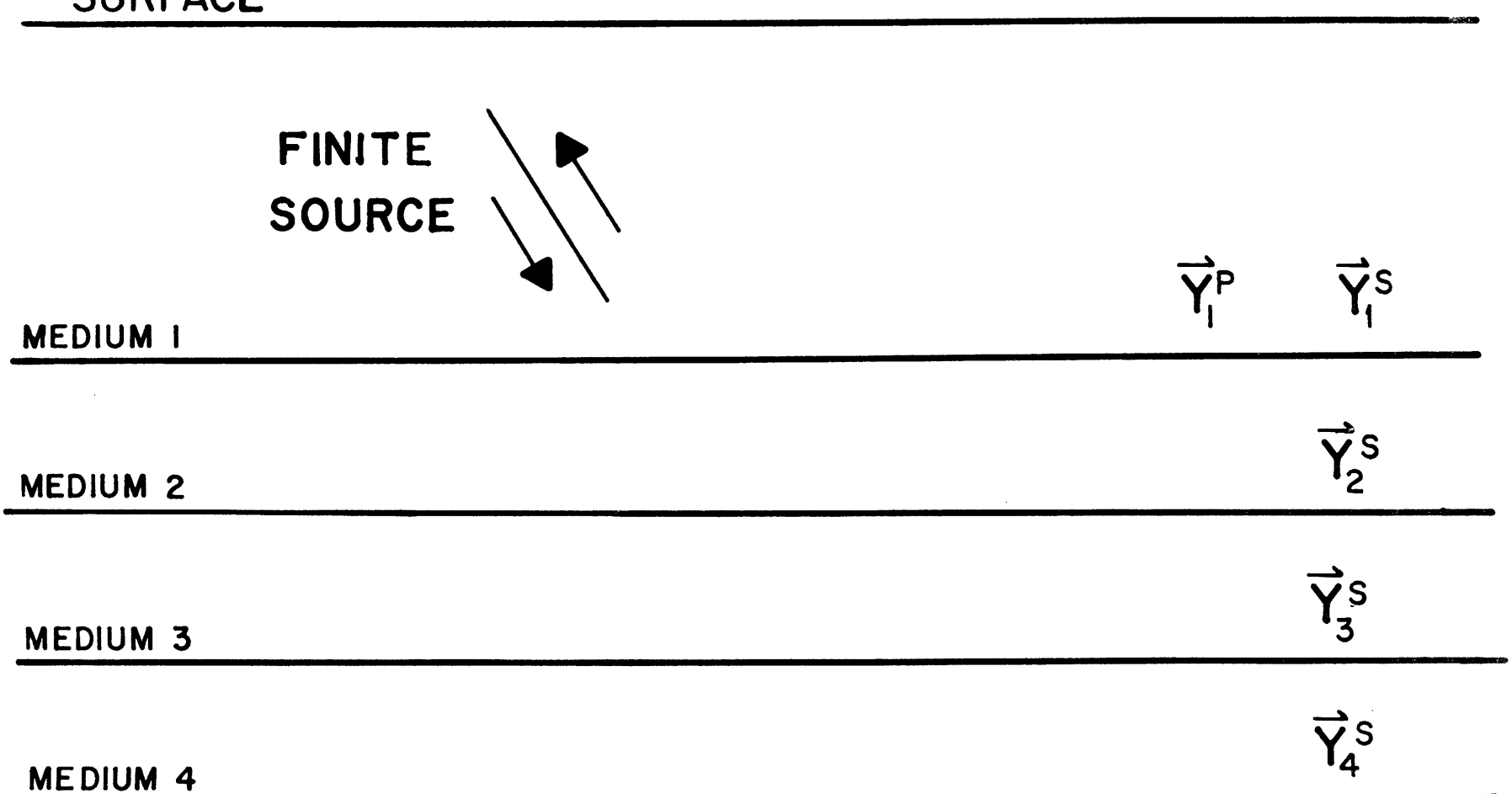
SURFACE
FINITE
SOURCE
$\vec{Y}_1^P$
$\vec{Y}_1^S$
MEDIUM 1
$\vec{Y}_2^S$
MEDIUM 2
$\vec{Y}_3^S$
MEDIUM 3
$\vec{Y}_4^S$
MEDIUM 4

Figure 3.1

Figure 3.2

(a) Schematic of a dislocation distributed through several layers.

(b) Source penetrating through a layer interface. In this case the discontinuity of the secondary fields across the layer interface equals the difference between the primary fields in the two media. Definitions of primary and secondary fields are given in figure 3.1.

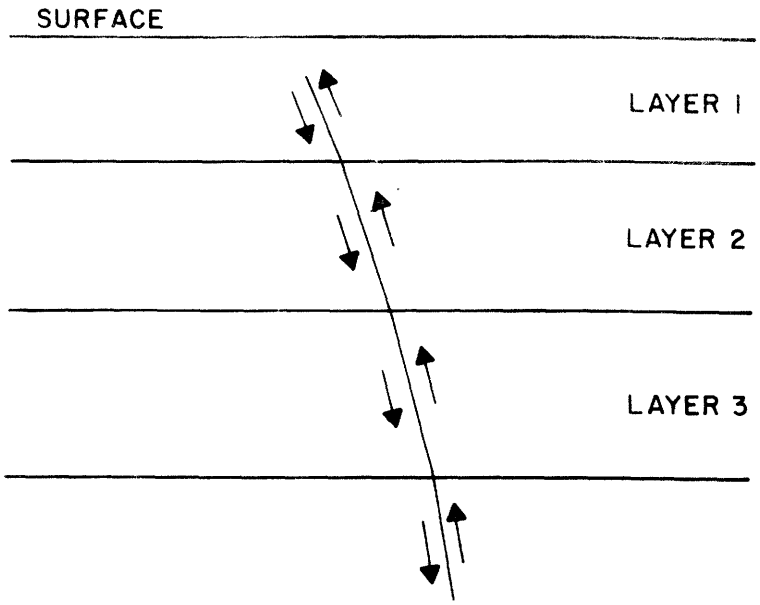

(a)

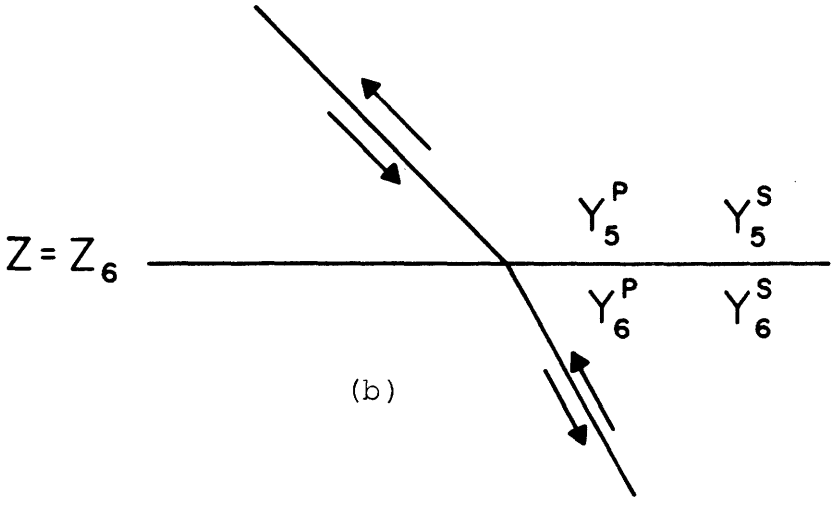

(b)

Figure 3.2

Figure 3.3

Homogeneous half-space model used to demonstrate the accuracy of the FSM. λ = 4 x 10" dynes/cm^2, μ = 3.58 x 10" dynes/cm^2, Depth (D) = 4 km, Length (L) = 4 km, WIDTH = 4 km, $\vec{B}$ = (0,0,1), DIP = 90°. The Burgers vector $\vec{B} = (B_1,B_2,B_3)$ will always be given in meters. In this model and all subsequent models to be discussed the fault is centered on and aligned with the x_2 axis. The dip direction is toward the positive x_1 axis. In order to present the results we have chosen to plot profiles perpendicular to the strike of the fault. The positions of the profiles are noted by their x_2 coordinate.

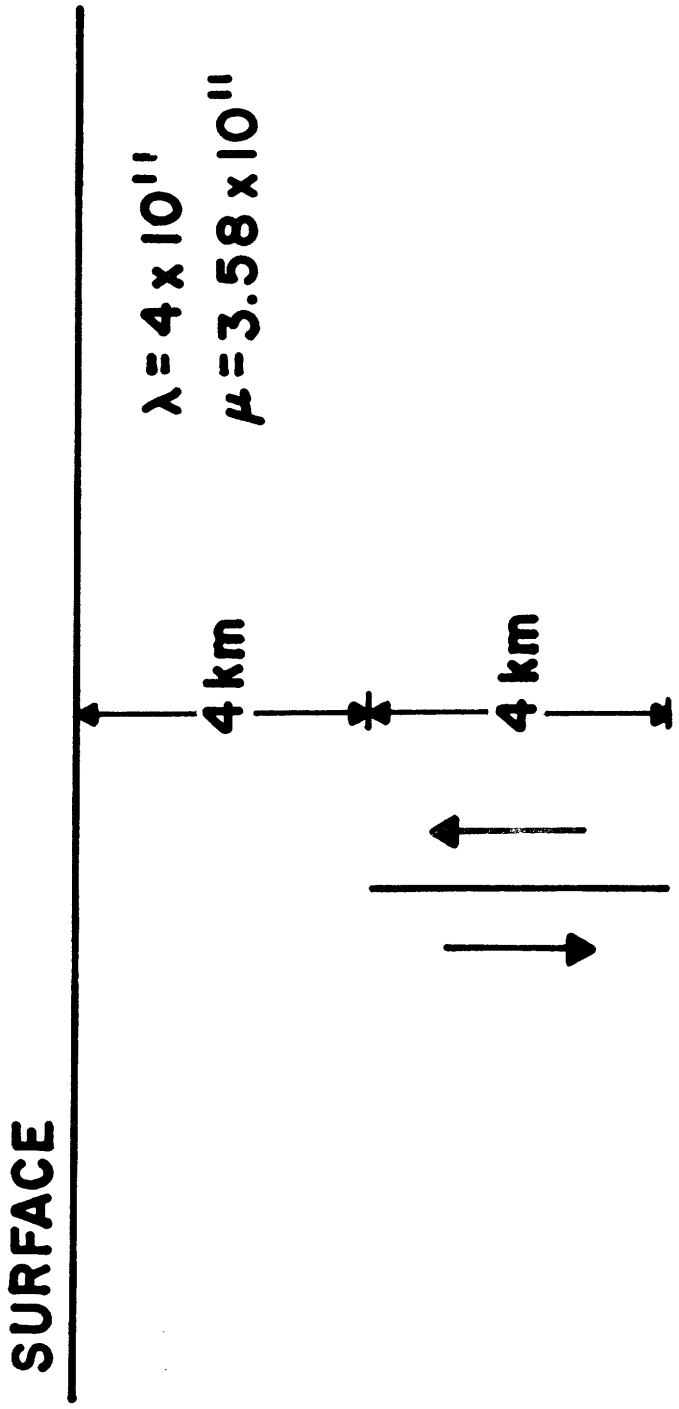

Figure 3.3

Figures 3.4 - 3.6

Comparison of displacements for exact half-space solutions (X) of the model shown in figure 3.3 with numerical solutions (□) obtained via a 64 x 64 grid. Sample sizes used were ΔX = 1 km and ΔY = 1 km. Profiles are taken at x_2 = 4 km. The symbols plotted (X and □) in these and all subsequent figures are used to differentiate between the respective curves. They do not represent actual grid points. However, the symbols are plotted at every fourth grid point and may be used to obtain a picture of how densely the curves are sampled. Figure 3.4 (u_1 displacement). Figure 3.5 (u_2 displacement). Figure 3.6 (u_3 displacement).

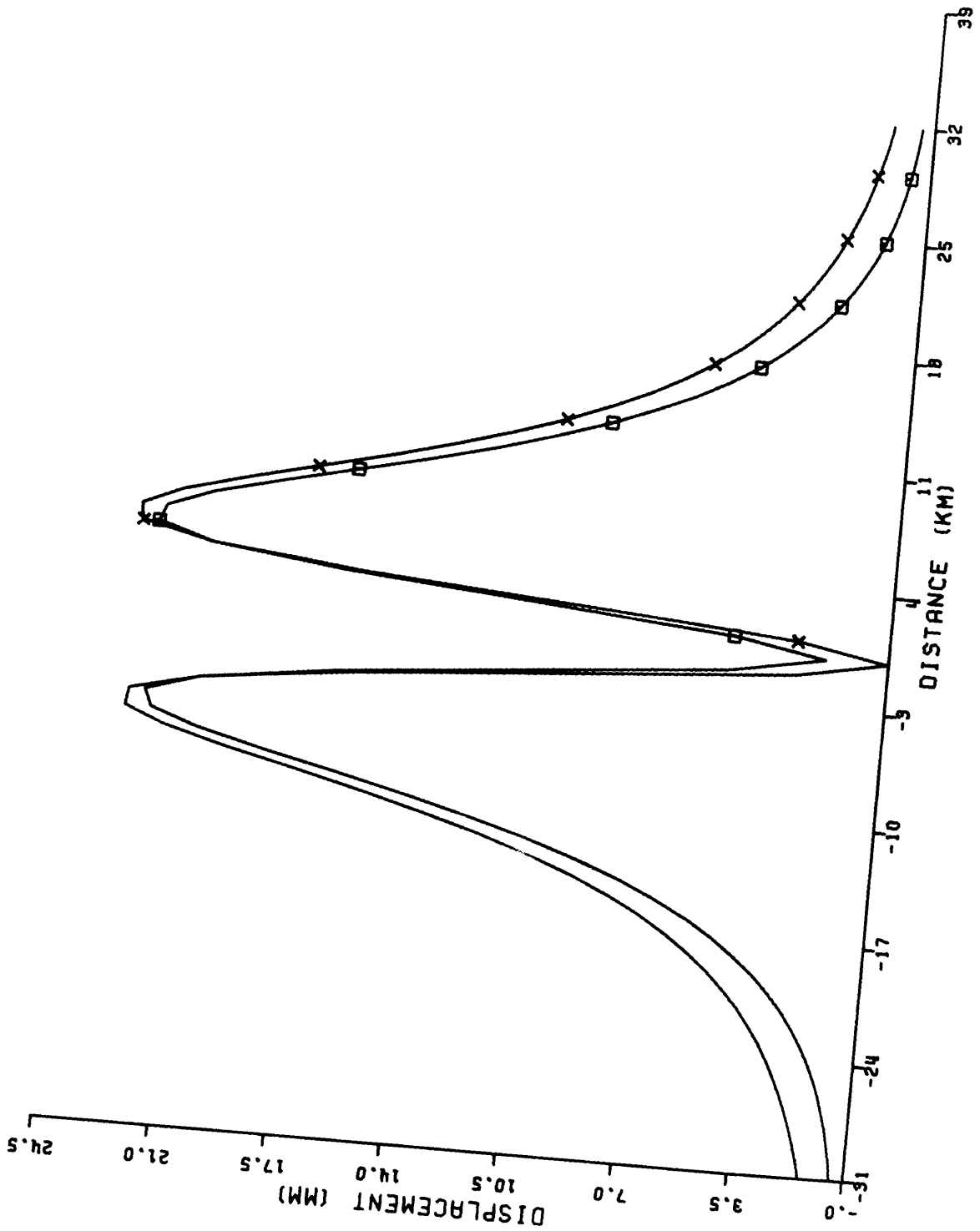
DISPLACEMENT (MM)
0.0
3.5
7.0
10.5
14.0
17.5
21.0
24.5
DISTANCE (KM)
-31
-24
-17
-10
-3
4
11
18
25
32
39

Figure 3.4

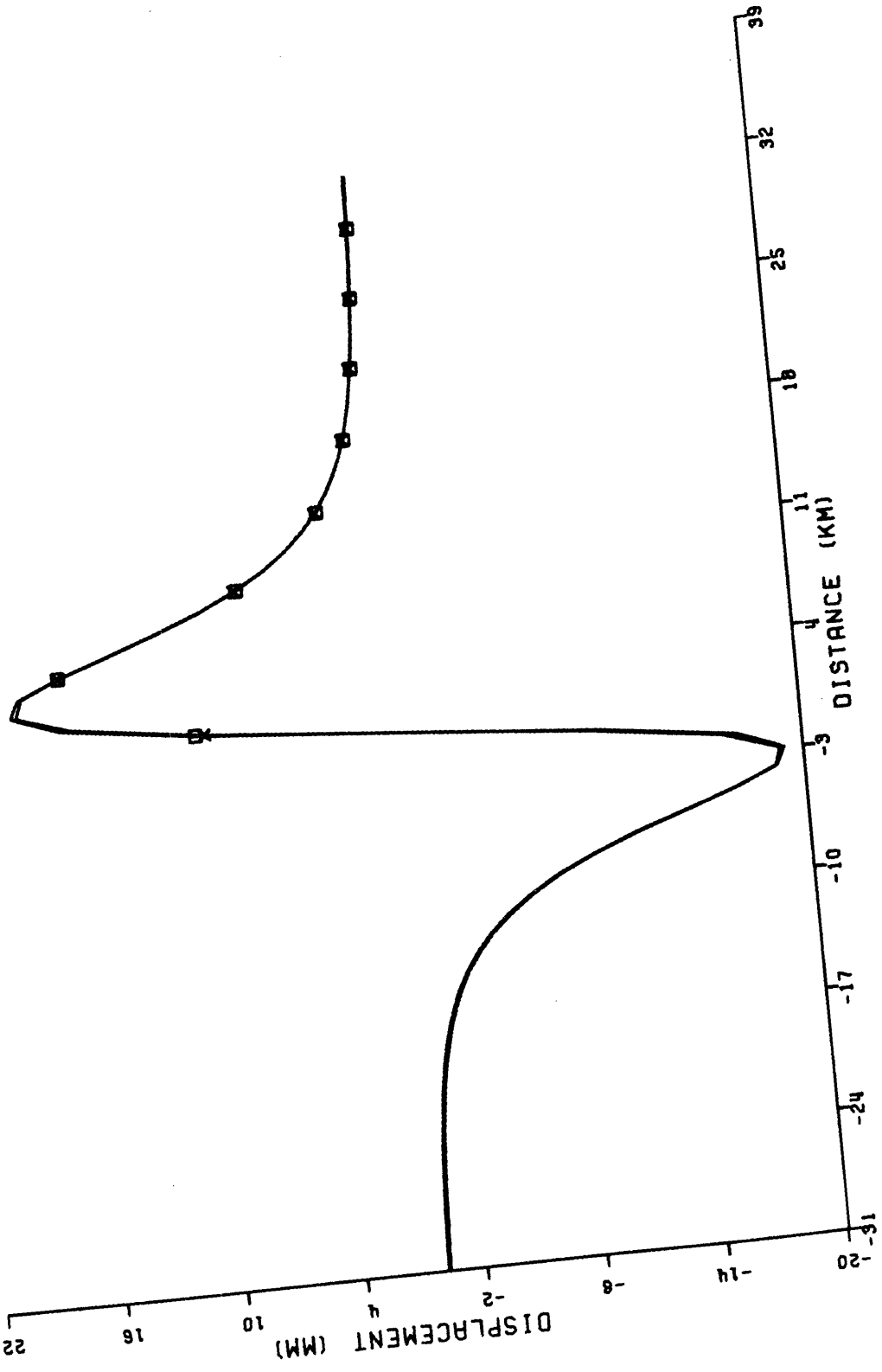
DISPLACEMENT (MM)
22
16
10
4
-2
-8
-14
-20
DISTANCE (KM)
39
32
25
18
11
4
-3
-10
-17
-24
-31

Figure 3.5

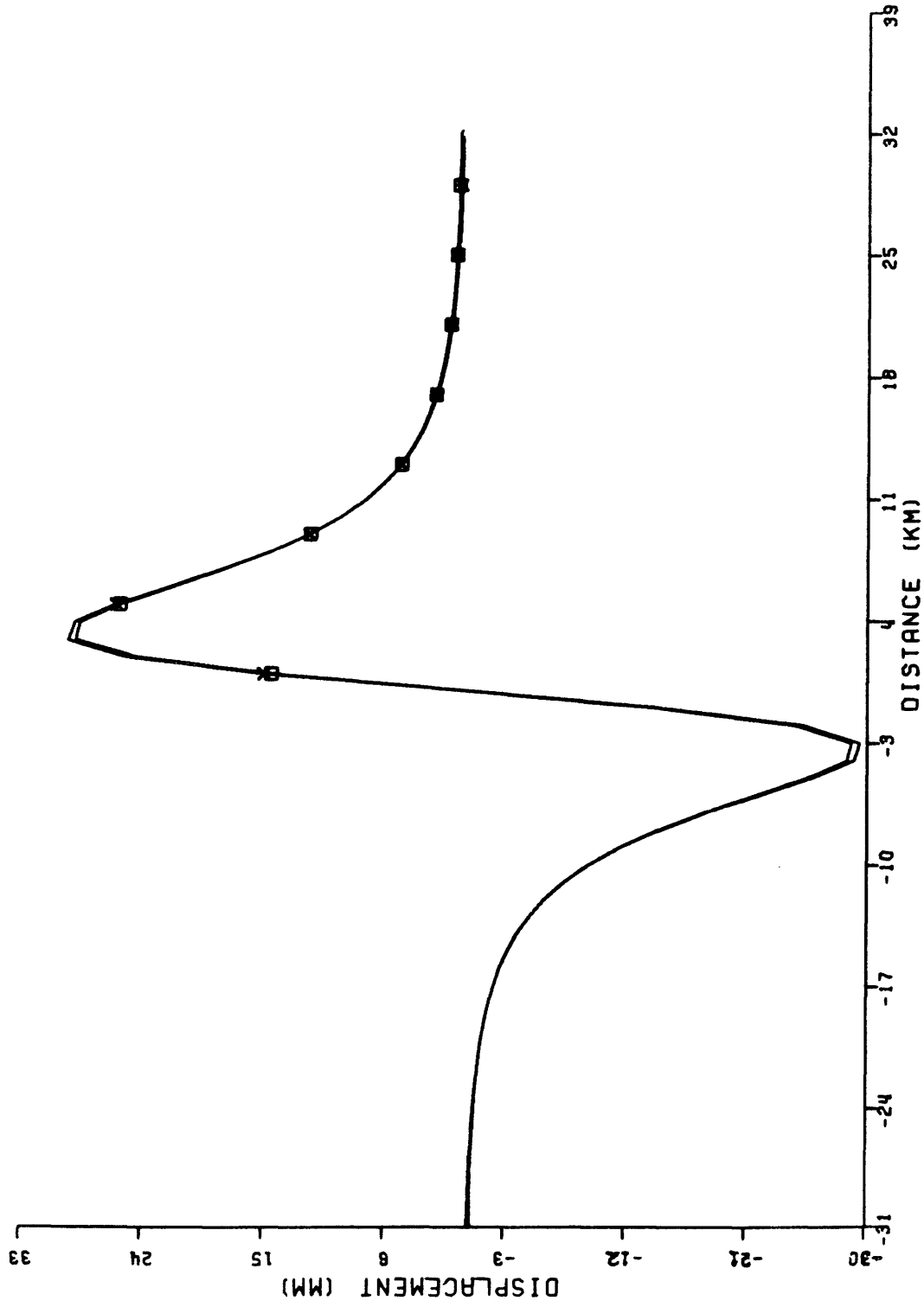
DISPLACEMENT (MM)
33
24
15
6
-3
-12
-21
-30
DISTANCE (KM)
-31
-24
-17
-10
-3
4
11
18
25
32
39

Figure 3.6

Figure 3.7

Improvement in the accuracy of the displacements may be obtained by increasing the number of points and decreasing the grid size. Compare the results here for $\Delta X_2 = .8$ km, $\Delta X_2 = .8$ km, and a 128 x 128 grid with those in figures 3.4-3.6 obtained with a 64 x 64 grid. Profiles taken at $X_2 = .8$ km, (a) u_1 displacement (b) u_2 displacement (c) u_3 displacement. Exact half-space solution (x), Numerical solution (▫).

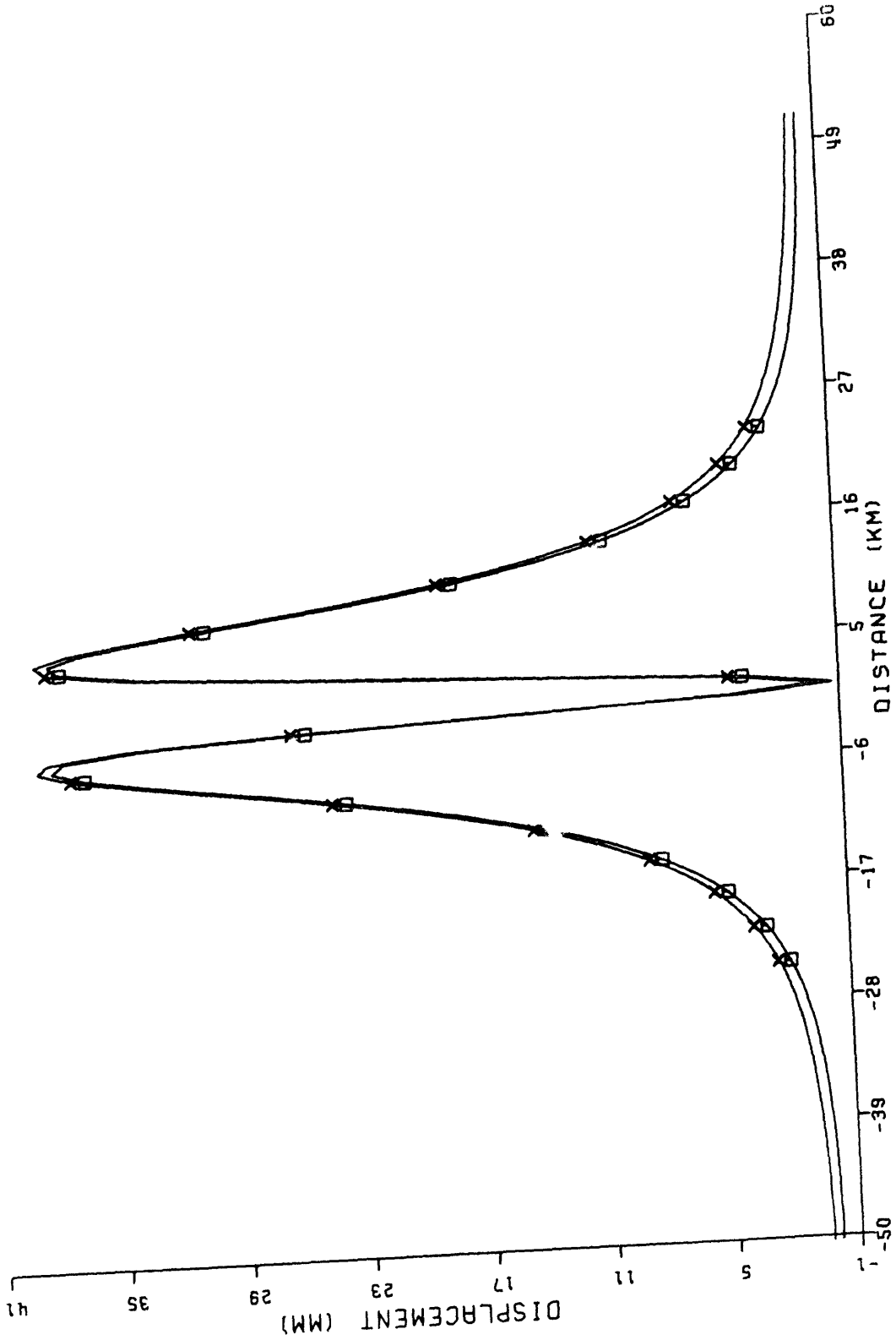
DISPLACEMENT (MM)
1
5
11
17
23
29
35
41
DISTANCE (KM)
-50
-39
-28
-17
-6
5
16
27
38
49
60

Figure 3.7 (a)

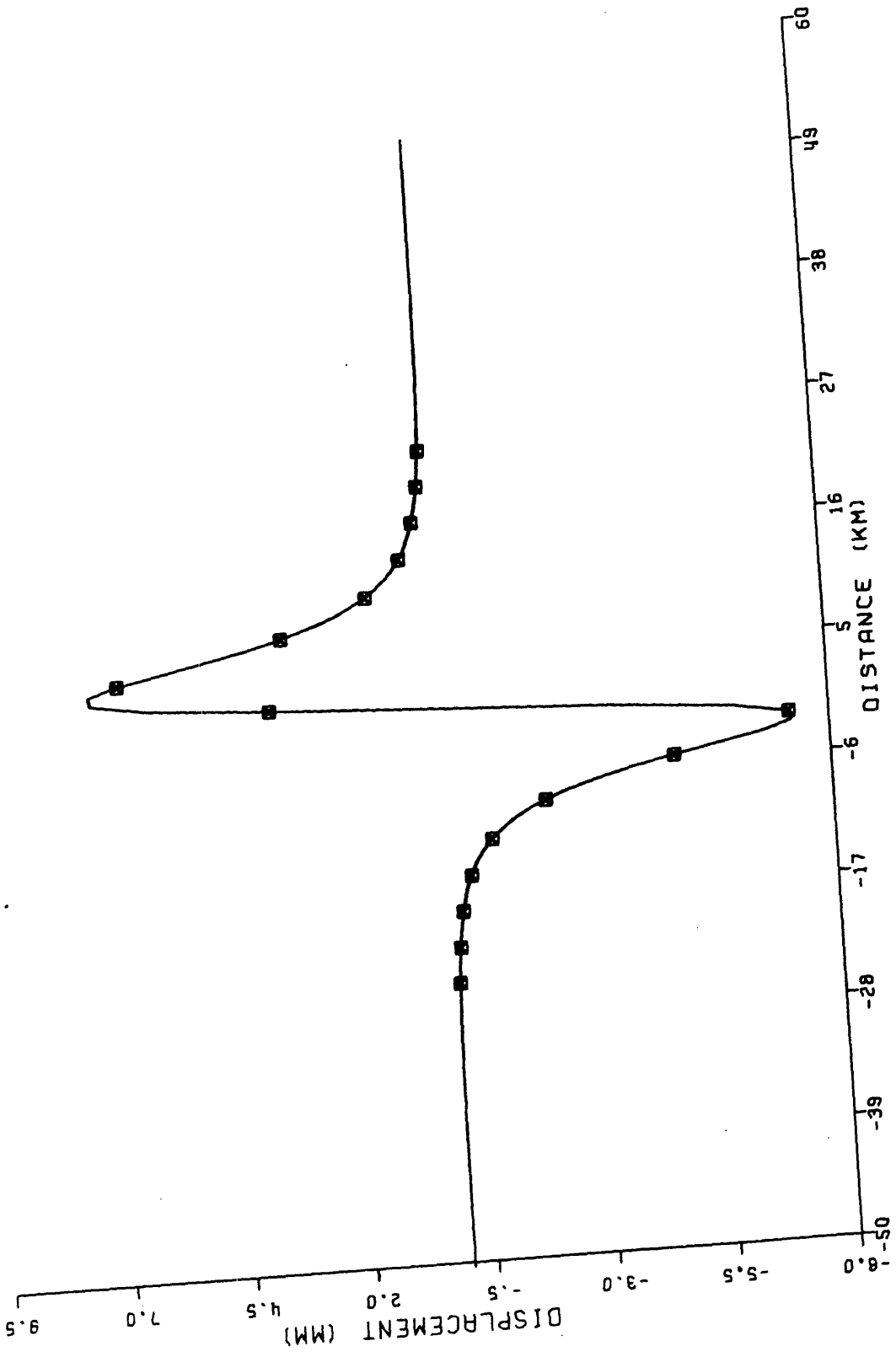
DISPLACEMENT (MM)
9.5
7.0
4.5
2.0
-.5
-3.0
-5.5
-8.0
DISTANCE (KM)
-50
-39
-28
-17
-6
5
16
27
38
49
60

Figure 3.7 (b)

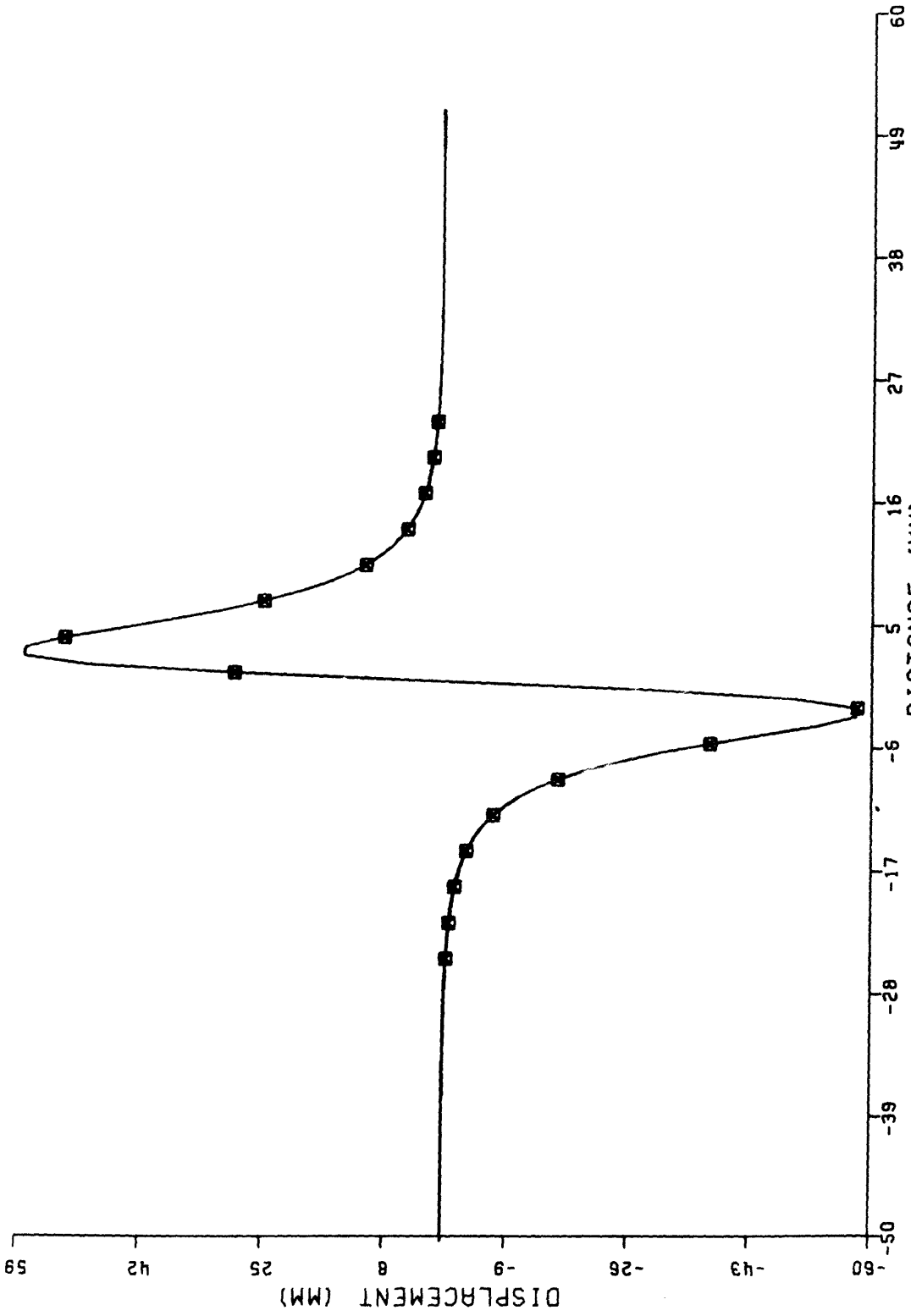
DISPLACEMENT (MM)
59
42
25
8
-9
-26
-43
-60
DISTANCE (KM)
-50
-39
-28
-17
-6
5
16
27
38
49
60

Figure 3.7 (c)

Figure 3.8

(a) Plot of the differences between the exact solutions for the half-space model shown in figure 3.3 and the numerical solutions obtained by the FSM as a function of distance away from the fault (the difference equals the numerical solution minus the exact solution). The circles represent points computed using a 64 x 64 grid, ΔX_1 = 1 km, and ΔX_2 = 1 km. The triangles are obtained using the results from a 128 x 128 grid with sample sizes of ΔX_1 = .8 km and ΔX_2 = .8 km. For the 128 x 128 grid none of the differences are visible on the scale shown. The solutions extend to 31 km for the 64 x 64 grid and to 50.4 km for the 128 x 128 grid.

(b) Plot of percent error versus distance for the 64 x 64 grid (●) and the 128 x 128 grid (Δ).

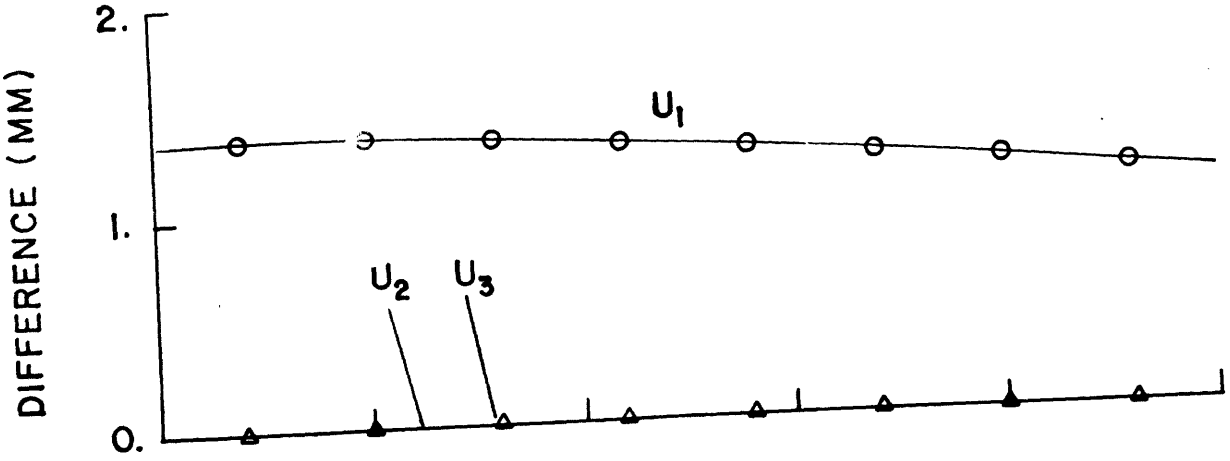
2.
1.
0.
DIFFERENCE (MM)
U1
U2
U3

(a)

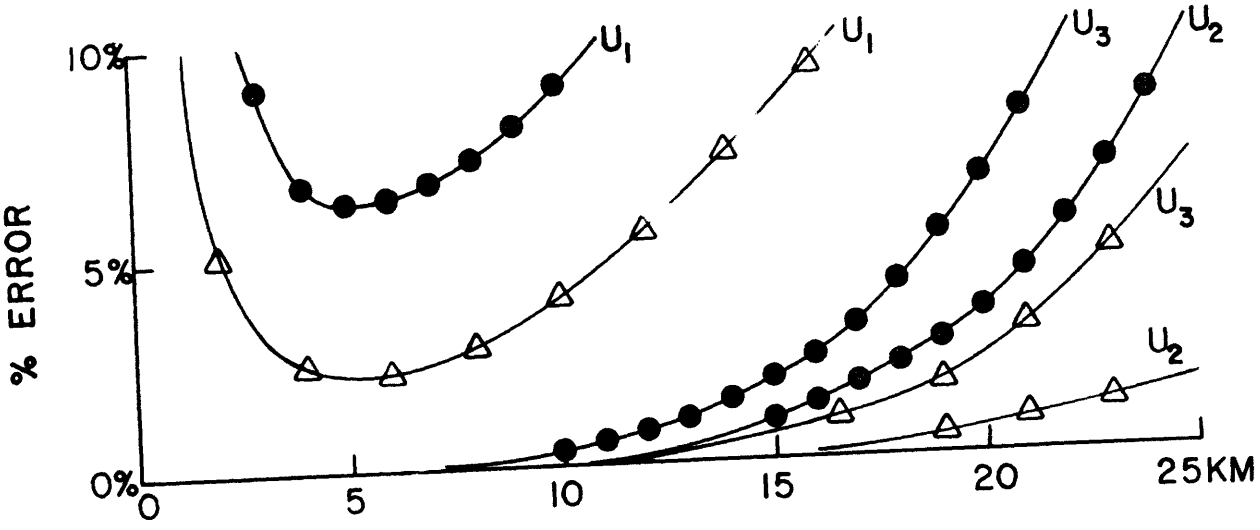
10%
5%
0%
% ERROR
U1
U1
U3
U2
U3
U2
0
5
10
15
20
25KM

(b)

Figure 3.8

Figure 3.9

Plot of the percent error over the full range of the solutions for the 64 x 64 grid (●) and the 128 x 128 grid (Δ).

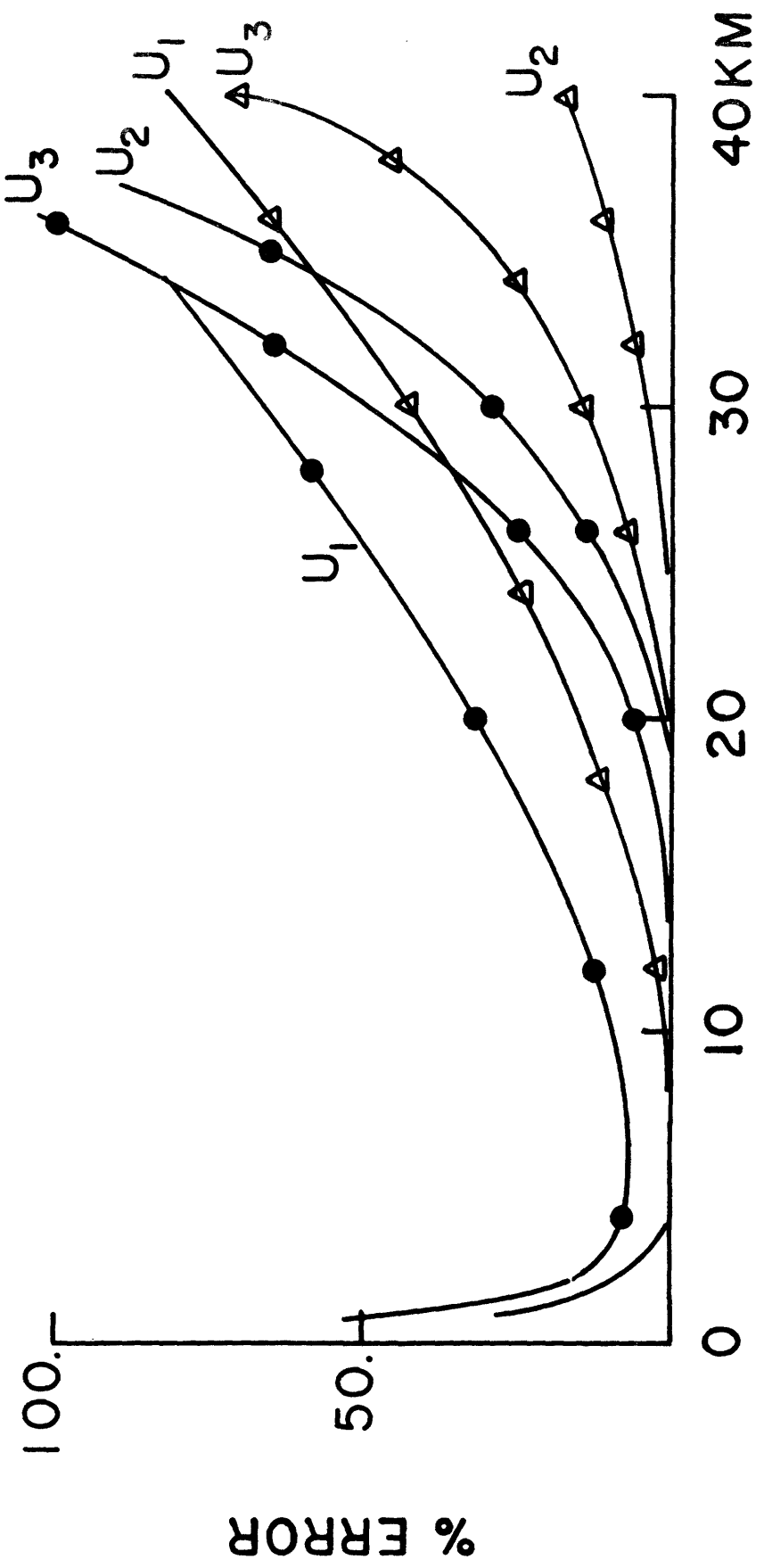

Figure 3.9

Figure 3.10

(a) Model VSTOP - strike-slip fault embedded in a soft layer (λ = 1.12 x 10^{11} dyne/cm^2, μ = .7 x 10^{11} dynes/cm^2) over a hard half-space (λ = 2.4 x 10^{11} dynes/cm^2, μ = 2.58 x 10^{11} dynes/cm^2). The fault extends along the x_2 axis from x_2 = +.25 to x_2 = -.25, has a depth of .5 km (to top edge), a width of .5 km and a burgers vector $\vec{B}$ = (0,1,0). The positive side of the dislocation is viewed from the positive x_1 axis. Sample sizes used in the numerical solutions: ΔX_1= .2 km, ΔX_2= .2 km.

(b) Model VSBOT - strike-slip fault below the soft layer in the model described in (a). The depth to the top edge of the fault is 3 km. The fault extends along the x_2 axis from x_2 = +1 to x_2 = -1, has a width of 2 km, and has a burgers vector B = (0,1,0). The sample sizes used in the numerical solutions are ΔX_1 = .5 km and ΔX_2 = .5 km.

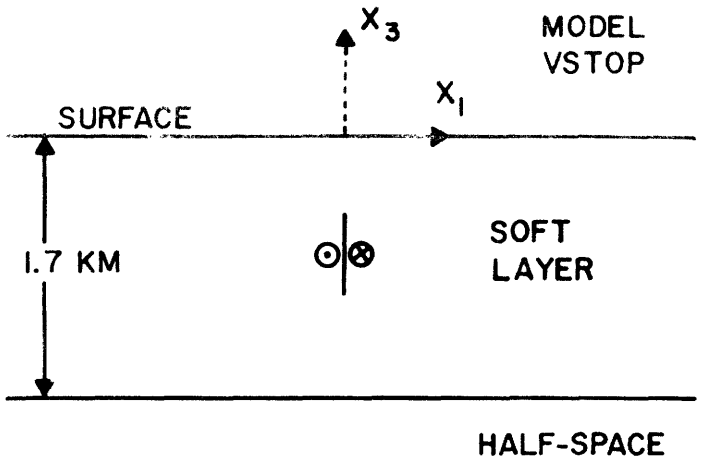

(a)

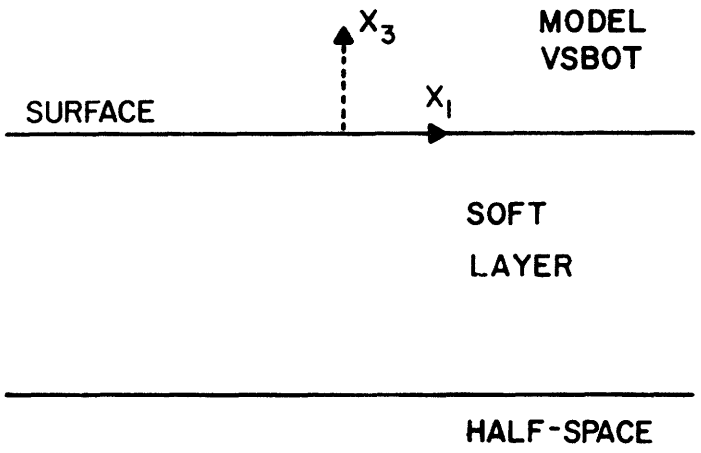

(b)

Figure 3.10

Figure 3.11

Comparison of u_1 displacements for model VSTOP (□) with displacements for a hard half-space (X) ($\lambda = 2.4 \times 10^{11}$ dynes/cm^2, $\mu = 2.58 \times 10^{11}$ dynes/cm^2). $X_2 = .2$ km.

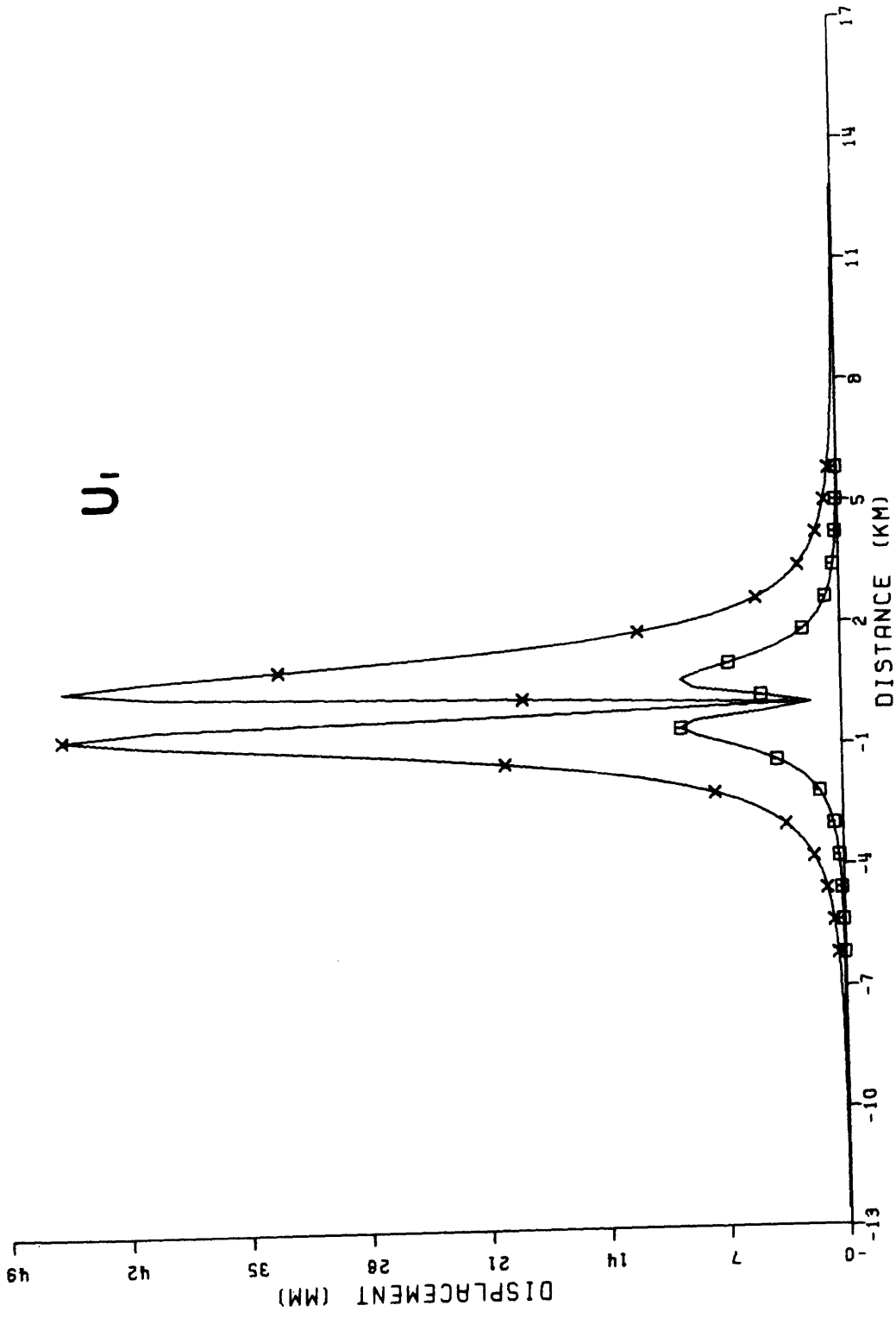
U1
DISPLACEMENT (MM)
0
7
14
21
28
35
42
49
DISTANCE (KM)
17
14
11
8
5
2
-1
-4
-7
-10
-13

Figure 3.11

Figure 3.12

Comparison of u_1 displacements for model VSTOP (□) with displacements for a soft half-space ($\lambda = 1.12 \times 10^{11}$ dynes/cm^2, $\mu = .7 \times 10^{11}$ dynes/cm^2). $X_2 = .2$ km.

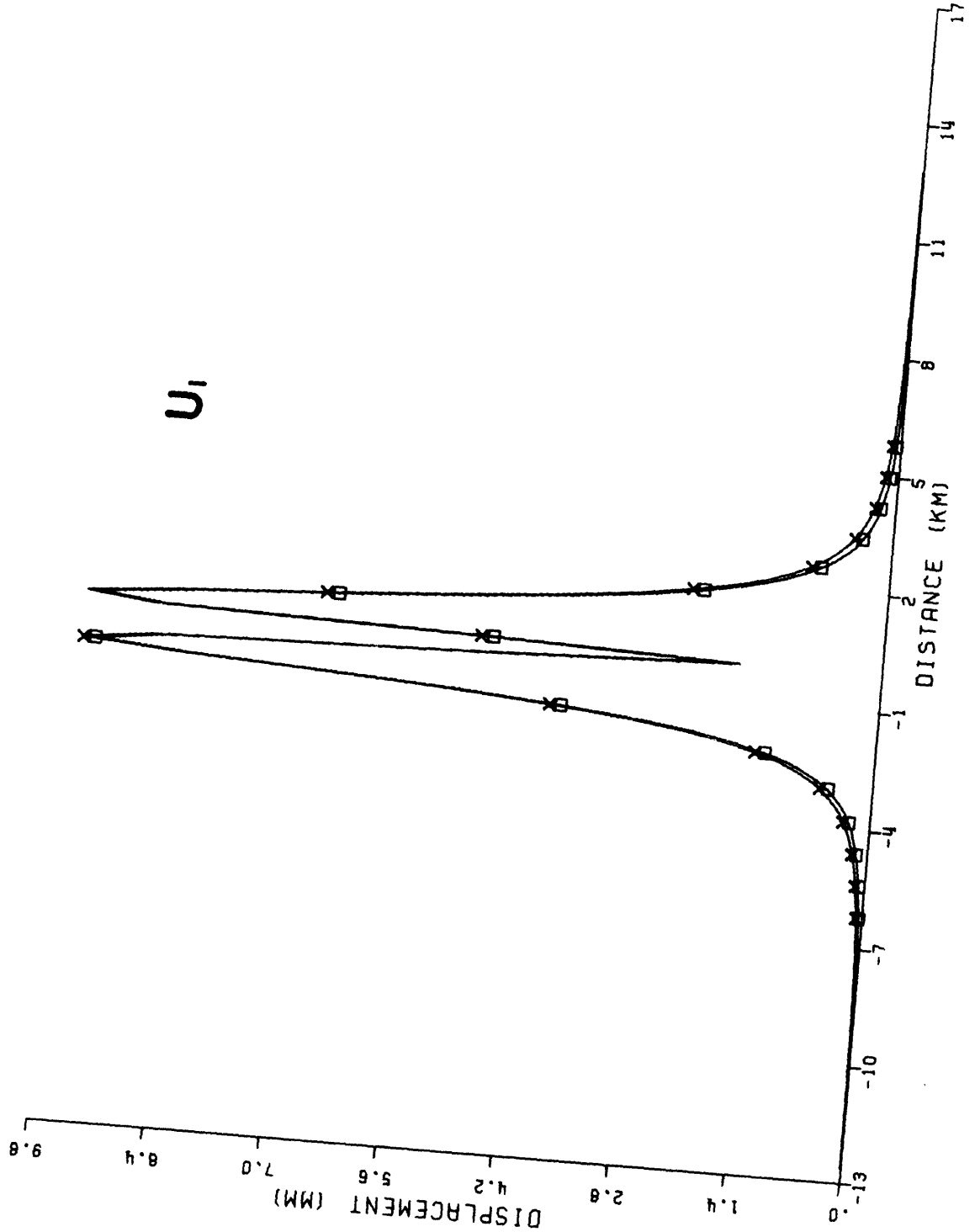
U
DISPLACEMENT (MM)
0.
1.4
2.8
4.2
5.6
7.0
8.4
9.8
-13
-10
-7
-4
-1
2
5
8
11
14
17
DISTANCE (KM)

Figure 3.12

Figure 3.13

Comparison of u_2 displacements for model VSTOP (□) with those of the hard half-space (X). X_2 = .2 km.

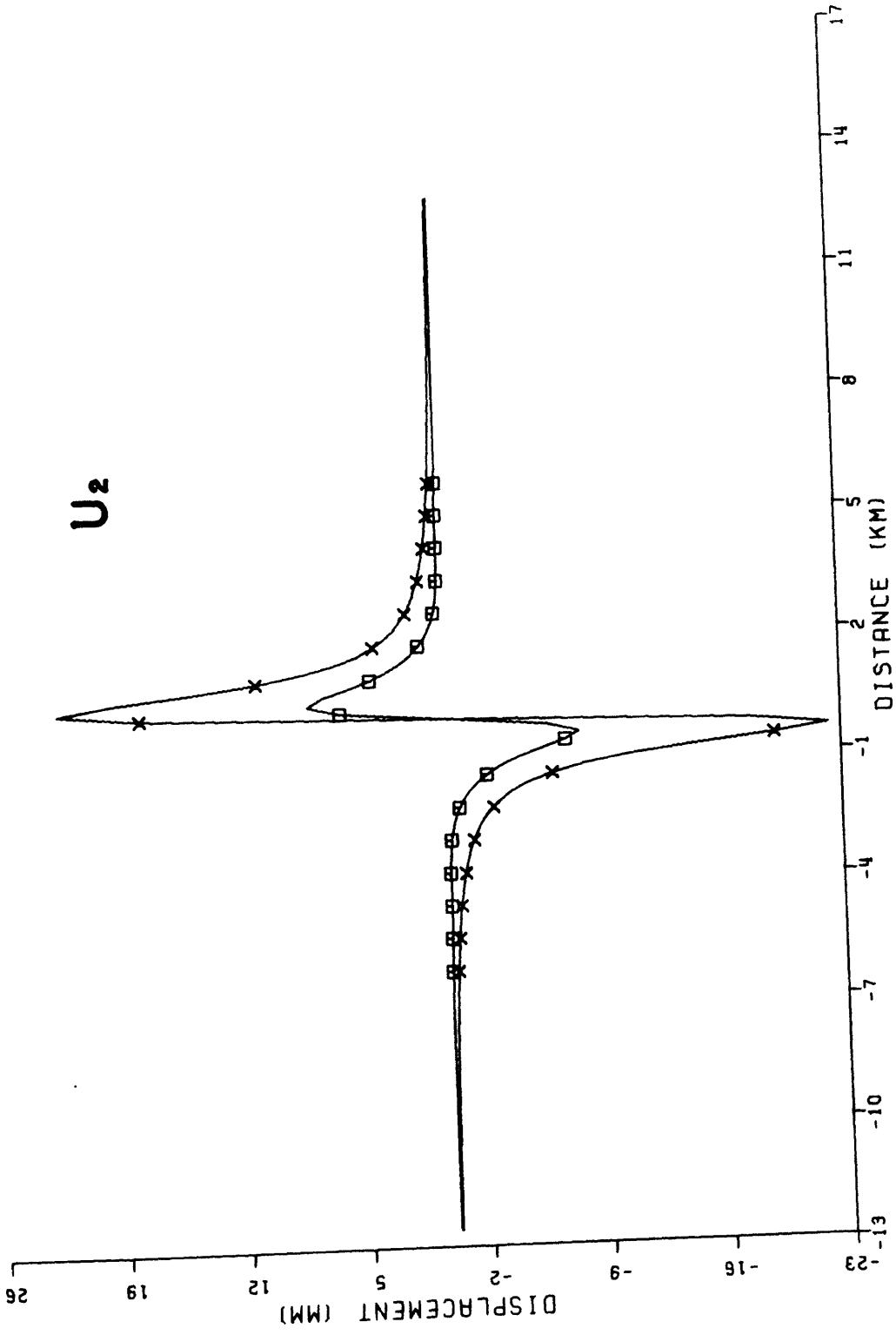
U2
DISPLACEMENT (MM)
26
19
12
5
-2
-9
-16
-23
DISTANCE (KM)
17
14
11
8
5
2
-1
-4
-7
-10
-13

Figure 3.13

Figure 3.14

Comparison of u_2 displacements for model VSTOP (□) with those of the soft half-space (X). X_2 = .2 km.

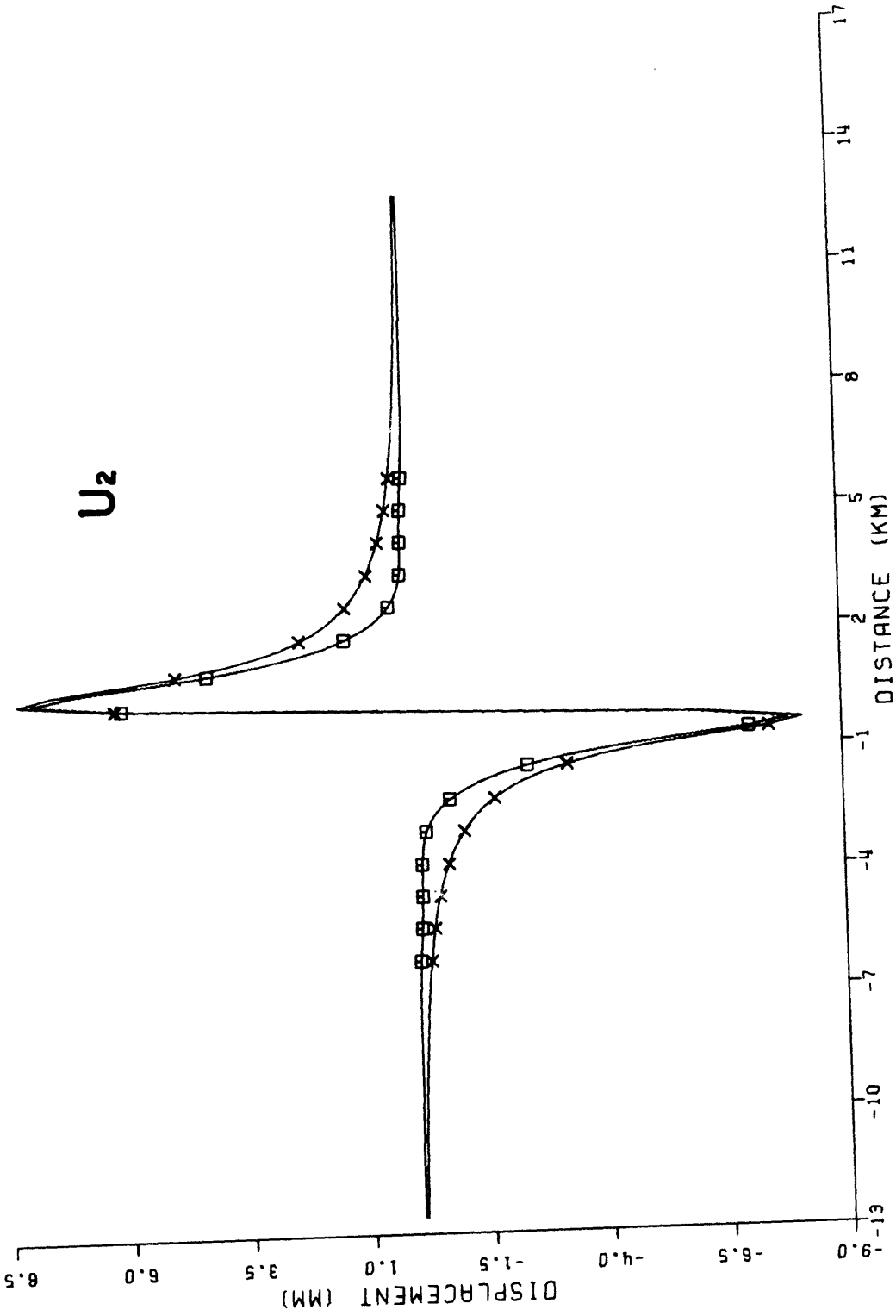
U2
DISPLACEMENT (MM)
8.5
6.0
3.5
1.0
-1.5
-4.0
-6.5
-9.0
DISTANCE (KM)
-13
-10
-7
-4
-1
2
5
8
11
14
17

Figure 3.14

Figure 3.15

Comparison of u_3 displacements for model VSTOP (□) with those of the hard half-space (X). X_2 = .2 km.

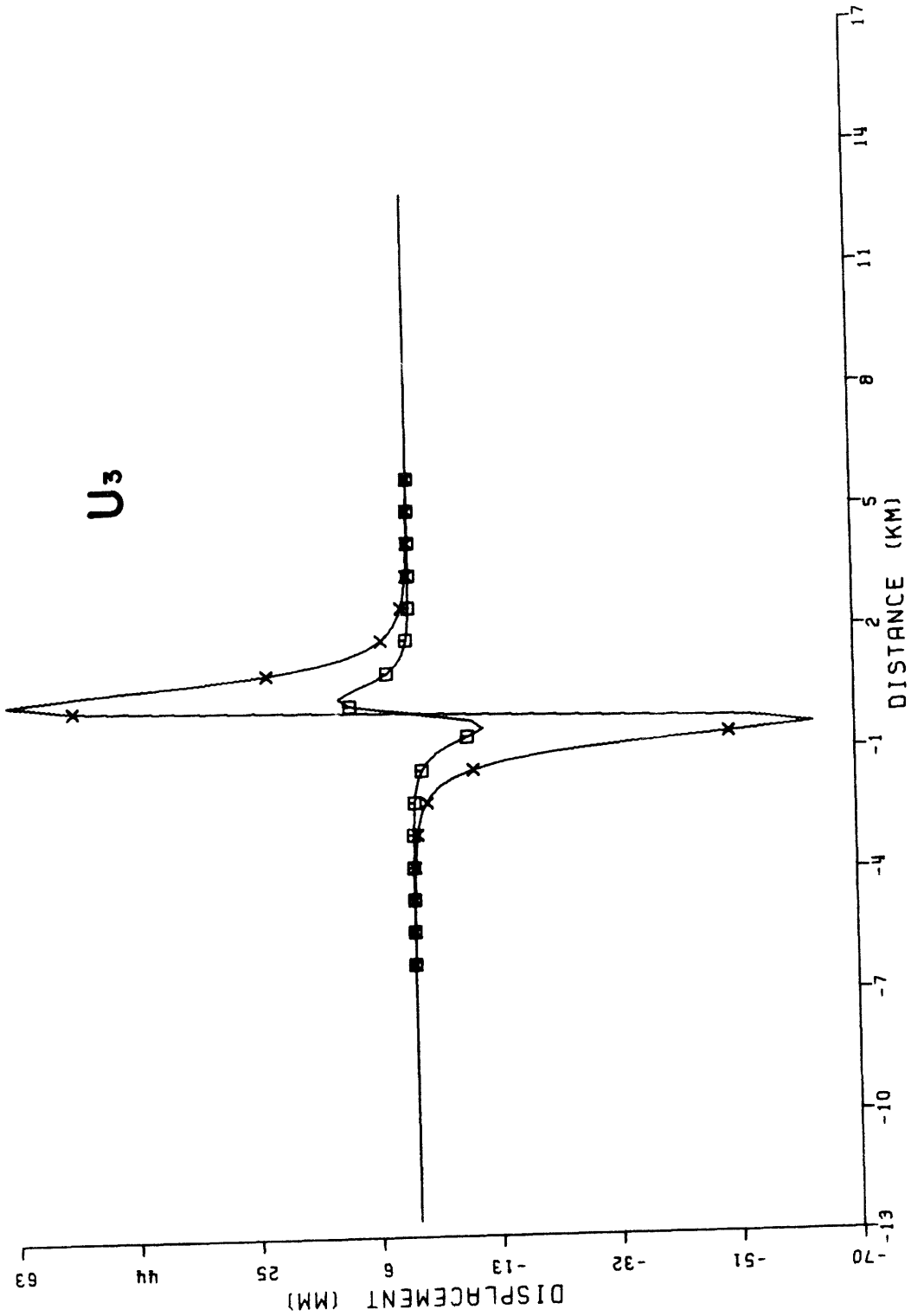
U3
DISPLACEMENT (MM)
63
44
25
6
-13
-32
-51
-70
DISTANCE (KM)
-13
-10
-7
-4
-1
2
5
8
11
14
17

Figure 3.15

Figure 3.16

Comparison of u_3 displacements for model VSTOP (□) with those of the soft half-space (X). Profile is taken at x_2 = .2 km.

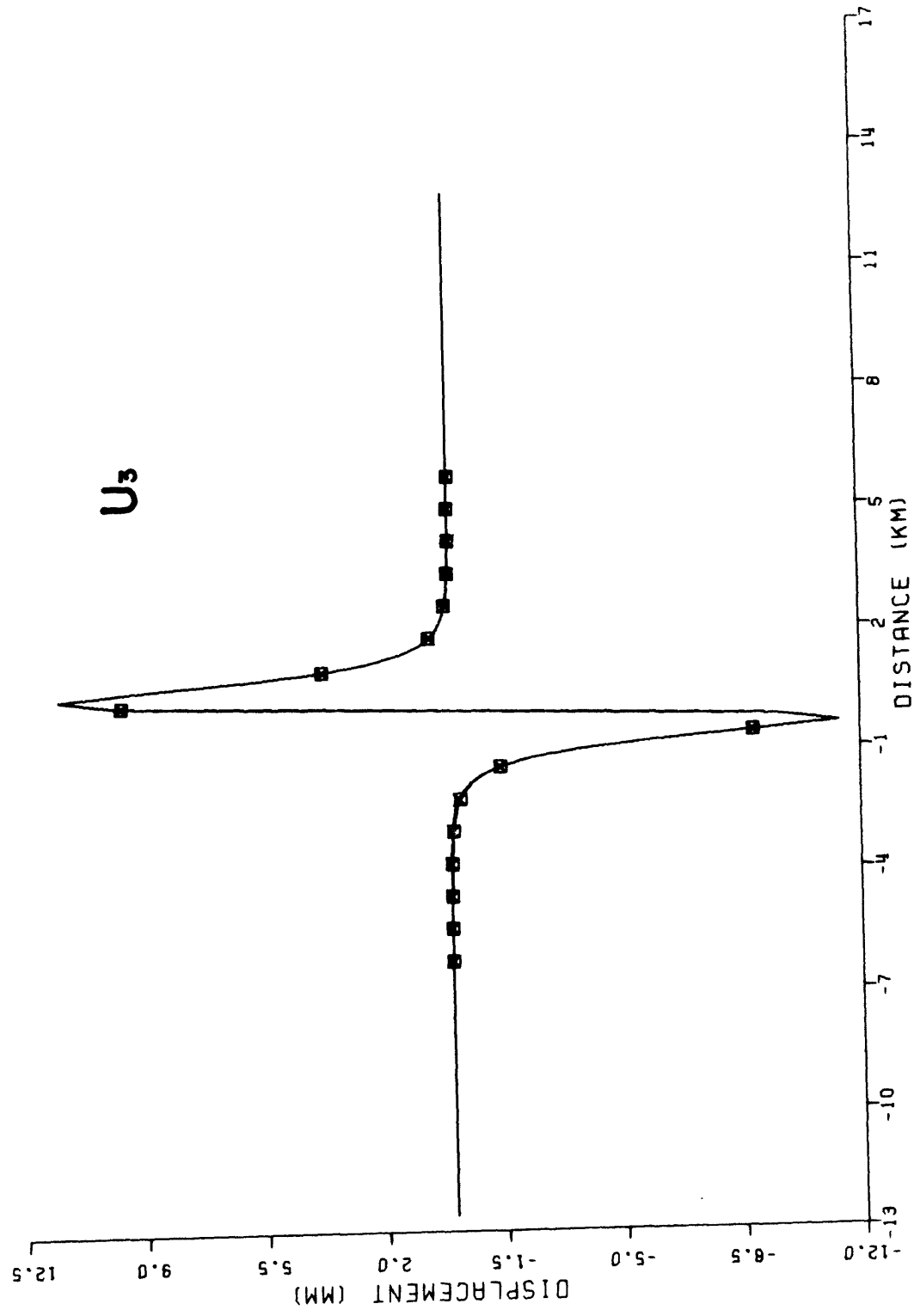
U3
DISPLACEMENT (MM)
12.5
9.0
5.5
2.0
-1.5
-5.0
-8.5
-12.0
DISTANCE (KM)
-13
-10
-7
-4
-1
2
5
8
11
14
17

Figure 3.16

Figures 3.17-3.20

Comparison of model VSBOT (□) with a half-space model (X). Half-space parameters: $\lambda = 2.4 \times 10^{11}$ dynes/cm^2, $\mu = 2.58 \times 10^{11}$ dynes/cm^2 ($\nu = .24$). Profiles in figures 3.17, 3.18, and 3.20 are taken at $x_2 = 2$ km. Figure 3.19 is at $x_2 = .5$ km.

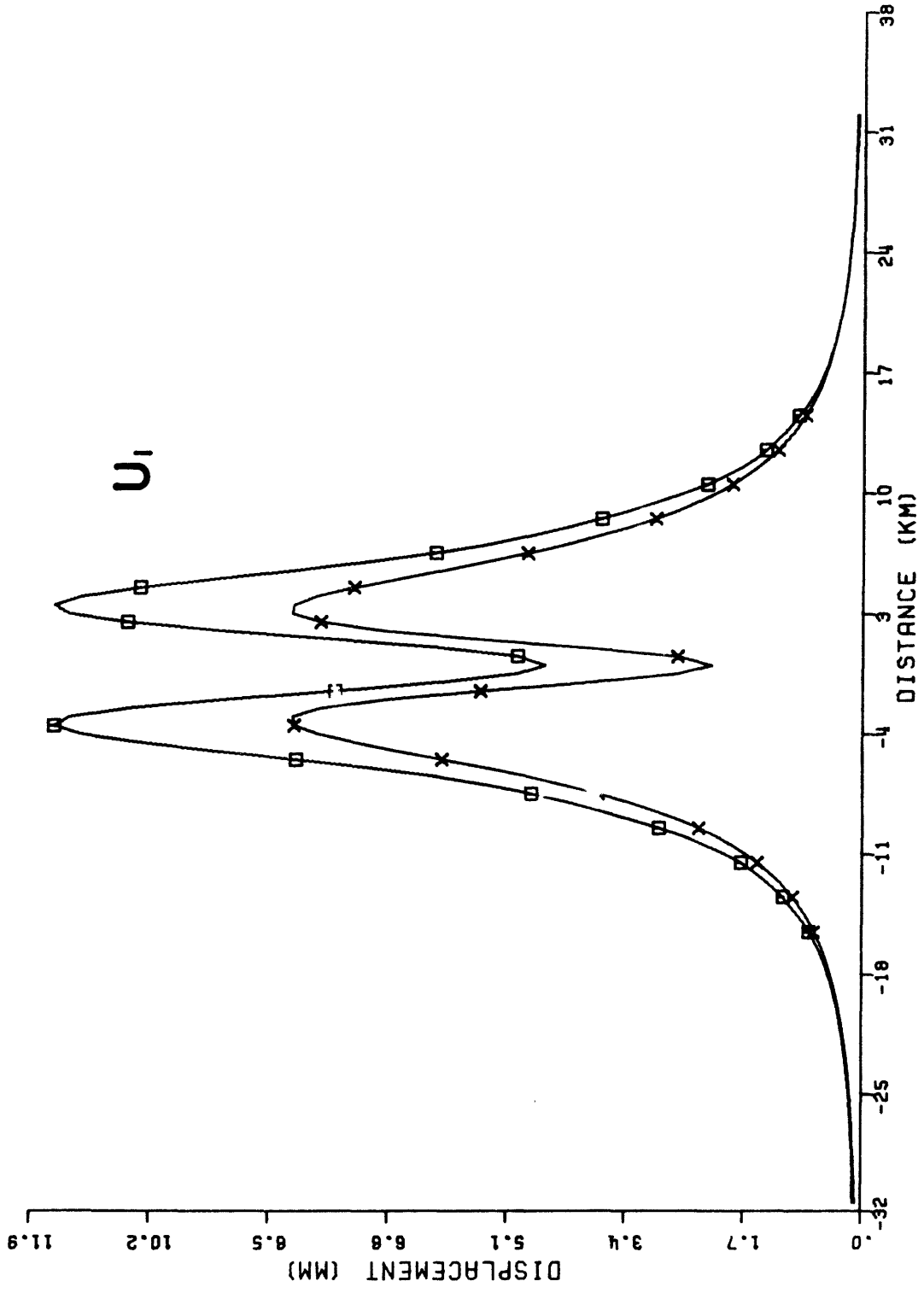
U_1
DISPLACEMENT (MM)
0.
1.7
3.4
5.1
6.8
8.5
10.2
11.9
DISTANCE (KM)
-32
-25
-18
-11
-4
3
10
17
24
31
38

Figure 3.17

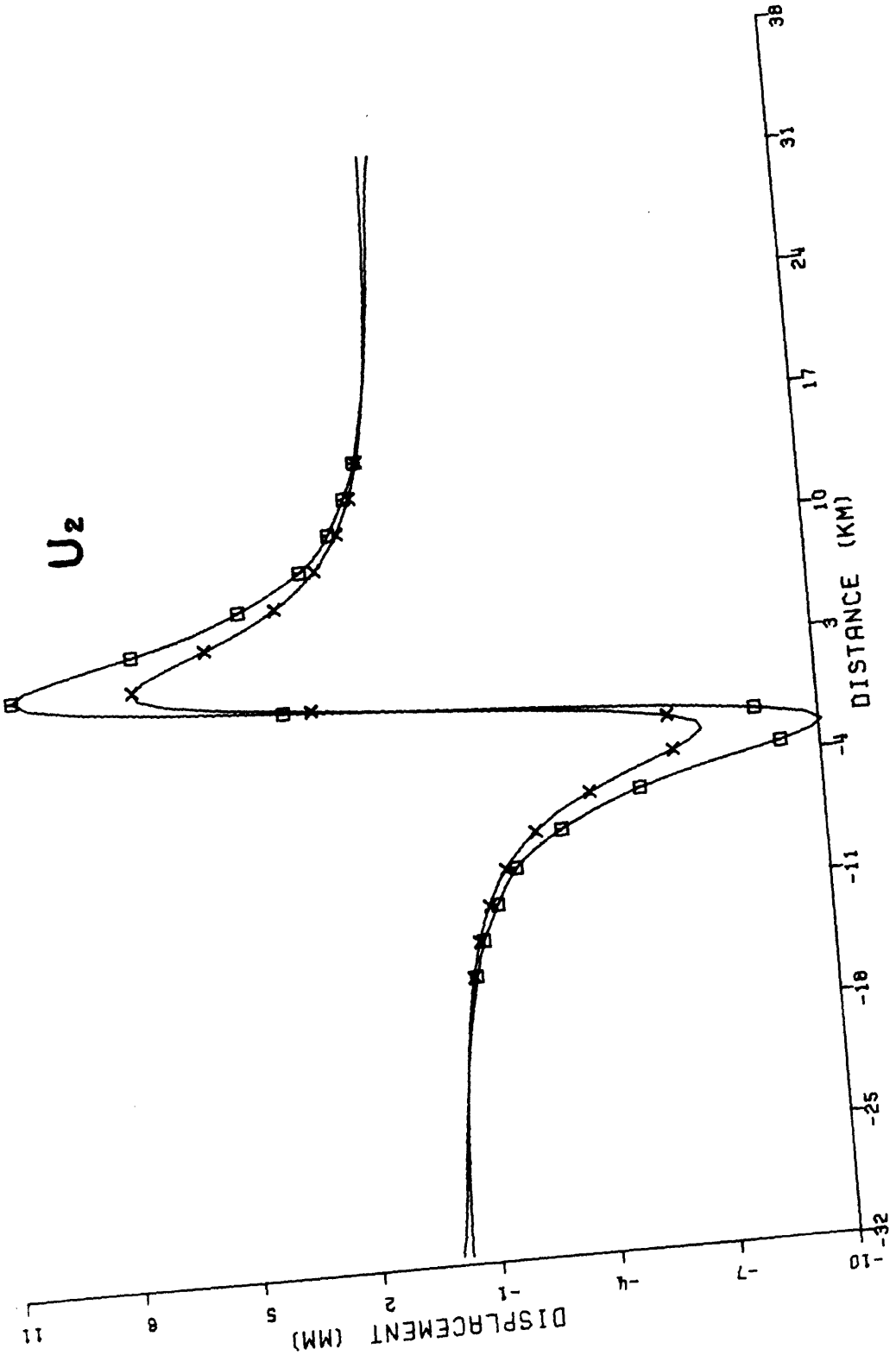
U2
DISPLACEMENT (MM)
11
8
5
2
-1
-4
-7
-10
DISTANCE (KM)
-32
-25
-18
-11
-4
3
10
17
24
31
38

Figure 3.18

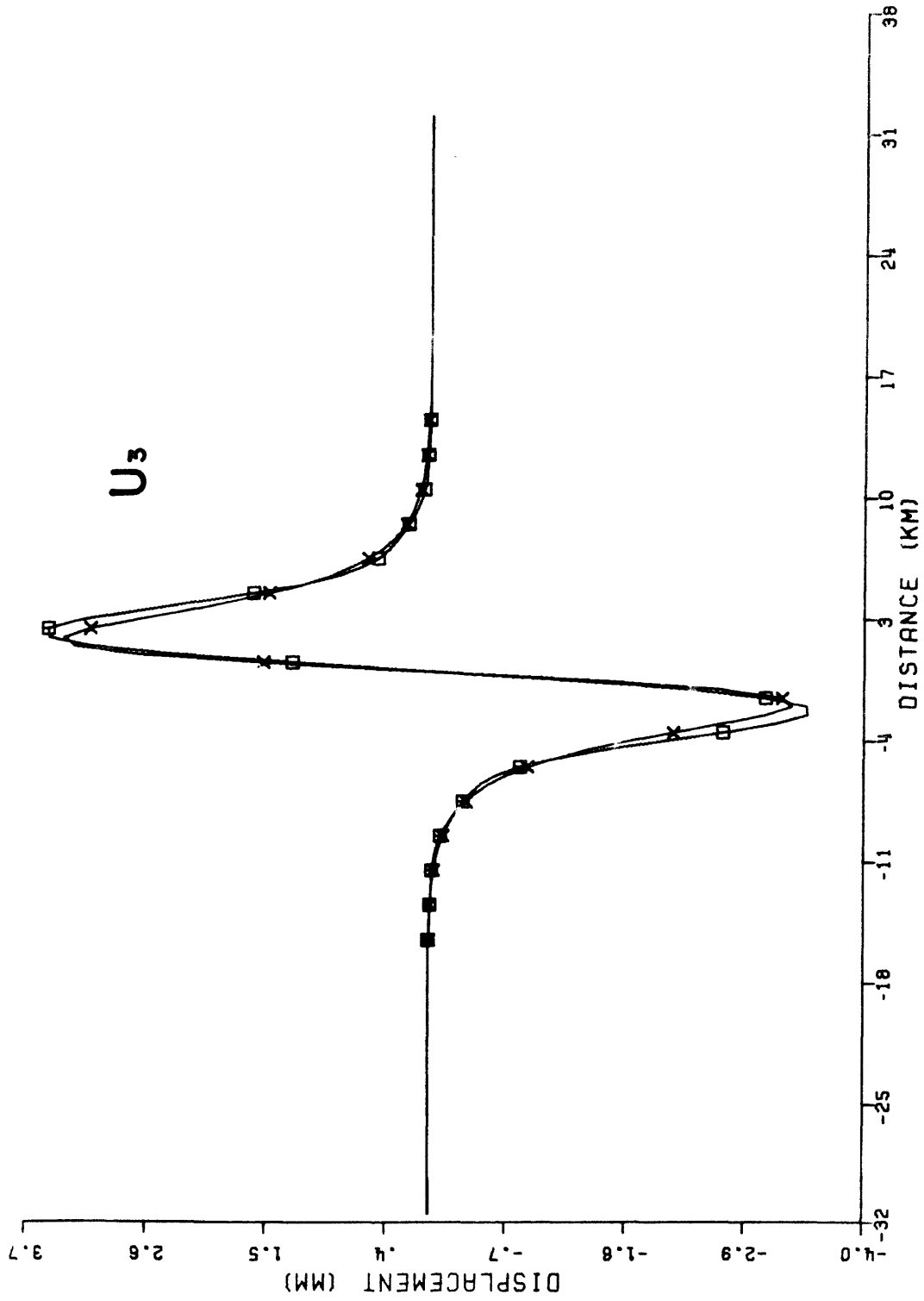
U3
DISPLACEMENT (MM)
3.7
2.8
1.5
.4
-.7
-1.8
-2.9
-4.0
DISTANCE (KM)
-32
-25
-18
-11
-4
3
10
17
24
31
38

Figure 3.19

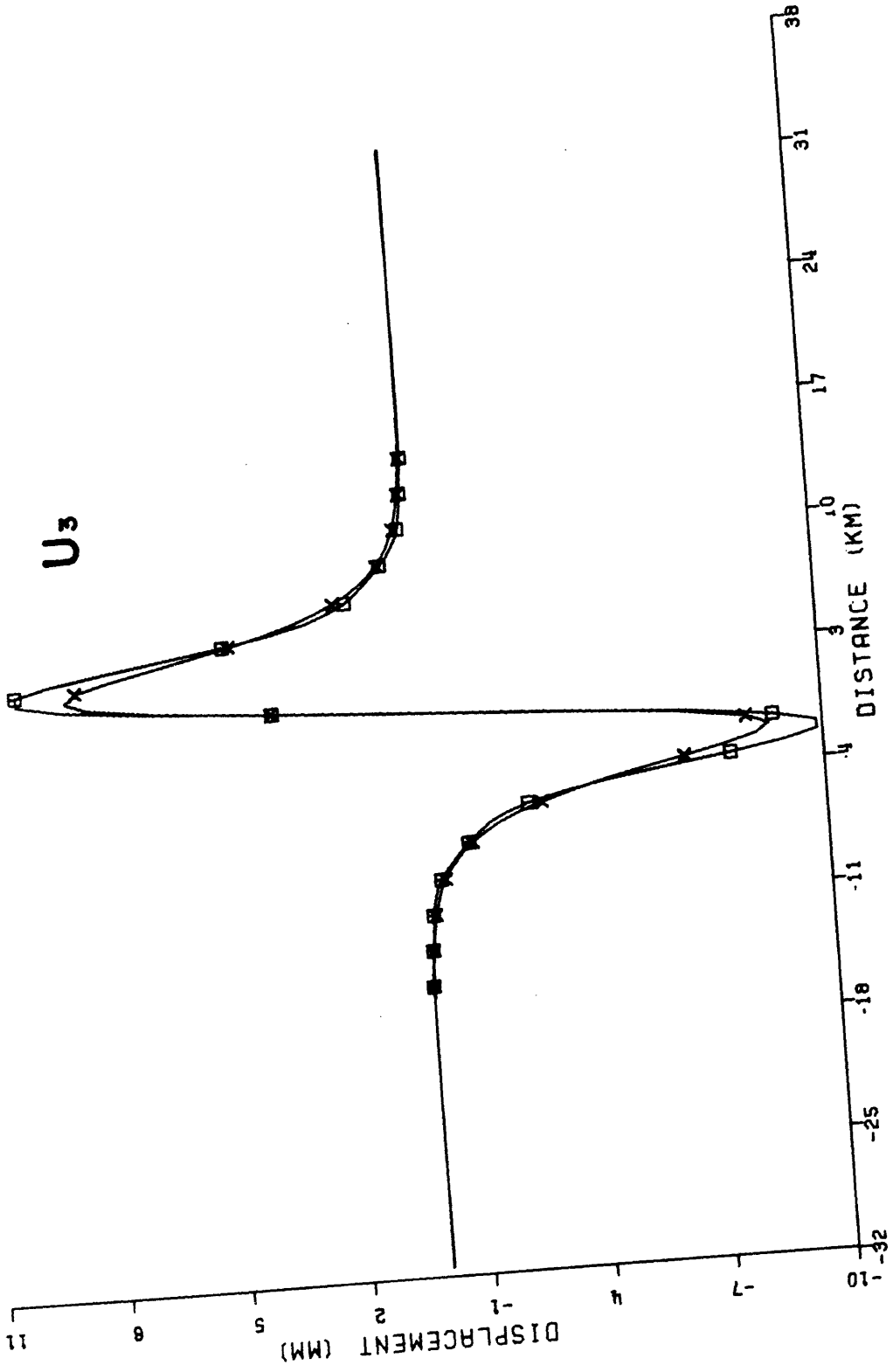

Figure 3.20

Figure 3.21

Crustal structure referred to as a realistic crustal structure in the text. Thickness of layers in km, λ and μ in dynes/cm^2 x 10^{11}, ν = Poisson's ratio, V_p and V_s are p and s velocities in km/sec, and p is density in gm/cm^3.

THICKNESS	λ	μ	ν	V_P	V_S	ρ	
1.7	1.12	.7	.3	3.56	1.90	2.0	LAYER 1
2.8	2.40	2.58	.24	5.49	3.20	2.5	LAYER 2
10.6	3.12	3.55	.23	6.15	3.60	2.7	LAYER 3
16.9	3.95	4.49	.23	6.70	3.94	2.88	LAYER 4
∞	6.64	7.17	.24	7.99	4.68	3.28	HALF-SPACE

Figure 3.21

Figure 3.22

(a) Model RVSS - a long, narrow strike-slip fault embedded in the realistic crustal structure shown in figure 3.21. The fault is 16 km long, 4 km wide, and has a burgers vector $\vec{B} = (0,1,0)$. The depth to the top edge of the fault is 3 km. Sample sizes used: $\Delta X_1 = 1$ km, $\Delta X_2 = 2$ km.

(b) Model RVDS - a dip-slip event embedded in the realistic crustal structure. L = 16 km, W = 8 km, $\vec{B} = (0,1,0)$, and D = 3 km. Sample sizes: $\Delta X_1 = .6$, $\Delta X_2 = 1.5$ km.

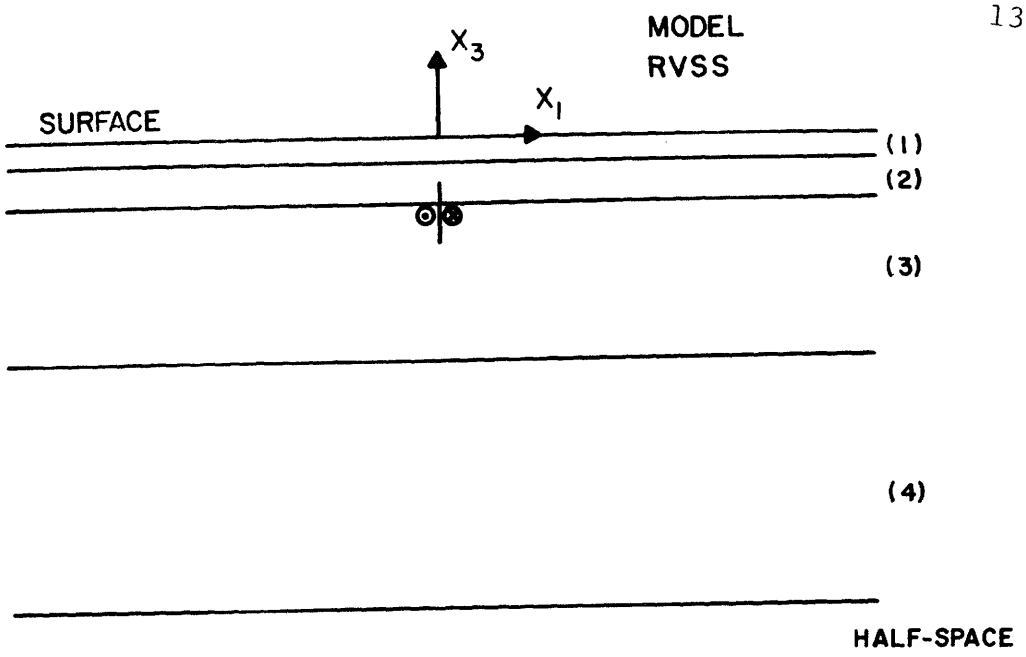

(a)

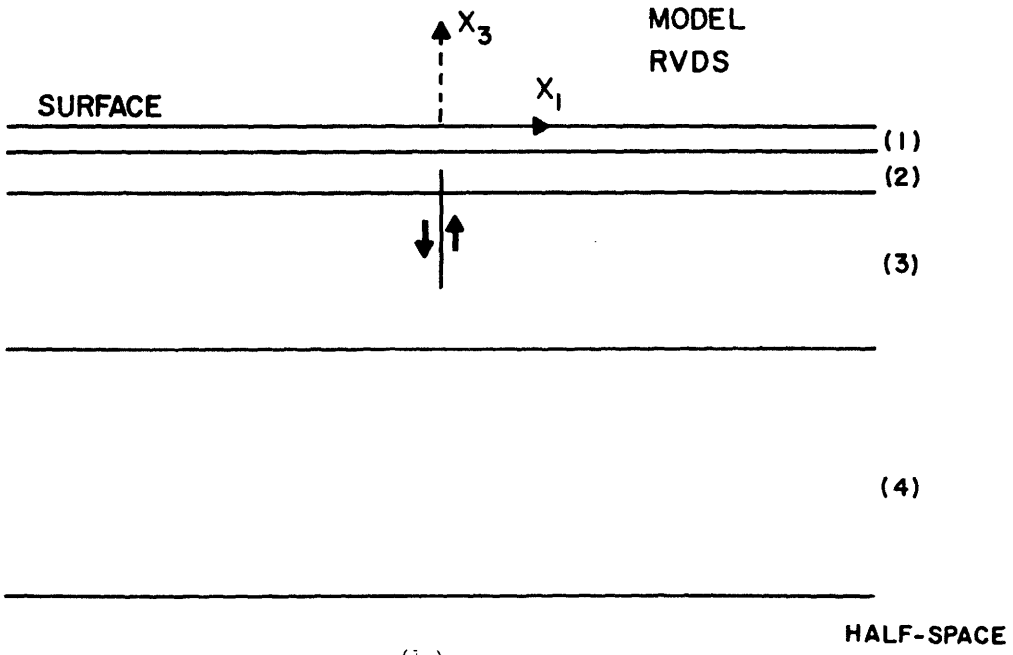

(b)

Figure 3.22

Figures 3.23-3.25

Comparison of model RVSS (□) with the solutions for a half-space (X) with elastic properties of the second layer in the realistic crustal model (ν = .24). Profiles are taken at x_2 = 4 km.

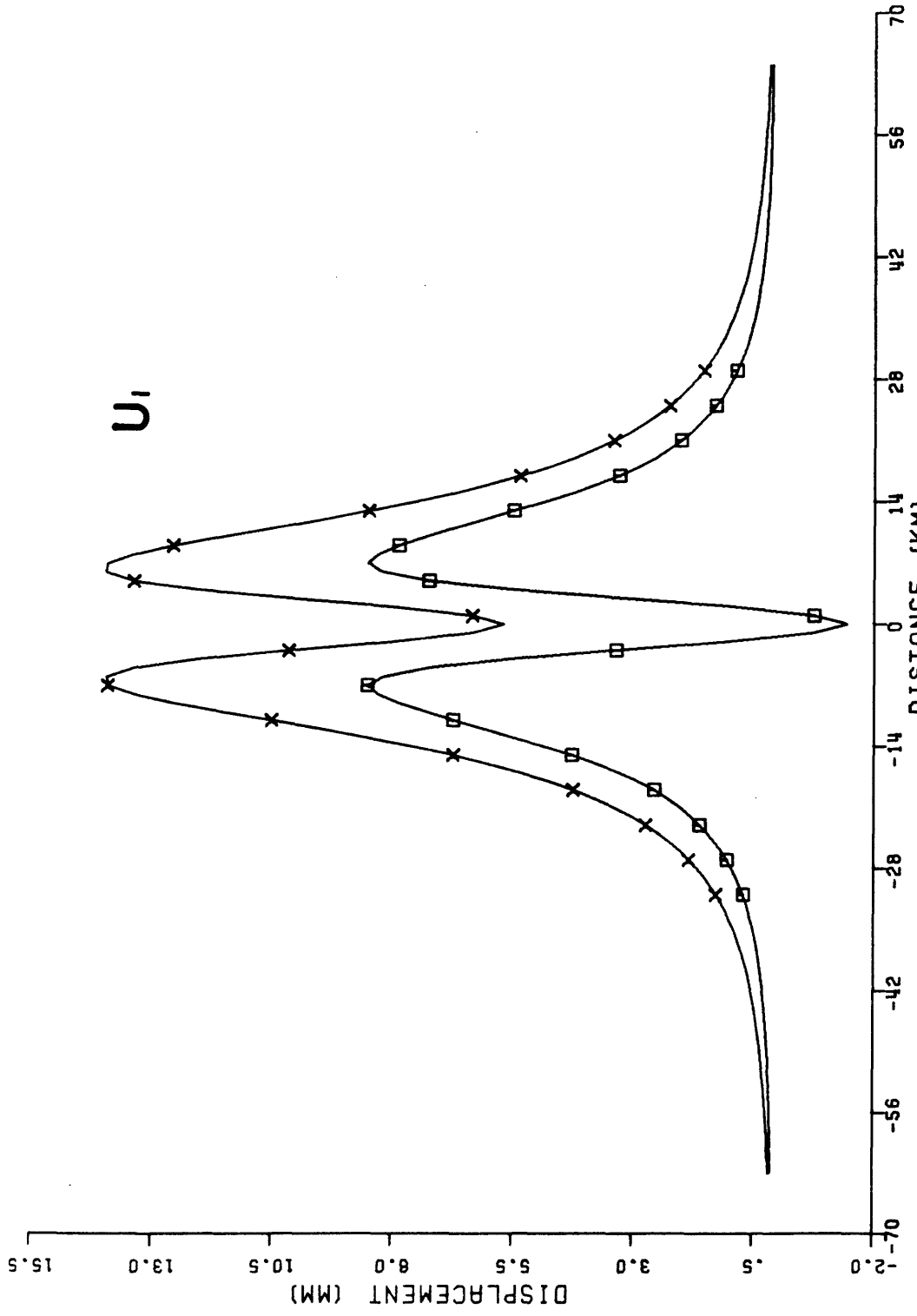
U1
DISPLACEMENT (MM)
-2.0
.5
3.0
5.5
8.0
10.5
13.0
15.5
DISTANCE (KM)
-70
-56
-42
-28
-14
0
14
28
42
56
70

Figure 3.23

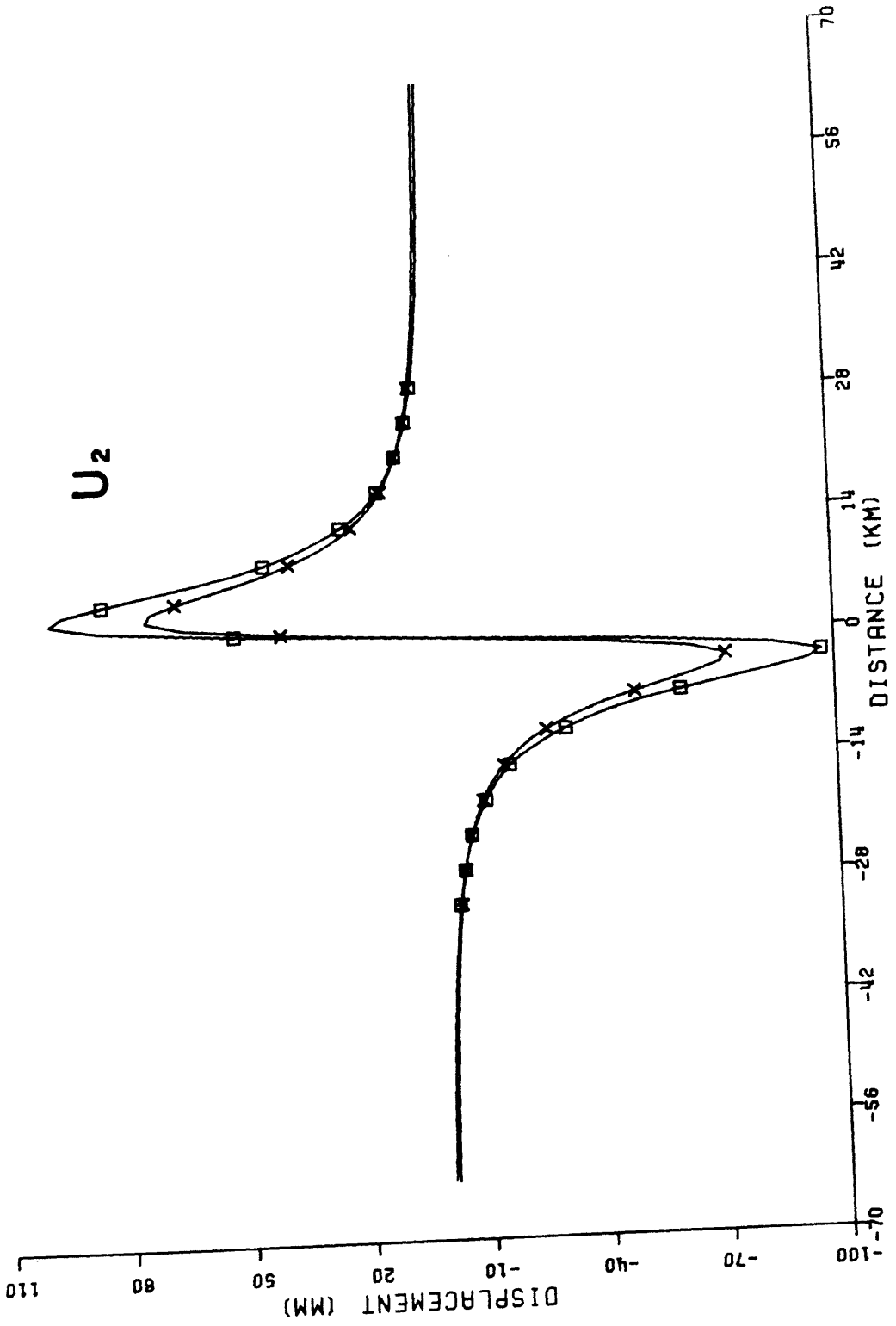
U2
DISPLACEMENT (MM)
110
80
50
20
-10
-40
-70
-100
DISTANCE (KM)
70
56
42
28
14
0
-14
-28
-42
-56
-70

Figure 3.24

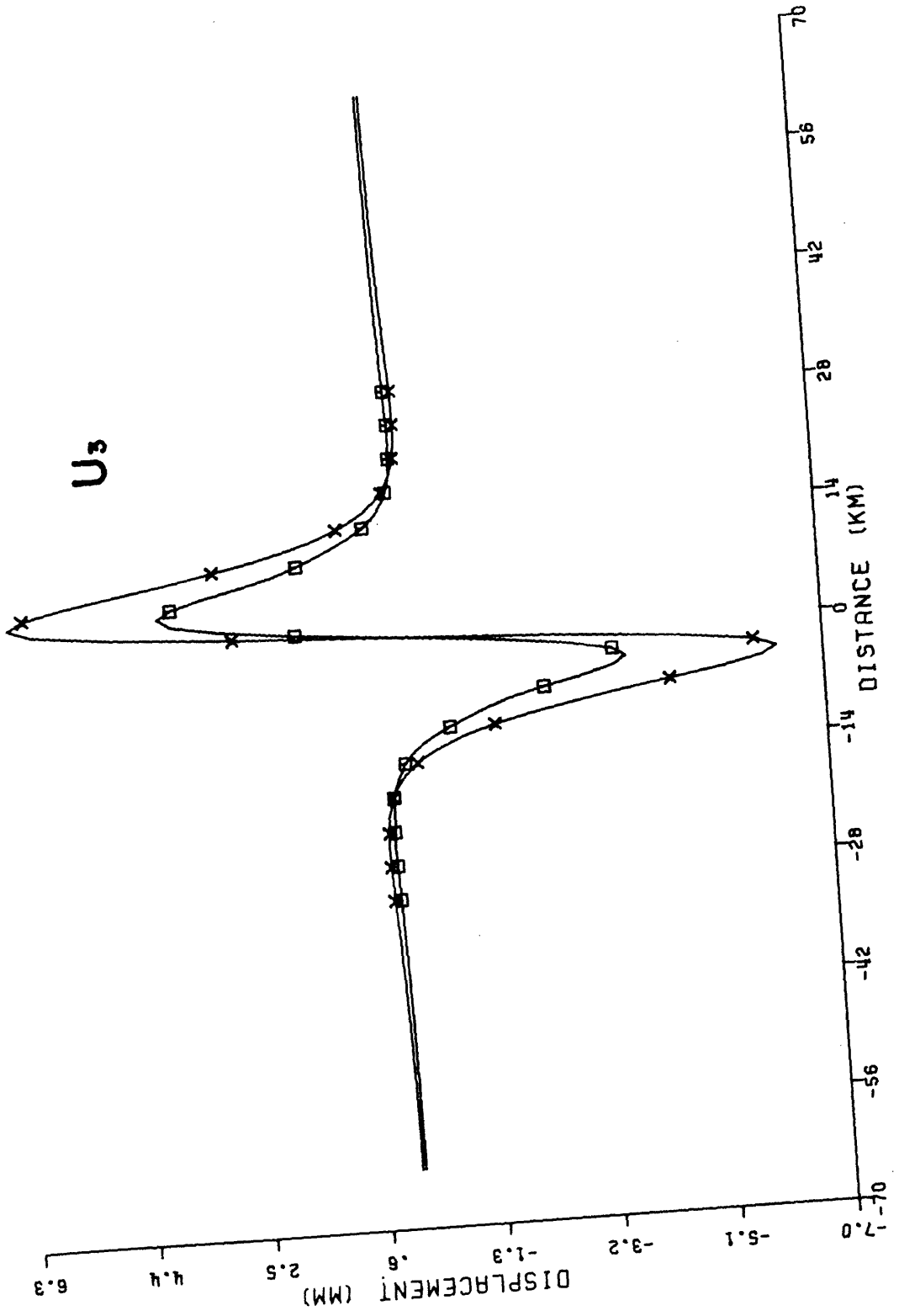
U3
DISPLACEMENT (MM)
6.3
4.4
2.5
.6
-1.3
-3.2
-5.1
-7.0
DISTANCE (KM)
-70
-56
-42
-28
-14
0
14
28
42
56
70

Figure 3.25

Figures 3.26 - 3.29

Comparison of displacements for model RVDS (□) with displacements of a homogeneous half-space model (X) with elastic constants equal to those of the second layer of the realistic crustal structure (ν = .24). Profiles in figures 3.26, 3.27, and 3.29 are at x_2 = 6 km. The profile in figure 3.28 is at x_2 = 1.5 km.

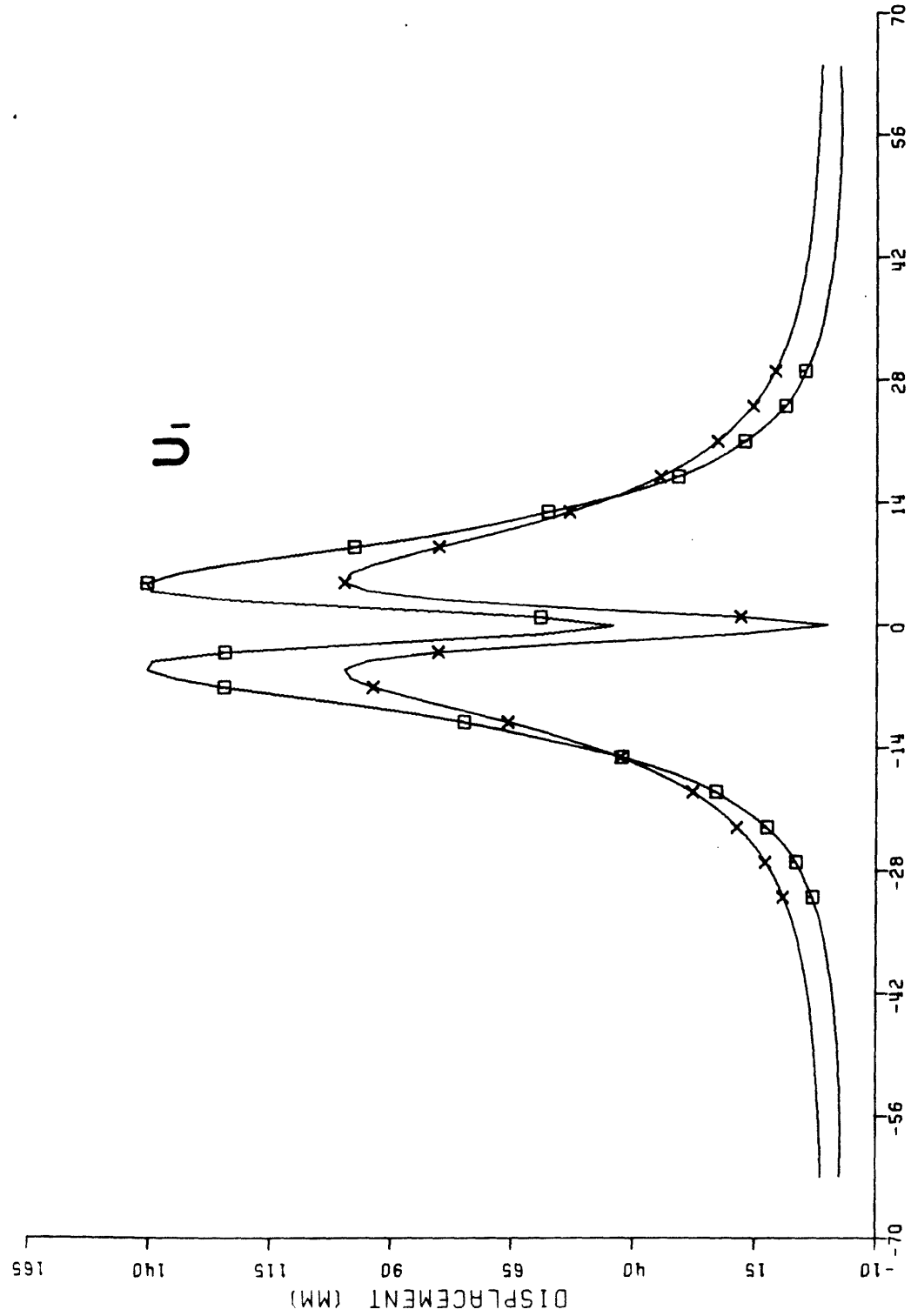
DISPLACEMENT (MM)
-10
15
40
65
90
115
140
165
DISTANCE (KM)
-70
-56
-42
-28
-14
0
14
28
42
56
70

Figure 3.26

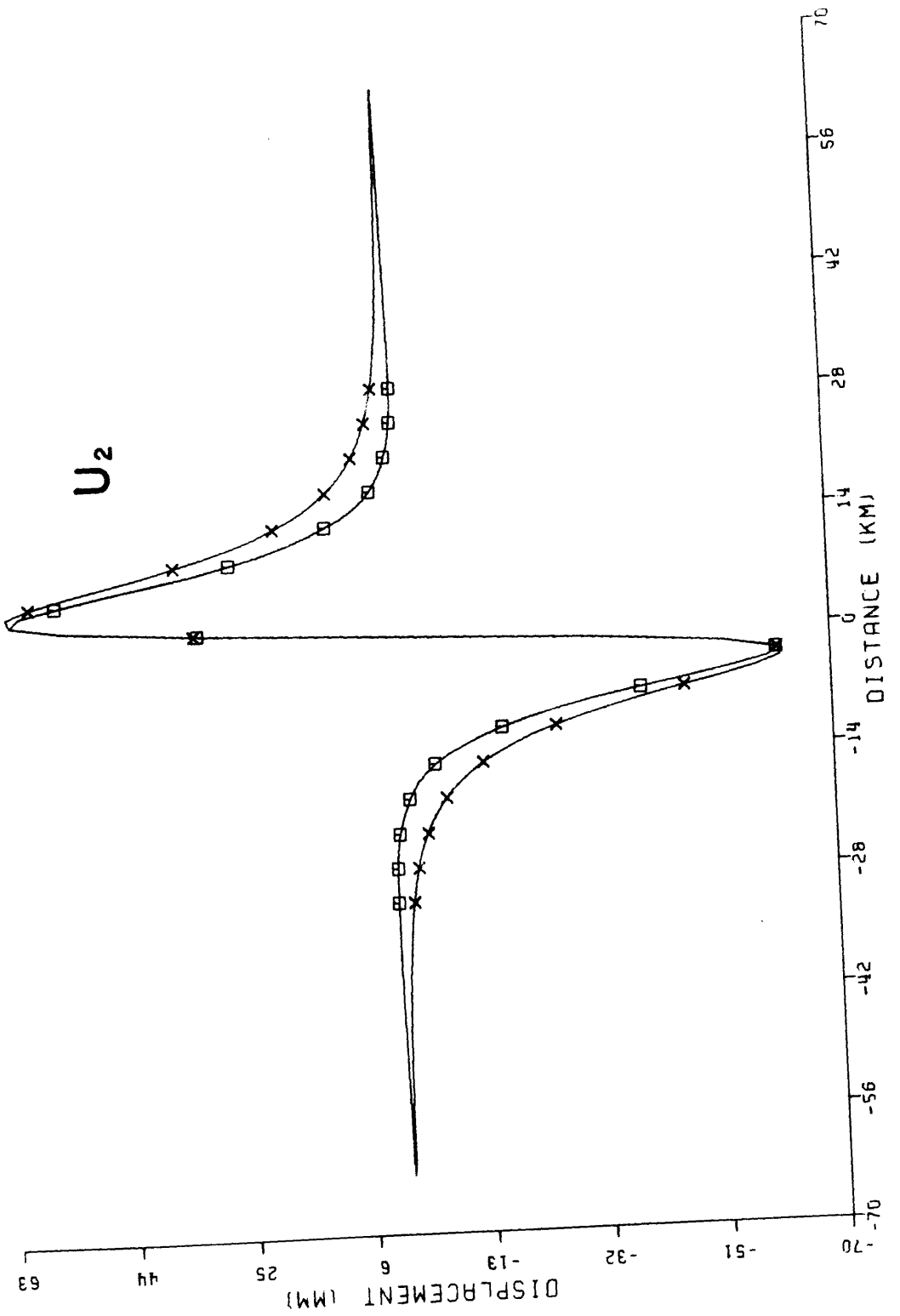
U_2
DISPLACEMENT (MM)
63
44
25
6
-13
-32
-51
-70
DISTANCE (KM)
70
56
42
28
14
0
-14
-28
-42
-56
-70

Figure 3.27

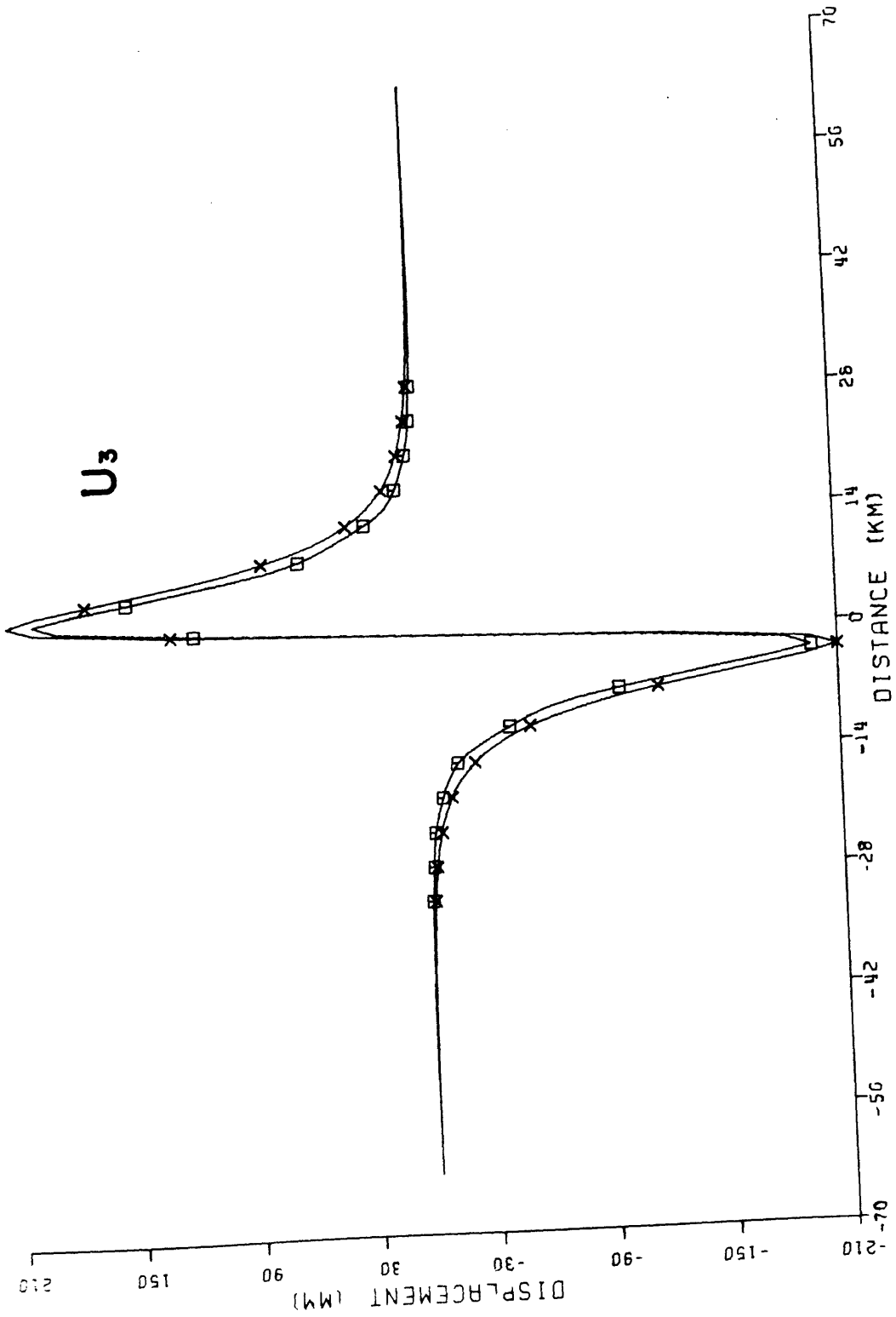
U3
DISPLACEMENT (MM)
210
150
90
30
-30
-90
-150
-210
DISTANCE (KM)
70
56
42
28
14
0
-14
-28
-42
-56
-70

Figure 3.28

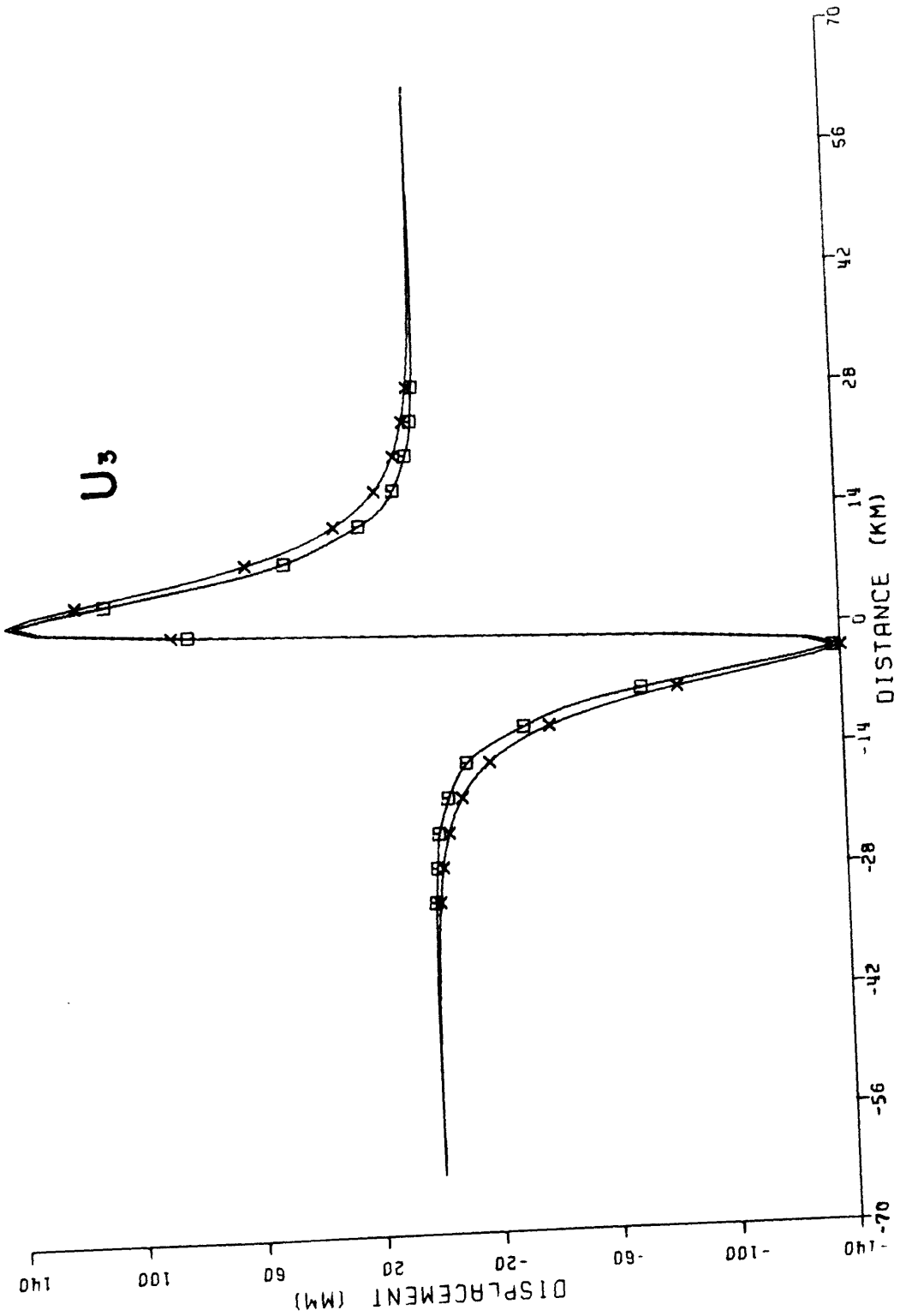
U3
DISPLACEMENT (MM)
140
100
60
20
-20
-60
-100
-140
DISTANCE (KM)
70
56
42
28
14
0
-14
-28
-42
-56
-70

Figure 3.29

Figure 3.30

(a) Model ROSS - oblique strike-slip fault embedded in realistic crustal structure. Fault parameters are L = 13.5 km, W = 8 km, dip angle = 30°, D = 3 km, and $\vec{B}$ = (0,1,0). Sample sizes used in the numerical calculations: ΔX_1 = .6 km, ΔX_2 = 1.5 km.

(b) Model RODS - oblique thrust fault embedded in realistic crustal structure. The fault parameters and sample sizes are the same as those in (a). $\vec{B}$ = (.866, 0, .5).

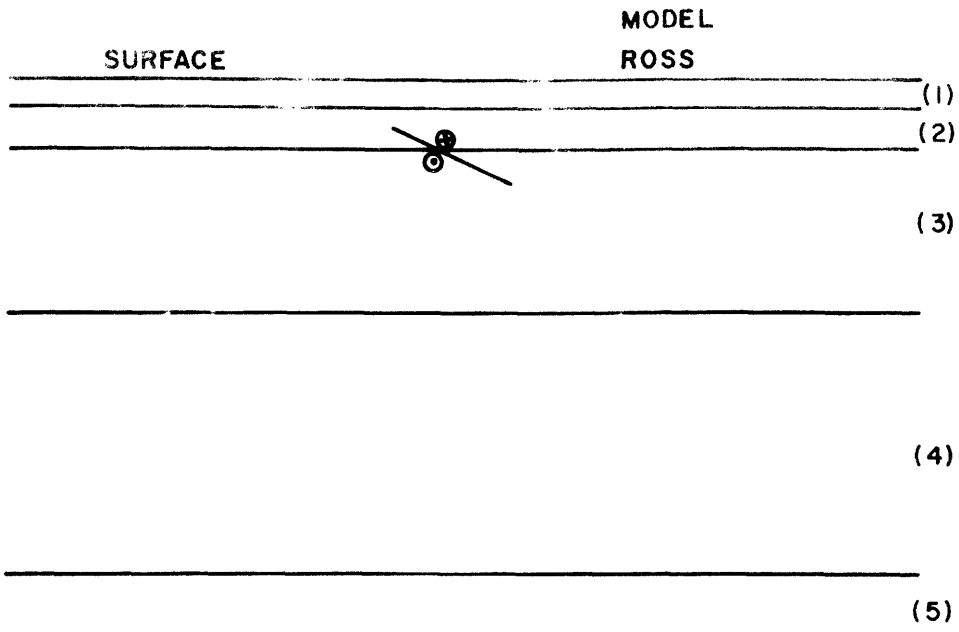

(a)

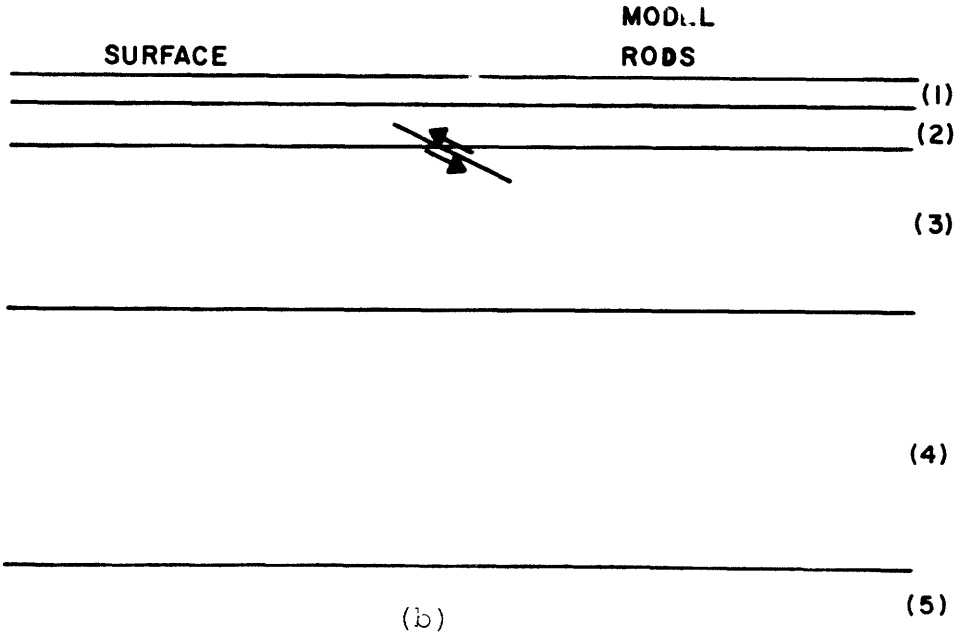

(b)

Figure 3.30

Figures 3.31 - 3.33

Comparison of displacements from model ROSS (□) with half-space solutions (X).

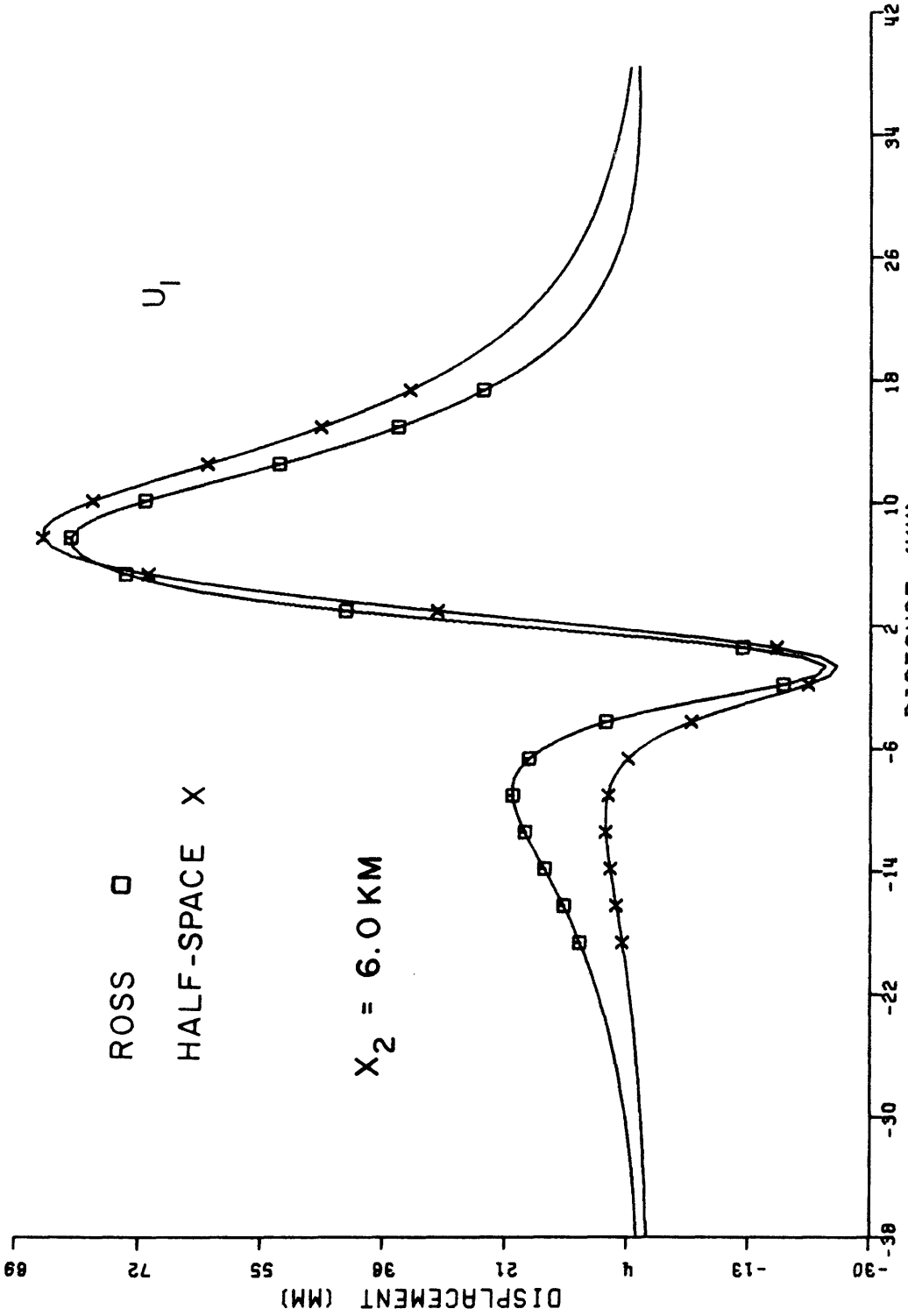
ROSS □
HALF-SPACE X
X_2 = 6.0 KM
U_1
DISPLACEMENT (MM)
-30
-13
4
21
38
55
72
89
-38
-30
-22
-14
-6
2
10
18
26
34
42
DISTANCE (KM)

Figure 3.31

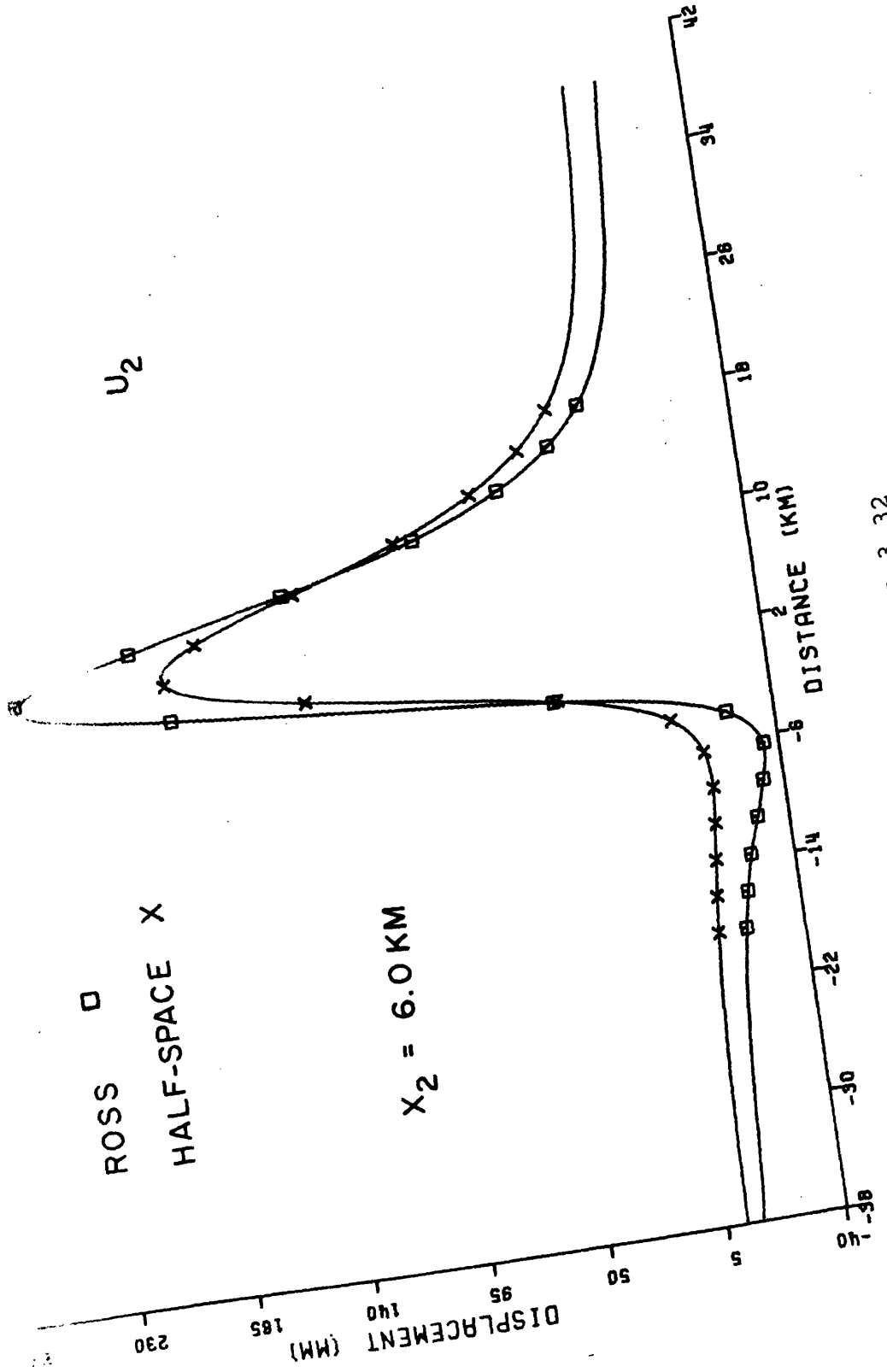
U_2
ROSS □
HALF-SPACE X
X_2 = 6.0 KM
DISPLACEMENT (MM)
230
185
140
95
50
5
-40
-36
DISTANCE (KM)
42
34
26
18
10
2
-6
-14
-22
-30

Figure 3.32

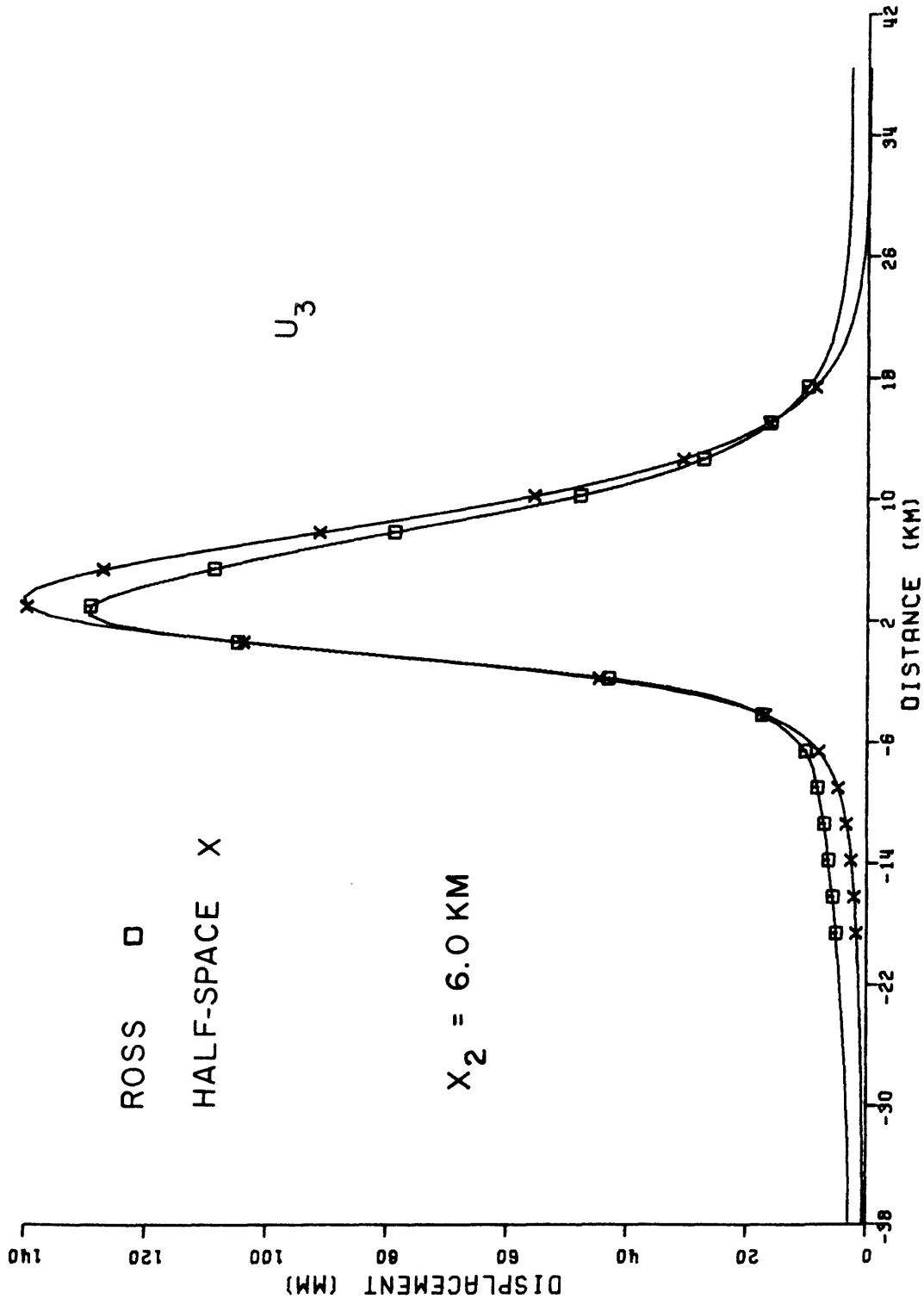

Figure 3.33

Figures 3.34-3.37

Comparison of displacements for model RODS (□) with those of a homogeneous half-space (X) with $\nu = .24$. Note the aliasing apparent in the u_1 component (figure 3.34). Aliasing in this component will not affect our results for the other components (compare figures 3.4-3.7 for the test case).

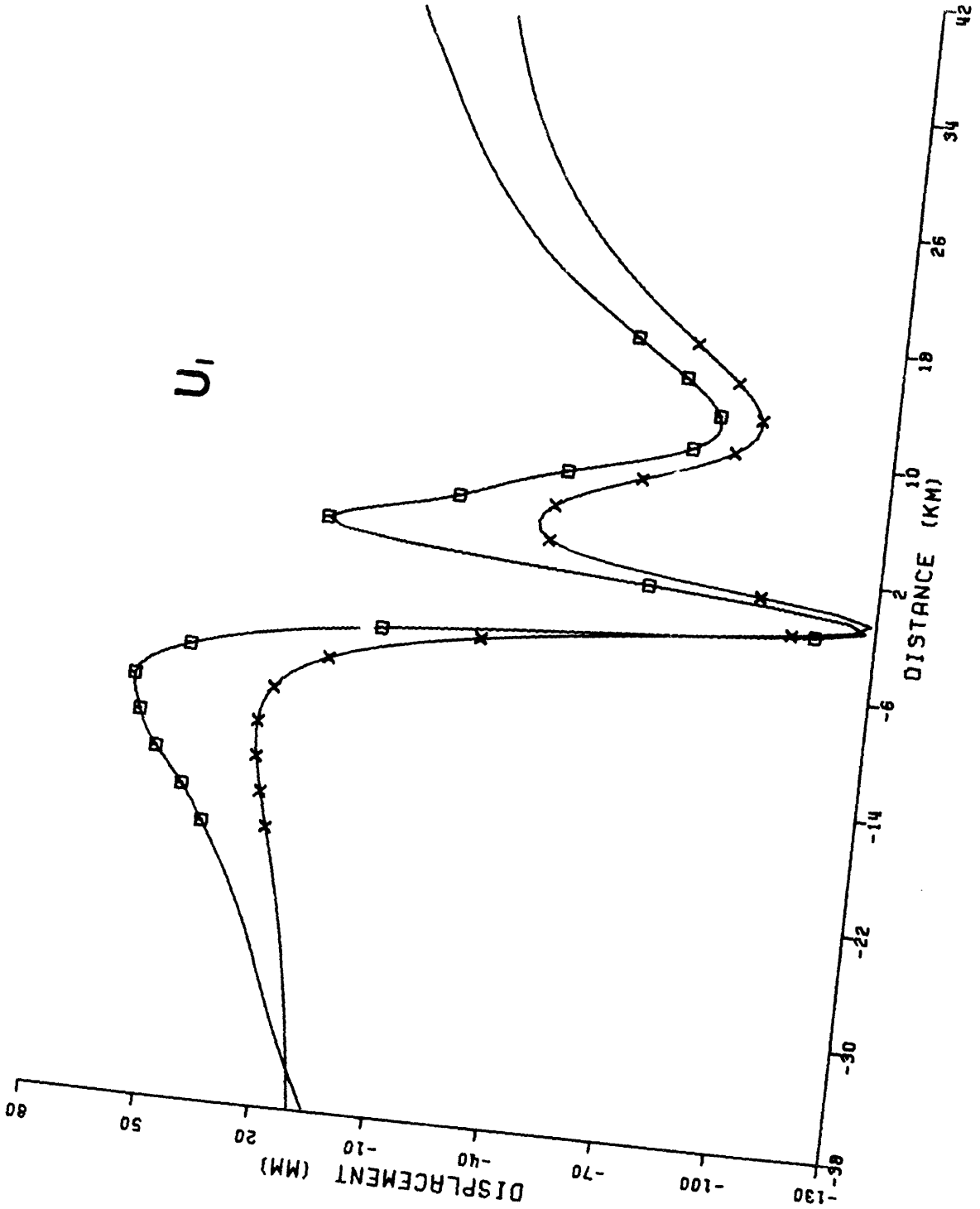
U1
DISPLACEMENT (MM)
80
50
20
-10
-40
-70
-100
-130
DISTANCE (KM)
-38
-30
-22
-14
-6
2
10
18
26
34
42

Figure 3.34

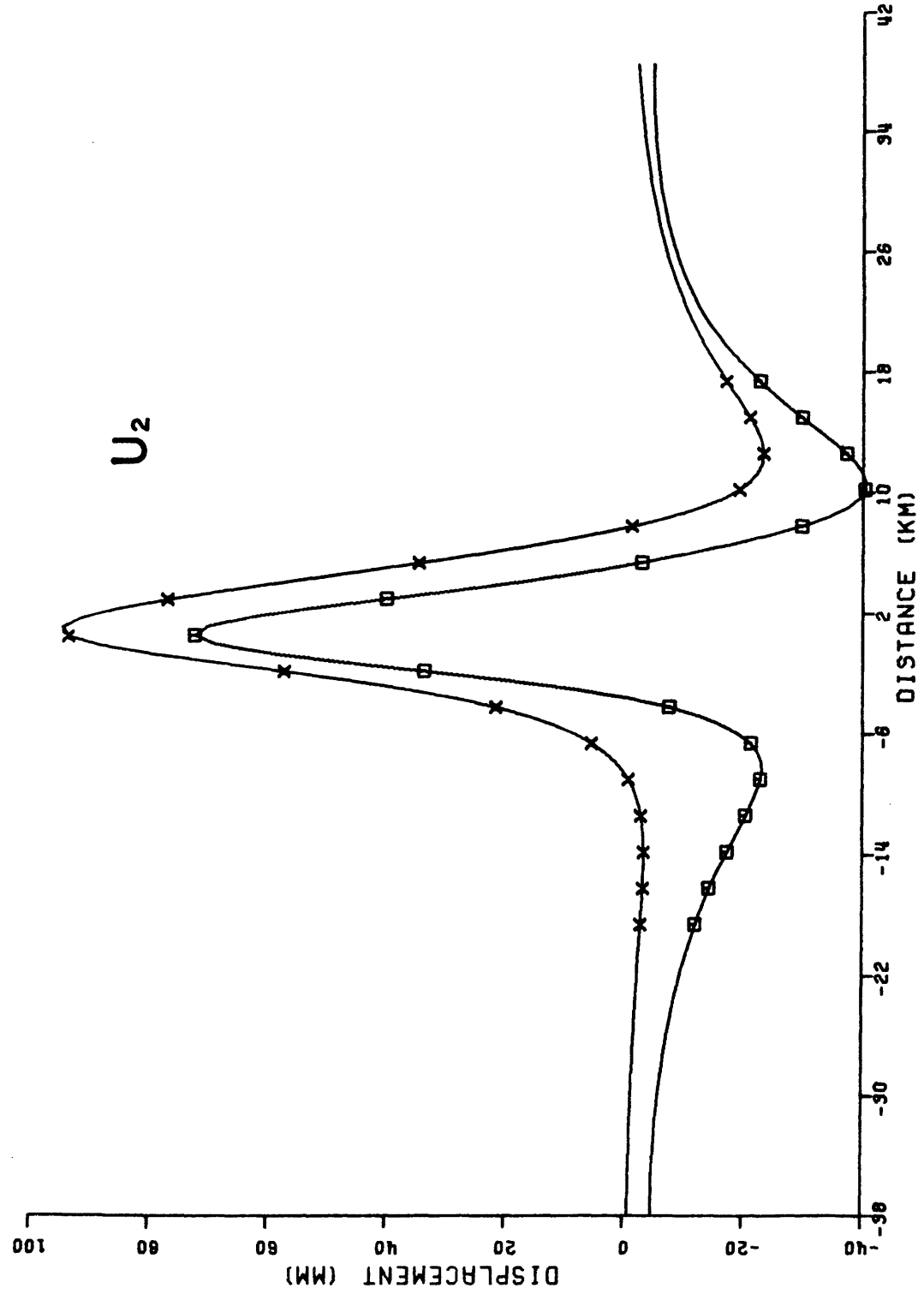
U_2
DISPLACEMENT (MM)
100
80
60
40
20
0
-20
-40
DISTANCE (KM)
-38
-30
-22
-14
-6
2
10
18
26
34
42

Figure 3.35

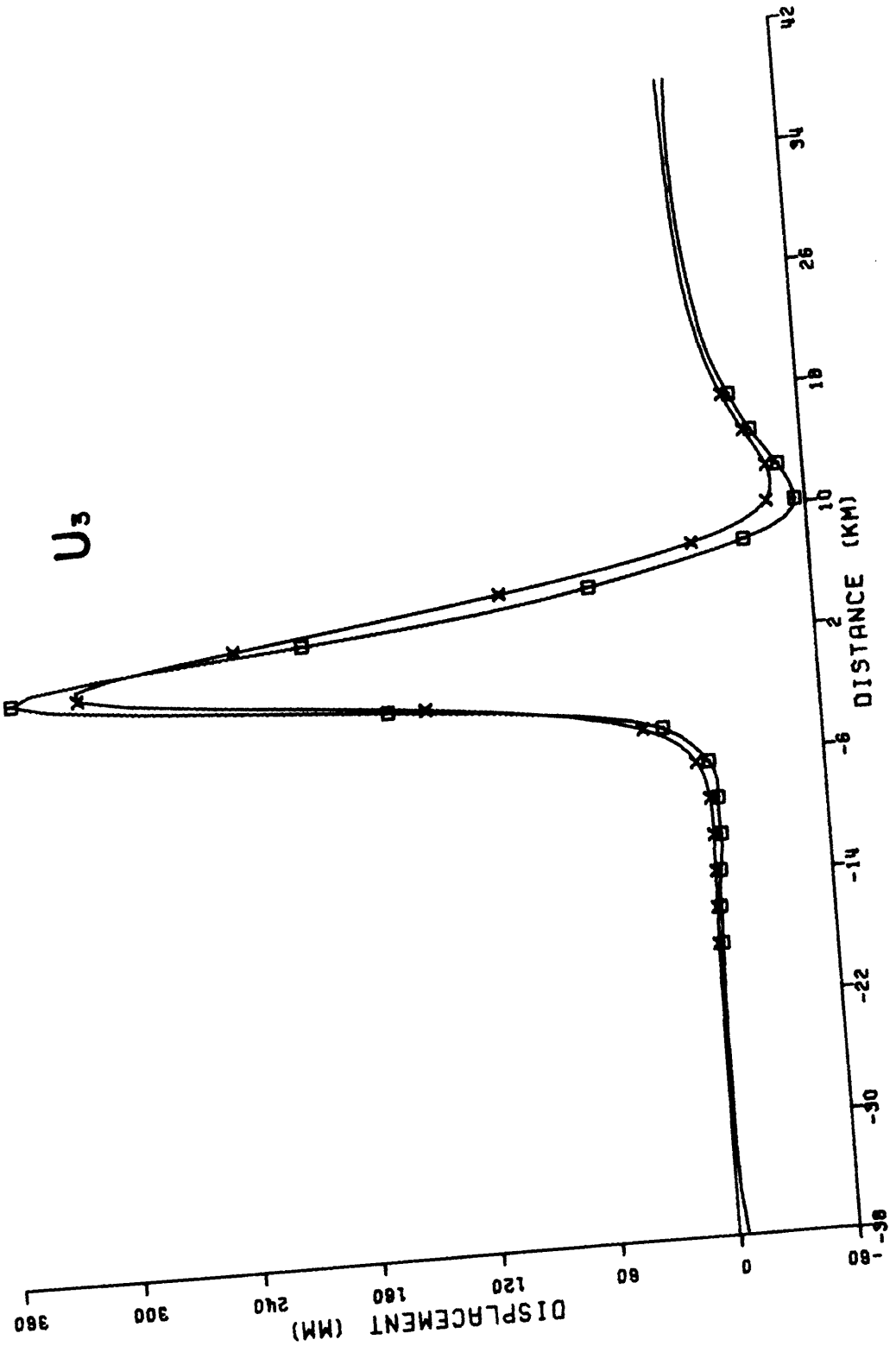
U3
DISPLACEMENT (MM)
360
300
240
180
120
60
0
-60
DISTANCE (KM)
42
34
26
18
10
2
-6
-14
-22
-30
-38

Figure 3.36

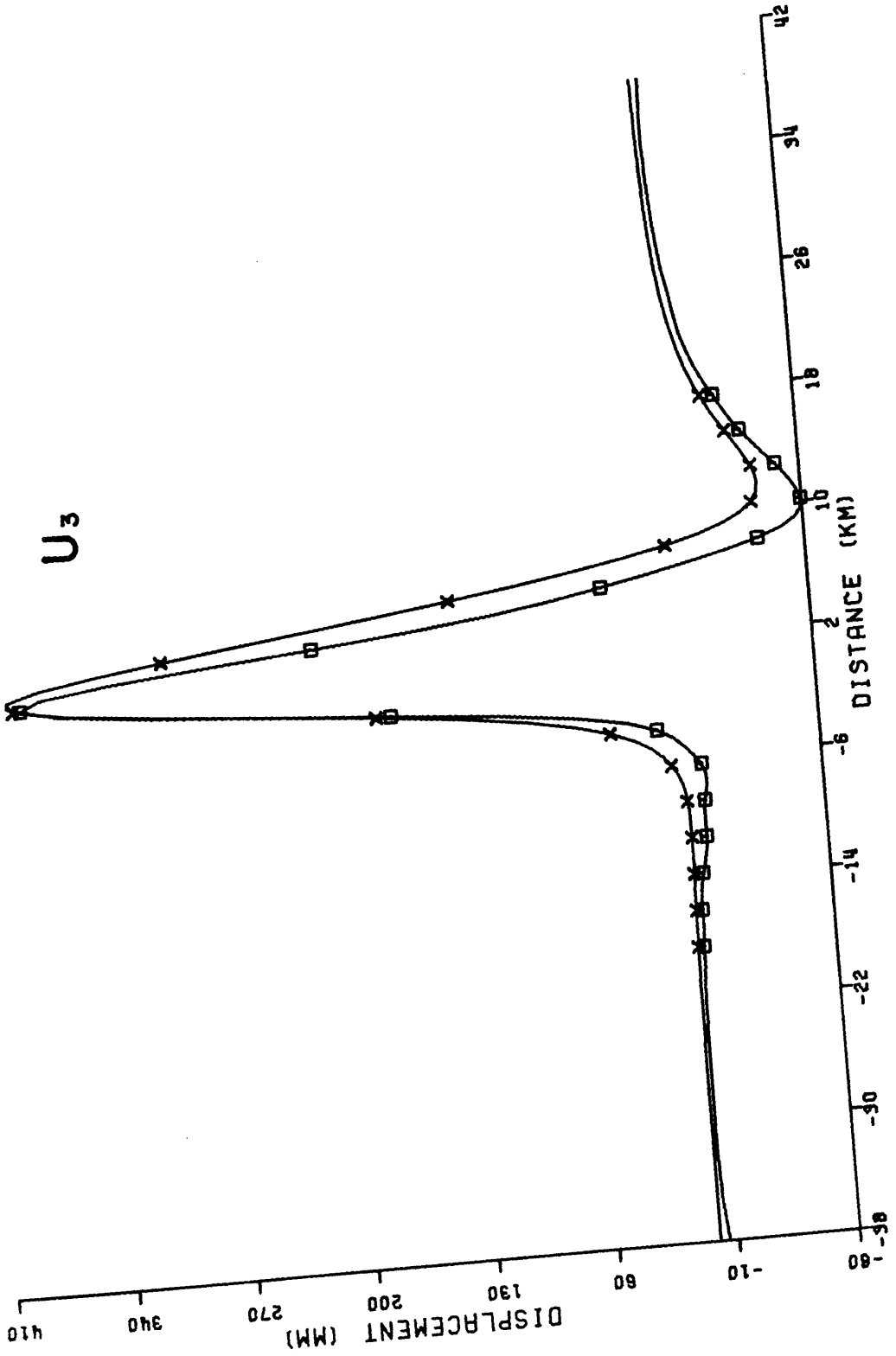
U_3
DISTANCE (KM)
42
34
26
18
10
2
-6
-14
-22
-30
-38
DISPLACEMENT (MM)
-60
-10
60
130
200
270
340
410

Figure 3.37

Figure 3.38

Model VASS - strike-slip fault penetrating a hard surface layer (λ = 3.12 x 10^{11} dynes/cm^2, μ = 3.55 x 10^{11} cynes/cm^2) overlying a soft half-space (λ = 1.12 x 10^{11} dynes/cm^2, μ = .3 x 10^{11} dynes/cm^2). The fault parameters are L = 300 km, D = 15 km, W = 80 km, and $\vec{B}$ = (0,1,0). Sample sizes used in the numerical calculation: ΔX_1 = 5 km, ΔX_2 = 50 km.

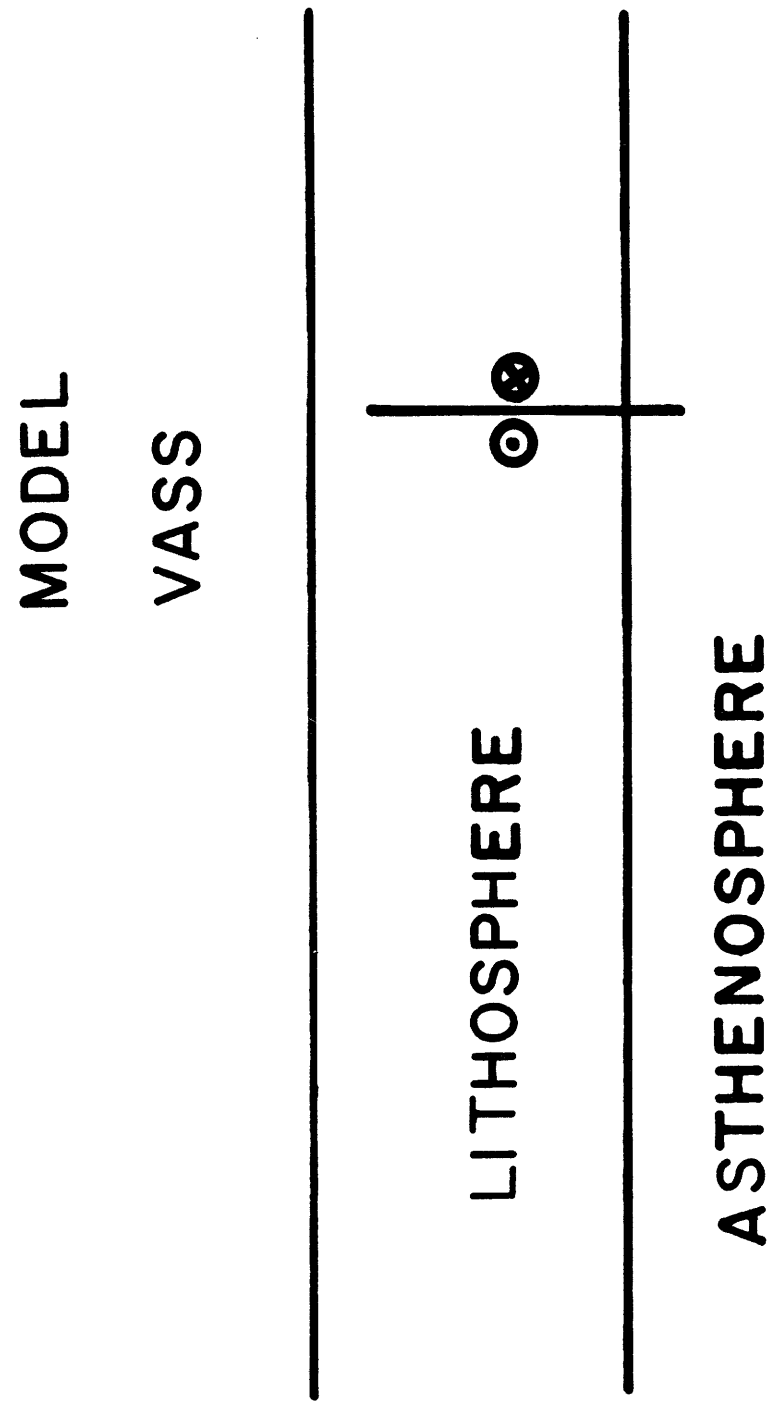

Figure 3.38

Figures 3.39-3.42

Comparison of displacements of model VASS (□) with those of a half-space model (x) with elastic constants equal to those of the hard layer in model VASS. The effect of the soft underlying layer is to extend the range of the displacements. This in turn makes our solutions more sensitive to the edge of the Fourier box. The resultant aliasing is most apparent in the u_1 component (figure 3.39). The profiles for figures 3.39-3.41 are taken at x_2 = 50 km. The profile in figure 3.42 is taken at x_2 = 200 km.

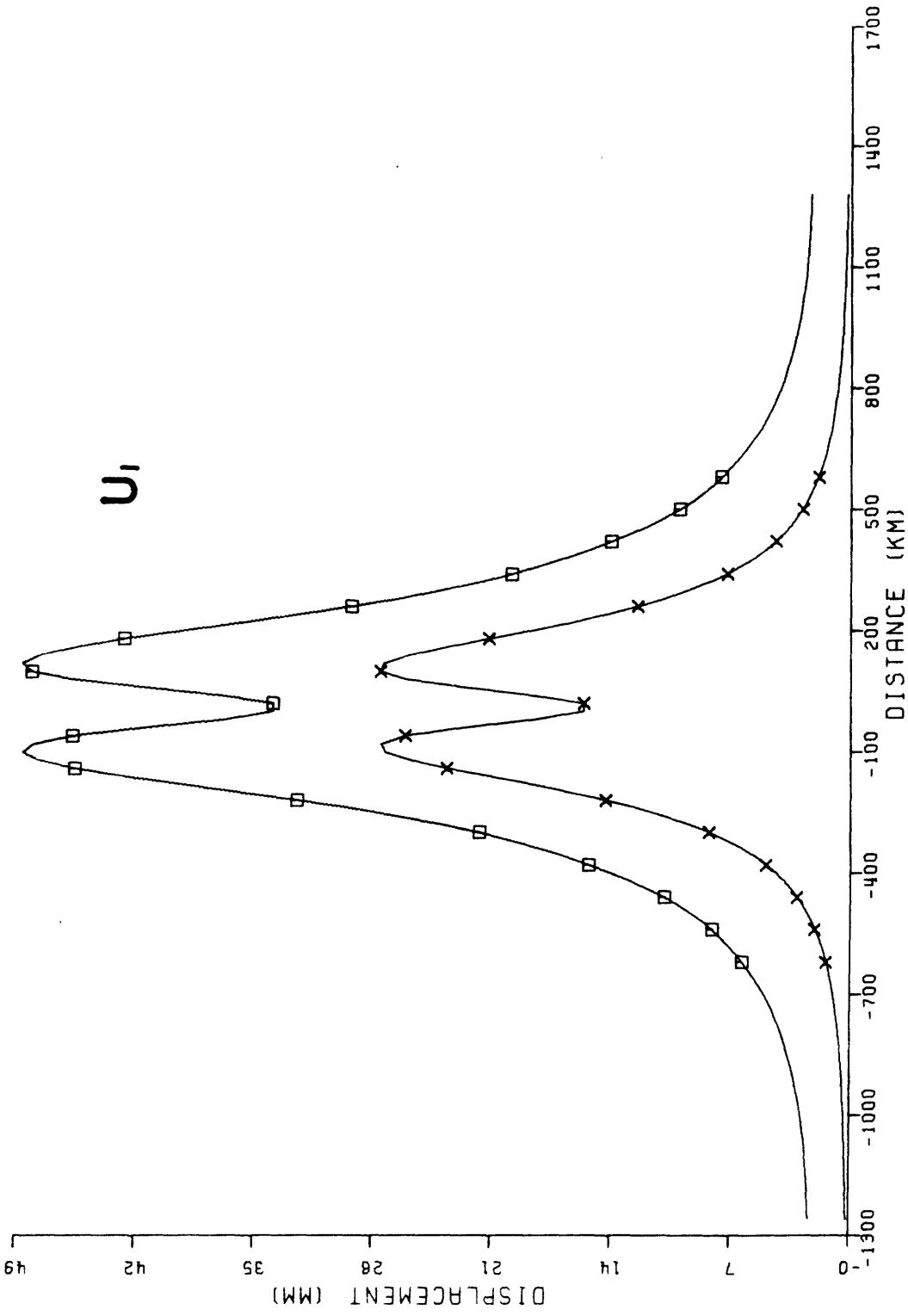
U
DISPLACEMENT (MM)
0
7
14
21
28
35
42
49
DISTANCE (KM)
-1300
-1000
-700
-400
-100
200
500
800
1100
1400
1700

Figure 3.39

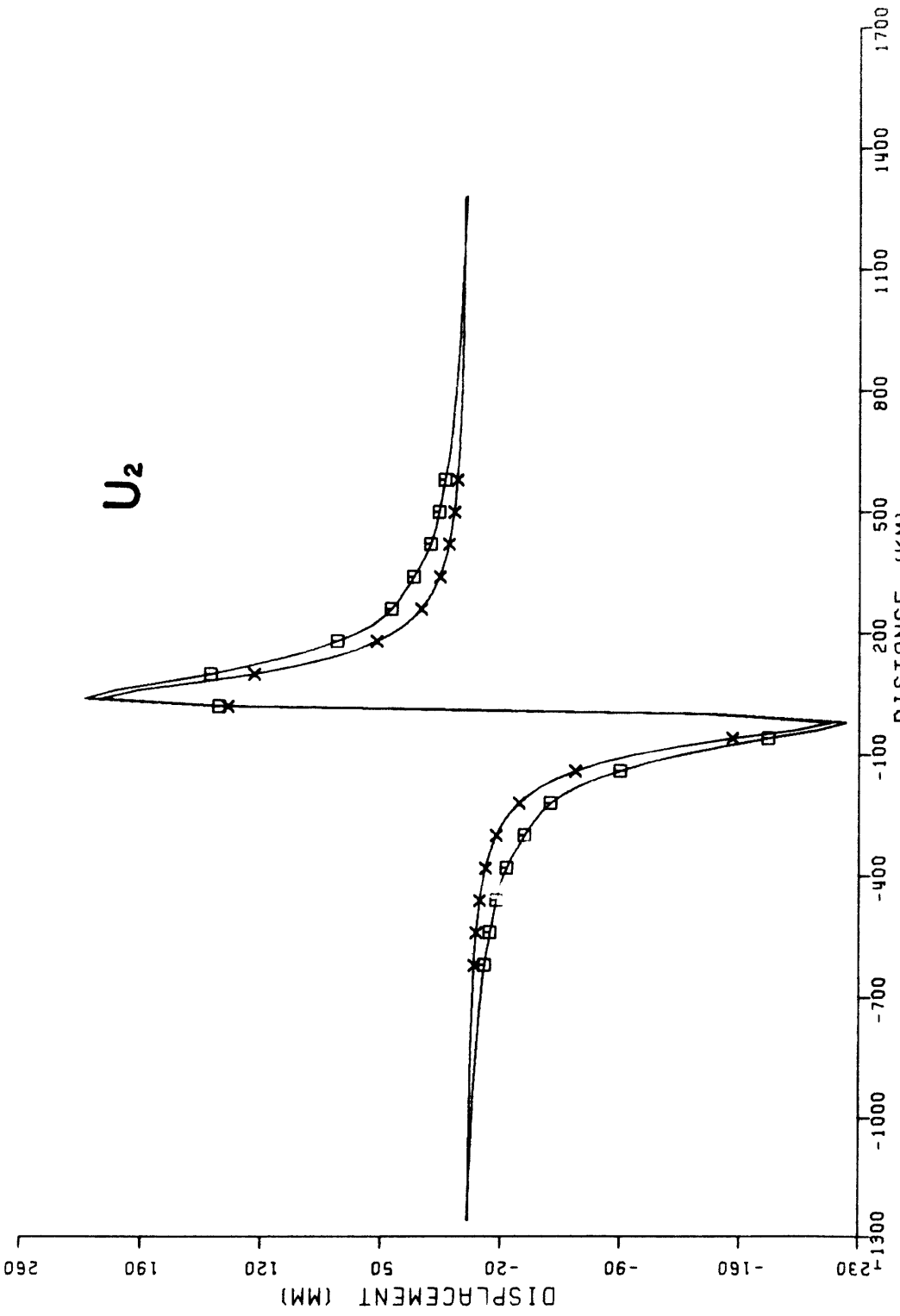
U2
DISPLACEMENT (MM)
260
190
120
50
-20
-90
-160
-230
DISTANCE (KM)
1700
1400
1100
800
500
200
-100
-400
-700
-1000
-1300

Figure 3.40

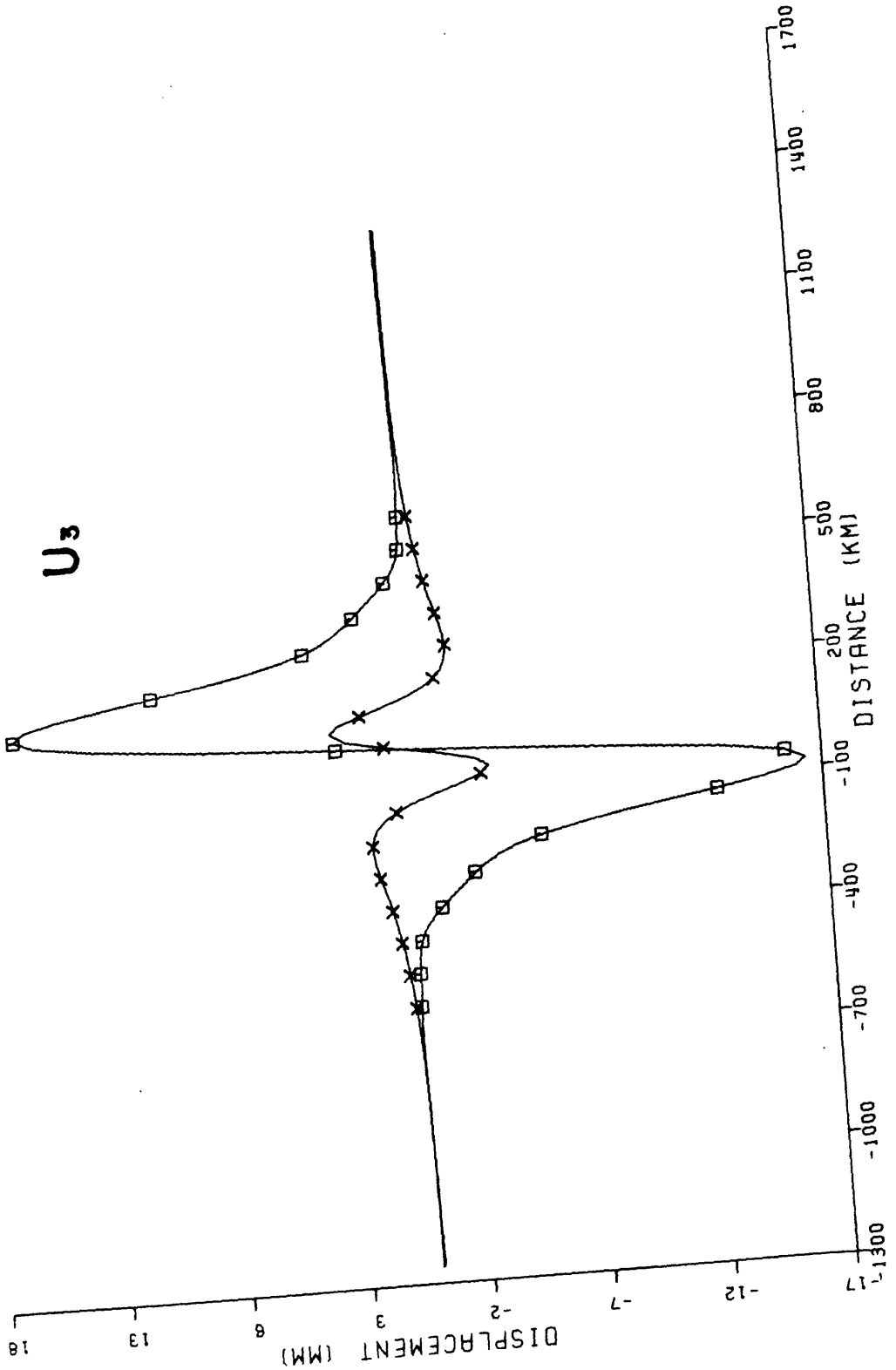
U3
DISPLACEMENT (MM)
18
13
8
3
-2
-7
-12
-17
DISTANCE (KM)
-1300
-1000
-700
-400
-100
200
500
800
1100
1400
1700

Figure 3.41

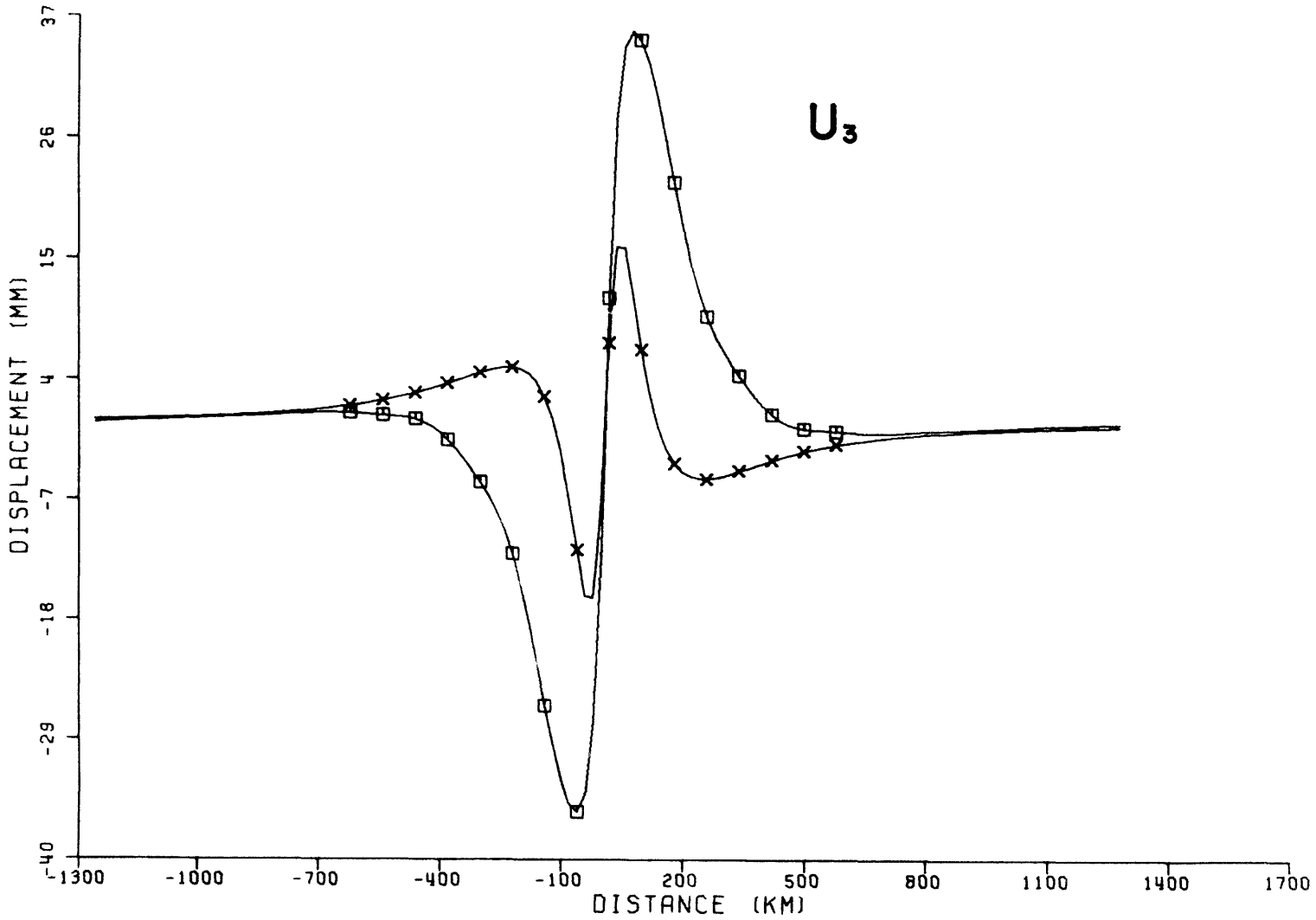
U_3
DISPLACEMENT (MM)
37
26
15
4
-7
-18
-29
-40
-1300
-1000
-700
-400
-100
200
500
800
1100
1400
1700
DISTANCE (KM)

Figure 3.42

Figure 3.43

Model VAC - dislocation model in which the sides of the dislocation are pulled away from one another. This dislocation will be used in Chapter IV to model the collision of lithospheric plates. The elastic properties are the same as those used in model VASS. The fault parameters are L = 80 km, W = 80 km, D = 15 km, and $\vec{B}$ = (1,0,0). The sample sizes used in the numerical calculation are: ΔX_1 = 5 km, ΔX_2 = 5 km.

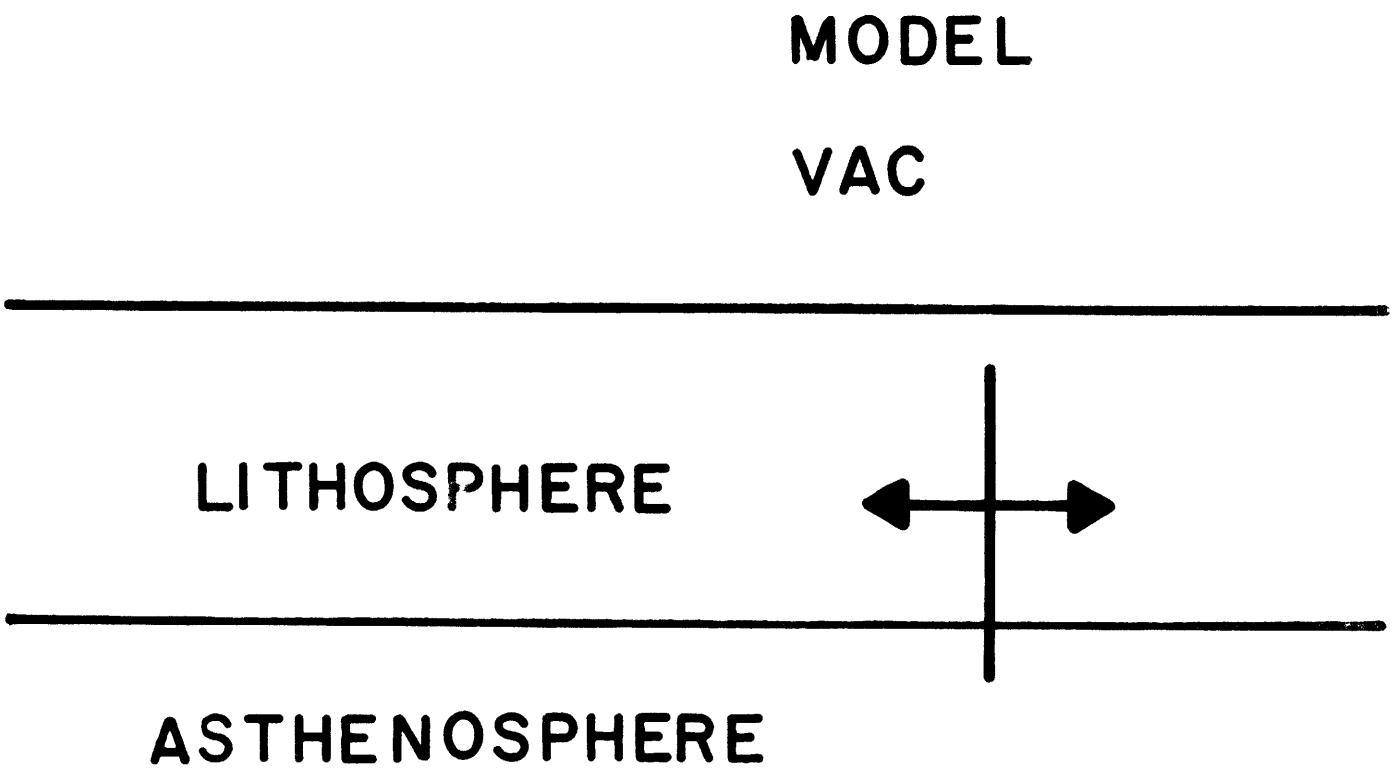

Figure 3.43

Figures 3.44-3.48

Comparison of displacements for model VAC (□) to those of a half-space model (X) with elastic constants equal to those of the harder surface layer. Figures 3.44, 3.45, and 3.47 are profiles taken at x_2 = 20 km. Figure 3.46 is a profile at x_2 = 80 km and figure 3.48 is at x_2 = 180 km. The field parallel to the Burgers' vector (u_1 in figure 3.44) is the least affected by the soft underlying layer. The u_2 and u_3 components show large changes from those of the half-space model.

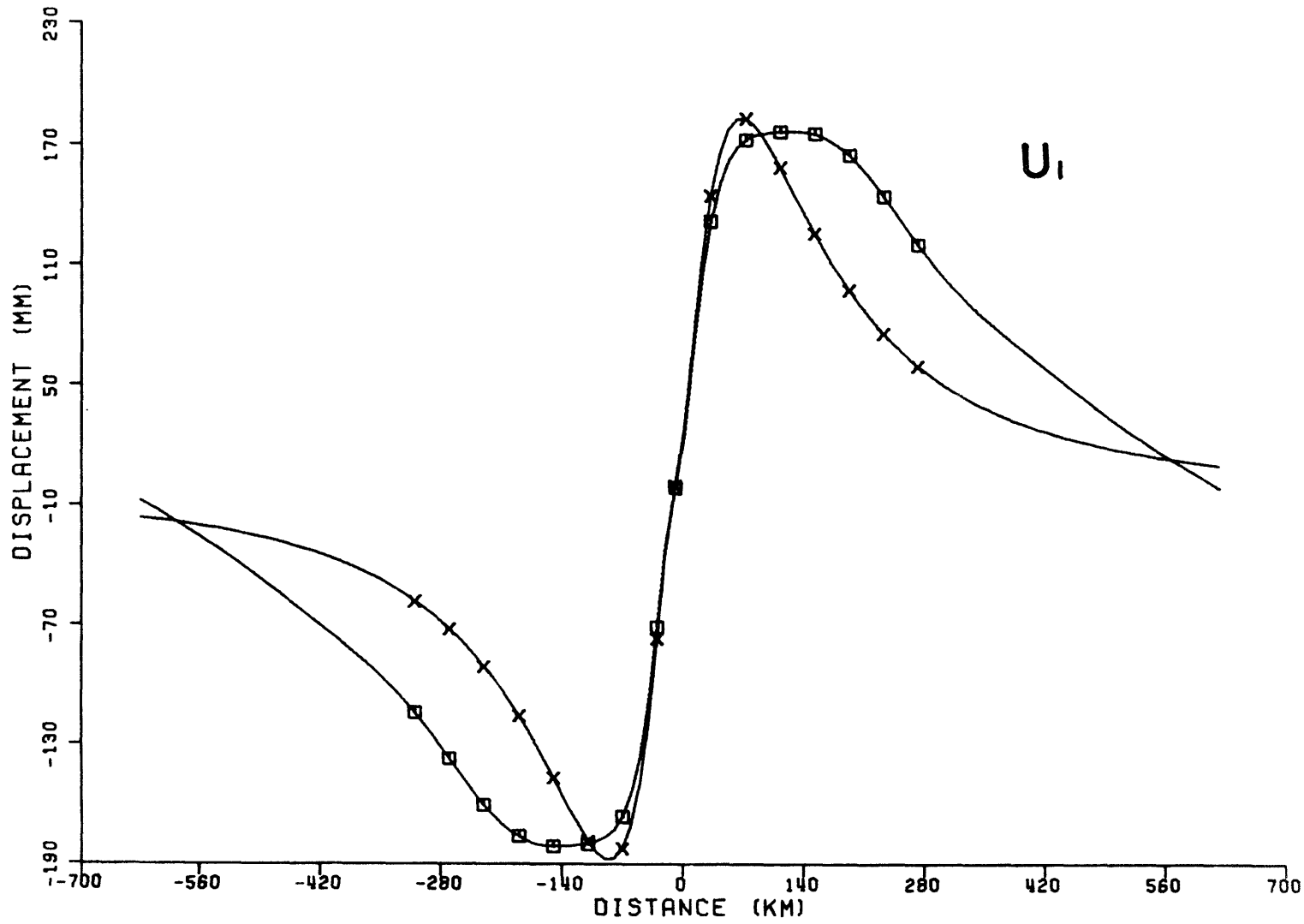
DISPLACEMENT (MM)
230
170
110
50
-10
-70
-130
-190
-700
-560
-420
-280
-140
0
140
280
420
560
700
DISTANCE (KM)
U1

Figure 3.44

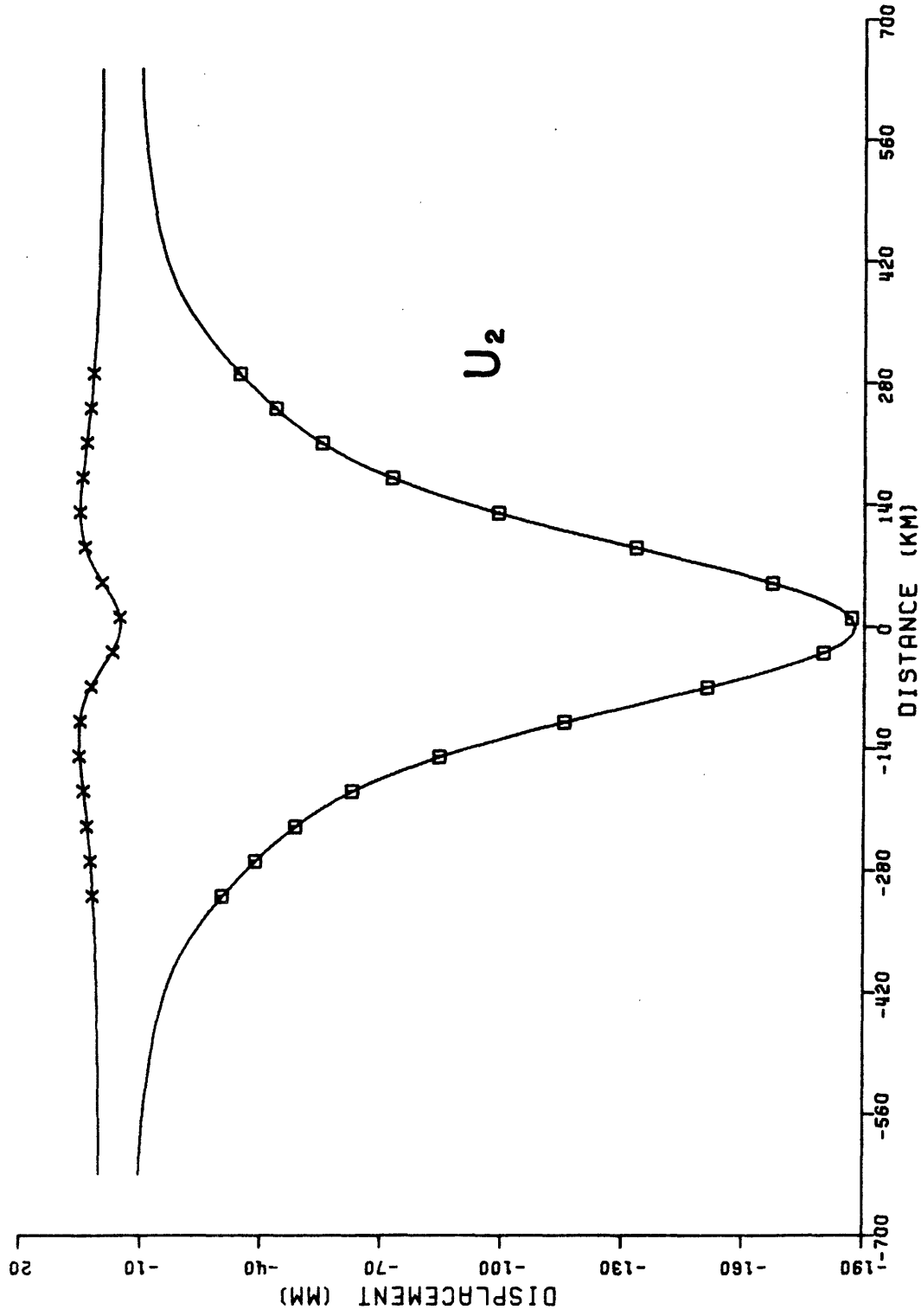
U_2
DISTANCE (KM)
700
560
420
280
140
0
-140
-280
-420
-560
-700
DISPLACEMENT (MM)
20
-10
-40
-70
-100
-130
-160
-190

Figure 3.45

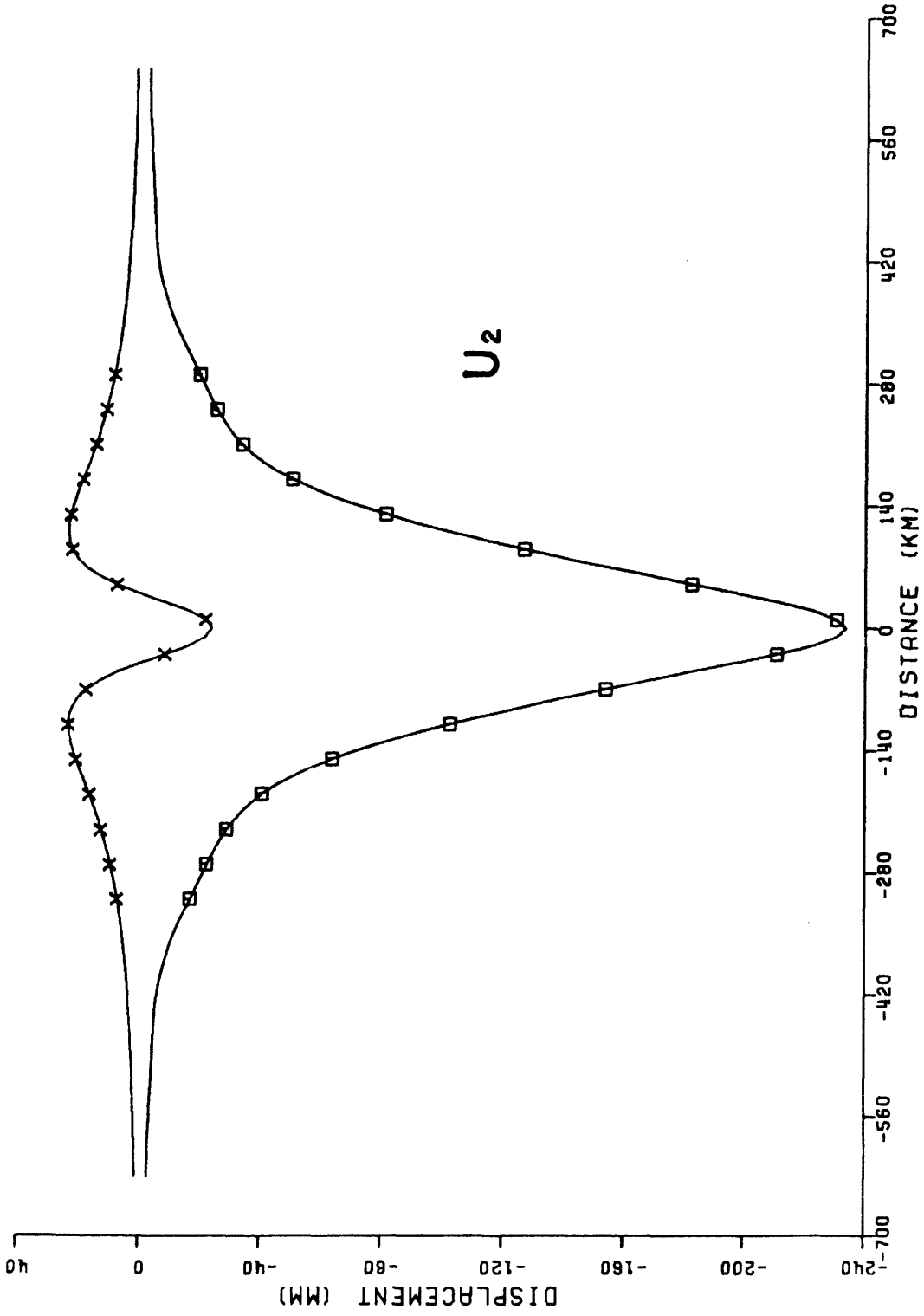
U_2
DISPLACEMENT (MM)
DISTANCE (KM)
40
0
-40
-80
-120
-160
-200
-240
700
560
420
280
140
0
-140
-280
-420
-560
-700

Figure 3.46

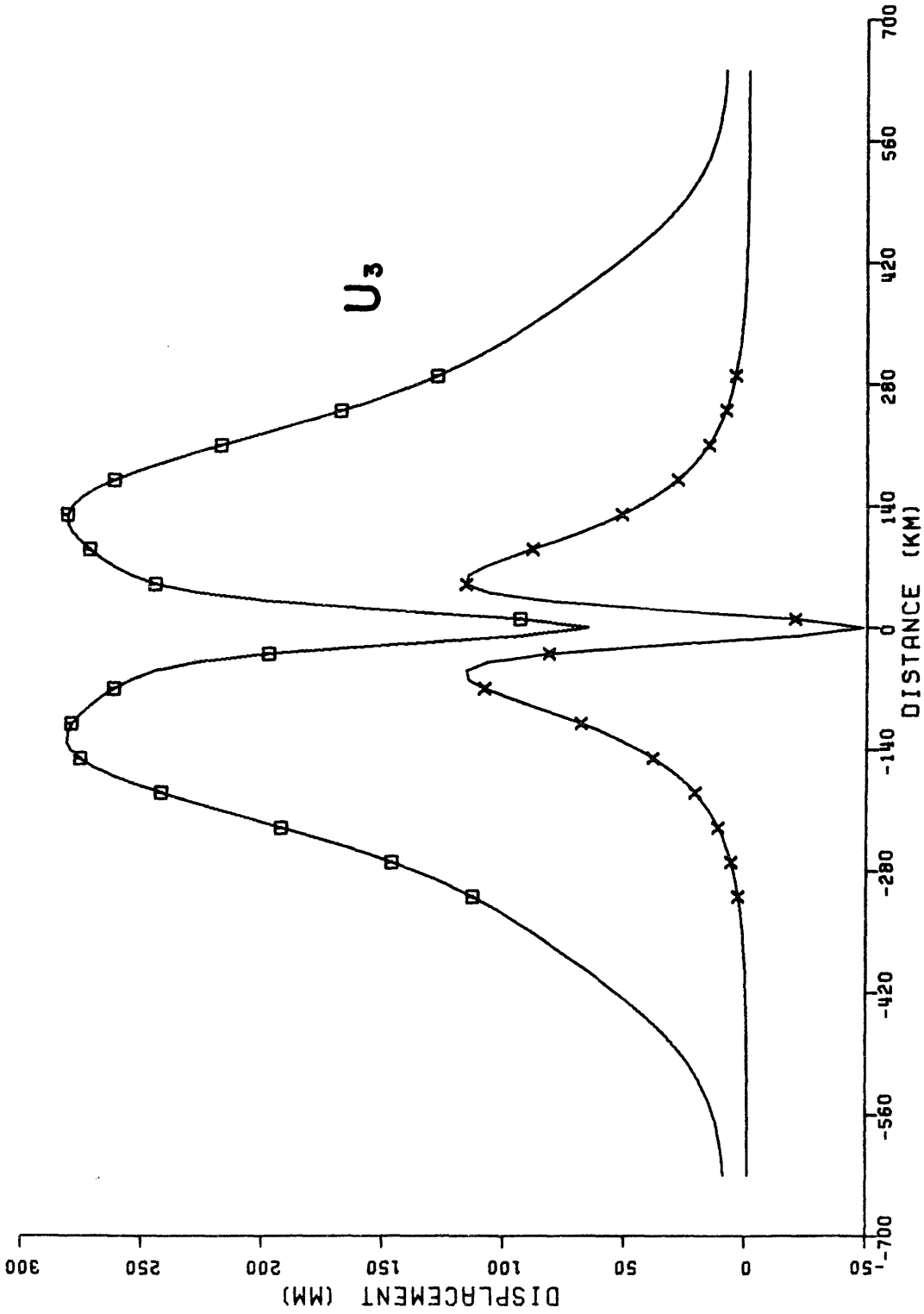
U_3
DISPLACEMENT (MM)
300
250
200
150
100
50
0
-50
DISTANCE (KM)
700
560
420
280
140
0
-140
-280
-420
-560
-700

Figure 3.47

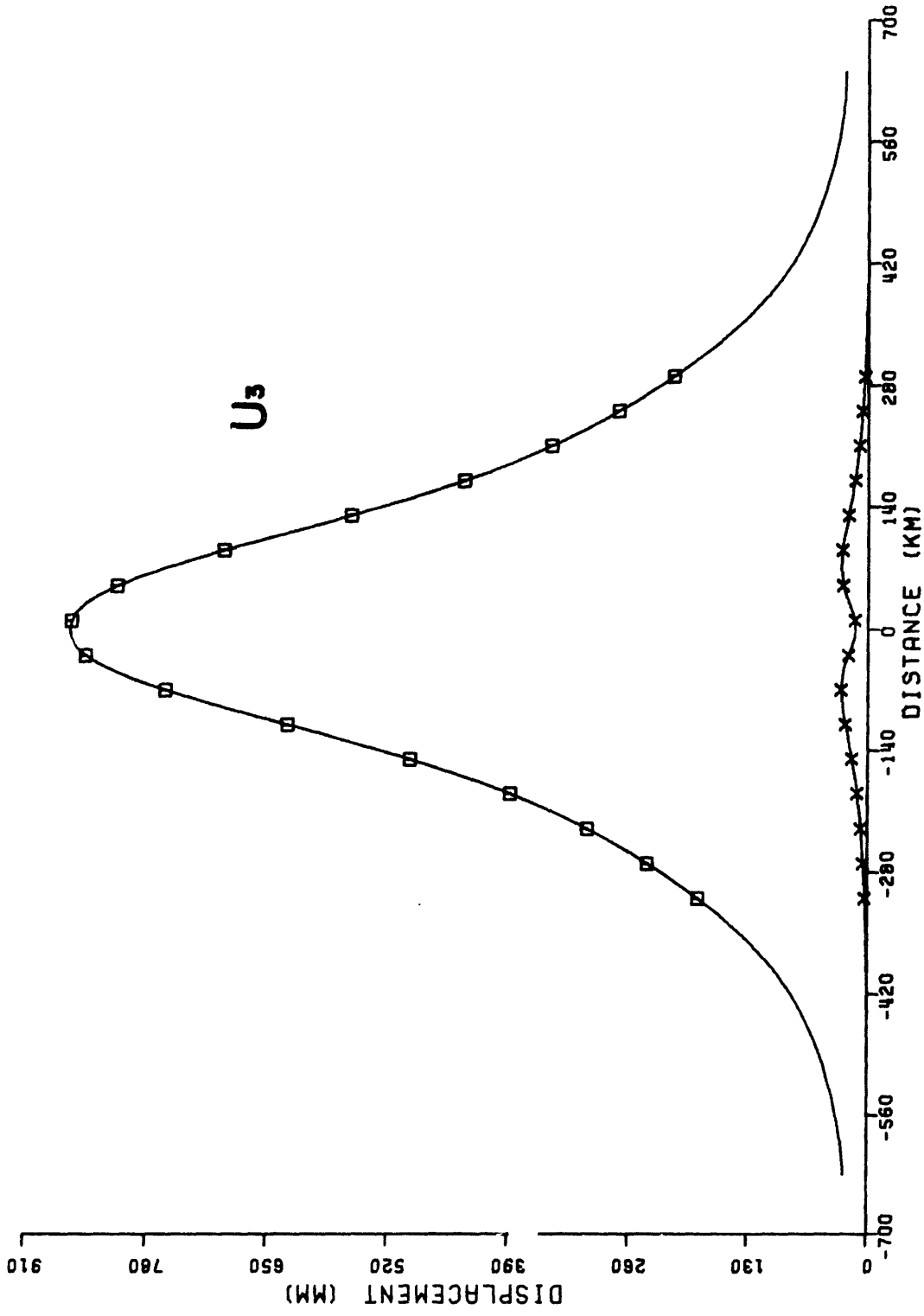
U3
DISPLACEMENT (MM)
0
130
260
390
520
650
780
910
DISTANCE (KM)
-700
-560
-420
-280
-140
0
140
280
420
560
700

Figure 3.43

Figure 3.49

Shallow fault model in a thick lithosphere (80 km). The fault is 5 km deep and 25 km wide. $\vec{B}$ = (0,1,0) and L = 56 km. Two cases are examined for this model. The first consists of a hard lithosphere ($\lambda = 8.05 \times 10^{11}$ dynes/cm^2, $\mu = 6.58 \times 10^{11}$ dynes/cm^2) overlying an extremely soft half-space ($\lambda = 1.12 \times 10^{11}$ dynes/cm^2, $\mu = .3 \times 10^{11}$ dynes/cm^2). The second case consists of the hard layer over a half-space with elastic parameters consistent with those of the low velocity zone in the Basins and Range province as determined by Herrin (1972). The half-space parameters in this case are $\lambda = 8.45 \times 10^{11}$ dynes/cm^2 and $\mu = 5.86 \times 10^{11}$ dynes/cm^2. Sample sizes are $\Delta X_1 = 2.5$ km, $\Delta X_2 = 5$ km.

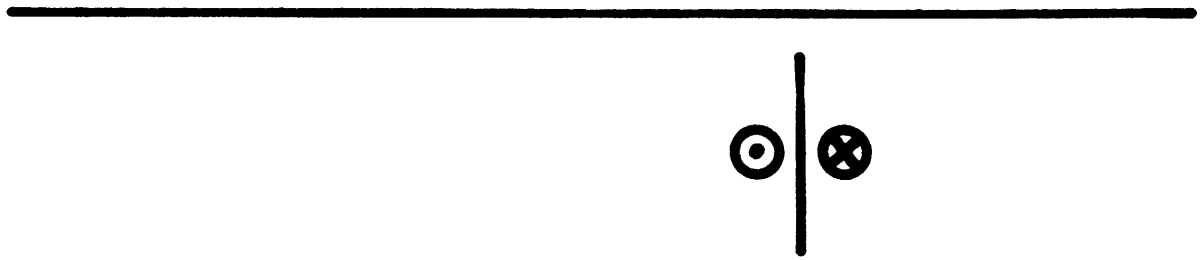

Figure 3.12

Figure 3.50 - 3.52

Comparison of displacements for the model shown in figure 3.49 (□) with those of a half-space (X). The elastic constants for the half-space are the same as those of the lithosphere. The asthenosphere is extremely soft in this model. The profiles are taken at x_2 = 5 km.

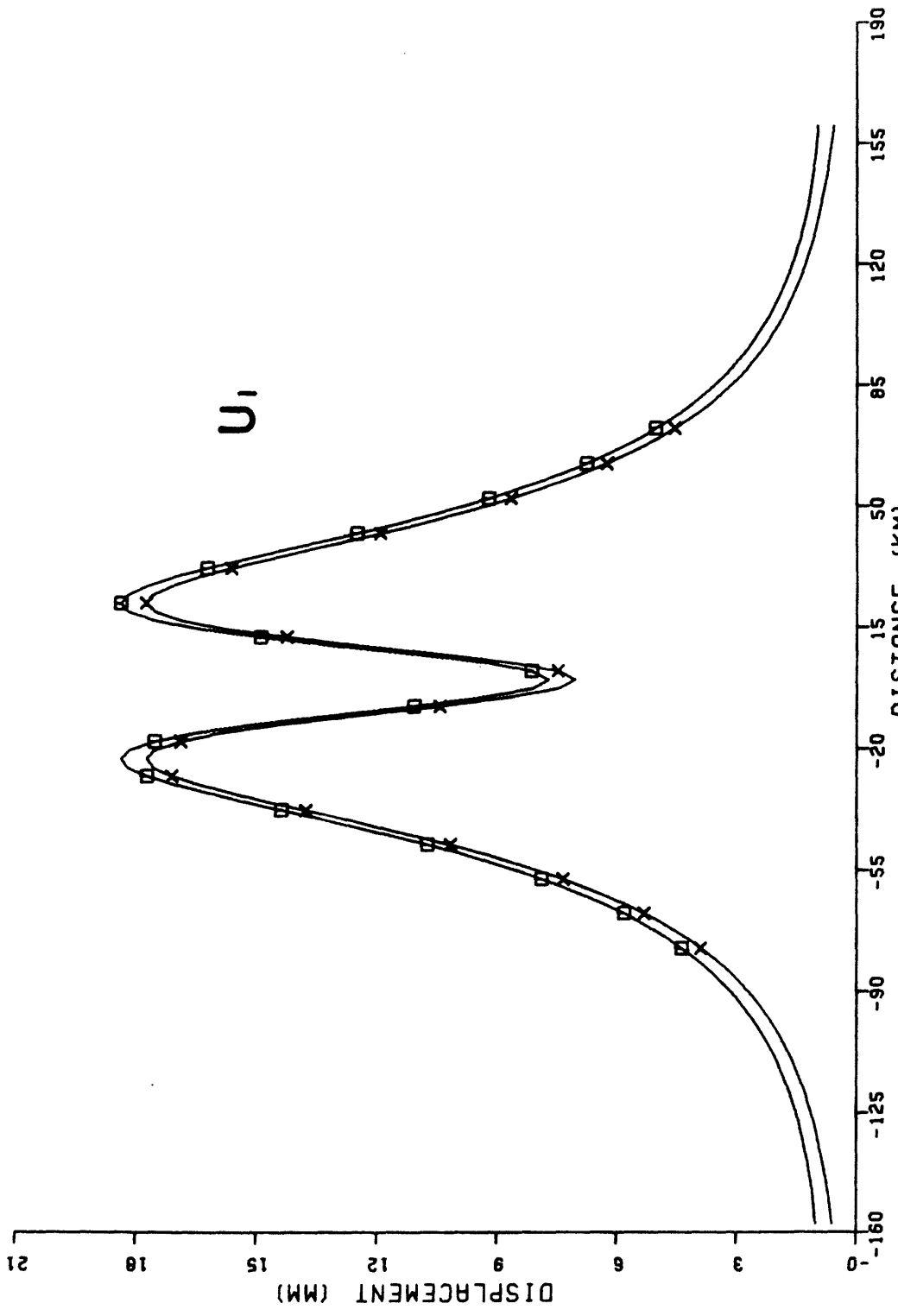
U1
DISPLACEMENT (MM)
0
3
6
9
12
15
18
21
DISTANCE (KM)
-160
-125
-90
-55
-20
15
50
85
120
155
190

Figure 3.50

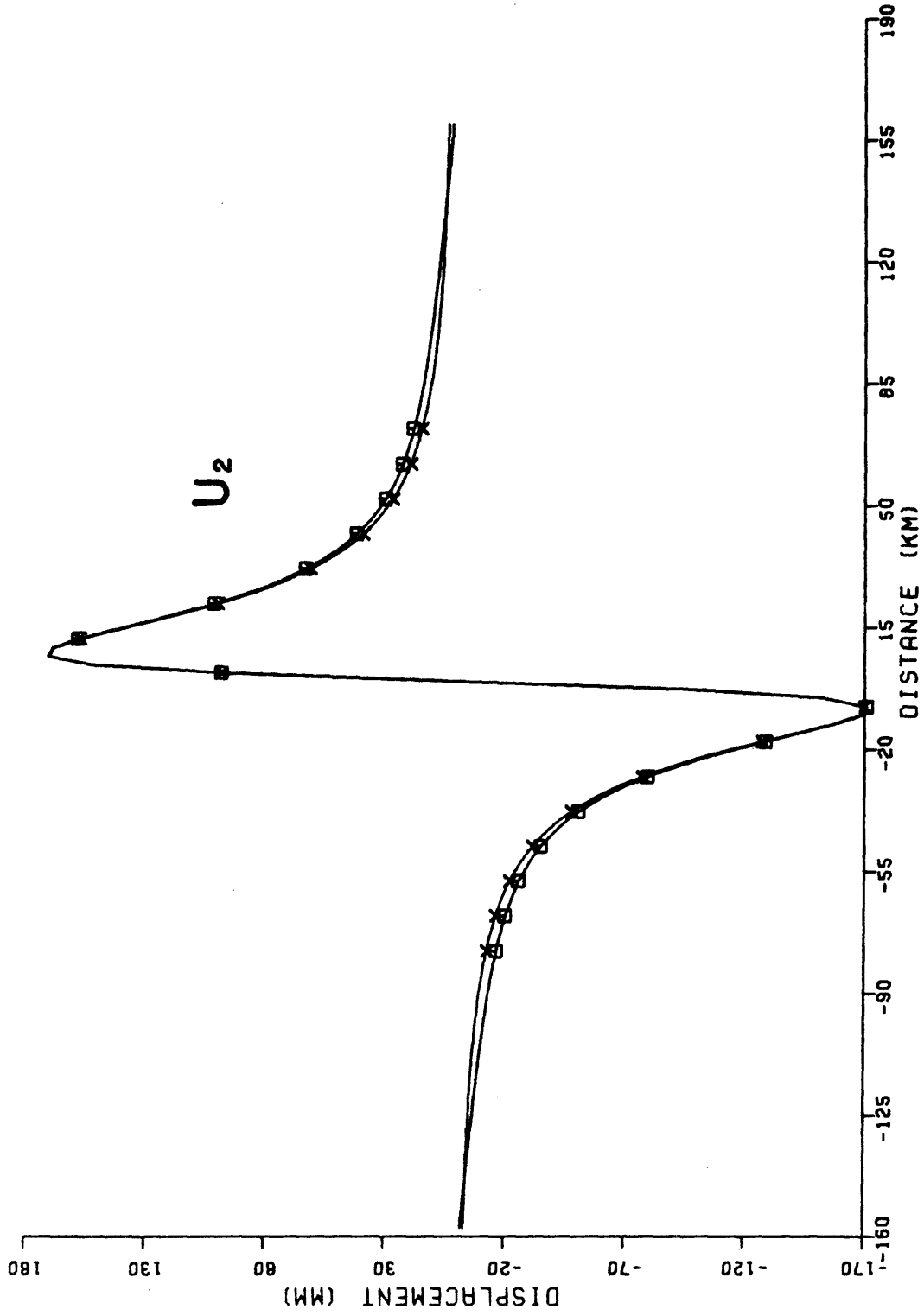
U_2
DISPLACEMENT (MM)
180
130
80
30
-20
-70
-120
-170
DISTANCE (KM)
190
155
120
85
50
15
-20
-55
-90
-125
-160

Figure 3.51

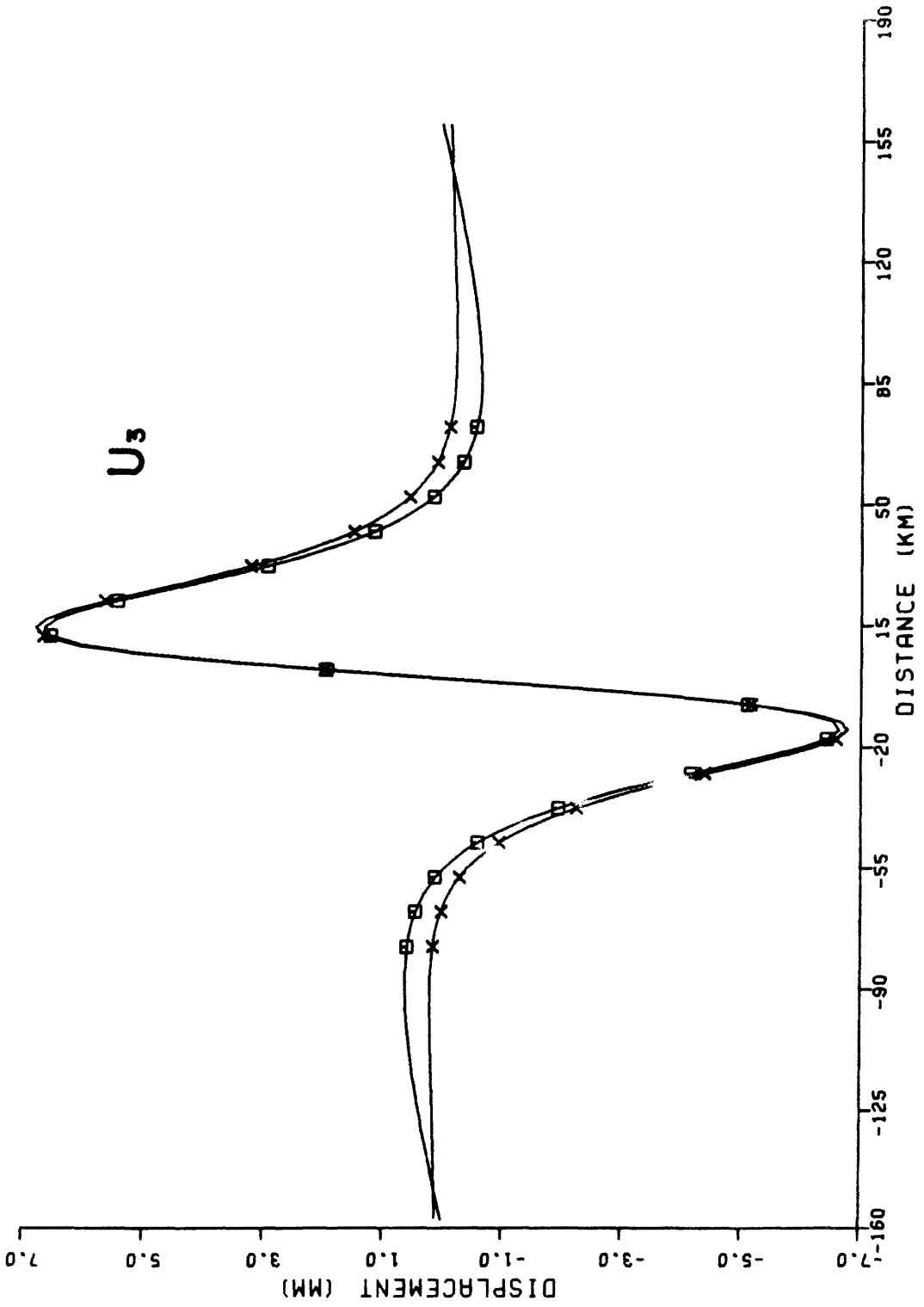
U3
DISPLACEMENT (MM)
7.0
5.0
3.0
1.0
-1.0
-3.0
-5.0
-7.0
DISTANCE (KM)
190
155
120
85
50
15
-20
-55
-90
-125
-160

Figure 3.52

Figures 3.53-3.55

Comparison of displacements for the lithosphere - asthenosphere model shown in figure 3.49 (□) with those of a homogeneous half-space with the same properties of the lithosphere (X). In this case the elastic properties of what we are calling the asthenosphere are consistent with seismic observations (λ = 8.45 x 10^{11} dynes/cm^2, μ = 5.86 x 10^{11} dynes/cm^2). Profiles are at x_2 = 5 km.

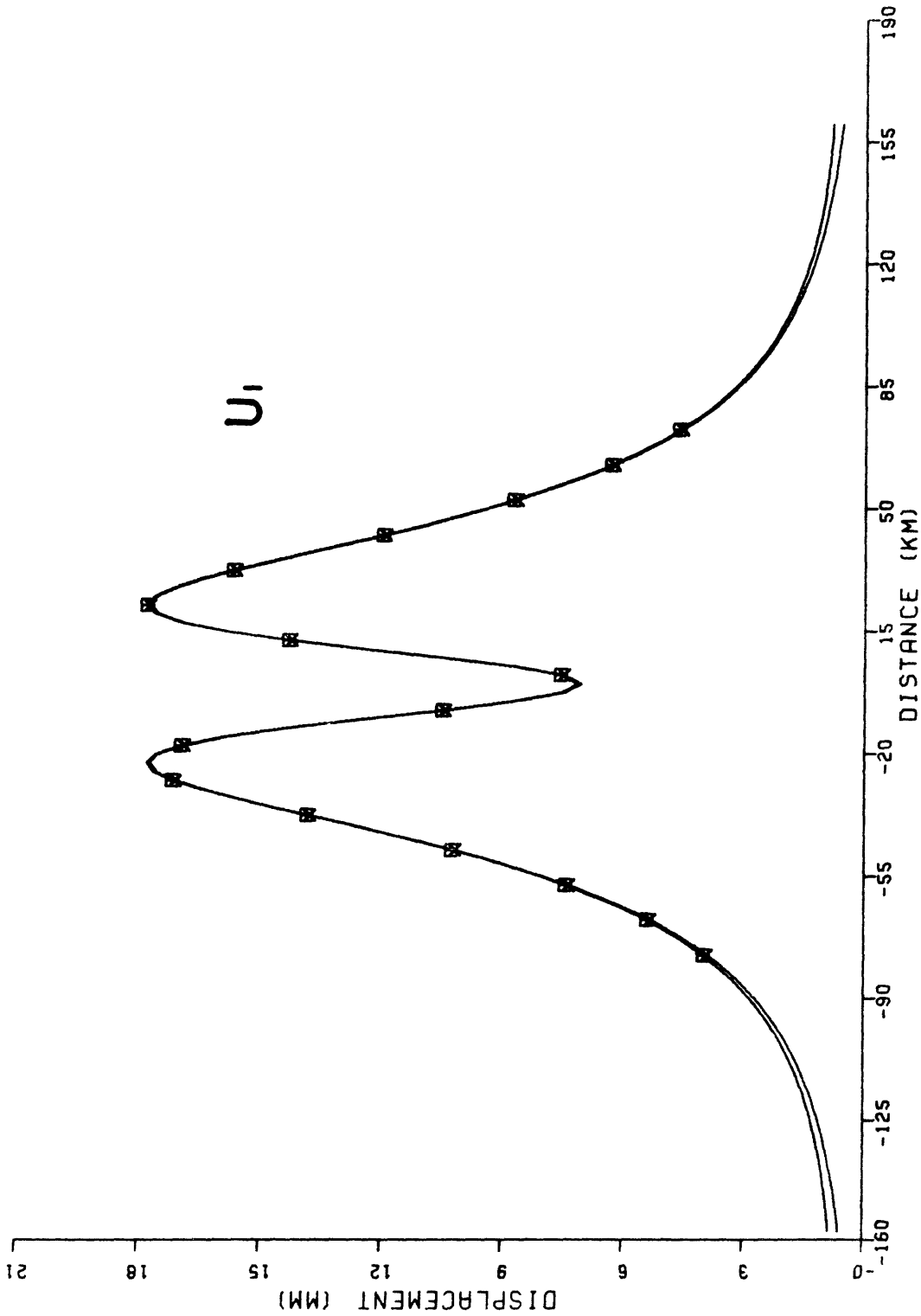
U1
DISPLACEMENT (MM)
0
3
6
9
12
15
18
21
-160
-125
-90
-55
-20
15
50
85
120
155
190
DISTANCE (KM)

Figure 3.53

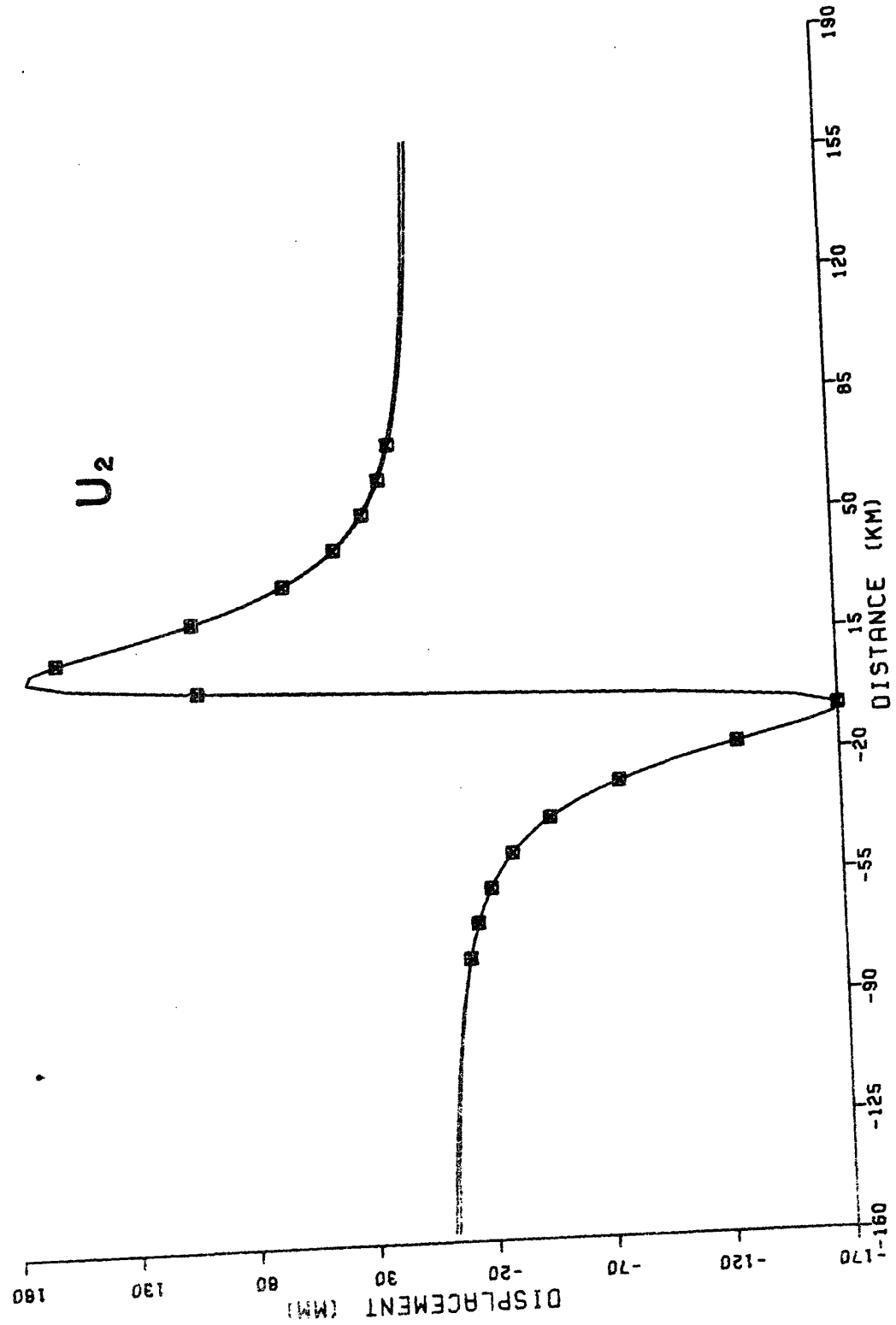
U2
DISTANCE (KM)
190
155
120
85
50
15
-20
-55
-90
-125
-160
DISPLACEMENT (MM)
180
130
80
30
-20
-70
-120
-170

Figure 3.54

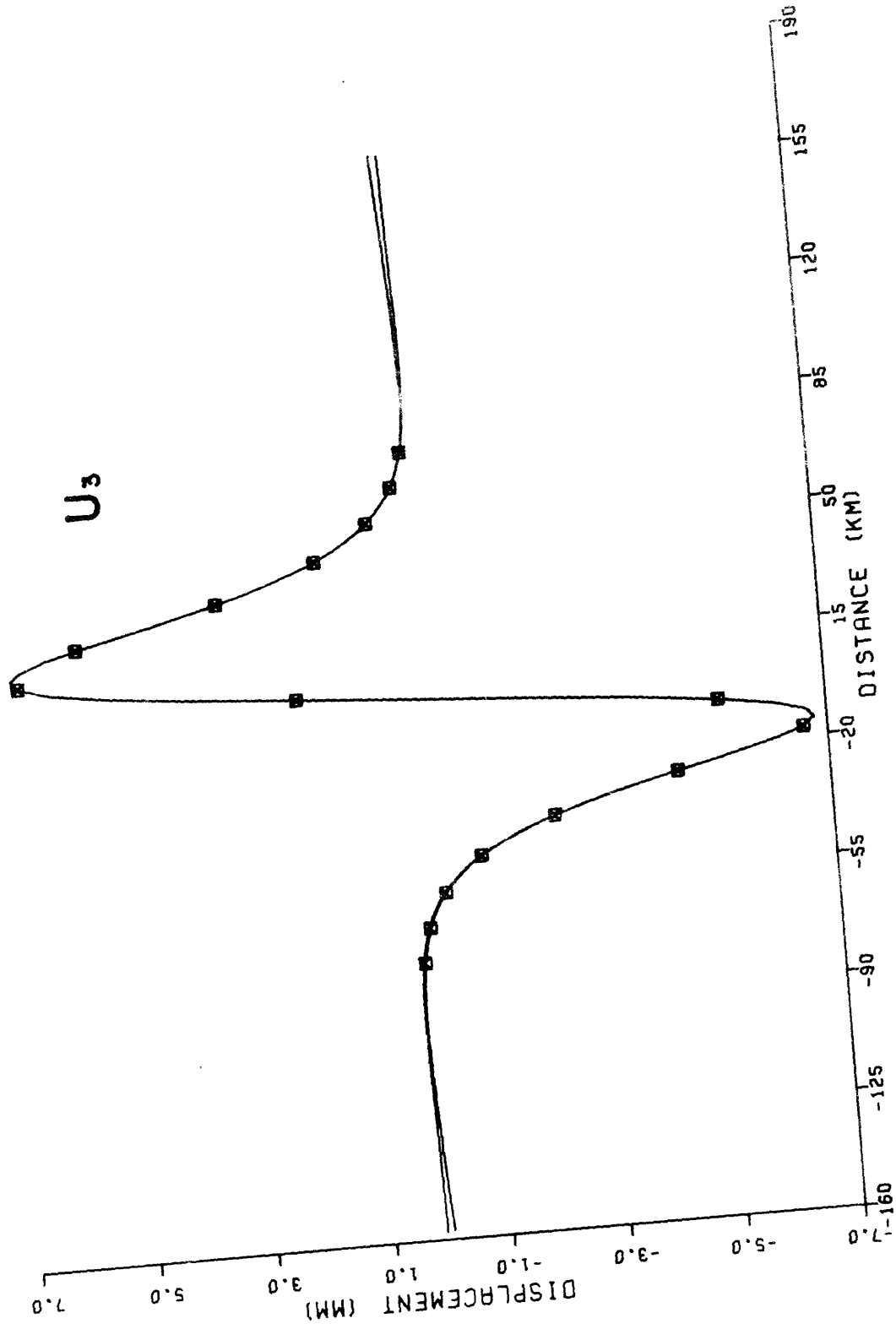
U3
DISPLACEMENT (MM)
7.0
5.0
3.0
1.0
-1.0
-3.0
-5.0
-7.0
DISTANCE (KM)
190
155
120
85
50
15
-20
-55
-90
-125
-160

Figure 3.55

CHAPTER IV

A Dislocation Approach to Plate Tectonics

4.1 Introduction

One of the primary goals of any program to predict earthquakes should be a study of the resultant strain accumulation due to the interaction of lithospheric plates. The U.S.G.S. is presently engaged in this problem from a standpoint of the analysis of geodetic data. Theoretically, however, little has been done because of the difficulty involved in posing the problem. We now present a method of modeling plate interaction in terms of dislocation theory and apply the method to two regions of the San Andreas fault system in California.

The development of the general modeling scheme for plate interaction is important because it will (1) allow us to gain a more detailed picture of the nature of the strain accumulation around a locked fault and (2) give us a means of quantitatively assessing the strain state of various segments of active fault zones. We shall first construct dislocation models of the section of the San Andreas fault in central California. This area is of interest because of its fault creep and because of a small bend in the fault just south of San Francisco. The second area of study will be the "big bend" in the San Andreas that occurs in southern California. The influence of this

bend upon the surrounding regions will be the major point of consideration.

In order to apply dislocation theory to the problem of plate interaction we will define a special class of dislocations called anti-dislocations (no relation to those used in the physics of solids). Once a plate problem has been posed in terms of anti-dislocations it can be converted to another form using what we shall call equivalent dislocations. We now wish to give a derivation of the above process and a discussion of the assumptions involved.

4.2 Anti-Dislocation Models of Plate Interaction

The development of plate tectonics has given geophysicists a fundamental understanding of earthquakes in terms of relative plate motions (Wilson, 1965; Isacks, Oliver, and Sykes, 1968; Brune, 1968; Wyss and Brune, 1968). A physical mechanism for these earthquakes is that of stick-slip proposed and studied in a series of papers by Brace and Byerlee (1966, 1968, 1970). Stick-slip offers a sound explanation for the shallow focii of earthquakes along a fault zone such as the San Andreas (Brace and Byerlee, 1970) in terms of the depth variation of the lock-release mechanism with pressure and temperature.

It is the success of stick-slip and the observation that most of the large earthquakes and relative movement in California occur on pre-established faults (Allen et al., 1965;

Tocher, 1958) that lead us to assume that the tectonic mechanism primarily responsible for large earthquakes along the San Andreas and similar fault zones is the locking interaction of plates in relative motion.

The earliest qualitative suggestion of the cause and nature of the strain accumulation around a locked fault was made by Reid (1910) in an analysis of the geodetic data collected before and after the 1906 California earthquake. The first quantitative description of the internal pre-stress associated with an earthquake was suggested by Whipple (1936). He derived the solution for a point strike-slip dislocation and suggested that the stress release of the dislocation model must be of the same form (only with opposite signs) as the pre-stress that exists before the earthquake.

In one of the earliest attempts to study the interaction of earthquake and tectonic fields Smith and Van de Lindt (1969) assummed a constant stress boundary condition at the edges of the plate. However, recent studies of the strain accumulation (via geodetic data) across the San Andreas fault have led to the use of the dislocation as a model for the internal strain accumulation due to strike-slip forms of plate interaction (Scholz and Fitch, 1969; Savage and Burford, 1970). The extension of dislocation theory to the problem of general forms of plate interaction was first made by this author at his general examination (M.I.T., 1972) and presented at the

spring AGU (Brown et al., 1972). We now wish to give a detailed derivation of the results of those talks. In particular, we shall examine the problem of plate interaction and show how to pose the problem in terms of dislocation theory.

Consider the two elastic plates, A and B, shown in figure 4.1(a) which together form one large plate. We shall assume here that the width and length of the combined plates are large enough to allow us to neglect the effects of the edges of the plate. This assumption is not a necessary one but it simplifies the following discussion. The term "plate" should be clarified as to its use in this chapter. The top surface of the plate is a free surface while the bottom surface is an interface between the plate and an elastic (or anelastic) half-space with the same or different elastic (or anelastic) constants. If the two plates shown in figure 4.1(a) move in opposite directions without friction along their interface we have relative rigid body motion. Since sliding never occurs in nature without friction, we made allowance for this fact by defining our zero strain state as that state that exists when the plates are in a condition of "stable sliding" (Brace and Byerlee, 1970). With this understanding, plates that are stably sliding past one another are in relative "rigid" body motion. "Rigid" will be defined throughout this chapter in terms of the zero strain state given above. Since stable

sliding varies according to rock type and temperature (Byerlee and Brace, 1968), the zero strain state, and therefore the reference state, should not be uniform over the length of the fault. In this thesis we neglect these predicted regional variations of the reference strain state.

The relative "rigid" body motion of A and B in figure 4.1(a) can be simply described by simply stating the displacements of A and B over a period of time. However, it will be to our advantage to describe this motion by means of dislocation theory. We shall begin by making a short review of dislocation theory.

Let us make an imaginary cut in an elastic solid, apply forces to distort the two sides of the cut, and require that the final configuration be in equilibrium. We define this to be a dislocation (Maruyama, 1964). In reality, it is nothing more than a boundary value problem with the displacements specified on the two surfaces of the cut. If we designate the surface along which the cut is made as Σ_A, the solution is (Maruyama, 1964)

$$4.1 \qquad U_m = \int_{\Sigma_A} \Delta u_R \, w^m_{kl} \, \nu_l \, d\Sigma$$

where U_m is the displacement in the m direction, ΔU_k is the displacement discontinuity (Burgers' vector) in the k-direction, ν_ℓ is the ℓ-component of the normal to the surface Σ_A and $W_{kl}^{\ m}$ is the Green's function for the problem.

We now proceed to formulate the problem of relative "rigid" body motion in terms of dislocation theory by merely letting ΔU represent the constant displacement discontinuity on the semi-infinite surface Σ_{AB} (figure 4.1(b). The solution for the plate A is

$$U_m = \int_{\Sigma_{AB}} \Delta u_k \, w_{kl}^{\ l} \, \nu_l \, d\Sigma + \int_{\Sigma_A} u_k^A \, w_{kl}^{\ m} \, \nu_l \, d\Sigma \qquad 4.2$$

where the $W_{kl}^{\ m}$ is the Green's function for a homogeneous half-space (or any other configuration of elastic or viscoelastic media). The first integral in equation 4.2 represents the contribution to the displacements from the interface. The second term represents the effects of the bottom of the plate. In essence we have also introduced a dislocation between plate A and the half-space below (with U_k^A as the displacement discontinuity). Implicit in equation 4.2 is the assumption that the final configuration be in equilibrium (no stress discontinuities allowed). A similar solution holds for plate B. We have thus described the relative "rigid" body motion by making a semi-infinite cut in our half-space (or in any other form of media) and specifying the relative motion of the two sides of the cut and the bottom of the plate.

Now consider the situation shown in figure 4.1(c) of two elastic plates, A and B, attempting relative "rigid' body motion

with a certain portion, Σ_c, of their interface, Σ_{AB}, locked. The dislocation solution to this problem (for plate A) is

$$4.3 \quad U_m = \int_{\Sigma_{AB}-\Sigma_C} \Delta u_k \, w^m_{kl} \, \nu_l \, d\Sigma + \int_{\Sigma_A} u_k \, w^m_{kl} \, \nu_l \, d\Sigma$$

where the first integral is over the unlocked portion of the interface. This particular kind of dislocation, i.e., one which would represent relative "rigid" body displacement were it not for a finite locked portion of the interface, is defined to be an anti-dislocation. Anti-dislocations are ideal for modeling the locking interactions of plates in relative motion.

We can avoid integrating over the surface $\Sigma_{AB}-\Sigma_c$ and the semi-infinite surface Σ_A (or Σ_B) by adding appropriate rigid body displacements to each plate. When we add these rigid body displacements, we must account for the addition by changing the specified displacements on the interface. We can therefore convert the anti-dislocation into an equivalent dislocation on the complimentary surface (the locked portion) with a displacement discontinuity in the opposite direction to that of the anti-dislocation (figure 4.1(d)). Thus, an equivalent solution to that given in equation 4.3 is

$$4.4 \quad U_m = - \int_{\Sigma_c} \Delta u_k \, w^m_{kl} \, \nu_l \, d\Sigma + u^A_m$$

where $-u_m$ is the added relative rigid body displacement. By taking the appropriate derivatives of equation 4.3 with respect to the observation point, we obtain for the strains due to the anti-dislocation

$$4.5 \qquad E_{mn} = \int_{\Sigma_{AB}-\Sigma_C} \Delta U_k \, T_{kl}^{mn} \, \nu_l \, d\Sigma + \int_{\Sigma_A} U_k \, T_{kl}^{mn} \, \nu_l \, d\Sigma$$

where the T_{kl}^{mn}'s are the derivatives of the W_{kl}^{m}'s (Maruyama, 1964). The strains obtained from equation 4.5 should be the same as those obtained by differentiating equation 4.4

$$4.6 \qquad E_{mn} = - \int_{\Sigma_C} \Delta U_k \, T_{kl}^{mn} \, \nu_l \, d\Sigma$$

The equivalence of equations 4.5 and 4.6 shows that if we wish to calculate the strain for an anti-dislocation, we need merely calculate the negative of the strain from a dislocation on the complimentary surface. A different approach to the above derivation may be found in Chapter II.

The equivalence between the two solutions may be thought of as the dislocation equivalent of Babinet's principle in optics for complimentary diffracting surfaces (Sommerfeld, 1964). In fact, we may state the above principle in the following form: the fields from an anti-dislocation and its equivalent dislocation add to give relative "rigid" body motion (zero strain with respect to our reference state).

4.3 Application to Plate Interaction

The above concepts may now be used to calculate the strain from the locking interaction of plates in relative motion. The simplest form of plate interaction is of the form shown in figure 4.1(c) where the plates slide past one another at depth but are locked near the surface. Figure 4.2 shows the resultant shear strain profile that would be observed across such a fault model on the surface. This simple model for strain accumulation has been used by Scholz and Fitch (1969) and Savage and Burford (1970) to study strain accumulation along the San Andreas.

We now extend these ideas to more complicated plate geometries. Consider figure 4.3(a) where plates A and B have the irregular interface shown. If the displacement of each of the plates is as shown by the solid arrows then the equivalent dislocation surface S will have the relative displacements shown by the dotted arrows. Thus the model of this form of plate interaction consists of an anti-plane dislocation on the surface S and simple shear dislocations on the other two surfaces of the form discussed in figure 4.1. As can be seen from the example in figure 4.3(a) the general problem of plate interaction can require the use of some rather complex dislocations.

It is useful at this point to consider some of the assumptions inherent in the model shown in figure 4.3(a). The jog in the interface between plates A and B may be similar to that of the San Andreas near the Tehachapi Mountains in

California. If plate B is the Pacific plate and plate A is the North American plate then the area around the bend is one of anelastic deformation and mountain building (in this case the Tehachapi Mountains). Figure 4.1(b) shows a side view of the proposed model. The displacements on the bottom of the plate are uniform if we are far away from the zone of convergence but gradually decrease to zero as we approach the anelastic zone. We associate with the anelastic zone two kinds of strains. The strains denoted e_{ij} are elastic strains and satisfy (along with the strains outside of the anelastic zone) the compatability conditions (Fung, 1965). The strains denoted e^T_{ij} are called transformation strains and represent the anelastic deformation (Eshelby, 1957). By the addition of relative rigid body displacements the problem in 4.3(b) may be converted to the one shown in figure 4.3(c). The problem as posed can be related to the problem of an elliptical inclusion as studied by Eshelby (1957). Thus, in figure 4.3(c) the anelastic zone corresponds to an inclusion which has undergone an anelastic expansion. The strain e^T_{ij} represents the transformation strain or the anelastic strain the inclusion would experience if it were not imbedded in the elastic medium (in this case plates A and B). The elastic strain e_{ij} is a result of the interaction of the inclusion with the elastic plates. If, for the moment, we make the assumption that the fall off of

displacements on the bottom of the plate takes place over a distance which is small in comparison to the other dimensions considered in the problem then we may neglect any integration over the bottom of the plate. If we also assume that the thickness of the anelastic zone (inclusion) is small in comparison with the other dimensions of the problem then the inclusion problem reduces to a dislocation (Eshelby, 1957) with the anti-plane displacements shown in figure 4.3(d). Figure 4.3(d) is a side view of the model shown in figure 4.3(a).

With the assumptions described above a simple model of a very general class of plate problems can be handled. The validity of the assumptions depends implicitly on the time scale of the problem. If we are considering the problem of plate interaction over a couple of hundred years then the thickness of the anelastic zone should be a few meters and the assumption of a thin anelastic zone is justified. Neglect of the effects on the bottom of the plate may not be justifiable for the same time periods. In this thesis we restrict ourselves to the simplest possible models and resort to the inclusion of the effects of the plate bottom only when the simpler models are found to be inadequate.

In order to compute the strains from the dislocation models described we shall use the method described in Chap. II which is based on the work of Comninou (1973). In particular, we use the angular dislocation shown in figure 4.4(a) to

construct π dislocations (figure 4.4(b)). The π dislocations are then used to construct general polygonal dislocations (e.g. figure 4.4(c)). We shall describe our models by giving the latitude, longitude, and depth of each corner of the dislocation in the sequence which will describe the sense of the dislocation as described in Chap. II (figure 4.4(d)). The Burgers' vector will be given in a cylindrical coordinate system referenced to a cartesian coordinate system with the positive y-axis pointing north, the positive x-axis pointing east, and the z-axis pointing up. The azimuthal angle B_ϕ, of the Burgers' vector is measured positive clockwise from North and the radial component, B_r, is the absolute value of the total horizontal Burgers' vector

$$B_r = (B_x^2 + B_y^2)^{1/2}$$

Two components of strains ($x10^{-7}$) from a model like the one shown in figure 4.4(d) are contoured in figures 4.5 and 4.6. The model parameters are given in table 4.1. Figure 4.5 shows the shear strain E_{12} in a coordinate system with the positive x_1 axis pointing N45°E and the positive x_2 axis pointing N45°W (negative shear strain corresponds to a right lateral shear on the San Andreas). Figure 4.6 shows the E_{22} strain in the same coordinate system. This simple model is not intended to be a model of the San Andreas but it will be

constructive at this point to point out the similarities and differences between the two.

The shear strain pattern (figure 4.5) is probably quite similar to that of the San Andreas. The E_{22} component of strain shows compression in the Tehachapi Mountain - Transverse Range region of California while the area towards the Basins and Range Province is put under a NW-SE extension. These features are in general agreement with the inferred tectonics of California (Savage and Burford, 1970, other refs.). However, a major difference occurs off the coast of Santa Barbara where compression occurs rather than extension as predicted from the model. This difference is important and will be discussed later in the chapter. We are now in a position to apply the concepts introduced in this section to the calculation of the internal strain generated by the locking interaction of plates in relative motion.

4.4 Hayward-Calaveras-San Andreas Fault Zone

4.4.1 Introduction

One of the primary goals of surface geodetic measurements in California is the detection of strain accumulation along the various portions of the San Andreas. However, the evaluation of geodetic measurements in regions exhibiting fault creep has not yielded a unique interpretation (Scholz and Fitch, 1969, 1970; Savage and Burford, 1970). One of the problems consists in making an accurate assessment of the role fault creep plays in releasing the strain that would be accumulating if the top 15 to 20 kilometers of the fault was completely locked. Toward a further understanding of this problem a fault model of the bend in the San Andreas, which occurs in the general vicinity of San Juan Bautista, California (hereafter referred to as the SJB bend), will be used to determine (a) to what exten the end contributes to the tectonics of the region a (b) how the strain accumulation observed by geodetic means is effected by near-surface fault creep. Of particular importance and relevance to question (b) is the question of whether or not strain can be accumulating for a major earthquake and still not be detected by geodetic measurements. This question will be studied by allowing the near-surface portions of the faults in the region to slip while the deeper portions are locked without slipping. The resultant strains are

easily calculated and added by the method described in Chapter II.

4.4.2 The SJB Bend

The particular area of interest to us in this section is shown in figure 4.7. The data for this figure was taken from a fault map of California compiled by Hill, et al. (1969). The major faults in this area are the San Andreas, the Calaveras, and the Hayward faults. Although most of the earthquakes and creep occur on these three faults there is some question as to the role of other faults in the area such as the Seal Cove-San Gregorio fault (Bolt et al., 1968) and the Sargent fault (Burford and Savage, 1972).

One of the most puzzling features in this region of California is the bend in the trace of the San Andreas south of San Francisco. The SJB bend has been described as a locking mechanism of the San Andreas fault in central California by Farrington and Myers (1973). Udias (1964) has suggested that the bend is responsible for the misalignment of the aftershocks of the 1963 Salinas-Watsonville earthquakes with the San Andreas. Bolt et al. (1968) have described the bifurcation of the San Andreas into the San Andreas and Calaveras as a possible cause of the earthquake clustering in this region. Burford and Savage (1972) have described the tectonics of this region in terms of a crustal wedge caught in between

the San Andreas and the Hayward-Calaveras fault zone. The feature we have described can be more clearly seen in figure 4.8. It is a 112 km long bend in the main trace of the San Andreas. The southern tip of the bend is 30 km southeast of Hollister (near Bear Valley) where the San Andreas changes from a strike of N40°W to N48°W. Near Black Mountain, which is approximately 105 km to the northwest, the fault bends eastward to N35°W. Farrington and Myers (1973) suggest that this westward shift (approximately 20 km) of the San Andreas is an area where the Pacific and North American plates impinge and do not slip freely by one another.

However, the surface trace of a fault may not be representative of the tectonics in a region (Richter, 1969; Richter and Nordquist, 1951). For example:(1) the seismic events at depth may not be directly reflected in the surface geology,(2) the seismic history of a region may not be long enough to adequately define the secular seismicity and its relation to the faults in the region,(3) earthquakes may not occur on pre-existing faults and,(4) from geologic evidence alone, it is difficult to define the degree of "activity" of a fault (Allen et al., 1965). In addition, there is the possibility that the fault trace is an older feature and is not representative of present day tectonics (McKenzie, 1969; Raleigh et al., 1970). In order to find

out:(1) if the bend is a deep seated feature and,(2) if the bend is responsible for the tectonics of central California, we now model the SJB bend using the dislocation modeling scheme presented in Chapter II.

To model the bend the dislocation line is made to follow the edge of that portion of the interface between the Pacific and North American plates which is assumed to be locked. Because the normal forces are going to be greater at the bend the locked area in this region is expected to extend to greater depths than in those areas where the relative motion is simple shear. It is customary to assume that since earthquakes do not occur below depths of 15 to 20 kilometers in this region that the fault does not lock below this depth. However, if the fault locks at approximately the same depth all along the San Andreas then we shall have a difficult task of explaining the variation of strain rates along the fault. For example two stations on opposite sides of the San Andreas in the area of the Carrizo plains show little (if any) relative motion (indicating a low strain rate) whereas just the opposite is true along a neighboring portion of fault between Parkfield and Cholame (Savage and Burford, 1970). If we restrict ourselves to the assumption of locking at a constant depth then we must explain the variation in strain rates along the San Andreas as a real

variation of the relative plate motions along the fault. This leads to a rather complicated, and perhaps unexplainable, model of the driving forces of the plates. On the other hand, if we allow the depth of locking to vary along the fault, then we may explain the variations of strain rates using the assumption of constant relative plate motion. To be more specific we assume that the San Andreas locks to a much greater depth in the Carrizo plains than does the San Jacinto in southern California.

Implicit in the assumption of variable depth of locking is the assertion that episodic aseismic slip occurs at depths below 20 kilometers. Scholz et al. (1972) have found in the laboratory that a condition of episodically stable sliding occurs between stick-slip and stable sliding. Thatcher (1975) has determined from the analysis of geodetic data that considerable aseismic slip occurred at depth after the 1906 San Francisco earthquake. When the proposed aseismic slip occurs at depth before an event it will load the near surface region: (1) accelerating the surface fault creep (Nason, 1973), (2) yielding precursory tilts and/or strains (e.g. Allen and Smith, 1966; Prescott and Savage, 1974; Mortensen and Johnston, 1974; Johnston and Stuart, 1974), and will have the effect of increasing the seismic activity in the region (Wesson and Ellsworth, 1973). Stuart and Johnston (1974) have determined that the moments for the precursory slips

before the earthquakes were approximately ten times the moments of the earthquakes.

In summary, we propose as a model to be tested for consistency a fault that is capable of locking to great depths (greater than 20 kilometers). In making the proposal we shall assume a modified version of the forms of slip as a function of depth on a fault that has been proposed by Scholz et al. (1969). In the near surface region (zone 1) the fault may slide by stick-slip or episodically stable sliding. The type of sliding will depend upon rock type and stress state (and perhaps loading rate). In zone 2 the sliding is predominantly stick-slip (earthquakes). Zone 3 represents the deviation from the zone of Scholz et al. (1969). We assume that it is a zone of episodically stable sliding. The deepest zone (zone 4) is of stable sliding. The depths and widths of these zones must certainly depend upon the time scales involved. For example over a period of several thousand years the whole fault interface could be viewed as a zone of stable sliding. For time periods on the order of 100 years or less we propose that all four zones exist. Thus along certain portions of the San Andreas zone 3 will be in a state of sliding while in other areas it will be locked. We shall thus use the depth of locking as a variable in our models. Earthquakes will then represent one of the later stages of

unlocking of a much larger region (Anderson and Perkins, 1974).

In figures 4.9, 4.10, and 4.11 the tensor strain contours are plotted for the SJB model given in table 4.2. The Pacific plate is assumed to have moved 5 meters N45°W with respect to the North American plate. The difference in shear strain between this model and a straight fault are insignificant (figure 4.9). The primary point to be noted is the apparent displacement of the maximum shear (in the coordinate system given) from the main trace of the San Andreas. This effect shows up in the data of Savage and Burford (1970) which will be discussed later. The important difference between a simple shear fault and the SJB bend model occurs in the e_{11} and e_{22} strains. (All strains are referred to a coordinate system in which positive x_1 points N45°E and positive x_2 points N45°W.) The e_{22} (figure 4.10) strains indicate a regional N45°W - S45°E extension. The extension is small and is not altered significantly by changing the direction of the relative motion between the plates. On the other hand the e_{11} strains are very sensitive to the direction of relative plate motion. Assuming that the Pacific plate moves N45°W with respect to the North American plate we see in figure 4.11 that the e_{11} strains are principally N45°E - S45°W extension with a slight compression in the vicinity of the San Andreas. If

the Pacific moves N30°W into North America then the e_{11} strains become compressive with the maximum compression occurring in the vicinity of the San Andreas. Thus, a primary test of which direction the Pacific is moving with respect to the North American plate is the principal stress (or strain) direction determined by the result (Fung, 1965)

$$\theta = \tan^{-1} \left[\frac{2E_{12}}{E_{11}-E_{22}}\right]$$

For most angles of relative motion (around N45°W) the E_{12} strains are large and negative while the E_{22} strains are small and positive. If the relative motion between the two plates is mostly shear then both E_{11} and E_{22} are small and the above equation yields a North-South principal axis of compression. If the Pacific moves N50°W with respect to North America then the E_{11} strains become larger and positive causing the principal axis of compression to rotate to a Northwest-Southeast position. If the Pacific moves into North America at an angle of N30°W then E_{11} becomes larger and negative rotating the principal axis of compression from a North-South position to a NE-SW position. A point to be discussed later is the fact that a thin fault (locked to a shallow depth) generates a very large negative strain. This makes the principal axis of

compression insensitive to the direction of plate motion. Thus the thicker the fault the greater the rotation of the principal axes of compression when the relative motion of the plates is rotated.

We now attempt to see if any general pattern of principal compression axes may be developed from earthquake focal plane solutions for the area. In figure 4.12 we have plotted the principal axes of compression as inferred by the author from the works of Bolt et al. (1968), Mayer-Rosa (1973), Ellsworth (1975), and Green et al. (1973). The numbered events correspond to those studied by Bolt et al. (1968). Event 1 is the 1966 Parkfield earthquake. Event 2 is approximately 25 kilometers from the main trace of the San Andreas. It is consistent with right lateral motion on a fault parallel to the San Andreas. Event 3 represents a cluster of events in Bear Valley. It is consistent with right lateral slip on the San Andreas. Events 4 and 5 occur in the SJB bend area. Both events depart from vertical planes and dip 65°-75° to the Northeast. Both are consistent with right lateral slip. The dip-slip component of number 4 could not be determined but number 5 showed a downward motion of the southwest block. Events 6 and 7 represent event clusters at the intersection of the Calaveras and Hayward faults. The pressure axes are consistent with slip on these faults. Event 8 deviates from the first seven

strike-slip events studied by Bolt et al. (1968). It is predominantly dip-slip and is consistent with reverse faulting. Event 9 is coincident with the San Gregorio fault (figure 4.7). It is consistent with predominantly right lateral strike-slip motion with some reverse component on a fault steeply dipping to the east. Although events 10 and 11 are approximately 3 kilometers apart, their fault plane solutions are significantly different. Event 10 may be associated with strike-slip motion on the Pilarcitos (figure 4.7) while event 11 is similar to event 8 which is consistent with a predominantly reverse dip-slip motion on a near vertical fault dipping to the northwest. The first motion data in the case of 8 and 11 do not allow us to firmly distinguish between the normal or reverse solutions. However, the reverse solutions yield pressure axes which are consistent with the other events in this region and these axes are plotted. This is in agreement with the solution chosen for event 11, the 1957 San Francisco earthquake, by Tocher (1959). Event 12 represents a cluster of events associated with the Hayward fault. The fault plane dips about 50° to the northeast but is predominantly strike-slip. Event 13 represents the main shock of the 1965 Antioch sequence and is very similar to event 12 but is consistent with faulting in a more northerly direction than the Hayward. Events 14 and 15 north of San Francisco Bay occur in the Northern Coastal Ranges away from the San

Andreas. Both are consistent with right lateral motion with some reverse component on faults dipping 70°-80° to the Northeast.

Events a, b, and c represent composite focal mechanisms presented by Mayer-Rosa (1973). Event b represents a cluster of events on the Silver Creek fault (figure 4.7) near the intersection of the Silver Creek with the Calaveras fault. The fault planes for this event are not aligned with the Silver Creek fault or the Calaveras fault. Events a and c represent composite focal mechanisms for segments for events on the Calaveras north and south respectively of the Silver Creek-Calaveras intersection. These events are consistent with right lateral motion on the Calaveras.

Events u and v represent a summary of the events in Bear Valley studied by Ellsworth (1975). The events summarized by u are coincident with the San Andreas and yield right lateral strike-slip. However, those events (v) that occur between the San Andreas and the Paicines-San Benito faults (not shown in figure 4.7) show a significant rotation of the pressure axes with respect to those that occur on the San Andreas. Ellsworth (1975) explains this in terms of the local coupling between two parallel dislocations, the San Andreas and the Paicines-San Benito faults.

Events r and s summarize two event clusters studied by Green et al. (1973) which have occurred in Monterey Bay.

The pressure axes for both of the events is N-S and these events represent right lateral strike-slip on a fault parallel to the San Andreas.

The general pattern of pressure axes seen in figure 4.12 is a rotation of the pressure axes from a predominantly north-south direction south of the SJB bend to a more northeastern-southwestern direction in the vicinity of San Francisco and perhaps a rotation back to a north-south direction north of San Francisco (event 15). In view of considerations put forward by McKenzie (1969) and Raleigh et al. (1970), it is difficult to argue that the pattern in figure 4.12 is representative of anything more than earthquakes on pre-established faults. To be more specific, they have shown that the true principal stress directions can vary by large angles from those estimated from fault plane solutions when the earthquake occurs on an established fault. If this is true then our earthquakes are insensitive to the direction of the pressure axes. However, events 2, 13, 14, 15, b, and v have no clear association with pre-established faulting in their areas. Further confirmation of this apparent trend comes from the geodetic data of Savage and Burford (1970, 1973). South of the SJB bend area the relative motion of geodetic stations is primarily compressive in a north-south sense and extensive in an east-west sense (consistent with right-lateral strain accumulation on the San Andreas).

however, in the vicinity of San Francisco Bay anomalous lines (1, 2, and 3 in figure 4.14) have been pointed out by Savage and Burford (1973) which are not consistent with accumulation of right lateral shear on a plane parallel to the San Andreas. Instead, lines 1 and 3 (see the lines in figure 4.14) show extension while line 2 shows compression in a more northwest direction. Thus the rotation of the pressure axes is consistent with the geodetic results (even though the first motion data must be contaminated by the pre-established faulting). However, the rotation may be exaggerated in the geodetic data by creep on the Hayward fault. In figure 4.13a we show the theoretical pressures axes for the SJB bend model given in table 4.2. However, the Pacific is assumed to move N25°W (B_ϕ = 155°) with respect to North America in order to rotate the pressure axes in the clockwise direction from north-south. A schematic of the model is shown in 4.13b. This model shows the apparent sensitivity of the direction of the pressure axes to the deeper section of locking on the SJB bend. However, this model does not significantly rotate the pressure axes in the vicinity of San Francisco Bay as is observed both in the fault plane solutions and the geodetic data. By allowing the northern section of the fault to lock to a greater depth (40 km) the amount of the rotation is increased in the Bay area and the agreement between this model and the data is as well as can be expected for such a simple model (Figure 4.14). The

depth of locking must begin to increase in the general area on the San Andreas north of Watsonville and reach a maximum depth under San Francisco. North of San Francisco Bay the data is scarce but the depth of locking must be shallow in the vicinity of Fort Ross (near Ross Mountain in figure 4.12) in order to explain the high strain rates (.55μ strain/year) reported by Meade (1971) (Savage and Burford, 1973). The depth of locking in this area is 9 km (Savage and Burford, 1973) assuming 3 cm/yr of relative motion between the plates or 15 km assuming 5 cm/yr. The north-south pressure axis of event 15 agrees with this general interpretation. Thus we conclude that the fault locks to shallow depths near Hollister and Ft. Ross but extends to depths of at least 40 km in the area of San Francisco. This result will be discussed further in the next section on fault creep.

4.4.3 Strain Release of Fault Creep

We now wish to consider the role of fault creep in central California and its effects upon the geodetic measurements. In particular we pose the question of how much of a fault can be locked and still be undetectable by geodetic measurements.

One of the earliest observations in California of fault slip without earthquakes was made at the Buena Vista thrust fault near Taft, California when Kock (1933) reported the bending of oil pipes. However, an active interest in the subject did not develop until fault slip was discovered at the Cienega Winery near Hollister, California (Steinbrugge and Zacher, 1960). The first instrumental recording of fault creep was made by Tocher (1960). The earliest report of fault creep on the Hayward fault was made by Bonilla (1966). A comprehensive review and compilation of the observations on fault creep in California may be found in the thesis by Nason (1971). For completeness we include here a presentation of the data for central California as presented by Nason (1971, 1973). In the discussion on the Hollister region the most recent measurements by Spieth et al. (1974) will be used.

The actively creeping faults are shown on the map in figure 4.15. The northernmost portion of the San Andreas

is locked from Pt. Arena to Watsonville with the possible exception of a small segment near Daly City. From Watsonville to San Juan Bautista the creep rate increases gradually from .3 cm/yr to .5 cm/yr. Just south of San Juan Bautista the creep rate shows a rapid increase from .5 cm/yr to 1.2 cm/yr. South of this rapid increase in creep rate the rate continues to gradually increase until it reaches a maximum (5 cm/yr?) approximately halfway between San Juan Bautista and Parkfield.

North of San Francisco Bay the path of the Hayward fault is unknown. It is thought to join the Rogers Creek-Healdsburg fault north of San Pablo Bay. From San Pablo to Fremont the Hayward is actively creeping. South of Fremont, however, the path of the Hayward is uncertain. It may join the Silver Creek fault southeast of San Jose.

The Calaveras fault is apparently locked from San Francisco Bay all the way to the vicinity of Anderson Resevoir. At Anderson Resevoir the creep rate is 1.2 cm/yr and increases southward until it reaches a point just north of Hollister. An interesting point that should be noted in this data is that the creep rate on the San Andreas picks up in the vicinity where the creep rate decreases on the Calaveras. This is indicative of a coupling between the two systems which will be explored later. South of Hollister, the path of the Calaveras becomes uncertain. It may become the Paicines fault (not shown in figure 4.7) which is 2 km

east of and parallel to the San Andreas.

We now present some simple models of fault creep in order to examine the effects of creep upon surface geodetic measurements.

In figure 4.16 we show the shear strain year profile expected across the middle of a 300 km long fault which is locked to a depth of 20 km. Slip is assumed to occur below 20 km at the rate of 5 cm/yr. Curve A represents the model with no fault creep. If we allow for 3 cm/yr of slip on the top 10 km of the fault the strain over the fault develops a trough which can even give the appearance of a strain accumulation in the opposite sense to that which is accumulating at depth on the locked section (curve b in figure 4.16).

To further investigate this effect we wish to present some simple two dimensional models of a locked fault with surface creep. The models will be constructed from screw dislocations. These simple models will allow us to clearly state the effects of fault creep in terms of analytic solutions.

The displacement for a screw dislocation in an infinite medium is (Weertman and Weertman, 1964).

$$4.7 \qquad W(x,y) = \frac{b}{2} \tan^{-1}\left(\frac{x}{y}\right)$$

where b is the burgers vector and the dislocation line is parallel to the z axis. If $\tan^{-1}$ is taken from $-\pi$ to π,

then the surface of discontinuity for this solution points along the negative y axis. If we allow the positive y axis to point down into the half-space, the half-space solution may be obtained by subtracting an image with a surface of discontinuity pointing in the same direction (figure 4.17a). This reduces the stresses on the free surface to zero and yields

$$4.8 \qquad W(x,y) = \frac{b}{2\pi}\left[\tan^{-1}\left(\frac{x}{y-d}\right) - \tan^{-1}\left(\frac{x}{y+d}\right)\right]$$

for the displacement and

$$4.9 \qquad E_{zx} = 1/2\ \frac{\partial w}{\partial x} = \frac{b}{4\pi}\left[\frac{y-d}{(y-d)^2 + x^2} - \frac{(y+d)}{(y+d)^2 + x^2}\right]$$

for the shear strain. The depth to the dislocation line is d. The result is a dislocation in a half-space on which slip occurs from the dislocation line to the surface.

Next we find the solution for a screw dislocation in which the surface of discontinuity (or slip) points down into the half-space away from the free surface (along positive y). For this problem we use the source term

$$4.10 \qquad W(x,y) = \frac{b}{2\pi}\tan^{-1}\left(\frac{x}{-y}\right)$$

with the surface of slip pointing down into the half-space.

The image which cancels the stresses (by addition) on the free surface is of the form given in 4.7 with the surface of slip pointing up. Thus the solutions for a dislocation in a half-space with the surface of slip pointing down into the half-space away from the free surface are

$$W = \frac{b}{2\pi} \left[\tan^{-1}\left(\frac{x}{d-y}\right) + \tan^{-1}\left(\frac{x}{y+d}\right)\right]$$

4.11

$$E_{zx} = \frac{b}{4\pi} \left[\frac{-(y-d)}{(y-d)^2 + x^2} + \frac{(y+d)}{(y+d)^2 + x^2}\right]$$

Adding the two solutions yields an ideal model for slip at depth, locking at an intermediate depth, and slip in the near-surface region (figure 4.17 c). Thus assuming b_1 cm/yr of creep down to a depth of d_1, locking below d_1 to a depth of d_2, and finally a slip of b_2 cm/yr below d_2 we may obtain the displacements anywhere in the halfspace by

$$W = \frac{b_1}{2\pi} \left[\tan^{-1}\left(\frac{x}{y-d_1}\right) - \tan^{-1}\left(\frac{x}{y+d_1}\right)\right]$$

4.12

$$+ \frac{b_2}{2\pi} \left[\tan^{-1}\left(\frac{x}{d_2-y}\right) + \tan^{-1}\left(\frac{x}{y+d_2}\right)\right]$$

and the strains by

$$E_{zx} = \frac{b_1}{4\pi}\left[\frac{y-d_1}{(y-d_1)^2 + x^2} - \frac{(y+d_1)}{(y+d_1)^2 + x^2}\right]$$

4.13

$$+ \frac{b_2}{4\pi}\left[\frac{-(y-d_2)}{(y-d_2)^2 + x^2} + \frac{(y+d_2)}{(y+d_2)^2 + x^2}\right]$$

Now, defining the parameters

$$Z = x/d_3$$

$$\varepsilon = b_1/b_2$$

and

$$\gamma = d_1/d_2$$

we may write equation 4.13 in the form

4.14 $$\frac{E_{zx}}{E_o} = \left[\frac{1}{1+z^2}\right] - \frac{\varepsilon}{\gamma}\left[\frac{1}{1+(z/\gamma)^2}\right]$$

where z is the distance away from the fault in terms of the depth to the bottom portion of the locked zone, ε is the ratio of fault creep to the relative plate motion, and γ is the measure of the percentage of the fault which is creeping. E_o is determined by

4.15 $$E_o = \frac{b_2}{2\pi d_2}$$

and represents the strain that would be observed directly over the fault if the fault were locked to a depth d_2. This simple expression shows the foundation of the assumptions described in the first section: faster strain rates are observed over shallow faults. E_{zx} represents the actual strain.

In figure 4.18 we have plotted the ratio of the two strains as a function of $z = x/d_2$ for various values of the parameters ε and γ. Curve A represents the ratio of strain for a completely locked fault (i.e. down to a depth d_2). Curve E on the other hand shows the case of 80% of the total fault (d_2) creeping at a rate of 90% of the relative plate motion at depth. The dashed line at $E_{xy}/e_o = .2$ represents the maximum value of the best fitting strain that occurs in the vicinity of the San Andreas north of Hollister as presented by Savage and Burford (1970). The value was obtained by taking their engineering strain over 32 years for the Hollister arc, converting it to tensor strain, dividing by 32 years to convert it to a yearly strain, and finally dividing this number by an estimated e_o that would be measured if no fault creep occurred. The value of .55μ strain/year obtained by Meade (1971)

near Ft. Ross should yield a good estimate of the strain rate at Hollister without creep. The highest dashed line at e_{zx}/e_o approximately equal to .4 was obtained in the same manner from the error bar of the data point used for the lower dashed line. It represents an estimate of the maximum strain allowable within the noise of the data.

The simplest model allowed by the data is relative rigid body motion (Savage and Burford, 1970). However, the data also allows as much as 70% of the fault to be locked as can be seen in figure 4.18. The possible contamination of this estimate by creep on the Calaveras could raise the estimate to 80%.

In figures 4.19 and 4.20 we have plotted the strain components

$$\gamma_1 = E_{ee} - E_{nn}$$

and

$$\gamma_2 = E_{ne} + E_{en}$$

of the geodetic data across the Hollister arc (Savage and Burford, 1970). The subscripts n and e refer to north and east respectively and are used to describe the sense of the engineering strain components (twice the tensor strain)

E_{ee}, E_{nn}, E_{ne} and E_{en}.

In order to match the observations with a theoretical model it is necessary to decide upon the relative plate motion between the Pacific plate and the North American plate. Unfortunately there is no general agreement on the rate of motion. Both the geologic (Dickinson et al., 1972) and the geodetic data (Savage and Burford, 1973) yield estimates of approximately 5 cm/yr for central California. In the Gulf of California the relative motion between the two plates has been determined to be 6 cm/yr (Larson et al., 1968) while Minster et al. (1974) have determined a gross relative motion between the Pacific and North America to be cm/yr. It is important to point out that each of the above measurements is associated with a different time scale. However,

because of the local nature of both the geologic and geodetic measurements, they may only represent a portion of the total plate motion. For example geologic determinations are often restricted to a single fault while there is evidence that several distinct blocks have moved northwest with respect to the North American plate (Clark, 1930). Thus, relative motion between the Salinian block and the Pacific could possibly account for the difference (Page, [illegible] are [illegible] by [illegible]

can be made. For measurements across a completely locked fault to represent 90% of the relative motion the stations on each side of the fault must be at least 6.3 D away from the fault where D is the depth of locking (Savage and Burford, 1973). In the area of Hollister, however, it has been suggested that the strain is negligible (Savage and Burford, 1970) and that most of the relative motion ($\sim$3 cm/yr) between stations in this area can be accounted for by fault creep.

C.A. Whitten in a personal communication to Bolt et al. (1968) determined that Farallon Light House has moved at the rate of 46 mm/yr with respect to Mt. Diablo, Sonoma Mountain, and Ross Mountain (see figure 4.12). The direction of the motion would have the Pacific moving N14°W with respect to North America. Savage and Burford (1973) suggest that Whitten's estimate may be biased by the proximity of Ft. Ross to the 1906 earthquake. Thus the assumption of fixed distance between Ft. Ross, Sonoma Mountain, and Mt. Diablo may not be valid. Savage and Burford (1973) have determined that Farallon L.H. moves 21$\pm$12 mm/year with respect to Sonoma Mountain (assuming right lateral motion and a fixed azimuth between Sonoma Mountain and Mt. Diablo).

If the results of the previous section hold then the measurement by Savage and Burford (1973) could represent only a fraction of the total motion between the plates.

using the results of Savage and Burford (1973) and assuming that the fault locks to 40 kilometers in the area between Mt. Diablo, Sonoma Mountain, and Farallon I.H. (figure 4.12) then equation 4.12 may be used (assuming no creep i.e. $b_1 = 0$) to obtain the total motion across the fault (b_2). With Sonoma Mountain at 32 kilometers and Farallon I.H. at 37 kilometers from the fault, equation 4.12 yields a total motion between the Pacific and North American plates of 4.6 cm/year. This value is in excellent agreement with the 5 cm/year determined by Minster et al. (1974). We shall therefore use 5 cm/year as the relative plate velocity between the Pacific and North American plates for the rest of our models.

Curve A in figures 4.19 and 4.20 represents the theoretical strain accumulation due to a completely locked bend model (table 4.3 or figure 4.14 b with $B_\phi = 155°$). Theoretical curves are calculated using the models described in table 4.3. Profiles of γ_1 and γ_2 were taken between point A (Latitude = 36.59, Longitude = 121.86) and point B (Latitude = 36.93, Longitude = 121.24). The direction (N55°W) and location of the profiles were made to conform as nearly as possible to the Hollister arc (Savage and Burford, 1970). The San Andreas was located on this profile and all distances were plotted as distances from the San Andreas so that the theoretical values would easily [illegible] the [illegible]

4.20 represents the inclusion of creep (see table 4.3) on the top 6 km at the rate of 2 cm/year (Spieth et al., 1974). The general feature of the maximum γ_1 (figure 4.19) being displaced from the trace of the fault cannot be explained by a straight vertical fault model but is consistent with the SJB bend model. The displaced maximum could also be explained by a fault dipping to the southwest. However, Healy et al. (1972) have shown that the San Andreas fault in this area dips to the northeast (87°). Their results are in excellent agreement with the slight dip to the northeast for the source mechanisms determined by Bolt et al. (1968). Further confirmation of a slight dip to the northeast has come from a three dimensional crustal inversion of this area. Aki (Keiiti Aki, personal communication, 1975) has determined a slight dip to the northeast of the crustal structure across the San Andreas. We feel, therefore, that a dipping fault to the southwest cannot be used to explain the displaced maximum.

The match between the best fitting data of Savage and Burford (1970) and the theoretical model of the SJB bend with creep (curve B) is indicative of a locked fault at depth ($\sim$20 km) with only a fraction ($\sim$6 km) of the near surface region creeping (at 2 cm/year). This conclusion is based on the assumption that the Calaveras is creeping at 20 mm/year (Spieth et al., 1974).

The γ_1 component shown in figure 4.20 is extremely erratic and no simple model could match this data. Fault creep on the San Andreas raises the value of γ_2 in the vicinity of the San Andreas. The addition of fault creep on the Calaveras is not required for the description of the γ_1 component (shear on the fault). This requires that either the creep on the Calaveras be very shallow (~1 km or less) in order to avoid creating negative troughs in the γ_1 component of the strain or very deep (~20 km or greater) so that the reduction of γ_1 from creep on the Calaveras is minimized. These conclusions are based on models including the Calaveras. Since creep on a fault raises γ_2 in the vicinity of a fault the data is suggestive of fault creep on the Calaveras (and perhaps the Sargent and Vergeles faults). We shall restrict ourselves at this point to the simplest of models and only note that the trend of the models is similar to that of the data for the γ_2 component. γ_2 becomes significantly negative away from the fault in both directions (N45°E - S45°W compression or N45°W - S45°E extension) but becomes small in the vicinity of the San Andreas.

The decision on whether the Calaveras extends to great depths (~20 km) or very shallow depths (~1 km) could be made if we knew the nature of the mechanism driving creep on the fault zone. If the mechanism is active only near the same

nature as the one driving creep on the San Andreas), then (1) the creep rates on the Calaveras should be independent of creep rate on the San Andreas and (2) the depth of the slipping on the Calaveras should be of the same order of magnitude ($\sim$5 km) as the slipping surface on the San Andreas. The second requirement is rather weak, but the γ_1 data presented earlier is not consistent with creep at intermediate depths (2-15 km). The first requirement is the strongest and can be tested in the region from Bear Valley to Anderson Resevoir. A passive mechanism (in particular coupling between the San Andreas and the secondary faults) requires

(1) slip on a deep surface ($\sim$20 kilometers) so that the secondary faults can be coupled to the primary fault (the San Andreas) and (2) that slip on the Calaveras be related to slip on the San Andreas. If coupling is the driving mechanism of creep on the Calaveras the following process is imagined to occur: the primary fault locks to some depth ($\sim$20 km) and remains locked while below that depth the plates continue to slide loading the locked fault and the surrounding volume until the shear stress reaches the frictional stress on pre-established faults in the area. From this point in time until the locked region slips the plate motion at depth on the primary fault drives the motion on the secondary fault.

The rate of creep on the secondary fault due to coupling should be a function of the applied stress, the frictional stress on the secondary fault, and the area of the secondary fault. In figure 4.21 we have drawn a schematic of the coupling between the San Andreas (SA) and the Calaveras faults. The stress which is applied to the Calaveras is a function of d_1,d_2, the rate of motion below d_2 (plate motion) and the rate of motion above d_1 (creep). To pose this problem mathematically we could use dislocations to model the applied stress due to slip above and below the locked portion of the San Andreas. However, to solve for the motion on the Calaveras (and/or Hayward) we would have to solve a three dimensional crack (since the distance between the two faults is not constant) with a variable stress drop. This problem is beyond the scope of the thesis. We can, however, point to certain features in the creep data which are indicative of the coupling process described.

In figure 4.22 we have plotted the observed fault creep for various faults on the ordinate axis. On the abscissa the fault separation distance (ΔX in figure 4.21) is plotted. This distance represents the distance between the observation of creep on the two faults. In the case of fault creep on the San Andreas we have plotted it as a function distance from the Calaveras fault. The creep rates for all [illegible] faults in figure 4.22 are plotted as a function

of distance from the San Andreas. The primary feature to be noted in this plot is the transferral of creep to the Calaveras as creep on the San Andreas drops off. This is exactly the behavior expected for the coupling model described above. The effect is due (at least in the model) to the increased area of locking which effectively extends the region of influence of the loading fault (the San Andreas in this case). Further to the north the fault separation between the Hayward and the San Andreas is about 32 km while for the Concord fault the separation distance is 52 km. The only fault being loaded by a creeping section of the San Andreas is the Calaveras. The apparent fall off of creep on the Calaveras and subsequent pick-up of creep on the Hayward and Concord faults can be interpreted as being a result of the deeper locking under San Francisco which was discussed in the previous section. Unfortunately, this interpretation for the creep distribution is not a unique one. It is, however, based on a simple hypothesis which is consistent with other data for this area.

4.4.4 Discussion

In summary we have applied some simple models to find out a great deal about the tectonics of central California. The models are based on the assumption that faults are capable of locking to great depths. It was found that

locking at depth has the ability to rotate the pressure axes (clockwise from north if the plates are impinging on one another). The model predicts that the pressure axes will rotate back to a north-south direction when the locked section becomes thin (a possible means of predicting earthquakes).

The consistency of the SJB bend model with the earthquake and geodetic data implies that the observed trace of the San Andreas is a deep-seated feature and is possibly responsible for a number of special features such as (1) the transferral of seismicity from the San Andreas to the Hayward and Calaveras faults (Bolt et al., 1968) (2) the transferral of fault creep to the Hayward and Calaveras faults (Nason, 1971) (3) Extensional faulting north of Hollister (Rogers, 1967) and (4) folding and uplift near San Juan Bautista (Nason 1971). In order to make the SJB bend consistent with the data it was necessary to give the Pacific a collisional component of motion with respect to North America. This seems reasonable in view of the thrust component of many of the events in the region (events 8, 11, 13, and 14). An important part of the SJB bend model is locking at shallow depths (~20 km) near Hollister and locking to considerable depths (~40 km) near San Francisco. The greater depth of locking near San Francisco is indicated in (1) the concentration

of the pressure axes from a north-south position to a northeast-southwest direction and (2) the wider zone of fault creep near San Francisco (if coupling is assumed to drive the creep on the Calaveras), and (3) the geodetic data.

Finally, it was found that fault creep is an effective means of hiding strain accumulation on a locked fault at depth. This is especially true when the assumption of homogeneous strain is made (Savage and Burford, 1973). We find as little as 30% of the top 20 km of the San Andreas could be slipping and still be consistent with the geodetic data (Savage and Burford, 1970). Thus we suggest that this area is one of rapid strain accumulation on a narrow strand of fault. We are unable to predict how this strain will be released. If the creep on the San Andreas is not effectively reducing the strain at depth it might be thought that creep on the Calaveras is releasing the strain. Using equation 4.13 evaluated at the center of the locked fault with an extra term to include creep on a nearby fault (see figure 4.21) we find that the strain rate is reduced by only 10-20% in the area near Hollister where the maximum coupling occurs. Thus it appears that fault creep in central California could have a negligible effect upon the accumulation of strain on the San Andreas.

TABLE 4.1

DISLOCATION PARAMETERS FOR SHARP BEND

Corne	Latitude	Longitude	Depth (km)
1	39.00	123.7	0
2	34.89	119.3	0
3	35.44	118.5	0
4	32.25	115.0	0
5	32.25	115.0	20
6	35.44	118.5	20
7	35.44	118.5	60
8	34.89	119.3	60
9	34.89	119.3	20
10	39.00	123.7	20

Burgers' vector

$B_\perp$ = . meters $B_\phi = 140^\circ$ $B_z = 0$

TABLE 4.2

PARAMETERS FOR SJB BEND MODEL

Corner	Latitude	Longitude	Depth
1	39.00	123.70	0
2	37.25	122.08	0
3	36.50	121.25	0
4	34.90	119.27	0
5	34.90	119.27	15
6	36.50	121.25	15
7	36.50	121.25	20
8	37.25	122.08	20
9	37.25	122.08	15
10	39.00	123.70	15

Burgers' vector

B_r = 2.5 meters $B_\phi = 135^\circ$ $B_z = 0$

TABLE 4.3

Parameters for SJB bend with deep locking under San Francisco

Corner Number	Latitude	Longitude	Depth(km)
1	39.00	123.70	0.
2	37.25	122.08	0.
3	36.50	121.25	0.
4	34.90	119.27	0.
5	34.90	119.27	10.
6	36.50	121.25	10.
7	36.50	121.25	20.
8	37.25	122.08	20.
9	37.25	122.08	40.
10	39.00	123.70	40.

B_r 1.6 meters B_φ = 155° B_z = 0

(Assuming cm/yr for 22 years.)

Fault creep on the bend

1	37.25	122.08	0.
2	36.50	121.25	0.
3	36.50	121.25	6.0
4	37.25	122.08	6.0

B_r = .64 meters B_ϕ = -48° B_z = 0

(Assuming 2 cm/yr of creep for 32 years.)

Fault creep south of bend

1	36.50	121.25	0.
2	34.90	119.27	0.
3	34.90	119.27	4.
4	36.50	121.25	4.

B_r = .64 meters B_ϕ = -41° B_z = 0

Figure 4.1

(a) Relative "rigid" body motion between plates A and B. Stable sliding is assumed to occur on the interface E_{AB}.

(b) Relative "rigid" body motion posed in terms of dislocation theory. The boundary conditions consist of displacements (shown by arrows) on the bottom of the plates and the interface between the two plates.

(c) Anti-Dislocation. When the dislocation problem is posed so that all but a finite portion of the interface is displaced, we define this to be an anti-dislocation. The anti-dislocation will be used as the model for the internal stress accumulation which causes earthquakes.

(d) An equivalent dislocation to the anti-dislocation shown in (c). The displacements differ by rigid body terms and the strains are identical.

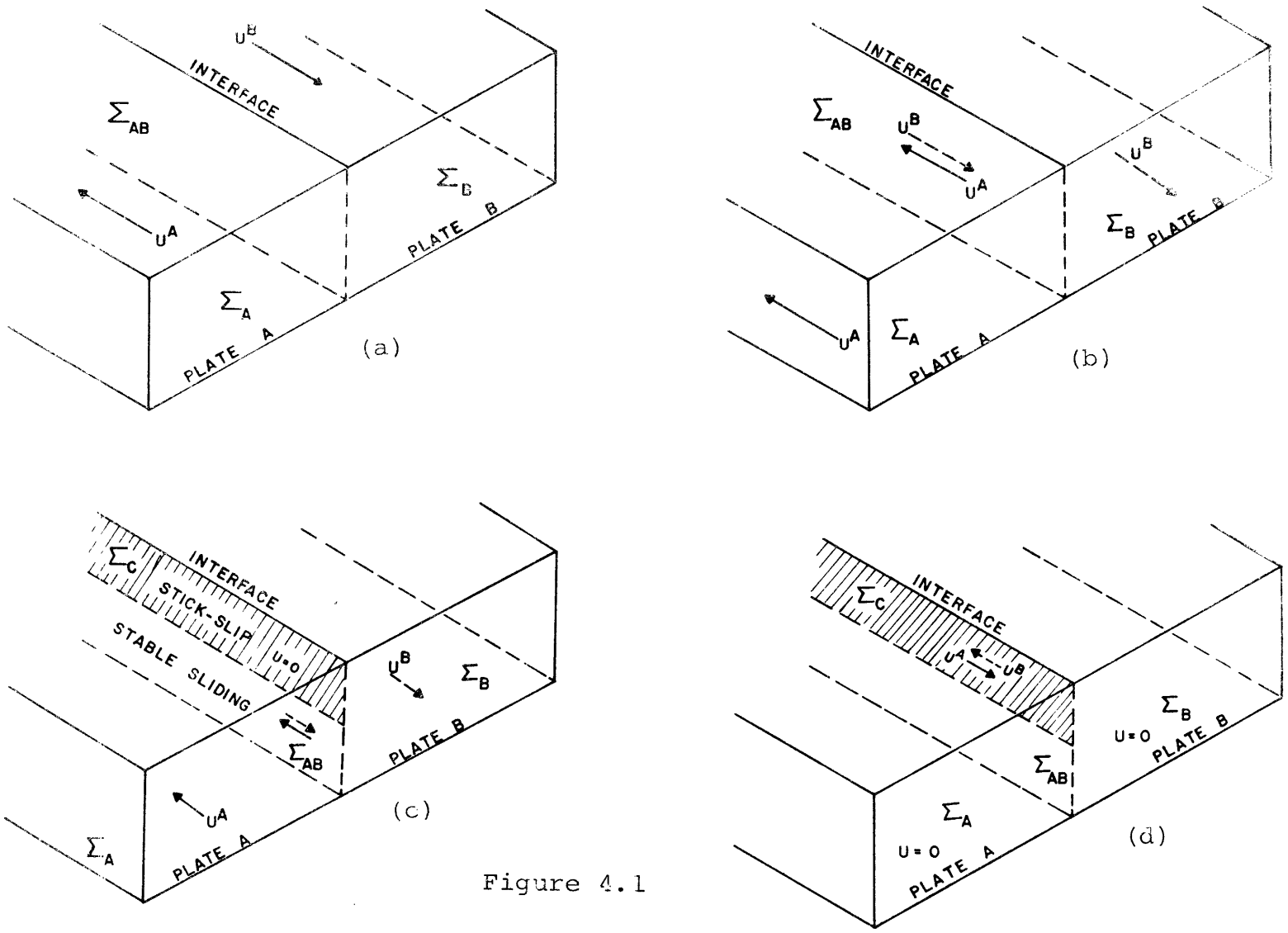
INTERFACE
Σ_{AB}
U^B
U^A
Σ_A
PLATE A
Σ_B
PLATE B
(a)
INTERFACE
Σ_{AB}
U^B
U^A
U^B
Σ_B
PLATE B
U^A
Σ_A
PLATE A
(b)
Σ_C
INTERFACE
STICK-SLIP
U=0
STABLE SLIDING
U^B
Σ_B
Σ_{AB}
PLATE B
U^A
Σ_A
PLATE A
(c)
Σ_C
INTERFACE
U^A
U^B
Σ_B
U=0
PLATE B
Σ_{AB}
Σ_A
U=0
PLATE A
(d)

Figure 4.1

Figure 4.2

(a) Shear strain (in the plane of the fault) across the simple strike-slip fault shown in (b).

(b) Fault model in which fault creep occurs below a depth of 20 km at the rate of 5 cm/yr. The top 20 km is completely locked. The shear strain in (a) represents the one year accumulation that would be observed on the surface.

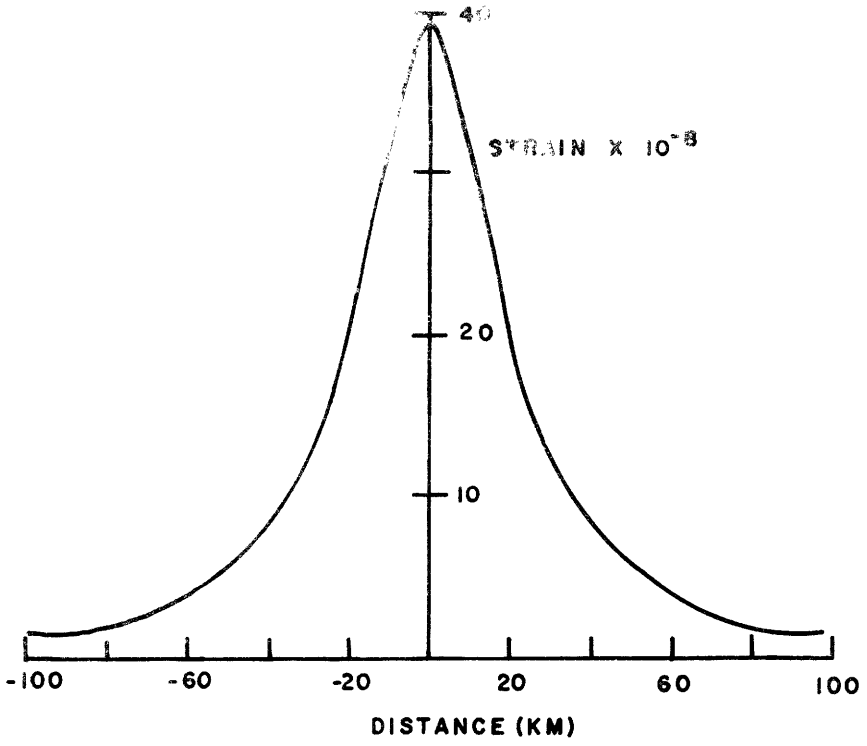
40
STRAIN X 10⁻⁸
20
10
-100
-60
-20
20
60
100
DISTANCE (KM)

(a)

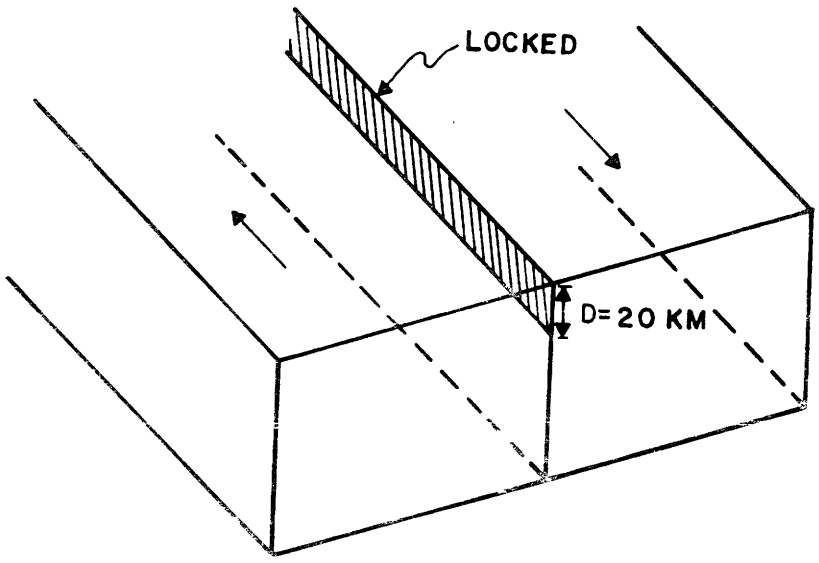
LOCKED
D= 20 KM

(b)

Figure 4.2

Figure 4.3

(a) Plate interaction across an irregular interface. The position of the interface between the two plates denoted by the letter S represents the area in which the plates are in direct collision. The dotted arrows pointing away from S represent the relative displacements for the equivalent dislocation to the anti-dislocation model.

(b) Side view of what is assumed to happen in the area around S. Constant displacements on the bottom of the plate begin to decrease to zero as a transition zone is reached. The region between the two sides of S represents a finite volume in which both elastic (e_{ij}) and anelastic (e_{ij}^{t}) strains occur. The anelastic strains represent the permanent deformation due to plate collision.

(c) Changing the frames of reference for the problem in (b). The displacements on the bottoms of the plates decrease to zero away from the transition zone. The displacements on the surface of the anelastic zone are equal and opposite to the assumed motions of the plates. In this frame of reference the problem is equivalent to an inclusion which has undergone an anelastic expansion (Eshelby 1957). Inside the inclusion (anelastic zone) the elastic strains e_{ij} is a result of the confinement of the anelastic transformation strain e_{ij}^{t} [illegible] (see Fig.

Figure 4.3 (Cont'd)

(d) If we assume that the fall off of the displacements on the bottom of the plate takes place over a very short distance in comparison to other distances in the problem, the displacements on the bottom of the plate may be neglected. (This assumption may not always be justified and will be discussed later in the text.) If we also assume that the volume of the inclusion is vanishingly small then the inclusion may be shown to reduce to the dislocation shown in (d) (Eshelby, 1957).

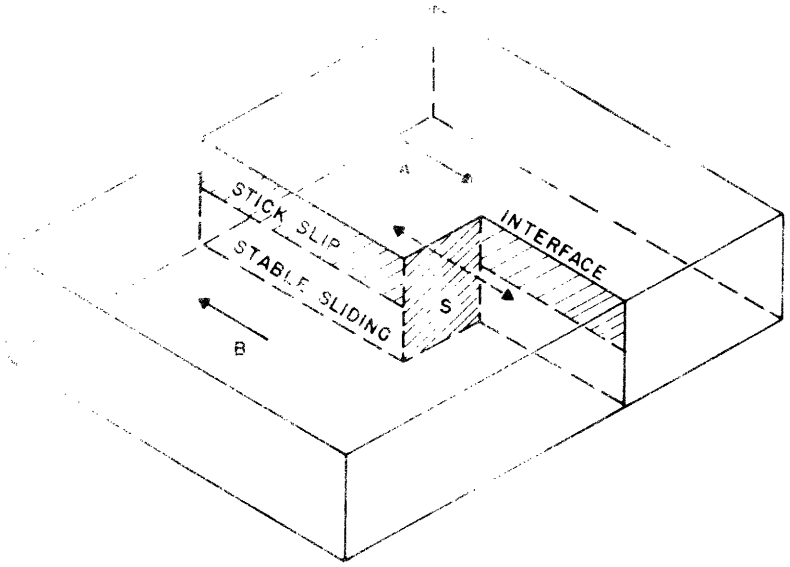

(a)

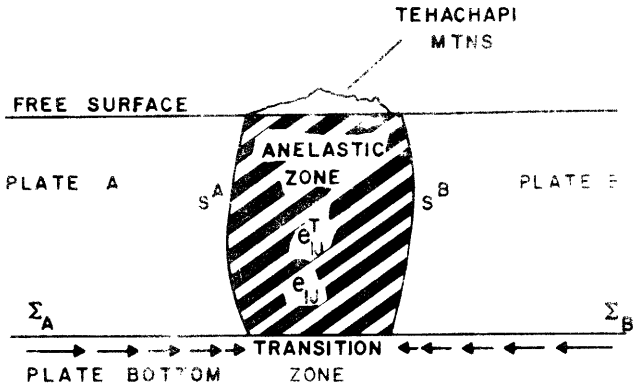

(b)

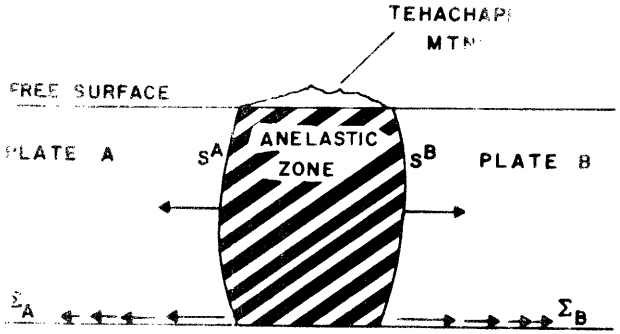

(c)

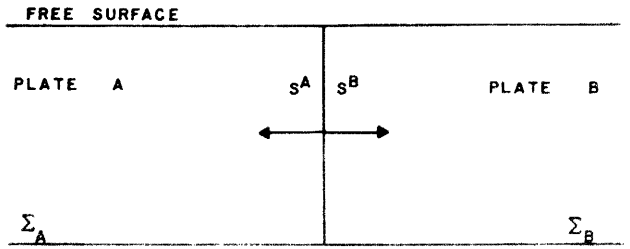

(d)

Figure 4.3

Figure 4.4

(a) Angular dislocation in a half-space (Comninou, 1973).

(b) Construction of a π dislocation from two angular dislocations.

(c) Construction of an oblique rectangular dislocation from π dislocations.

(d) Convention used to describe fault models. Latitude, longitude, and depth of the corners are given in a particular sequence so as to define the direction of the dislocation line. The Burgers' vector represents the motion of the positive side of the dislocation with respect to the negative side. It will be given in cylindrical coordinates (B_r, B_ϕ, B_z). The B_r and B_z components will be in meters. B_ϕ is the azimuthal angle in degrees (positive clockwise) from the positive Y-axis (North).

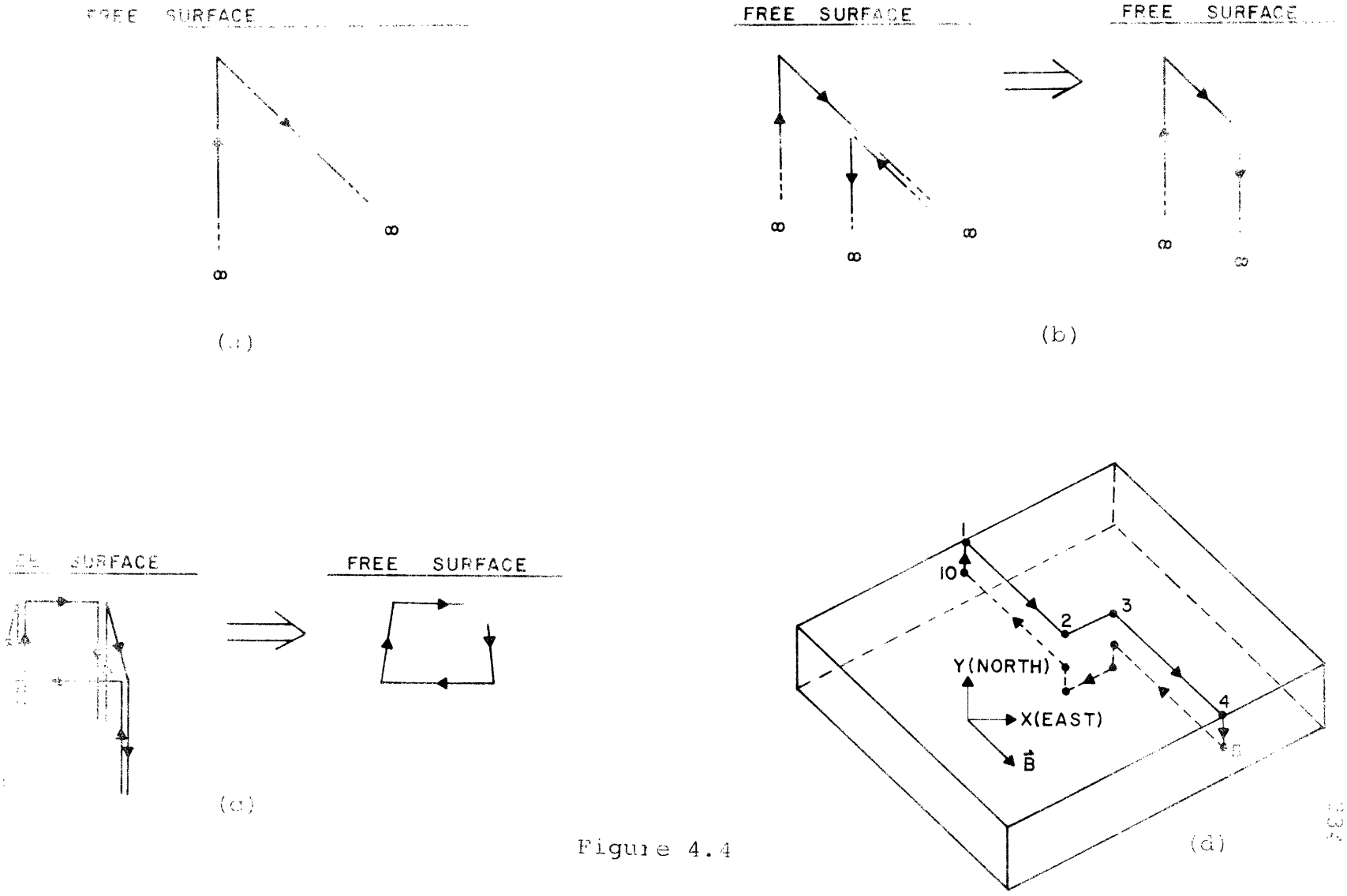

(a) (b) (c) (d)

Figure 4.4

Figure 4.9

Shear strain contours (x 10^{+7}) for the sharp bend model given in table 4.1. The positive X_2- points N45°W and the positive X_1- axis points N45°E. Negative E_{12} represents a right lateral strain on a fault striking N45°W.

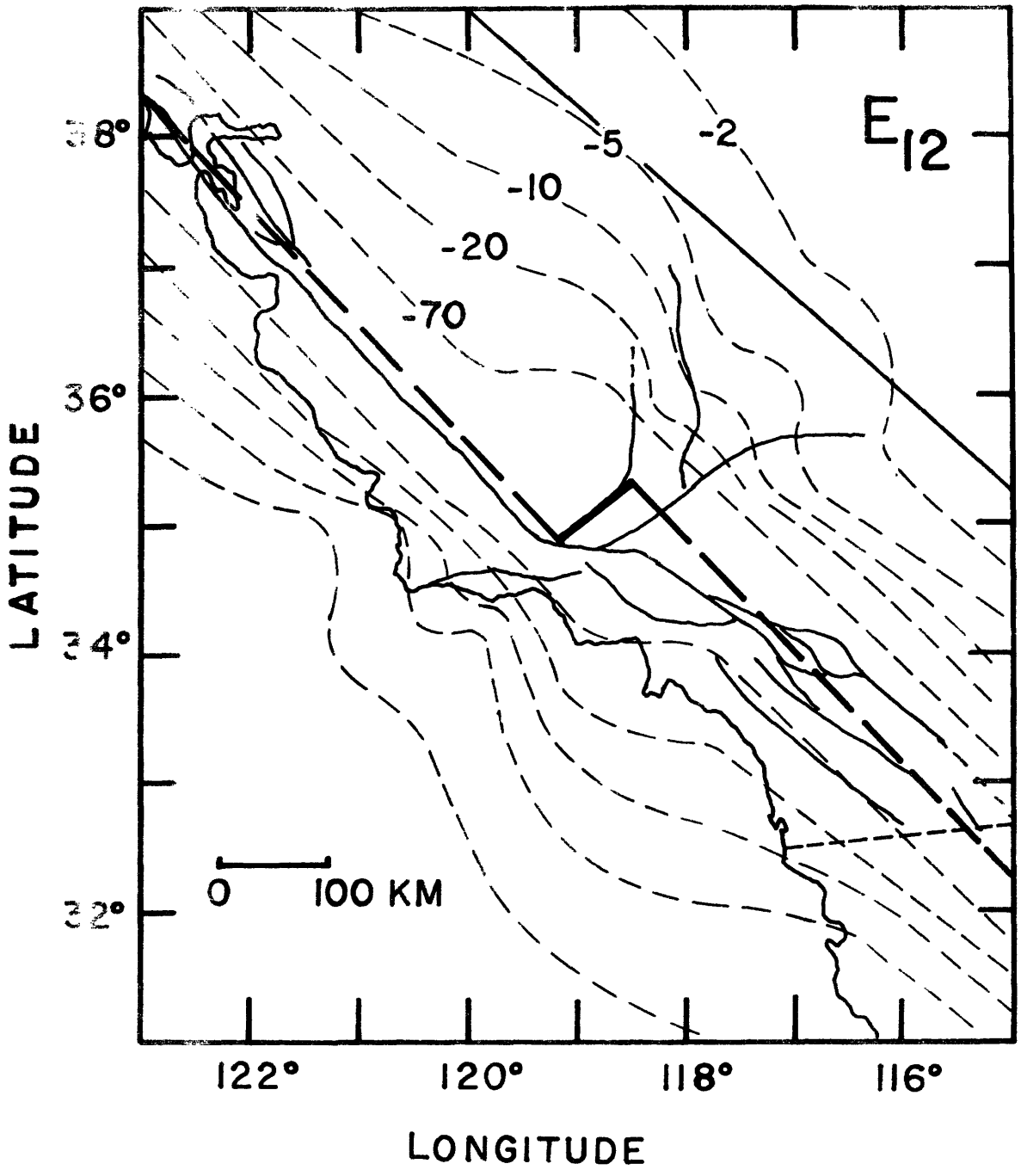
E12
-5
-2
-10
-20
-70
38°
36°
34°
32°
0
100 KM
122°
120°
118°
116°
LATITUDE
LONGITUDE

Figure 4.7

Figure 4.6

E_{22} strain contours ($X10^{+7}$) for the sharp bend model. Positive X_2- axis points N45°W. Negative E_{22} indicates compression. This model yields NW-SE extension in the Basin and Range Province and the Santa Barbara channel-Point Arguello Canyon area. NW-SE compression occurs in the transverse range province.

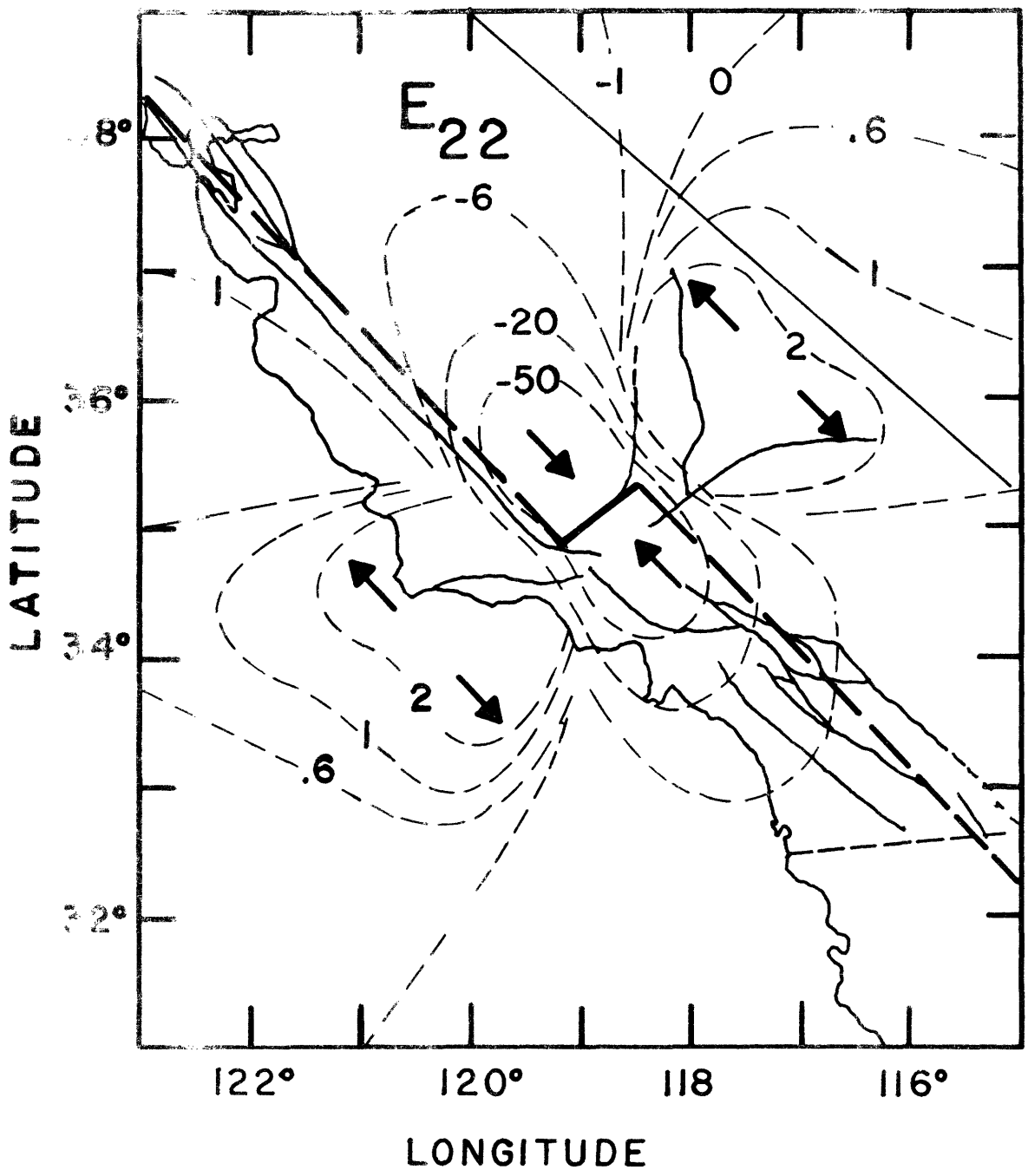
E_{22}
-1
0
.6
-6
1
-20
-50
2
2
1
.6
1
38°
36°
34°
32°
LATITUDE
122°
120°
118
116°
LONGITUDE

Figure 4.6

Figure 4.7

A map of faulting in the vicinity of San Francisco. Faults are taken from a map compiled by Hill et al. (1969). Faults shown are:

(1) San Andreas

(2) Calaveras

(3) Hayward

(4) Sulphur Springs, Concord, and Greenville

(5) nameless

(6) Silver Creek

(7) nameless

(8) Sargeant

(9) Sargent

(10) Pilarcitos

(11) Seal Cove-San Gregorio

(12) Ben Lomond

(13) Butano

(14) Vergeles

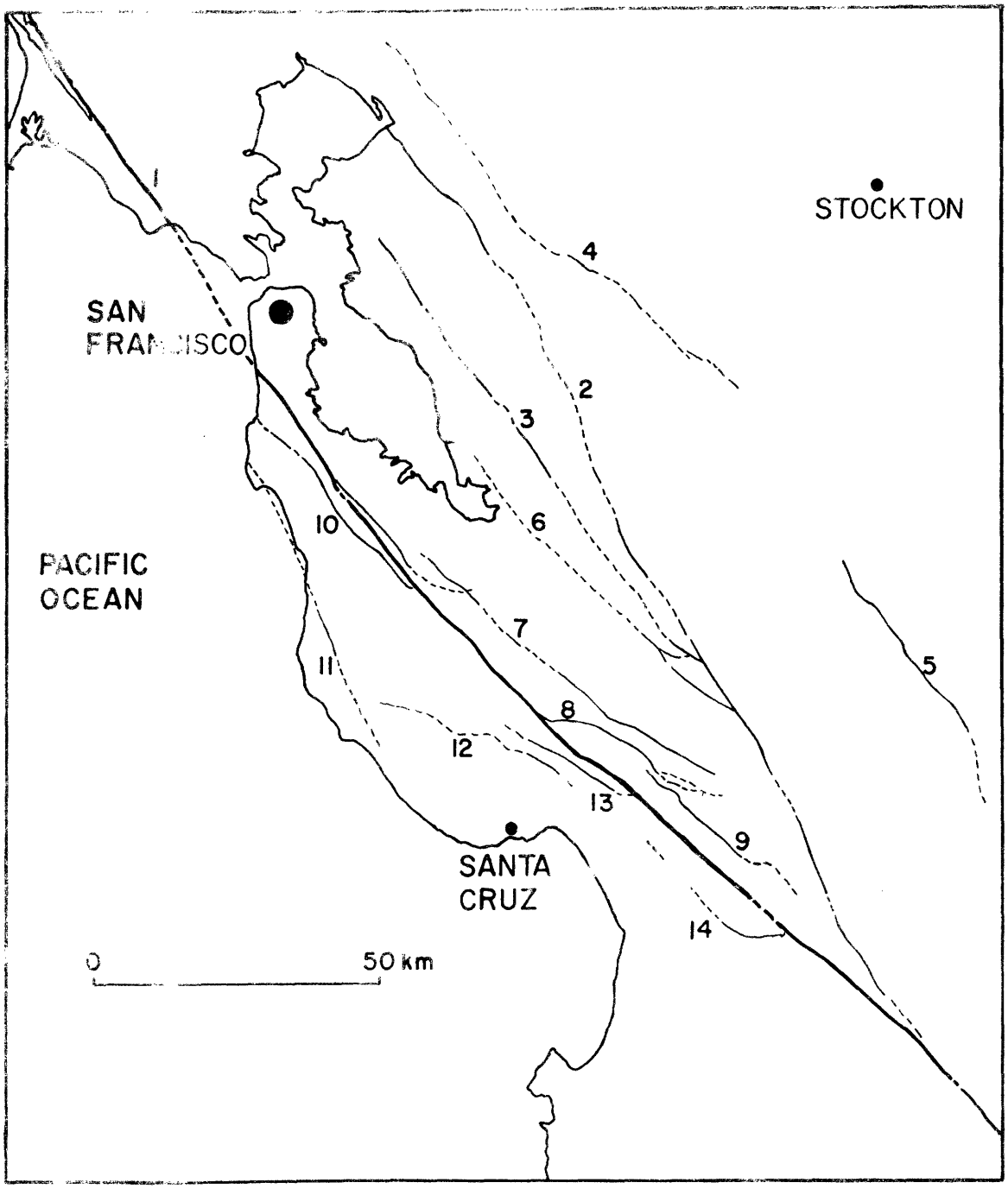
STOCKTON
SAN
FRANCISCO
PACIFIC
OCEAN
SANTA
CRUZ
0
50 km
1
2
3
4
5
6
7
8
9
10
11
12
13
14

Figure 4.7

Figure 4.8

The SJB (San Juan Bautista) bend represents a change in the strike of the San Andreas in the area just south of San Francisco. South of a point just north of Bear Valley the average trend of the San Andreas is N40°W. To the north from Bear Valley the San Andreas trends approximately N48°W. Finally, in the vicinity of Black Mountain the San Andreas bends back to a more northerly strike (N35°W).

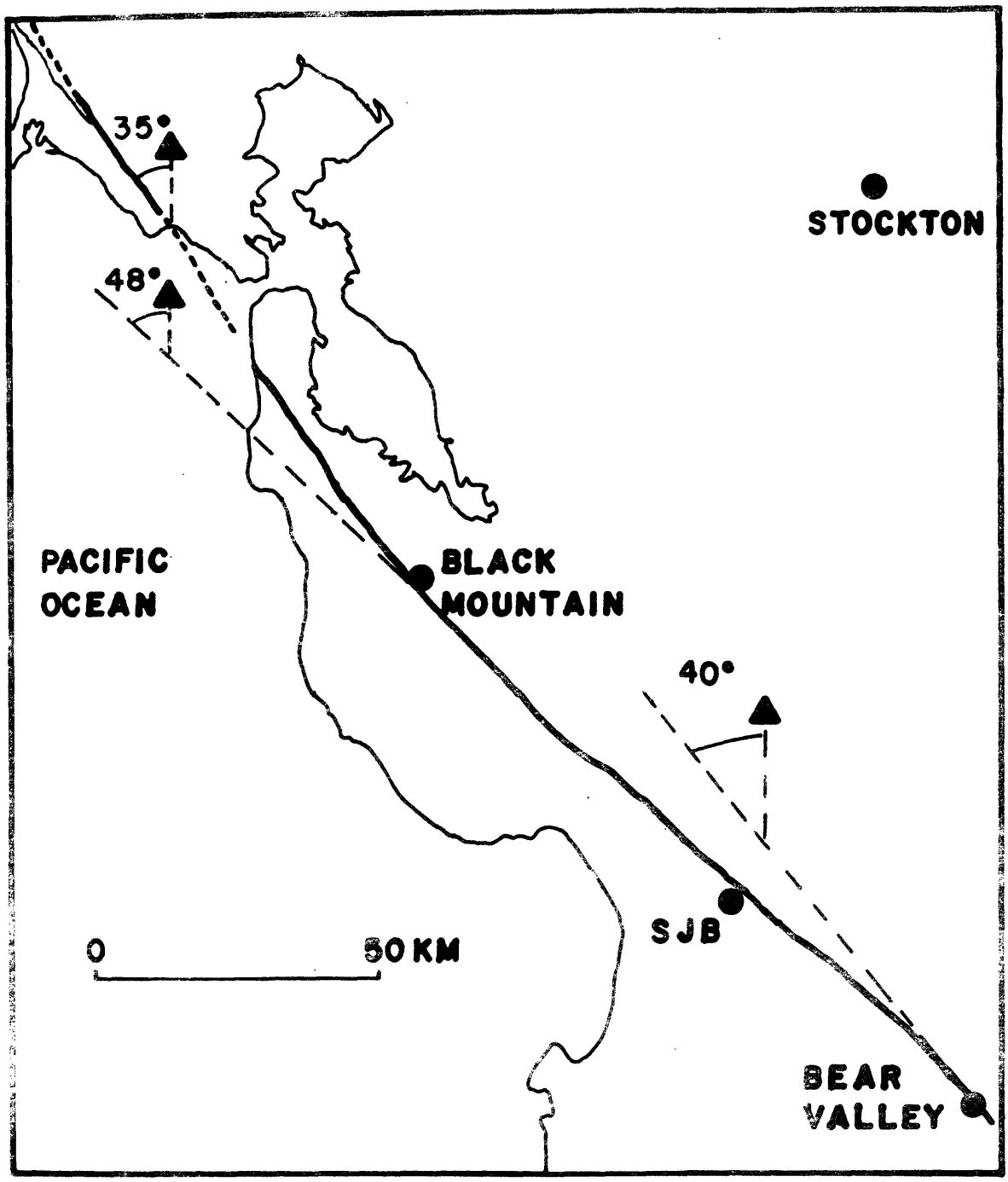
35°
48°
40°
STOCKTON
PACIFIC
OCEAN
BLACK
MOUNTAIN
SJB
0
50 KM
BEAR
VALLEY

Figure 4.8

Figure 4.9

Shear strain contours ($X10^{+7}$) for the SJB bend model described in table 4.2.

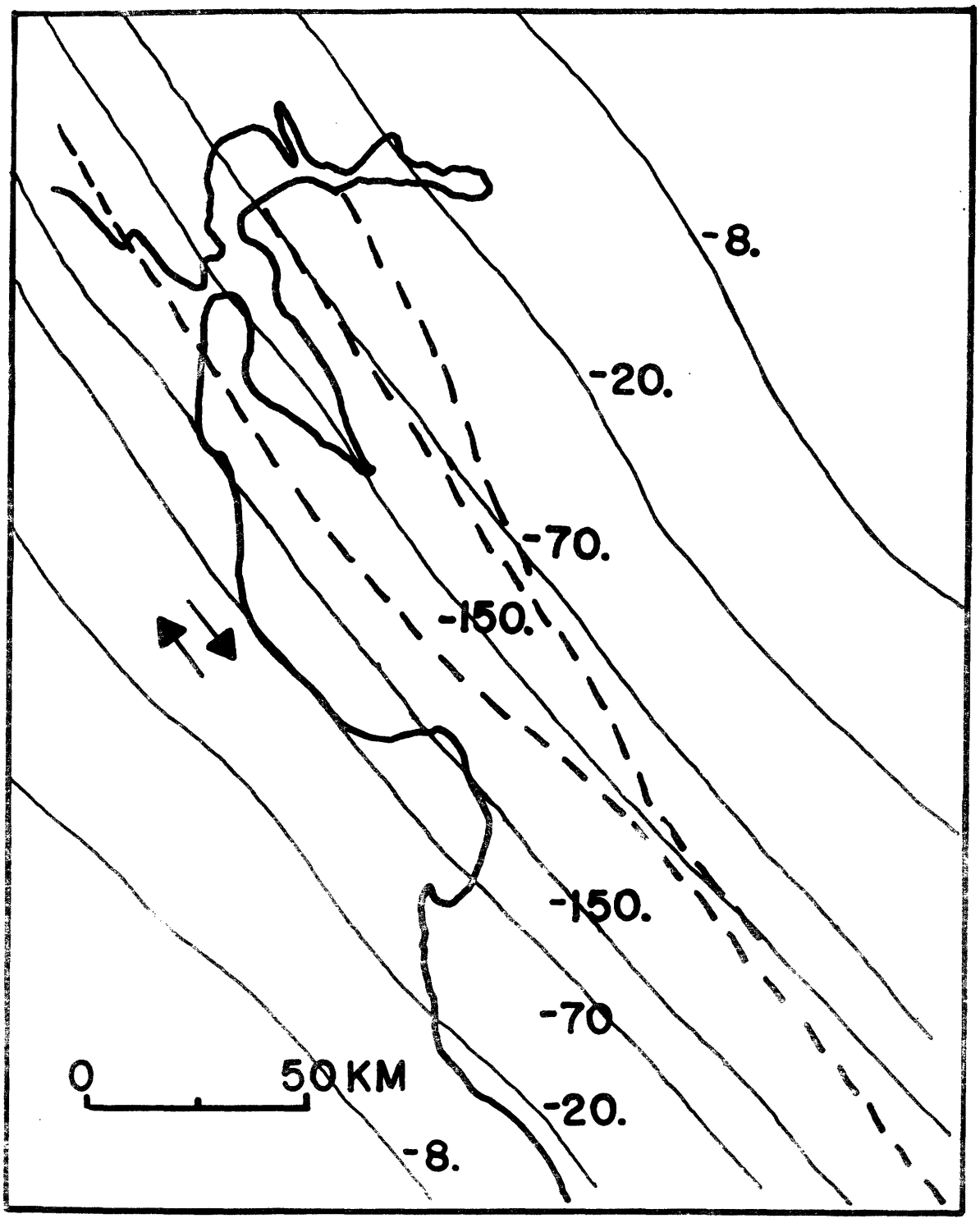

Figure 4.9

Figure 4.10

E_{22} strain contours for SJB bend model (table 4.2). Note the general NW-SE extension in the area.

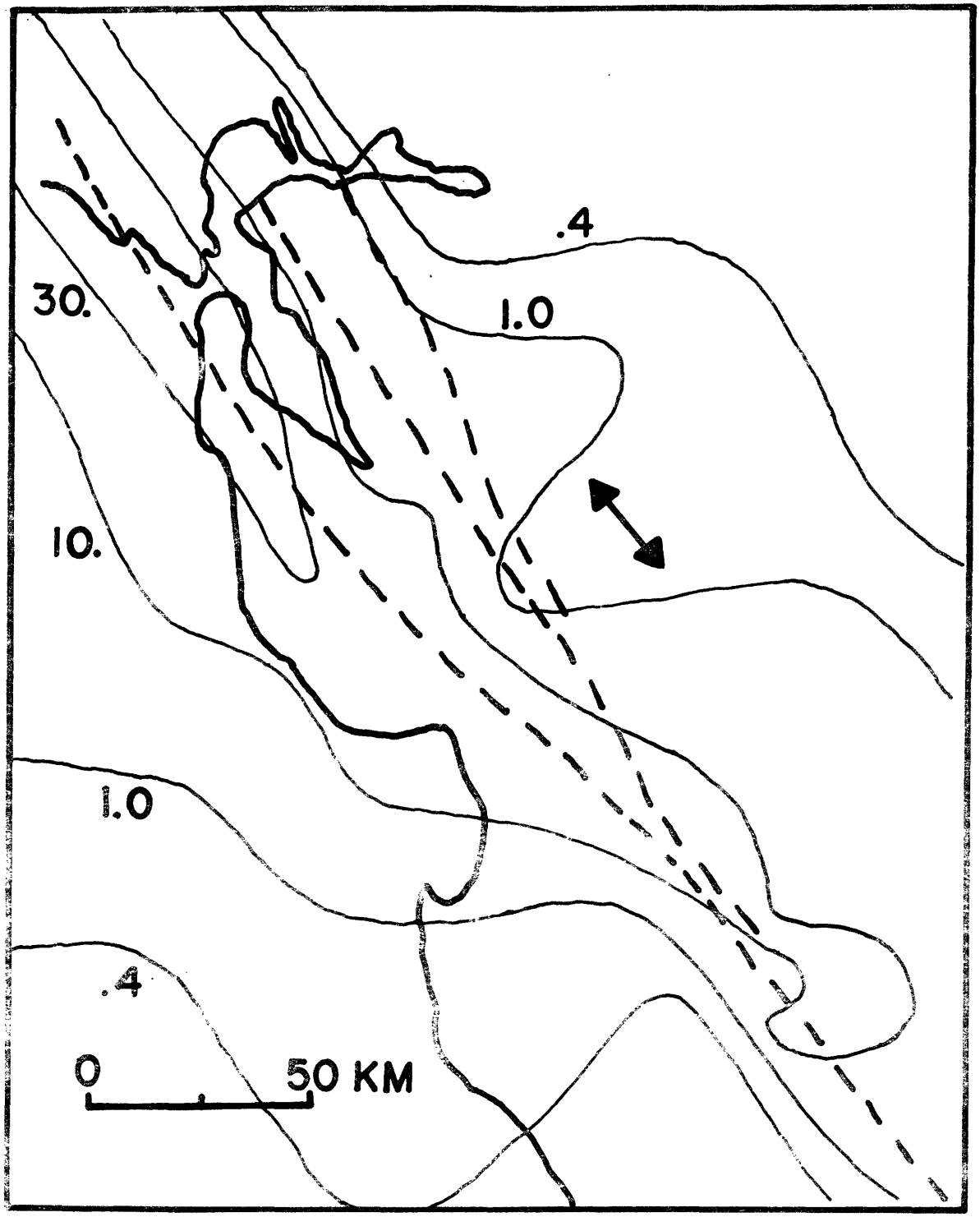

Figure 4.10

Figure 4.11

E_{11} strain contours for SJB bend model (table 4.2). Note the reduced normal strain in the vicinity of the Hayward and Calaveras faults and on the southwestern side of the San Andreas.

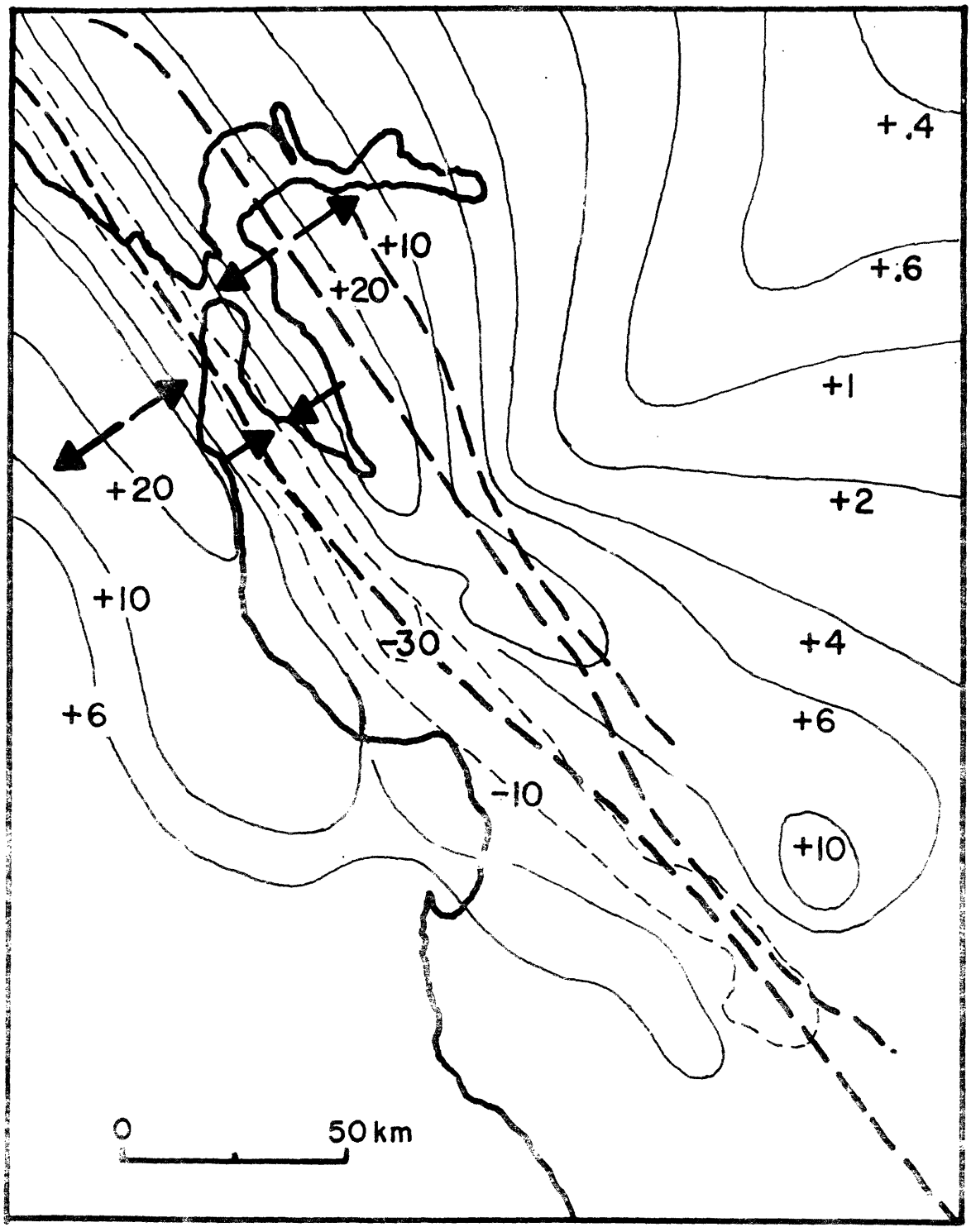

Figure 4.11

Figure 4.12

Inferred principle compressive stress axes from earthquakes in central California. Events 1-15 (●) are from Bolt et al. (1968). Events U and V (o) are taken from Elsworth (1975). Events a, b, and c (Δ) represent the results of Mayer-Rosa (1973). Events r and s (O) summarize two event clusters studied by Green et al. (1973). The important feature of this plot is a change of the pressure axes from a north-south direction in the southern portion of the map to a northeast-southwest direction near San Francisco.

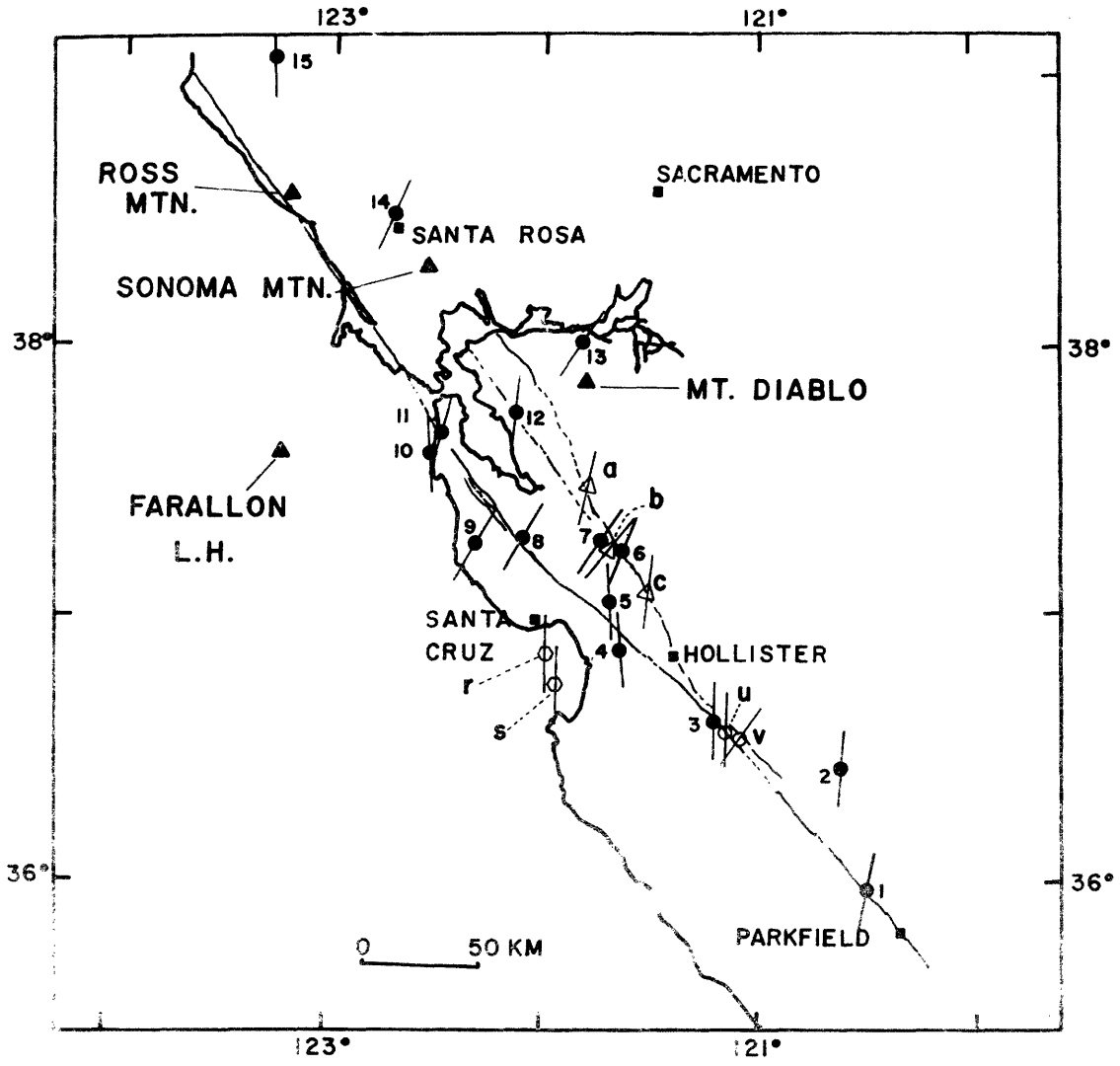
123°
121°
38°
36°
15
ROSS
MTN.
SACRAMENTO
14
SANTA ROSA
SONOMA MTN.
13
MT. DIABLO
11
12
10
a
b
FARALLON
L.H.
9
8
7
6
c
5
SANTA
CRUZ
4
HOLLISTER
r
s
u
3
v
2
1
PARKFIELD
0
50 KM

Figure 4.12

FIGURE 4.13

(a) Contours of pressure axes (principal axis of compression) for SJB bend model. Note the change in direction from north-south to northeast-southwest associated with the SJB bend.

(b) Schematic diagram of SJB bend model used to calculate the pressure axes in (a).

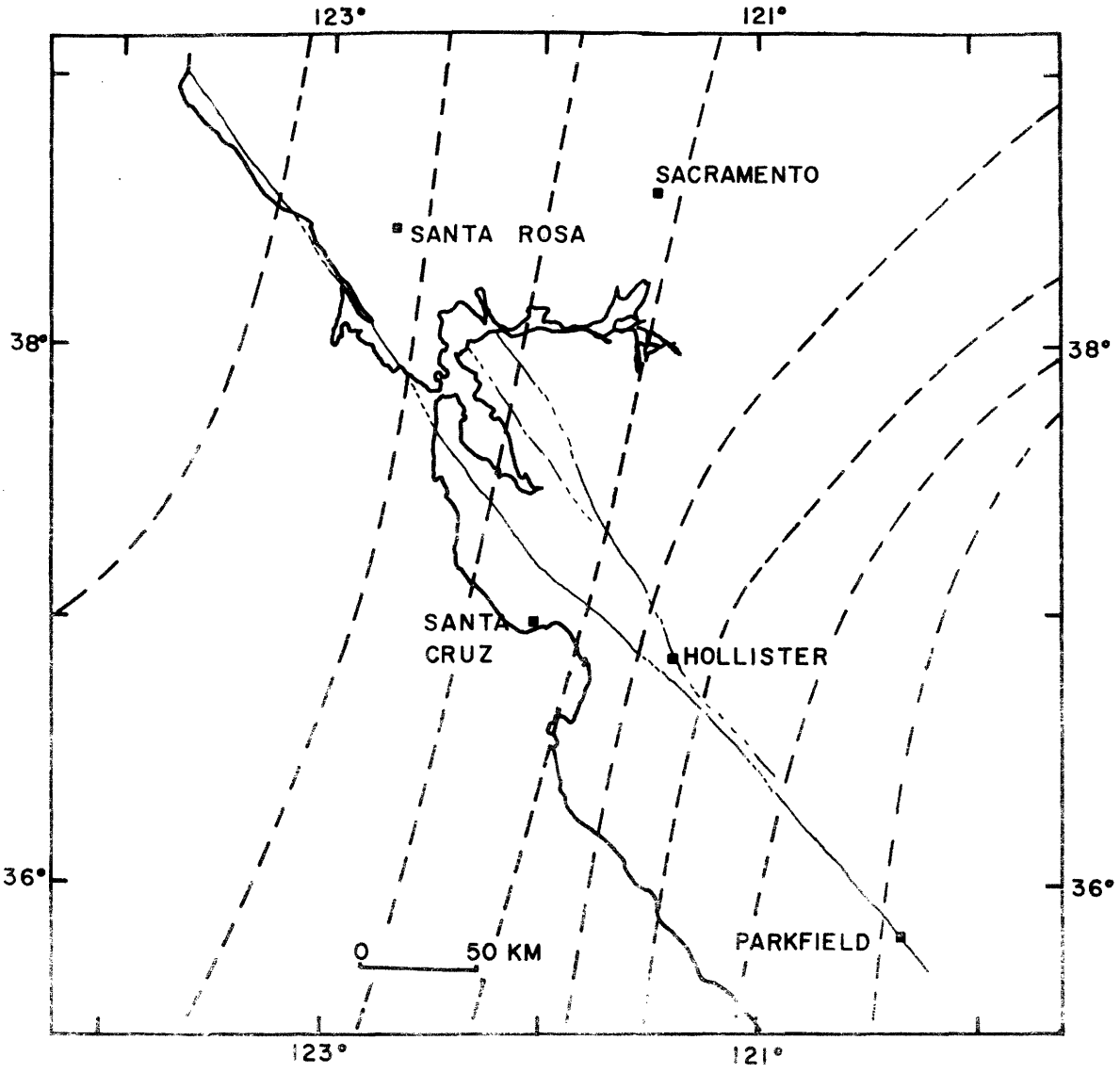

(a)

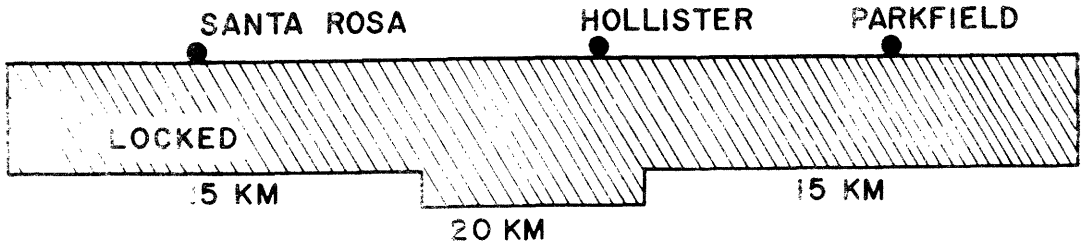

SLIP = 5 CM / YR

(b)

Figure 4.13

FIGURES 4.14

(a) Contours of pressure axes for SJB bend model with an increased depth of locking on the northern section.

(b) Schematic diagram of a model used to calculate the pressure axes shown in (a).

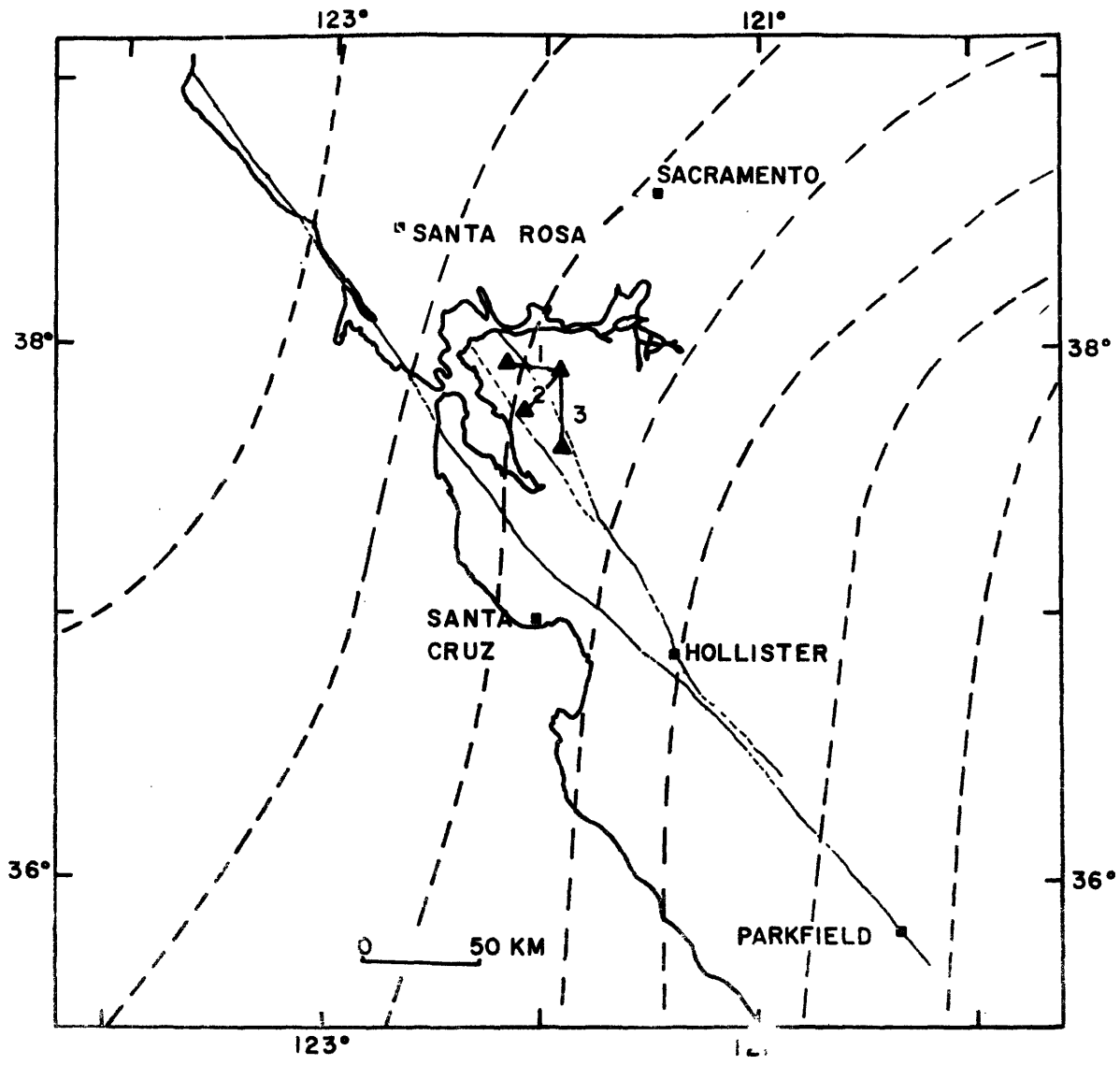

(a)

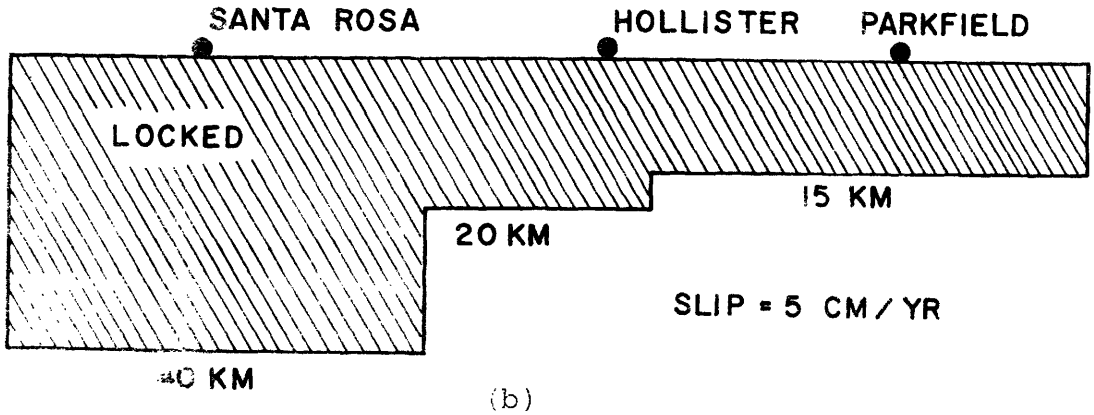

(b)

Figure 4.14

FIGURE 4.15

Areas of fault creep (shown by dark wavy lines on faults) on the San Andreas-Calaveras-Hayward system. The numbers beside the faults represent the fault creep in cm/year as presented by Nason (1971). His results have been modified recently by Nason (1973) and Spilth et al. (1974). North of Anderson Resevoir the fall-off from 1.2 cm/year to 0.0 is uncertain, i.e., the creep occurs in patches (Nason, 1973). North of Fremont the creep rate picks up on the Hayward. Northeast of San Pablo fault creep has recently been observed on the Concord fault (Nason, 1973).

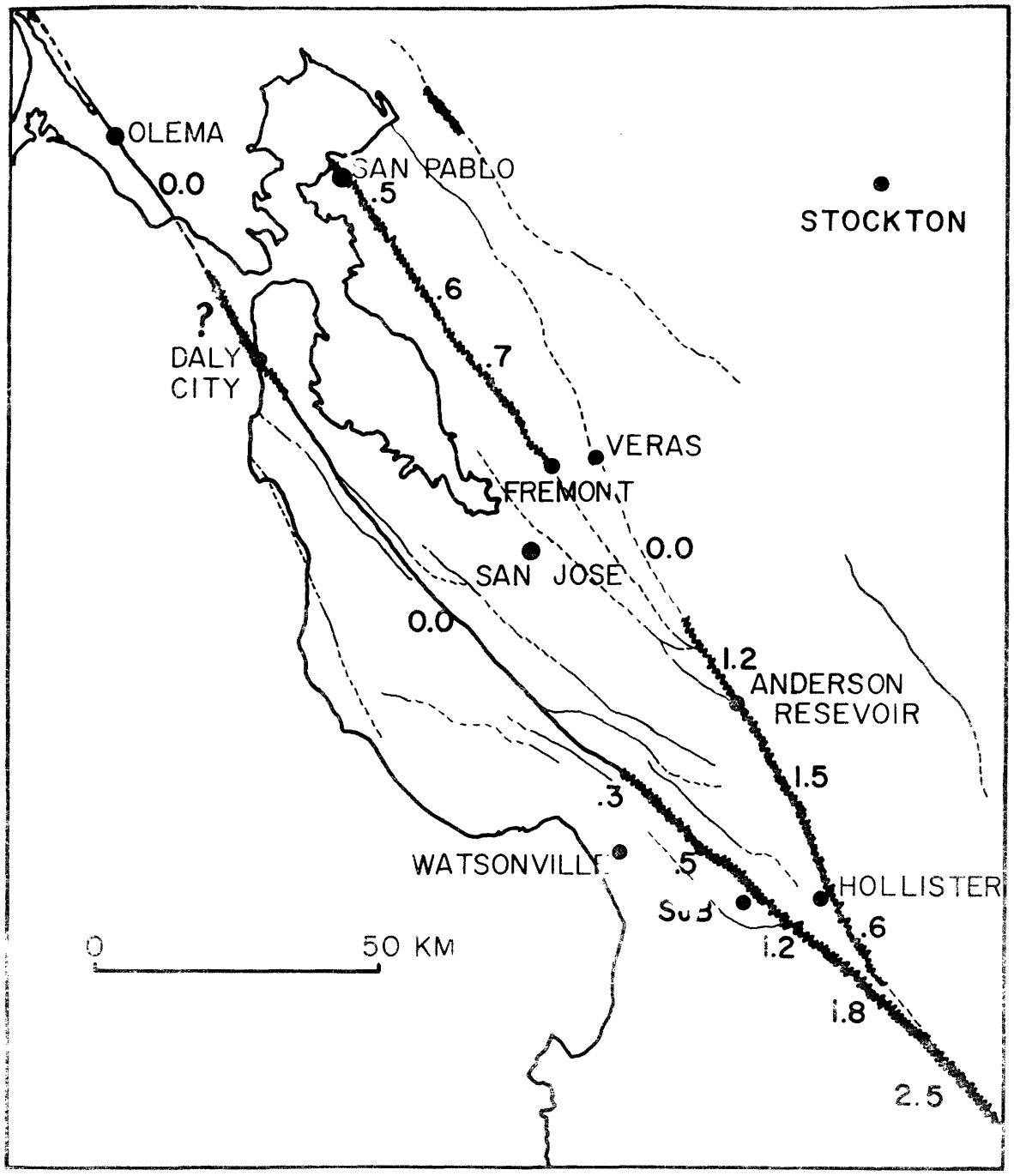
OLEMA
0.0
SAN PABLO
.5
.6
.7
STOCKTON
?
DALY
CITY
VERAS
FREMONT
0.0
SAN JOSE
0.0
1.2
ANDERSON
RESEVOIR
1.5
.3
WATSONVILLE
.5
HOLLISTER
.6
1.2
1.8
2.5
0
50 KM

Figure 4.15

FIGURE 4.16

(a) Yearly shear strain accumulation across a fault completely locked to a depth of 20 km and slipping at 5 cm/year.

(b) Yearly shear strain accumulation for the same fault as (A) but with the addition of 3 cm/year of slip on the top 10 km.

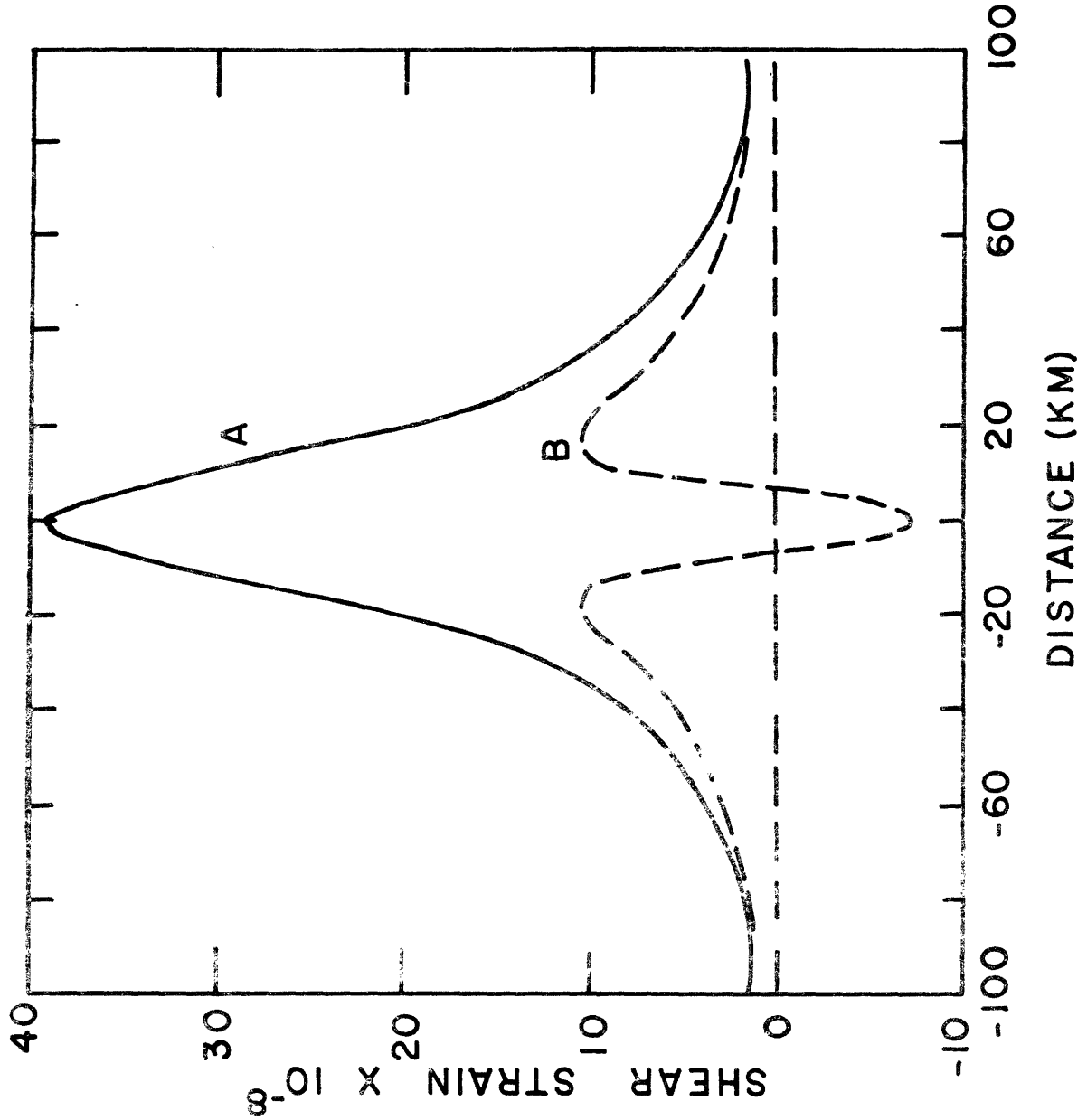
SHEAR STRAIN X 10^{-8}
40
30
20
10
0
-10
A
B
100
60
20
-20
-60
-100
DISTANCE (KM)

Figure 4.16

FIGURE 4.17

(a) Subtraction of two screw dislocations in an infinite medium to obtain the solution for a dislocation in a half-space with the surface of slip extending from the dislocation line to the surface (surface fault creep).

(b) Addition of two screw dislocations with their surfaces of discontinuity pointing in opposite directions to obtain the solution for a screw dislocation in a half-space with the surface of discontinuity pointing away from the surface (locked fault with a slip below d_2).

(c) Addition of (a) and (b) yields a model for a fault slipping in the near surface region, locked at intermediate depths, and slipping below the locked region.

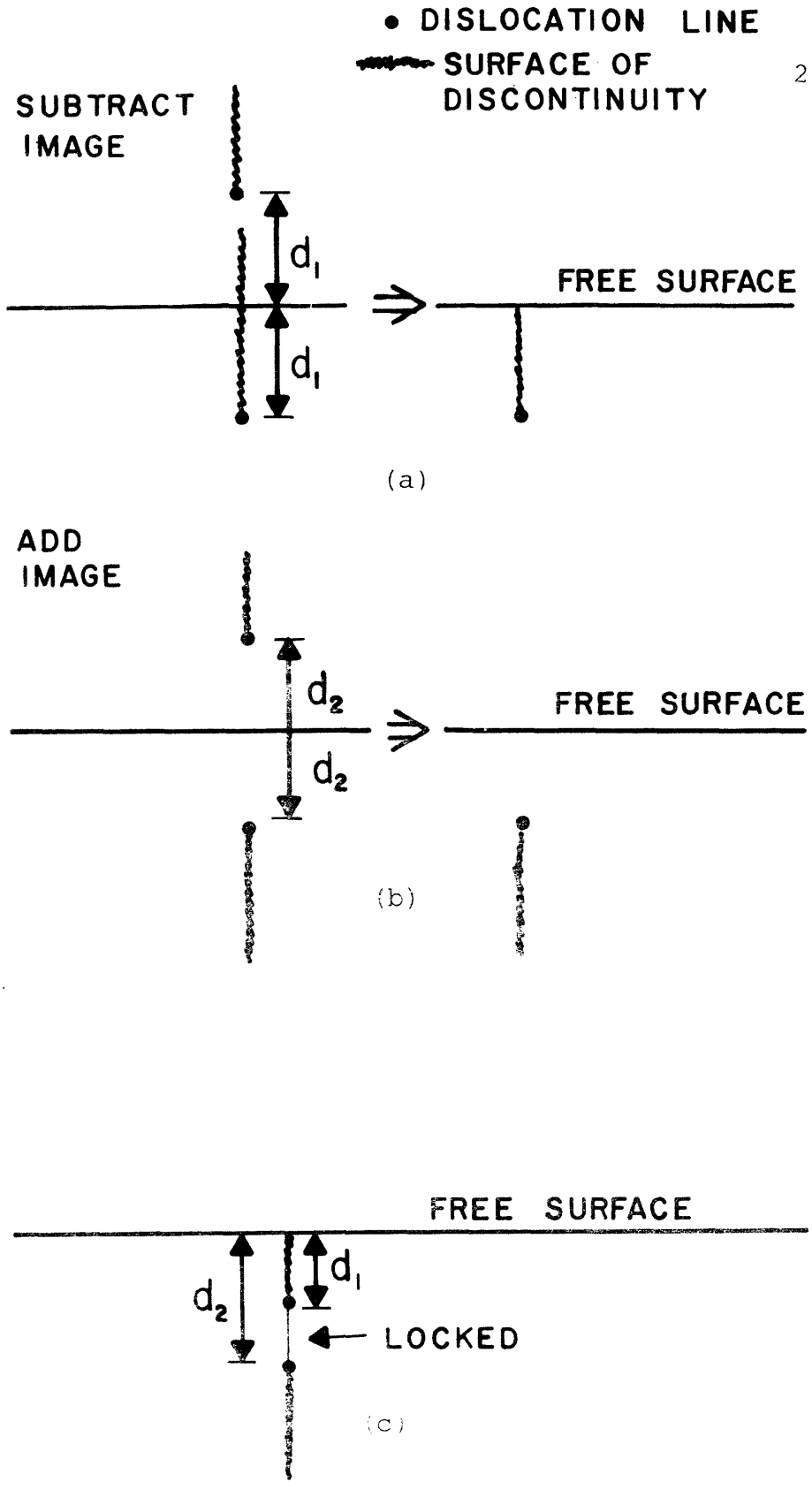
• DISLOCATION LINE
SURFACE OF DISCONTINUITY
SUBTRACT IMAGE
d_1
d_1
FREE SURFACE
(a)
ADD IMAGE
d_2
d_2
FREE SURFACE
(b)
FREE SURFACE
d_2
d_1
LOCKED
(c)

Figure 4.17

FIGURE 4.18

Plot of shear strain E versus distance X from a fault model.

The strains are divided by $E_o = b_2/(2\pi d_2)$ and the distances by d_2. Lower dashed line represents the maximum shear strain in the vicinity of the San Andreas as determined by Savage and Burford (1970). Their measurement is divided by $E_o = .55 \times 10^{-6}$ found by Meade (1971) on a completely locked section of fault near Ft. Ross. The upper dashed line represents the maximum shear strain within one standard deviation of the data point used for the lower line. The data allow 70% of the fault to be locked.

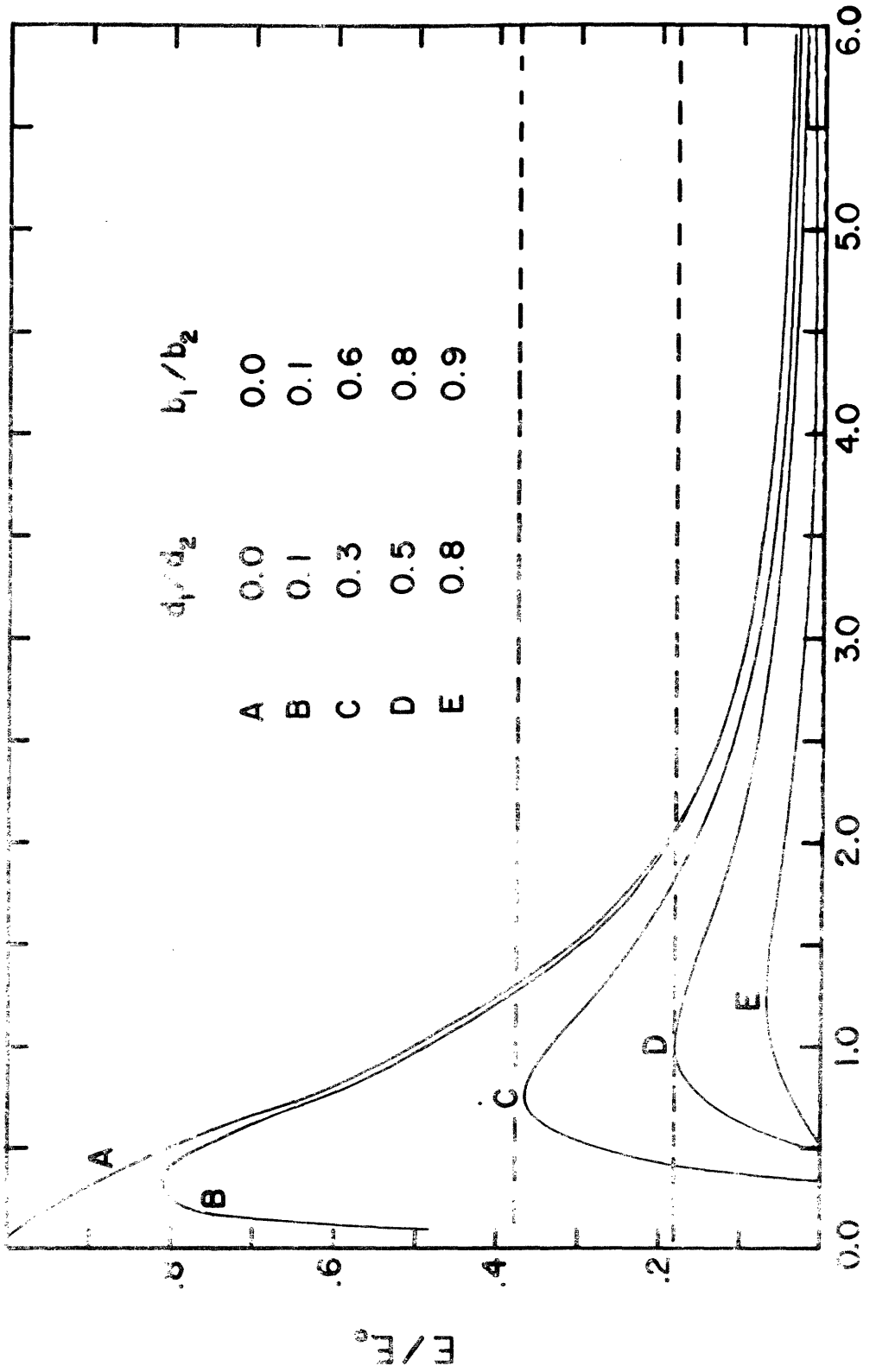
E / E₀
X / d₂
d₁ / d₂
b₁ / b₂
A 0.0 0.0
B 0.1 0.1
C 0.3 0.6
D 0.5 0.8
E 0.8 0.9
A
B
C
D
E
.8
.6
.4
.2
0.0
1.0
2.0
3.0
4.0
5.0
6.0

Figure 4.18

FIGURE 4.19

γ_1 component of strain (equivalent to shear strain across a fault oriented N 45° W) across the Hollister arc as determined by Savage and Burford (1970) (solid circles). Curve A represents the γ_1 strain across a completely locked SJB bend model. Curve B is the theoretical γ_1 strain across an SJB bend model in which the top 6 km creeps at the rate of 2 cm/year. The time period represented in the plot is 32 years.

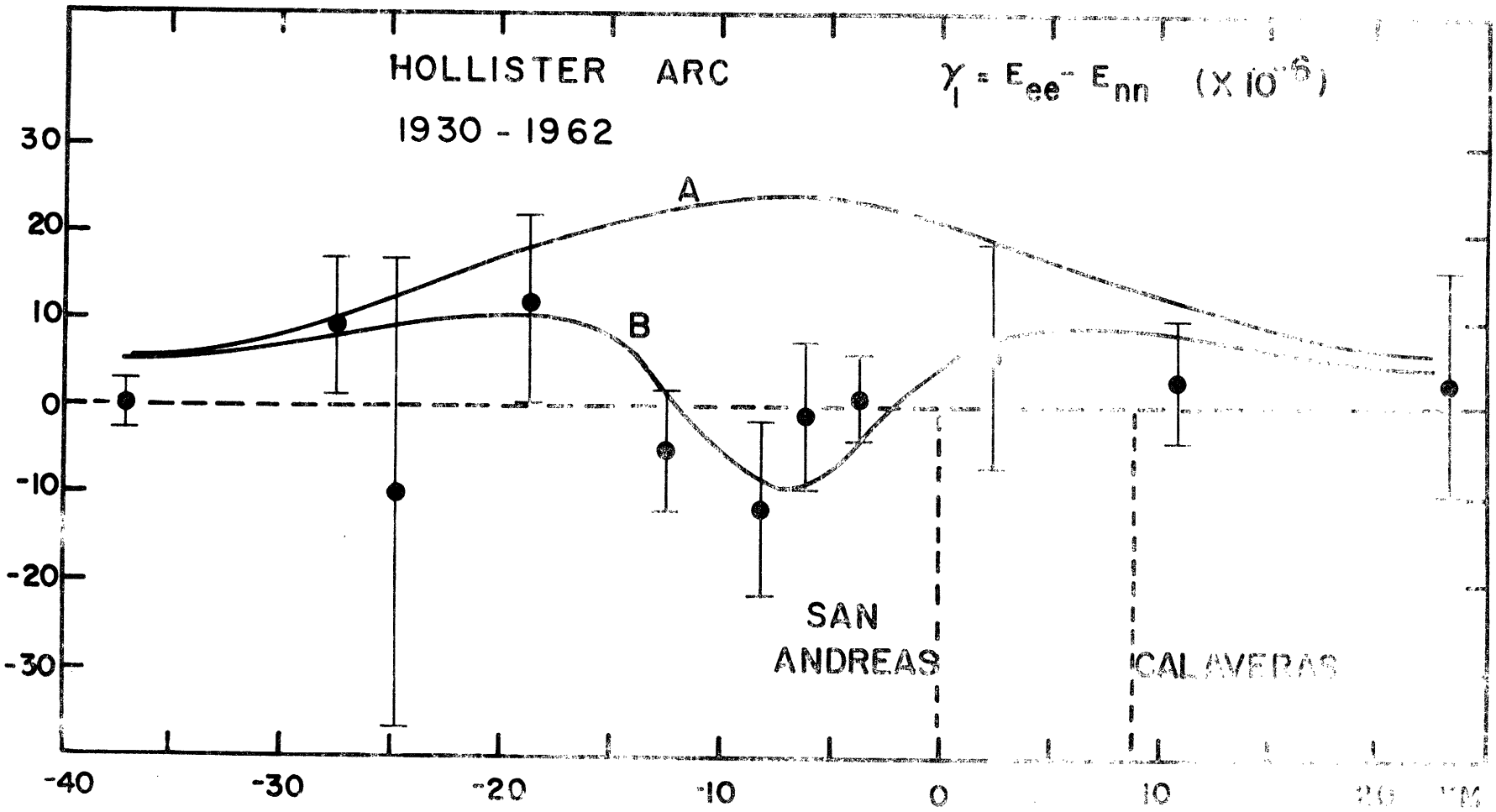
HOLLISTER ARC
1930 - 1962
$\gamma_1 = E_{ee} - E_{nn}$ (X 10^{-6})
30
20
10
0
-10
-20
-30
A
B
SAN
ANDREAS
CALAVERAS
-40
-30
-20
-10
0
10

Figure 4.19

FIGURE 4.20

γ_2 component of strain for the Hollister arc (see figure 4.19). A and B represent SJB bend models without and with fault creep respectively (table 4.3).

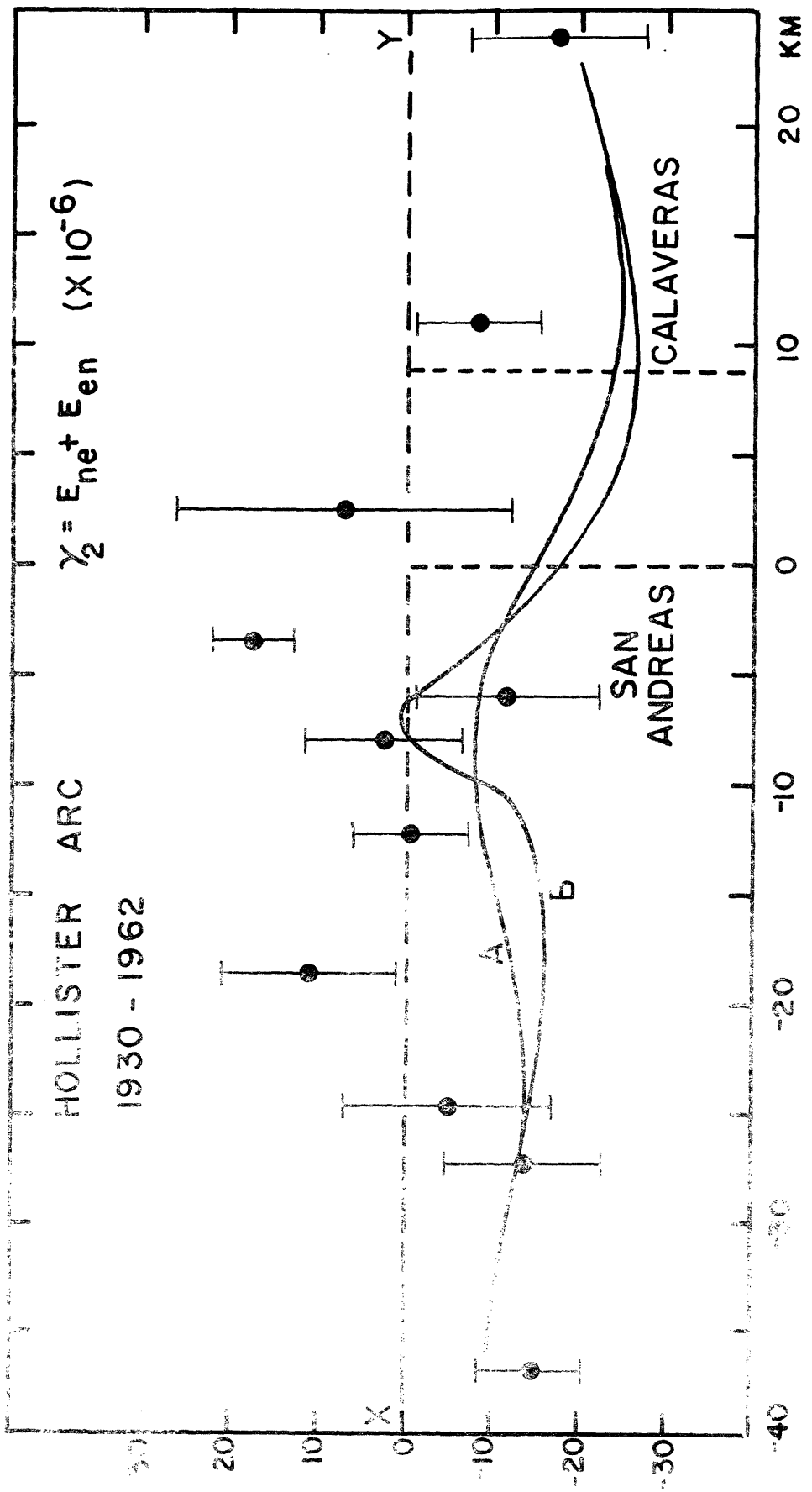
HOLLISTER ARC
1930 - 1962
$\chi_2 = E_{ne} + E_{en}$ (X 10^{-6})
Y
X
KM
CALAVERAS
SAN ANDREAS
A
b
20
10
0
-10
-20
-30
-40

Figure 4.20

Figure 4.21

Model of fault locked between depths d_1 and d_2 with slip above and below the locked section. The locked section will, after a period of time, begin to drive a secondary fault that extends to a depth d_3. The rate of creep on the secondary fault will be a function of the applied stress from the locked fault, the area of the secondary fault, and the frictional properties of the secondary fault.

Figure 4.21

Figure 4.22

Plot of fault creep on various faults in central California as a function of distance from the San Andreas fault. The fault creep on the San Andreas is plotted as a function of its distance from the Calaveras. The apparent relation between creep on the Calaveras and San Andreas faults can be explained by elastic coupling of the two faults. The pick up of creep on the more northerly faults can be interpreted as being the result of deeper locking on the San Andreas near San Francisco.

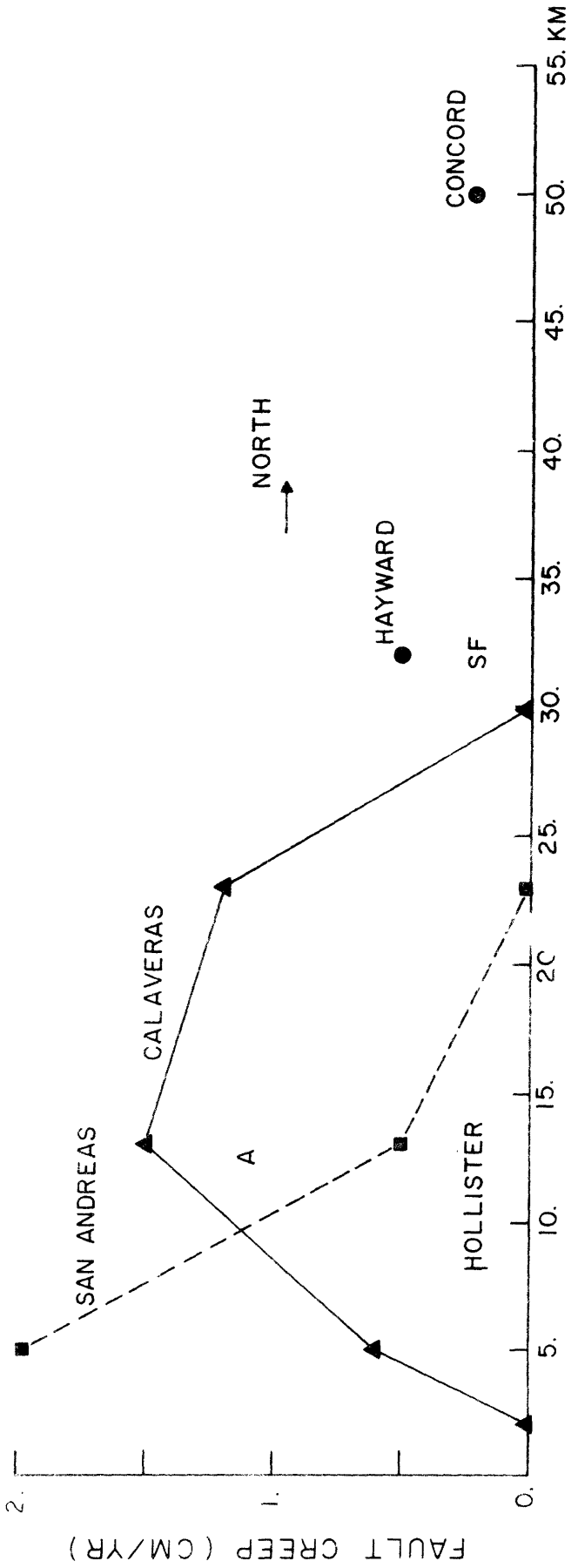
FAULT CREEP (CM/YR)
2.
1.
0.
5.
10.
15.
20
25.
30.
35.
40.
45.
50.
55. KM
FAULT SEPARATION
SAN ANDREAS
CALAVERAS
HOLLISTER
A
NORTH
HAYWARD
SF
CONCORD

Figure 4.22

4.5 The Fort Tejon Bend and Its Role in the Tectonics of Southern California

4.5.1 Introduction

One of the more salient features of a fault map for California is a "big bend" (Hofmann, 1968) in the San Andreas fault (figure 4.23). Because much of the bend is coincident with the faulting of the 1857 Fort Tejon earthquake we shall refer to the bend as the Tejon bend. The origin of such a feature is still uncertain but several explanations may be proposed. Hill and Dibblee (1953) have explained the origin of the bend in terms of the transverse motion on the Big Pine and Garlock faults (figure 4.23). On the other hand the direct alignment of the Tejon bend with the Murray fracture zone off the coast of California suggests that the bend may be a result of motion on the Murray fracture. However Von Huene (1969) has shown that there is no apparent physical connection between the two features.

In an analysis of fault splaying and secondary faulting Chinnery (1966 a,b) found that the direction of new faulting around the end of an existing fault is dependent upon the angle between the fault and the principle axes of the tectonic stress. Thus it is possible that the Tejon bend was created by a local (or even regional) variation in the principle tectonic stress direction.

Our interest in this problem is not concerned with the origin of the Tejon bend but with its present importance in the tectonic picture of California. If it is anything more than a surface feature then it must represent an area in which the continent of North America is in direct collision with the Pacific plate. For this to happen the plates must interact throughout the thickness of the plates. Thus the equivalent dislocation for a model of plate collision should extend through the lithosphere. Under these conditions the stress fields at the surface may be strongly affected by either (a) a change in material property across the bottom of the plate (interface between lithosphere and asthenosphere) and/or (b) a change in boundary conditions on the bottom of the plate. For this reason the first section of our study will be focused on the plate bottom effects. It will be shown that the change in boundary condition on the bottom of the plate is the largest of the two plate bottom effects (when earth models consistent with seismic data are used).

Next, three models of the Tejon bend will be presented and evaluated in terms of their resultant strain patterns and principle stress directions. All three of the models are made to follow the Tejon bend but each differs in character below the surface. The first model represents a shallow fault (15 km). The other two represent deep faults and one

of these includes additional boundary conditions on the bottom of the plate. These models will give us an understanding of the strain accumulation around the Tejon bend and will allow us to predict the principle stress directions in remote areas where little or no information is available (e.g. off the coast near Pt. Aguello).

4.5.2 Plate bottom effects

Consider now the model VBAS shown in figure 4.24 (a). It represents a strike-slip fault penetrating an earth model consistent with seismic observations in the Basin and Range province (Herrin, 1972). In figures 4.25-4.27 we compare the displacements for this model with those of a half-space model with elastic parameters equal to those of the second layer in model VBAS. The effects of what we choose to call the plate (top 80 km) in this model are negligible. In the first 200 km away from the fault the U_1 displacement of the layered model in figure 4.25 is sensitive to the top layer (crust). However as we move further away from the fault the layered solutions begin to fall off at the same rate as the half-space solutions. The same behavior may be observed in the U_2 and U_3 displacements shown in figures 4.26 and 4.27 respectively.

In figure 4.24 (b) we show model VBAC which is the equivalent dislocation for a collisional type interaction

between two plates. It is embedded in the same earth model as VBAS. The displacements for this model are compared with a half-space model in figures 4.28-4.30. Generally the results differ by 10% or less (except for the U_3 component at $x_2 = 0$).

From a study of these two models we conclude that the effects of the low velocity zone (asthenosphere) are negligible. Implicit in our conclusion, however, is the assumption that the elastic constants determined by seismic means are close to those of the asthenosphere. This will depend heavily upon the loading rate (plate velocity) and asthenospheric viscosity (Sleep, 1975). Since there have been no observations in California of time dependent deformation of the sort found in Japan which can be associated with the asthenosphere (Nur and Mavko, 1974), we shall assume that the above conclusions are valid. Even if we are incorrect in our assumption and the asthenosphere is extremely soft, those fields parallel to the direction of plate motion (the largest in the near field) will be of the same form as the half-space solutions (see Chapter III). We believe, therefore, that this plate bottom effect is of second order over a period of 100 years or less.

The second plate bottom affect is associated with the additional boundary conditions which may be introduced on the bottom of the plate. These boundary conditions may be due to either the drag or the push of the asthenosphere on the lithosphere. Because of the localized nature (in comparison to the lateral dimensions of plates) of the

internal deformation due to plate motion the author feels that the plates must be driven by the asthenosphere. However, we admit the question of the driving mechanism is still an open one.

In view of the author's personal bias and recent observations (Aki, 1975), we shall discuss the boundary conditions on the bottom of the plate with the implicit assumption that the plates are driven from below. This assumption allows us to specify constant displacements on the bottom of the plate. Far away from the interface between two plates in relative motion this assumption should be a valid one. However, as we approach the interface between the two plates the contrary flows under the plates must be retarded and approach zero at the plate interface. This boundary layer or transition zone will effectively introduce an equivalent dislocation on the bottom of the plates (see figure 4.31). The Burgers' vector for this dislocation should be a maximum near the plate interface (equal to the plate displacement at distances far from the interface). At the far edge of the transition zone the Burgers' vector must fall off to zero. The width of this zone will necessarily be dependent upon the viscosity of the asthenosphere. For a low viscosity asthenosphere the width of the transition should be small (making the material change across the lithosphere-asthenosphere interface more important). For a high viscosity asthenosphere (which we are assuming) the effective width of the transition zone will be significantly larger.

We now model the plate bottom boundary conditions shown in figure 4.3 by assuming a constant Burgers' vector on dislocations coincident with the bottom of the plate and extending approximately a plate thickness away from the interface. This model should be interpreted as an extreme case for the plate bottom effect. In figure 4.32 we compare the strains E_{11}, E_{22} and E_{12} for this model with those of a simple half-space model. It appears that although the two models differ in amplitude that the half-space model is quite representative of the problem even when the boundary conditions on the bottom of the plate are applied over a region comparable to the plate thickness.

Now consider the model of plate collision shown in figure 4.33. We may model this problem with the same dislocation geometry as that shown in figure 4.31. In this case, however, we use a Burgers' vector which is perpendicular to the interface between the two plates. The strains for this model are compared with those of a simple half-space model in figure 4.34.

The E_{22} and E_{12} strains of the two models differ by a small amount. However, over the region of the transition zone (150-375 km in figure 4.34) the component of strain parallel to the Burgers' vector is changed significantly. From this we conclude that in consideration of problems in which plates are in collision that the effects due to the

boundary conditions on the bottom of the plate must be considered. For the strike-slip case, however, we may use half-space models without much loss of information.

4.5.3 Models of the Fort Tejon Bend

At first glance the faulting in the vicinity of the Tejon bend appears extremely complex and impossible to describe with any simple models (figure 4.23). Even the bend itself is not absolutely established. The northern portion of the bend extends northward from Ft. Tejon. In the region of the bend the San Andreas is the youngest of the faults and represents the only throughgoing feature in the Transverse Range Province. South of Cajon Pass, however, the activity of the San Andreas fault seems to have transferred to the San Jacinto fault (Hileman, et al. 1973). We shall follow Rogers and Chinnery (1973) and define the Tejon bend as the San Andreas fault north of Cajon Pass and the San Jacinto fault south of this point.

We may gain a clearer picture of the tectonics in the vicinity of the Tejon bend by considering the tectonic map in figure 4.35. In this figure we have drawn geologically determined displacement directions on various faults (see e.g. Ellsworth, 1973) in the region and the inferred pressure axes for a number of earthquakes. Surprisingly, these data allow us to form a simple consistent picture of

the pressure axes for this region (figure 4.36).

In figure 4.36 the principle compressive stress directions are contoured to be north-south in the vicinity of the Tejon bend. This direction is consistent with the faulting and most of the earthquakes in the region (see figure 4.35). This characteristic north-south compression may also be inferred from recent studies of the geodetic data for this region (Hofmann, 1968; Scholz and Fitch, 1969; Savage and Burford, 1970).

In the northeast corner of figure 4.36 the principle compressive stress axes are drawn in a northeast-southwest direction. This direction is consistent with the observed northwest-southeast extension (Smith and Kind, 1972; Gumper and Scholz, 1971) and the right lateral motion on the north-south trending faults (figure 4.35). It also agrees with the sense of motion of the 1872 Owens Valley earthquake (event I in figure 4.35).

The primary feature to be noted in figure 4.36, therefore, is the approximately 45° degree rotation of the pressure axes from a north-south direction in the immediate vicinity of the bend to a northeast-southwest direction in the area north of the junction of the Sierra-Nevada fault and the Garlock fault. Unfortunately, only a small amount of data exists for the offshore regions of California and we are unable to give a clear presentation of the pressure

axes for this region. The U.S.G.S. is currently undertaking an extensive study of this offshore region (Ellsworth, 1975) and a more complete picture should soon be available. Tentatively, we conclude that the pressure axes are more north-south near the shore and begin a rotation to a north-east-southwest direction further out in the Sanat Barbara Channel (figure 4.36). This rotation is consistent with the more oblique thrust faulting near the shore (on east-west trending faults) changing to left lateral strike-slip faulting out in the Santa Barbara Channel (Hamilton et al., 1969; Lee and Vedder, 1973; Ellsworth et al., 1975).

One of the most important regions necessary for our understanding of the tectonics around the Tejon bend is the offshore region near Point Arguello. Unfortunately, less is known about the earthquakes and faulting in this area than any other region in California. Although the Murray fracture zone (Menard, 1959) lines up offshore with the Santa Ynez fault zone, no connecting fault has been found (Von Huene, 1969). The only large earthquake to be recorded for this area is the 1927 Point Arguello event (M = 7.5) (Byerly, 1930; Richter, 1958). It could be associated with the northeast-southwest trend of activity in this region pointed out by Vrana (1971). We shall describe later why this offshore area (and perhaps the 1927 earthquake) is of primary importance in resolving between the various models

of the Tejon bend. Fortunately a detailed study of the 1927 event is currently being made (Gordon Stewart, personal communication, 1975).

Consider now the shallow fault model (Tejon 1) of the Tejon bend shown in figure 4.37. It represents a modified version of the dislocation model for this region presented by Rogers and Chinnery (1973). The primary modification consists in the Burgers' vector. Their model is made up of shear dislocations while ours includes the component of plate motion perpendicular to the fault. The strains (E_{11}, E_{22}, E_{12}), the maximum shear stress and the sum of the stresses τ_{kk} (sum over k) are contoured in figures 4.38-4.42. In figure 4.43 the principle stress directions for Tejon 1 are plotted. The components of strains plotted (for all models) are computed in a coordinate system in which the positive x_2 axis points N45°W and the positive x_1 axis points N45°E. With this coordinate system the E_{11} strains represent compression (-) or extension (+) perpendicular to faults which are oriented N45°W, the E_{22} strains represent compression or extension perpendicular to faults oriented N45°E, and a negative E_{12} strain will be associated with a right lateral strain accumulation on a fault oriented N45°W.

The primary point to be observed in the E_{11} and E_{22} strains (figures 4.38 and 4.39) is the compression in the vicinity of the bend. The compression, however, turns to

extension along the northern leg of the model. The E_{12} strains shows little character and simply follows the fault (figure 4.40).

In figure 4.41 and 4.42 we have plotted the maximum shear stress and the sum of the stresses τ_{kk} for model Tejon 1.

As expected for such a shallow fault model the maximum shear stress is concentrated primarily on the fault. We argue against the shallow Tejon 1 model for this reason. Hoffmann (1968) has deduced from the geodetic data that the strain accumulation in the vicinity of the Tejon bend is of a regional character (north-south compression) and does not seem to be associated with any one fault in the area. We believe this eliminates the shallow Tejon 1 model. Following Rogers and Chinnery (1973) we have also plotted the sum of the stresses (τ_{kk}). They have interpreted regions of negative τ_{kk} (compression) and/or low maximum shear stress as regions less likely to have future seismic activity. With this interpretation applied to the Tejon 1 model the northern leg of our model is the most likely region for activity.

In figure 4.43 we have plotted the principle stress directions for model Tejon 1. Straight lines represent compression and lines with balls at the end represent extension. These results should be compared to those of figure 4.36 in which we have plotted the principal compressive stress direction inferred from geodetic, geologic,

and seismic data. The agreement with the rotation of the pressure axes in the northeast portion of the map is not very satisfactory although there is some rotation in the northeast corner of the map shown in figure 4.43. On the northern and southern legs of the bend the north-south compression (with east-west extension) is in excellent agreement with the inferred principal stress. However, near the intersection of the Garlock and San Andreas faults (see fault map in figure 4.23) the principal stresses rotate to a northwest-southeast orientation. This orientation is not in agreement with those inferred in figure 4.36 or with geodetic observations for this area (Hofmann, 1968; Scholz and Fitch, 1969).

In the southern region of the principal stress map both principal stresses are compressive (off the coast of southern California). Off the coast of Point Arguel on the eastern side of the principal stress map both principal stresses are tensional. These features will be apparent in all the Tejon bend models and represent an important predictive test of our models which will be discussed later.

For now we conclude on the basis of (1) the localized nature of a shallow fault and (2) the misalignment of the principal stress directions that the model Tejon 1 is not a satisfactory one. It does, however, exhibit some of the principal stress characteristics of the subsequent models

to be studied indicating that the geometry of the bend plays an important role in the tectonics of the neighboring region.

Now consider model Tejon 2 shown in figure 4.44. It is a model of the interaction throughout the thickness of the plate (80 km). In this case, however, we neglect the addition of possible boundary conditions on the bottom of the plate.

The strains and stresses for Tejon 2 are shown in figures 4.45-4.50. The primary features to be noted in the E_{11} and E_{22} strains are the large neighboring lobes which subject the region to short wavelength variations. The shear strains (figure 4.47), however, are relatively smooth and have a broad regional effect as would be expected for a deep fault model. The lobes for the E_{11} and E_{22} strains are a result of the rapid increase of the depth of locking in the vicinity of the bend.

It is surprising at first to find that the Tejon bend represents the region of the lowest maximum shear stress accumulation on the San Andreas (figure 4.48). This is effectively a feature of the depth to which the plates are interacting. This lower rate of shear stress accumulation spread over a larger region is most likely responsible for the general tectonic behavior in this region.

In figure 4.49 the sum of the stresses for model Tejon 2 are plotted. The regions most likely for fracture (Rogers and Chinnery, 1973) are the areas of tension (positive τ_{kk}). This implies that likely areas of high activity for this model are the eastern edge of the Mojave desert, the northern leg of the San Andreas, and the area near the intersection of the White Wolf and San Andreas faults (in the general vicinity of the Kern County earthquake of 1952). North and South of the bend, however, are regions of compressive stresses. The compressive stresses on the southern leg of the San Andreas and the tensional stresses on the northern leg of the Tejon bend can be explained by the different orientations of these legs with respect to the direction of relative motion assumed for the plates (Pacific plate moves N45°W) with respect to North America. The northern leg of the San Andreas strikes N40°W while the San Jacinto fault in southern California strikes N45°W.

The principal stress directions for Tejon 2 are plotted in figure 4.50. The agreement with the inferred principal stress directions in figure 4.36 is as good as could be expected from such a simple model. The desirable features of this model are (1) the rotation of the pressure axes in the northeast portion of the map (2) the near north-south compressive axis throughout much of the vicinity of the bend,

(3) north-south compression on the northern and southern legs of the San Andreas fault zone and (4) a rotation of the pressure axes from north-south near Pt. Mugu (Ellsworth et al., 1973) to a northeast-southwest position further out in the Santa Barbara Channel (Lee and Vedder, 1973; Hamilton et al., 1969).

Again, as for model Tejon 1, the pressure axes further out in the Santa Barbara channel and off the coast of Point Arguello become tensional. The reality of this effect cannot be checked here because of the apparent lack of interest in this region in the past.

Now consider model Tejon 3 in figure 4.51 in which additional boundary conditions are added to the bottom of the plate. We do not pretend to know what these conditions are in reality, but include a possible example in order to examine the kinds of changes that take place when these effects are included. The strains and stresses for model Tejon 3 are shown in figures 4.52-4.57.

In figure 4.52 we see that the only major change due to the plate bottom boundary conditions is a shift to the east of the northernmost negative lobe (from the southern portion of the Sierra Nevada fault to the Great Valley-Carrizo plain area). Otherwise the only effect is a general broadening of the features present in model Tejon 2.

In figure 4.53, the E_{22} strains for Tejon 3 show only slight changes from those for Tejon 2. One significant difference exists however in the small negative lobe extending off the coast around the end of the Santa Ynez fault. Probably associated with this lobe is the lobe of left lateral strain (positive E_{12}) in figure 4.54.

The maximum shear stress contours (figure 4.55) show the least change of all the fields studied. The sum of the stresses τ_{kk} plotted in figure 4.56 show a southward displacement of the region of positive τ_{kk} which was over the area of the Kern County earthquake for model Tejon 2.

The principal stress directions (figure 4.57) for model Tejon 3 show distinct differences from those of Tejon 2. In the vicinity of the bend the principle compressive axis rotates from the north-south direction of Tejon 2 to a position more in line with the San Andreas fault. The most important change, however, occurs along the Sierra-Nevada fault where the northwest-southeast tension in model Tejon 2 is replaced by a northwest-southeast compression. This is definitely in disagreement with the observations presented in figure 4.36. For this reason the Tejon 3 model may be eliminated as a satisfactory model of the Tejon bend.

4.5.4 Discussion

In summary we have made a study of Tejon bend models in which the depth of fault penetration and plate bottom boundary conditions could be important. We find that the effect of the plate interface is the most important feature of such models and that the fields of this feature can be adequately described by half-space models. However, localized regions can undergo large changes in strain pattern when the boundary conditions on the bottom of the plate are considered and this should be kept in mind during future studies of the Tejon bend.

The success of model Tejon 2 in matching the main features of the principle stress field lead us to believe that the Tejon bend really represents an effective interface between the continent of North America and the Pacific plate. The real test of our model, however, lies in the prediction of a region of tension off of Point Arguello. This region does have dip-slip events of either the thrust or normal type (since Tsumanis have been generated by many of them (e.g. 1812 Santa Barbara, (Richter, 1953); 1927 Point Arguello (Byerly, 1930)). Fortunately, the U.S.G.S. is currently interested in this offshore region and our predictions can be tested. If the predicted region of tension is not observed we may conclude that either (a) the Pacific moves in a more northerly direction with respect to North America

than the N45°W direction used in our Tejon models or (b) the Tejon bend is not the primary cause of the tectonics of the offshore region. In either case this region is important in the tectonic scheme of California and deserves further study.

Figure 4.23

Fault map of the Tejon bend region and some of the major faults in the area. Points of common reference in the text are Tejon Pass (near the intersection of the Garlock and San Andreas faults), Cajon Pass (at the intersection of the San Andreas with the San Jacinto fault), and Point Arguello (the point on the coast toward which the Santa Ynez fault is aligned).

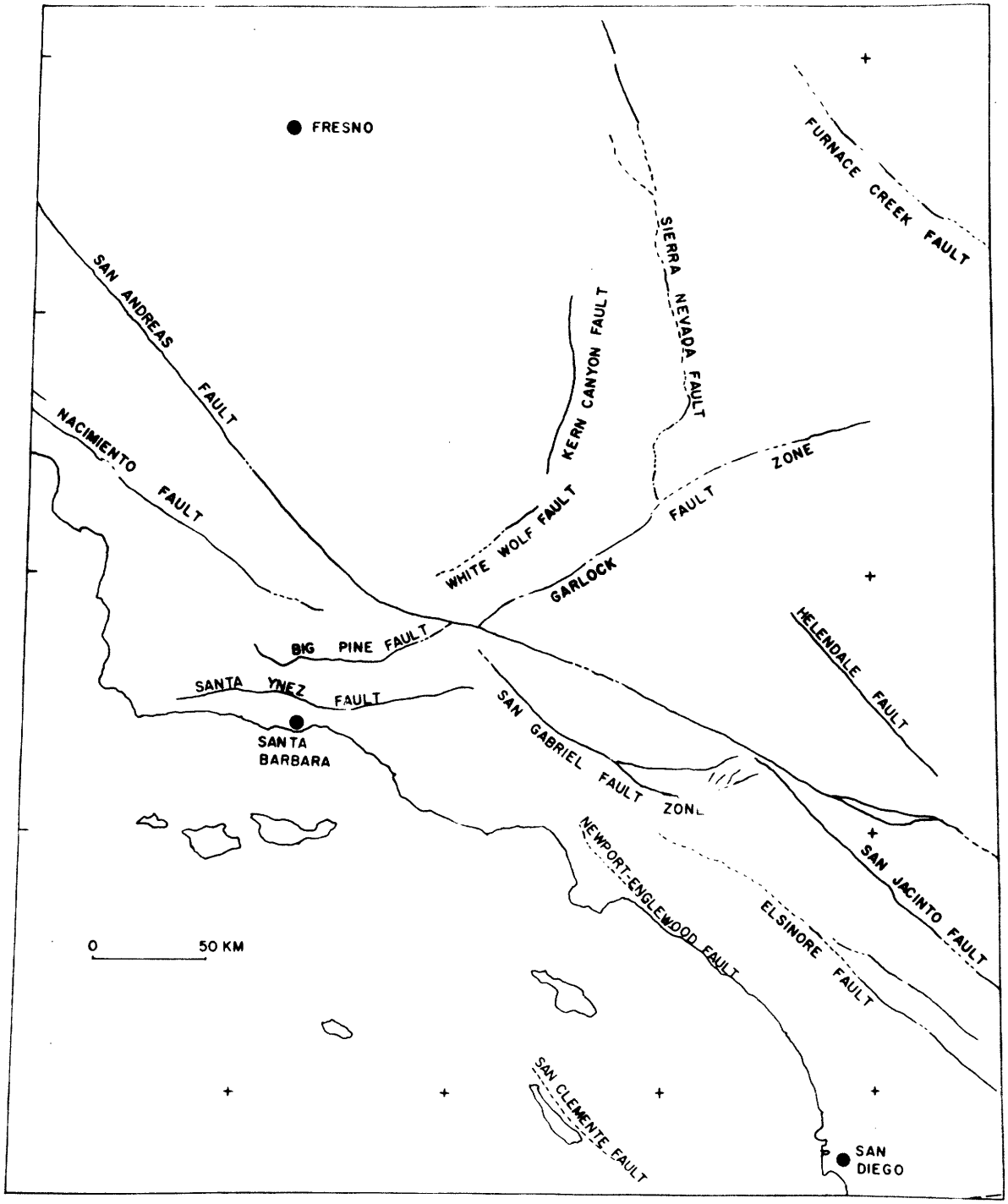
FRESNO
SAN ANDREAS FAULT
NACIMIENTO FAULT
KERN CANYON FAULT
SIERRA NEVADA FAULT
FURNACE CREEK FAULT
WHITE WOLF FAULT
GARLOCK FAULT ZONE
BIG PINE FAULT
SANTA YNEZ FAULT
SANTA BARBARA
HELENDALE FAULT
SAN GABRIEL FAULT ZONE
NEWPORT-ENGLEWOOD FAULT
ELSINORE FAULT
SAN JACINTO FAULT
0 50 KM
SAN CLEMENTE FAULT
SAN DIEGO

Figure 4.23

Figure 4.24

(a) Model VBAS - a vertical strike-slip fault embedded in a Basins and Range type structure (Herrin, 1972). The elastic constants λ and μ are given in dynes/cm^2 x 10^{11} and the layer thicknesses are in kilometers. The fault is 25 km deep, 260 km long, and 70 km wide. The Burgers' vector for this model is $\vec{B}$ = (0, 1, 0). The solutions are obtained by the FSM using a 128 x 128 grid, ΔX_1 = 25, ΔX_2 = 40 kilometers.

(b) Model VBAC - a vertical collisional fault in the Basins and Range like structure described in 4.24 (a). The fault is 25 km deep, 120 km long, and 70 km wide. The Burgers' vector is $\vec{B}$ = (1, 0, 0). A 128 x 128 grid was used with sample sizes of ΔX_1 = 25 and ΔX_2 = 20 kilometers.

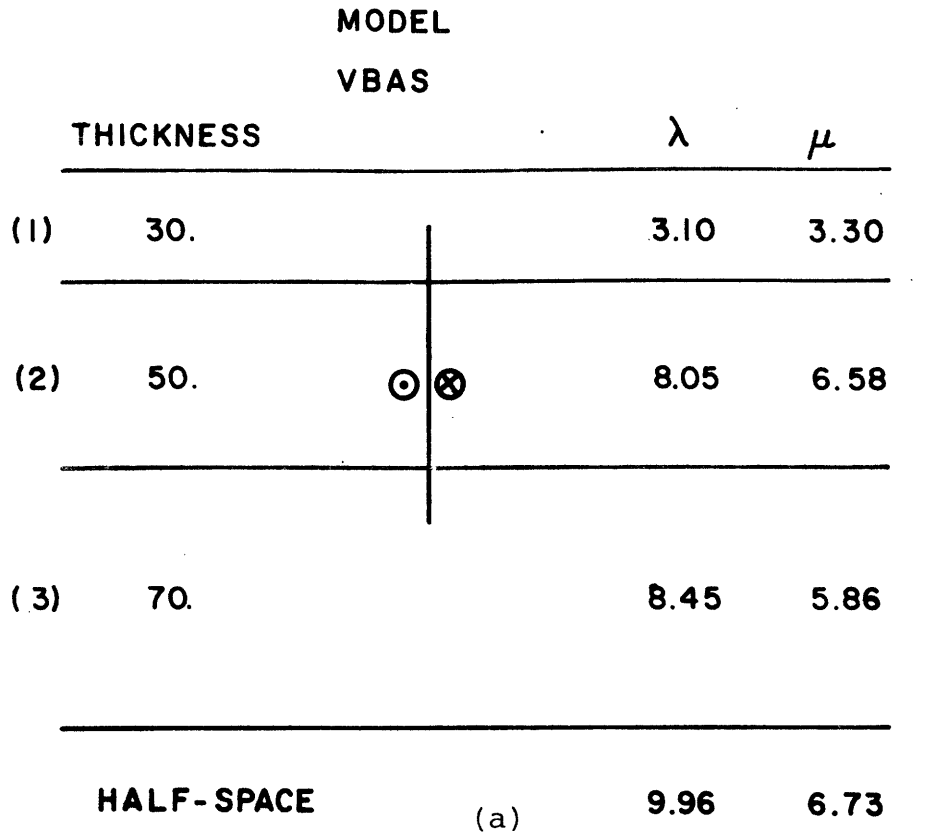

(a)

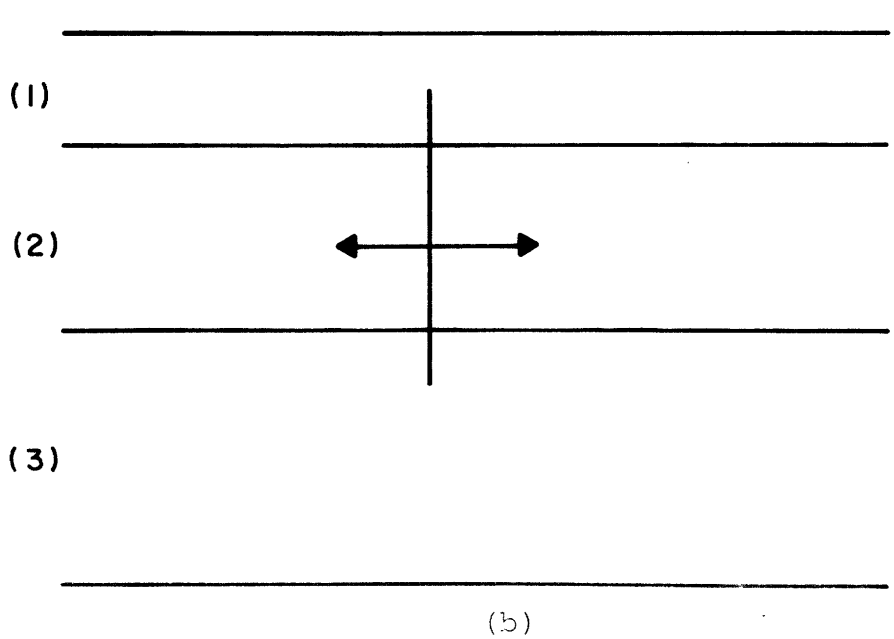

(b)

Figure 4.24

Figures 4.25-4.27

Profiles of the displacements (at x_2 = 160 km) for model VBAS (□). The solutions are compared to those of a half-space model (x) with elastic properties equal to those of the second layer in model VBAS.

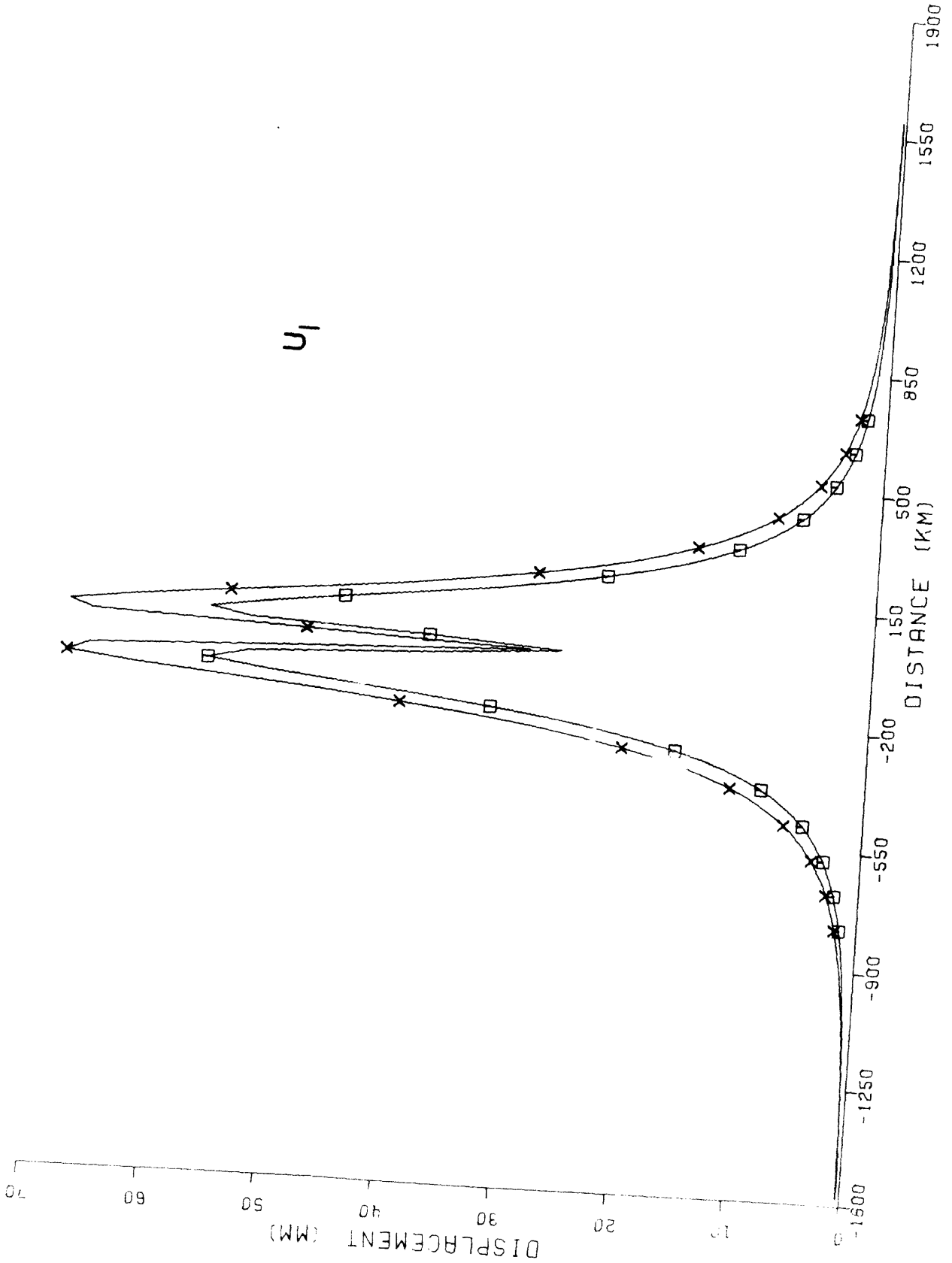
DISTANCE (KM)
1900
1550
1200
850
500
150
-200
-550
-900
-1250
-1600
DISPLACEMENT (MM)
0
10
20
30
40
50
60
70

Figure 4.25

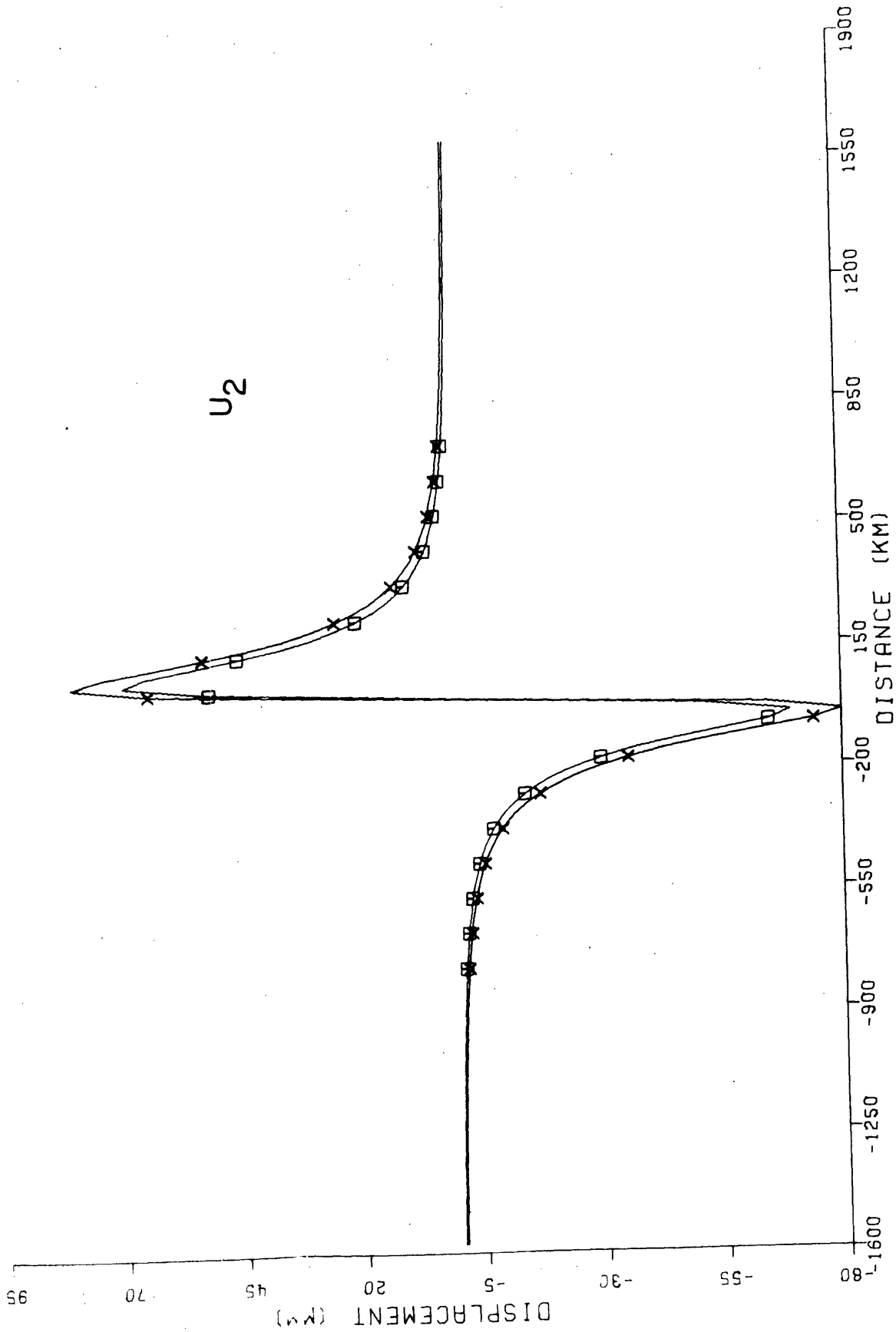
U_2
DISTANCE (KM)
1900
1550
1200
850
500
150
-200
-550
-900
-1250
-1600
DISPLACEMENT (M)
95
70
45
20
-5
-30
-55
-80

Figure 4.26

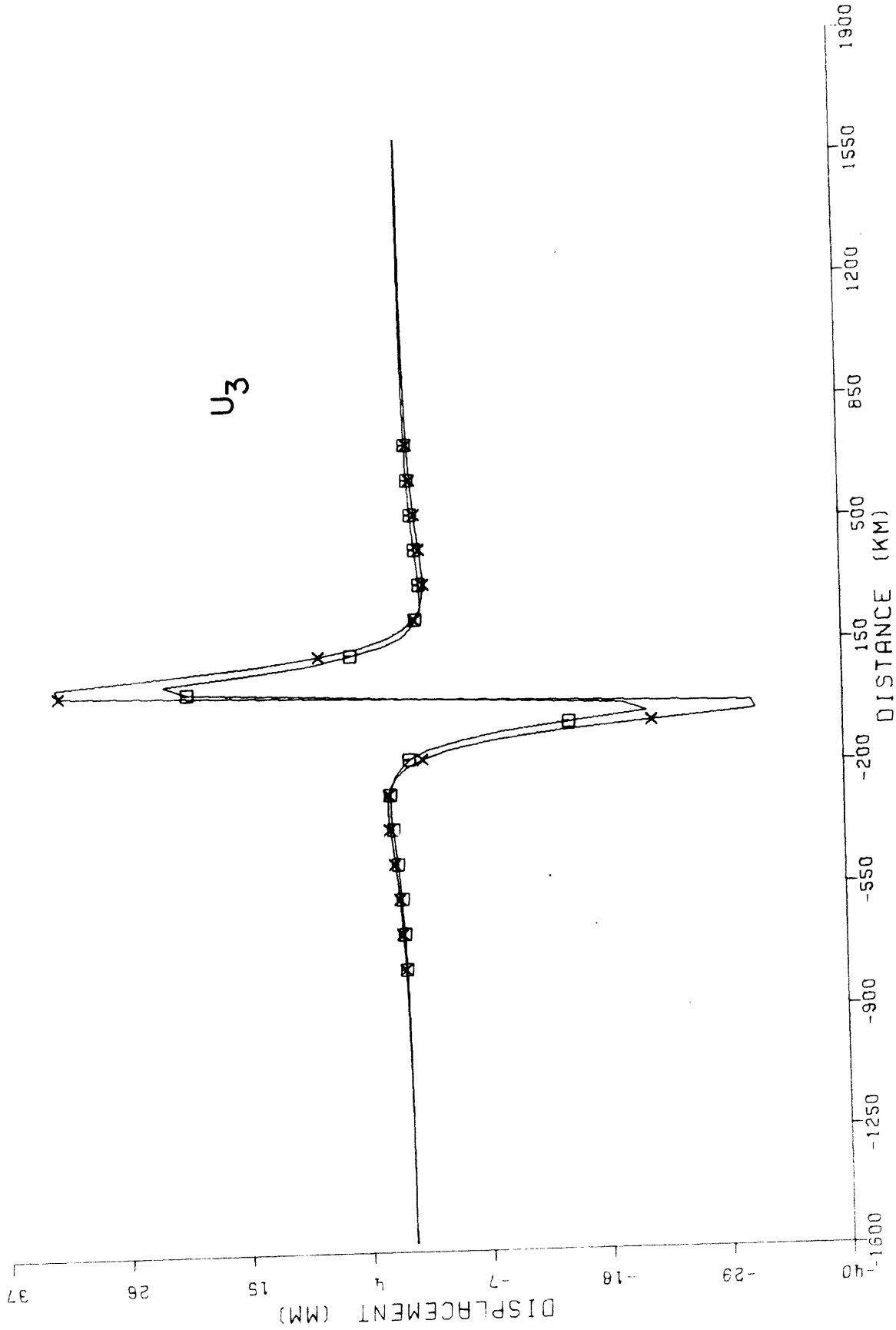
U_3
DISPLACEMENT (MM)
37
26
15
4
-7
-18
-29
-40
DISTANCE (KM)
1900
1550
1200
850
500
150
-200
-550
-900
-1250
-1600

Figure 4.27

Figures 4.28-4.30

A comparison of the displacements of model VBAC (□) to those of a half-space (X) with elastic parameters equal to those of the second layer of VBAS (figure 4.24 (a)). The profiles are taken at x_2 = 15 km.

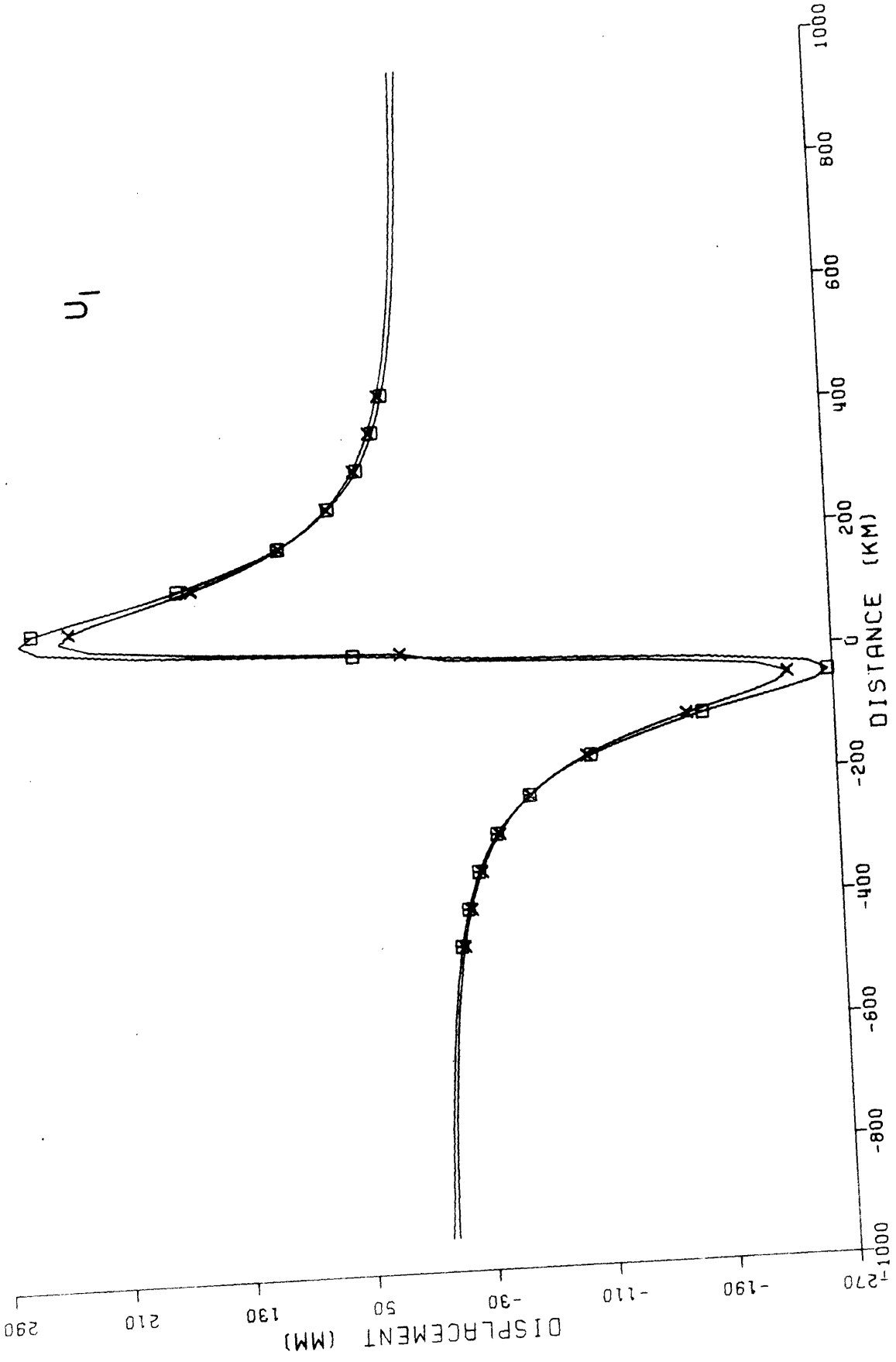
U1
DISPLACEMENT (MM)
290
210
130
50
-30
-110
-190
-270
DISTANCE (KM)
1000
800
600
400
200
0
-200
-400
-600
-800
-1000

Figure 4.28

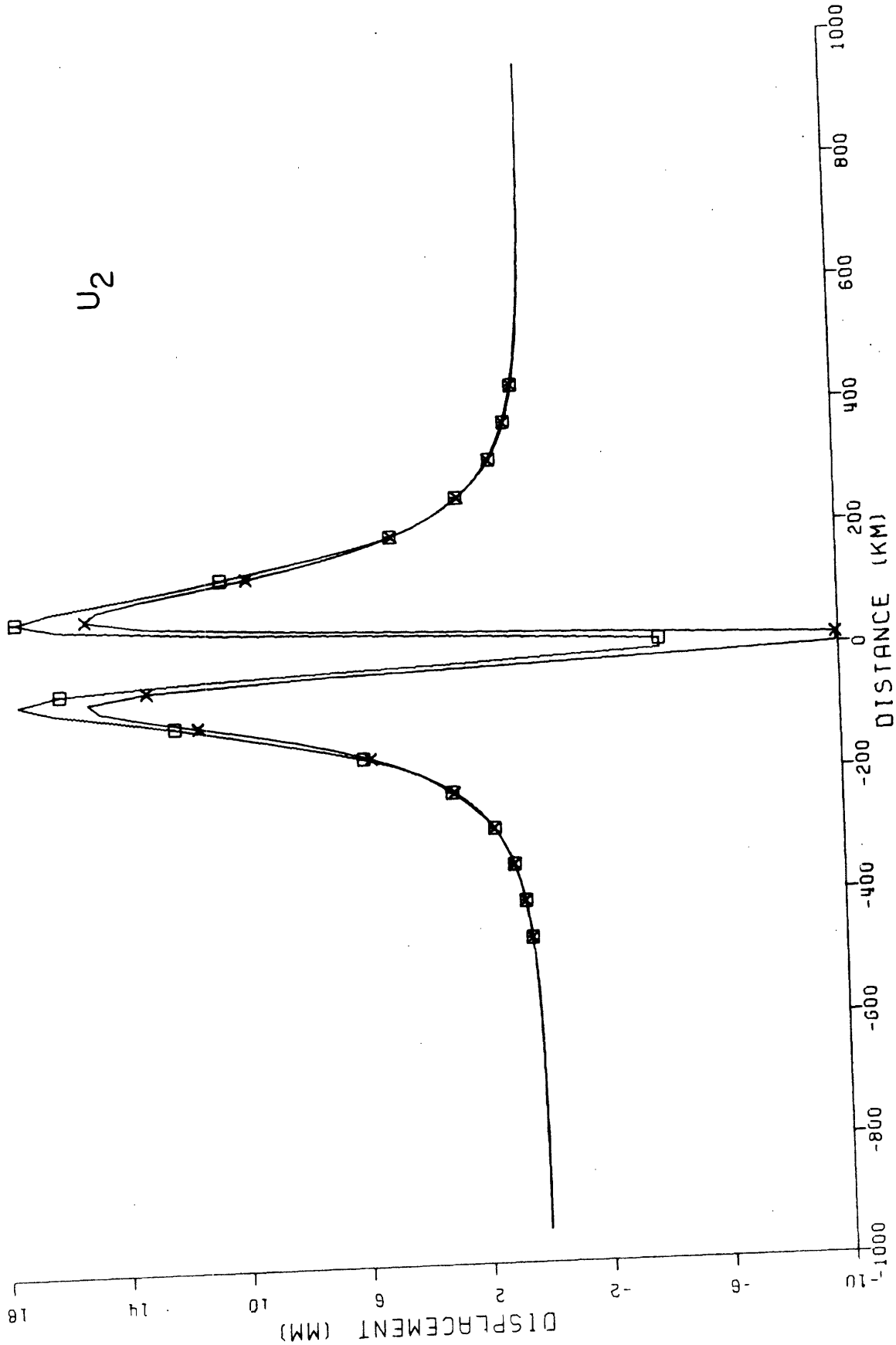
U_2
DISPLACEMENT (MM)
18
14
10
6
2
-2
-6
-10
DISTANCE (KM)
1000
800
600
400
200
0
-200
-400
-600
-800
-1000

Figure 4.29

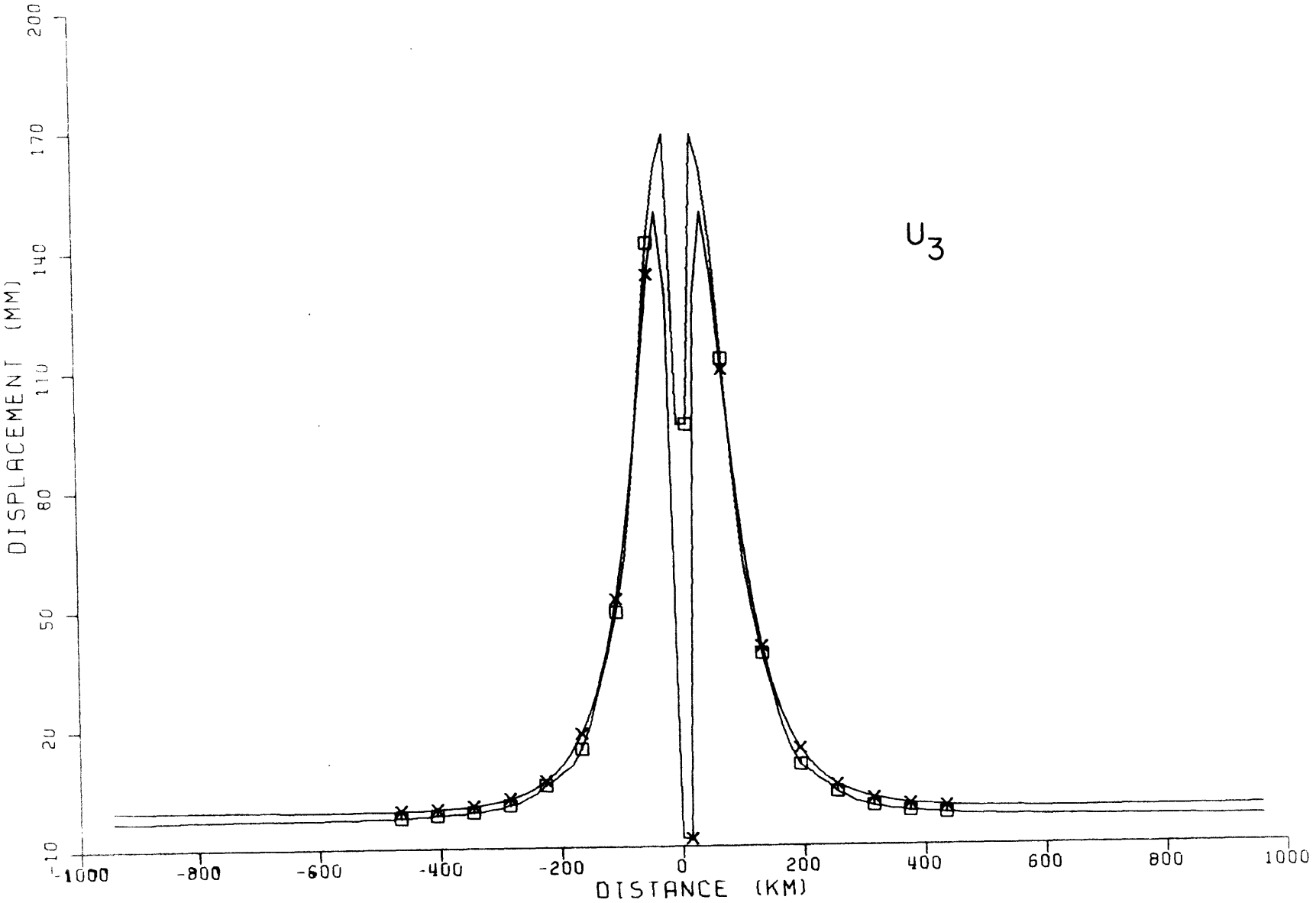
DISPLACEMENT (MM)
200
170
140
110
80
50
20
-10
-1000
-800
-600
-400
-200
0
200
400
600
800
1000
DISTANCE (KM)
U3

Figure 4.30

Figure 4.31

A schematic of displacement boundary conditions on lithospheric plates. The large open arrows indicate the direction of plate motion. On the bottom of the plate the boundary conditions are constant (equal to open arrows) until the counter flows near the interface begin to slow down reducing the effective displacements on the bottom of the plate near the interface. The equivalent dislocation motions (smaller dark arrows) which result are shown in the shaded region.

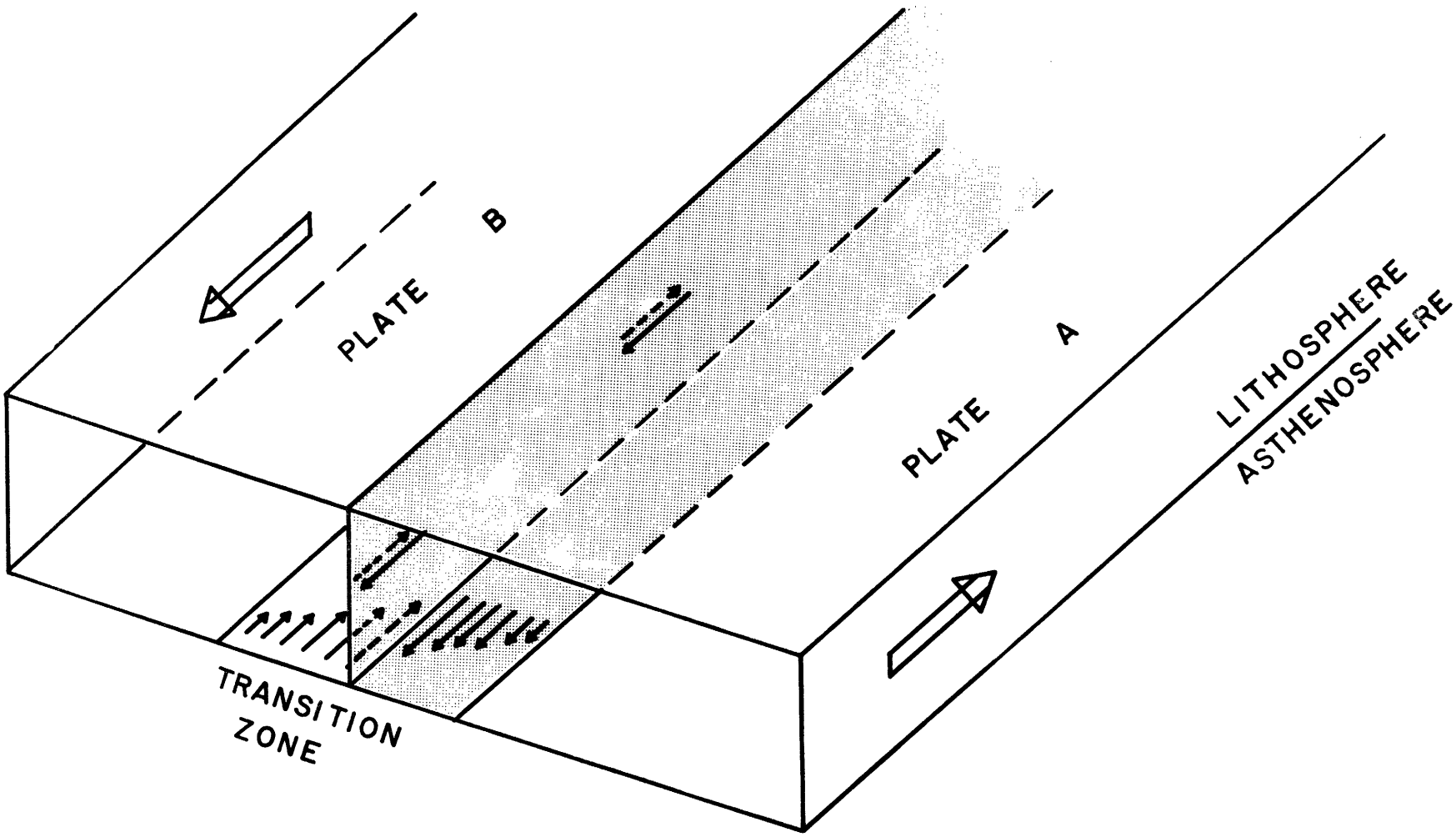
PLATE B
PLATE A
LITHOSPHERE
ASTHENOSPHERE
TRANSITION ZONE

Figure 4.31

Figure 4.32

Strain profiles for a model of the type shown in figure 4.31. The elastic parameters are λ = 8.05 E11 dynes/cm^2 and μ = 6.58 E11 dynes/cm^2. The profile is taken from point A (latitude = 36°N, longitude = 122°W) to point B (36°N, 116°W). The point A corresponds to 0 km and point B to 550 km on the profile shown.

Three dislocations are used to construct the model. The corners of the dislocations are:

	Latitude	Longitude	Depth (km)
1st dislocation			
	37°	119°	0
	34°	119°	0
	34°	119°	80
	37°	119°	80
2nd dislocation			
	37°	119.5°	80
	37	119.0°	80
	34	119.0°	80
	34	119.5	80

	Latitude	Longitude	Depth (km)
3rd dislocation			
	37	118.5	80
	37	119.0	80
	34	119.0	80
	34	118.5	80

The Burgers' vector components are $B_r = 1$, $B_\phi = 0°$, $B_z = 0$. The X's are placed on the solution for the first dislocation only while the ◘'s are placed on the sum of the three dislocations.

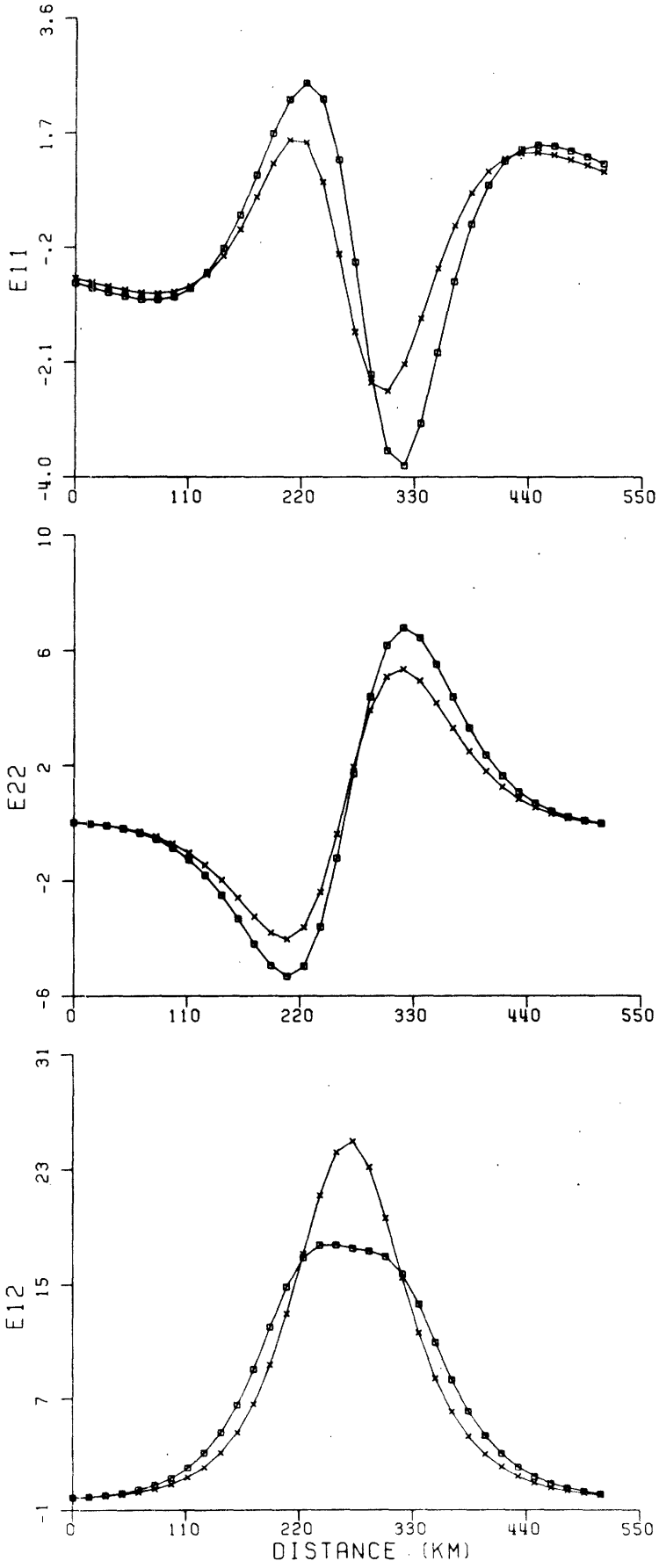
E11
3.6
1.7
-.2
-2.1
-4.0
0
110
220
330
440
550
E22
10
6
2
-2
-6
0
110
220
330
440
550
E12
31
23
15
7
-1
0
110
220
330
440
550
DISTANCE (KM)

Figure 4.32

Figure 4.33

Schematic diagram of plates in collision. The large open arrows indicate the sense of motion for plates A and B. The dark arrows represent the equivalent dislocation vectors for the model. On the bottom of the plate the Burgers' vector of the equivalent dislocation is non-zero over the transition zone beneath the plates. This effect will be approximated in the following figure by a constant dislocation over a distance comparable to the plate thickness.

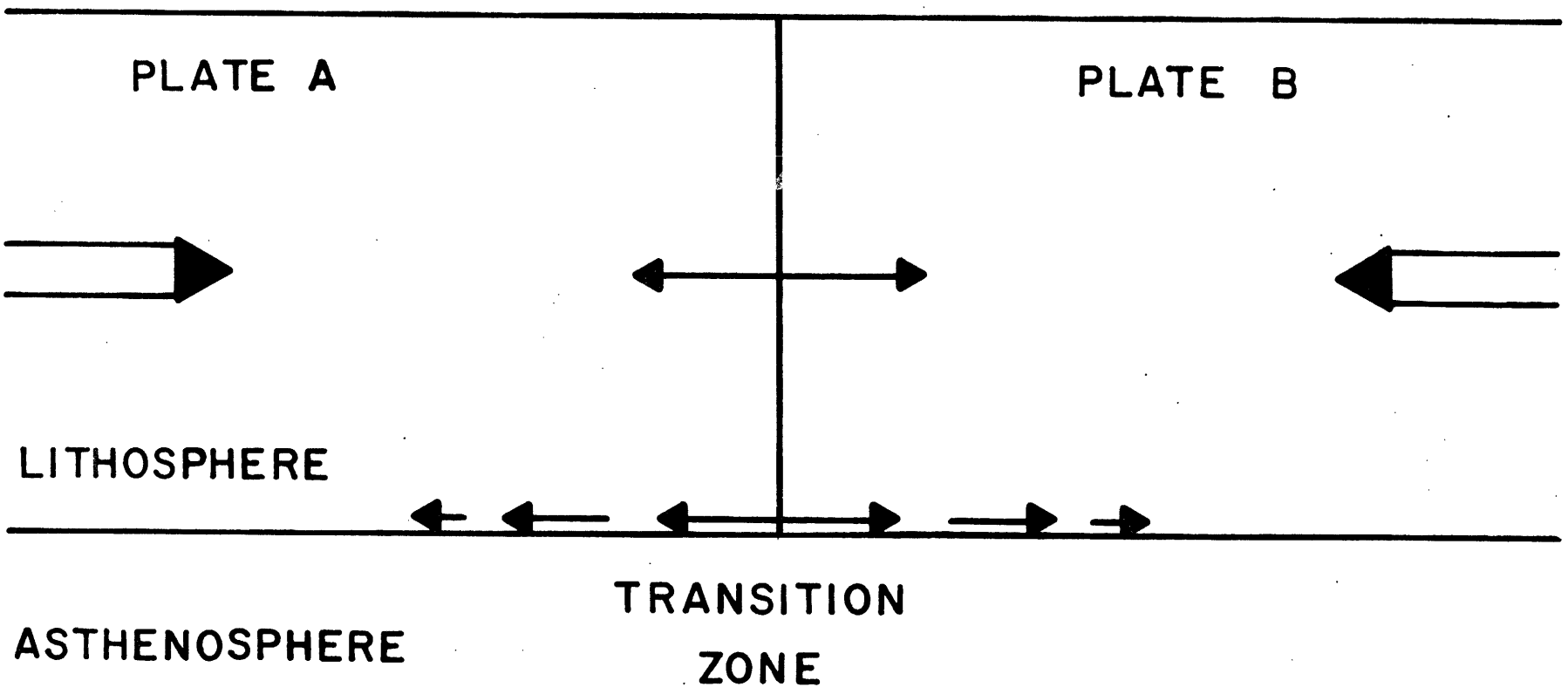
PLATE A
PLATE B
LITHOSPHERE
ASTHENOSPHERE
TRANSITION
ZONE

Figure 4.33

Figure 4.34

Strain profiles for model shown in figure 4.33. The dislocation and profile parameters are the same as those in figure 4.32. The Burgers' vector, however, is perpendicular to the fault ($B_r = 1$, $B_\phi = -90$, $B_z = 0$).

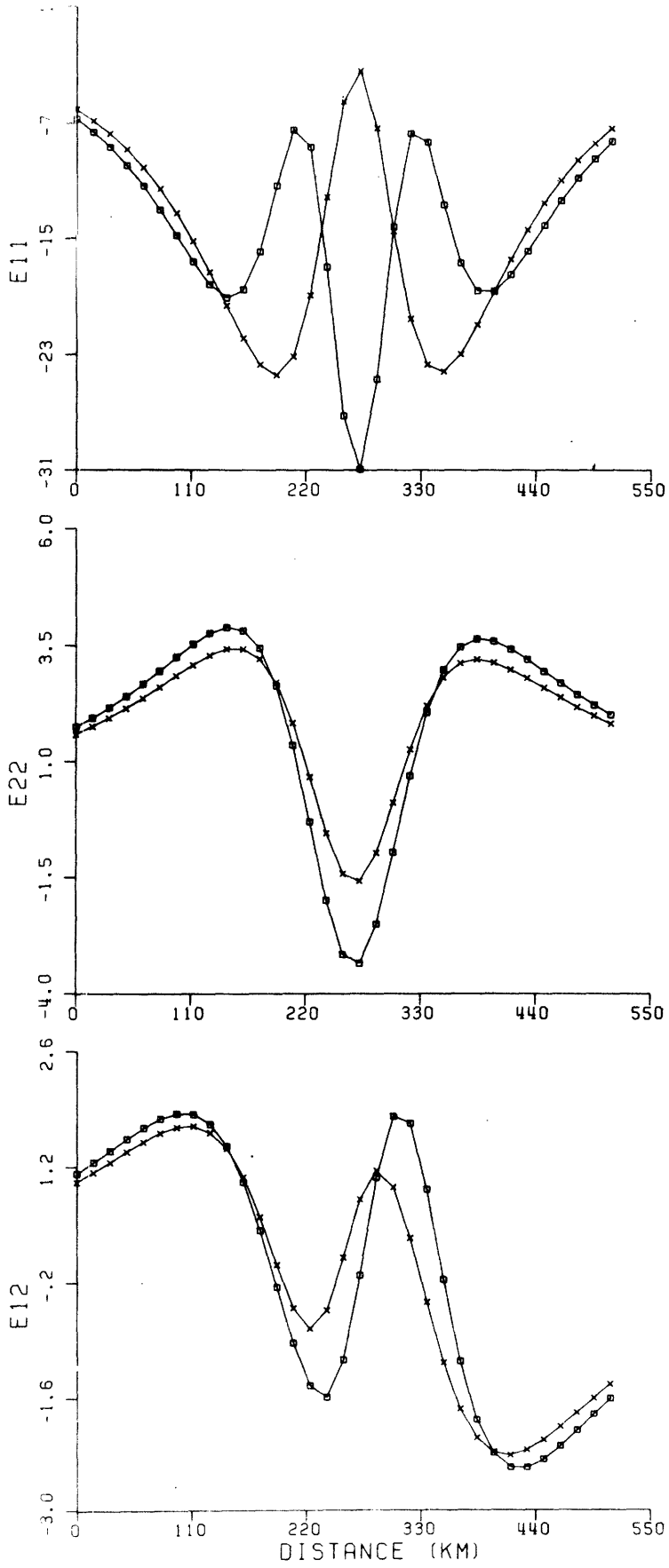
E11
-7
-15
-23
-31
0
110
220
330
440
550
E22
6.0
3.5
1.0
-1.5
-4.0
0
110
220
330
440
550
E12
2.6
1.2
-.2
-1.6
-3.0
0
110
220
330
440
550
DISTANCE (KM)

Figure 4.34

Figure 4.35

Tectonic map of the Tejon bend region. Arrows on faults indicate sense of inferred motion (see e.g. Ellsworth, 1973). Thrust faults and their direction of dip are indicated by faults with dark triangles pointing in the direction of the dip. The principal stress directions inferred from earthquakes are denoted by circles with a bar through them indicating the direction of the principal compressive stress. Events A through F represent smaller ($M \leq 6$) events studied by Hamilton et al. (1973), Lee and Vedder (1973), and Ellsworth et al. (1974). Event G represents the San Fernando (1971) earthquake (see e.g. Cannitez and Toksöz (1971)). We have considered this event inconsistent with the regional trend. It is, however, consistent with the local geology. Event H is the 1952 Kern County earthquake and event I is the 1872 Owens Valley earthquake (Hileman et al., 1972).

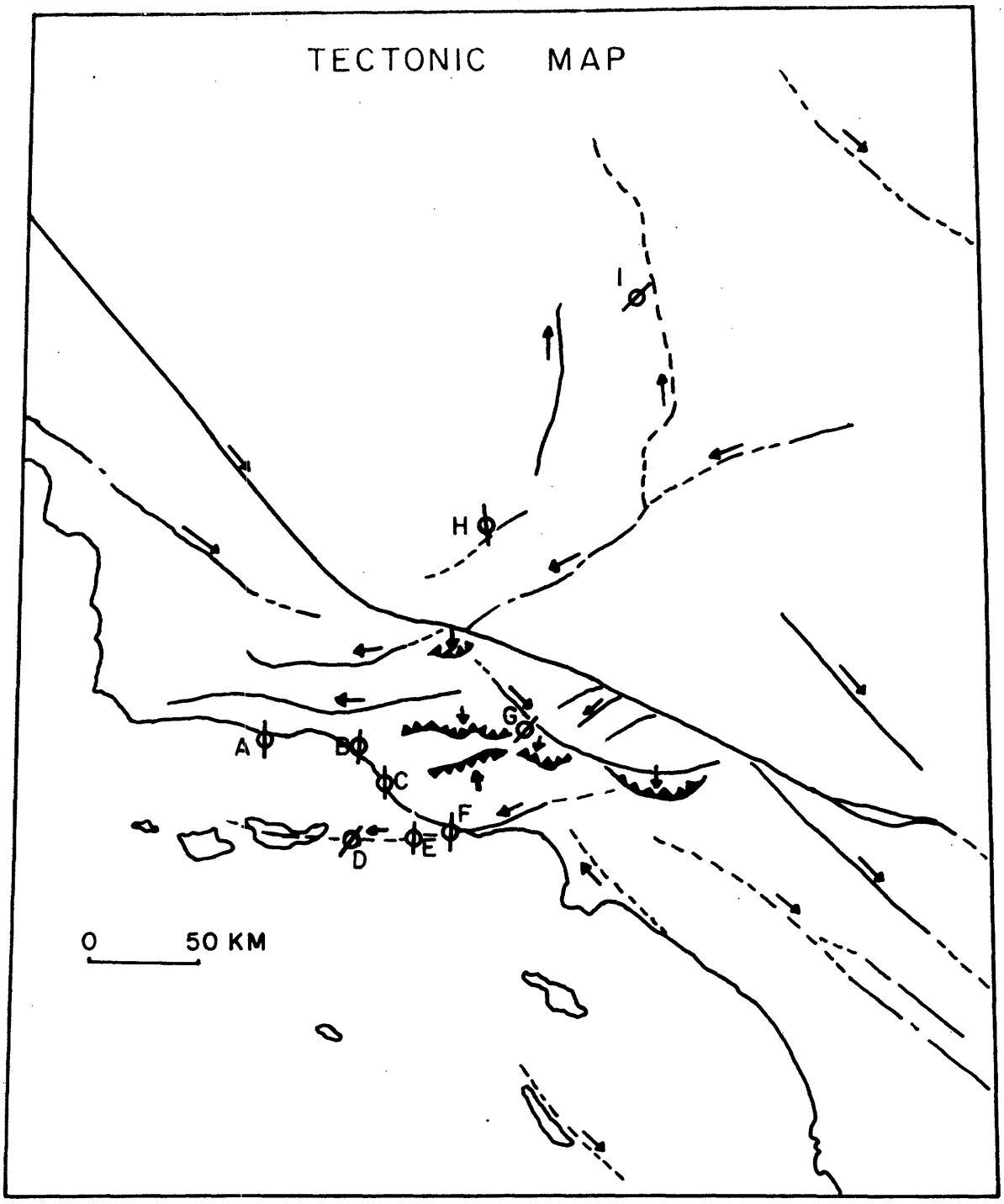

Figure 4.35

Figure 4.36

Contours of directions of principal compressive stress inferred for southern California from seismic (see figure 4.36) and geodetic data (Hofmann, 1968; Scholz and Fitch, 1969; Savage and Burford, 1970). A more detailed description of how these directions are obtained may be found in section 4.4.3.

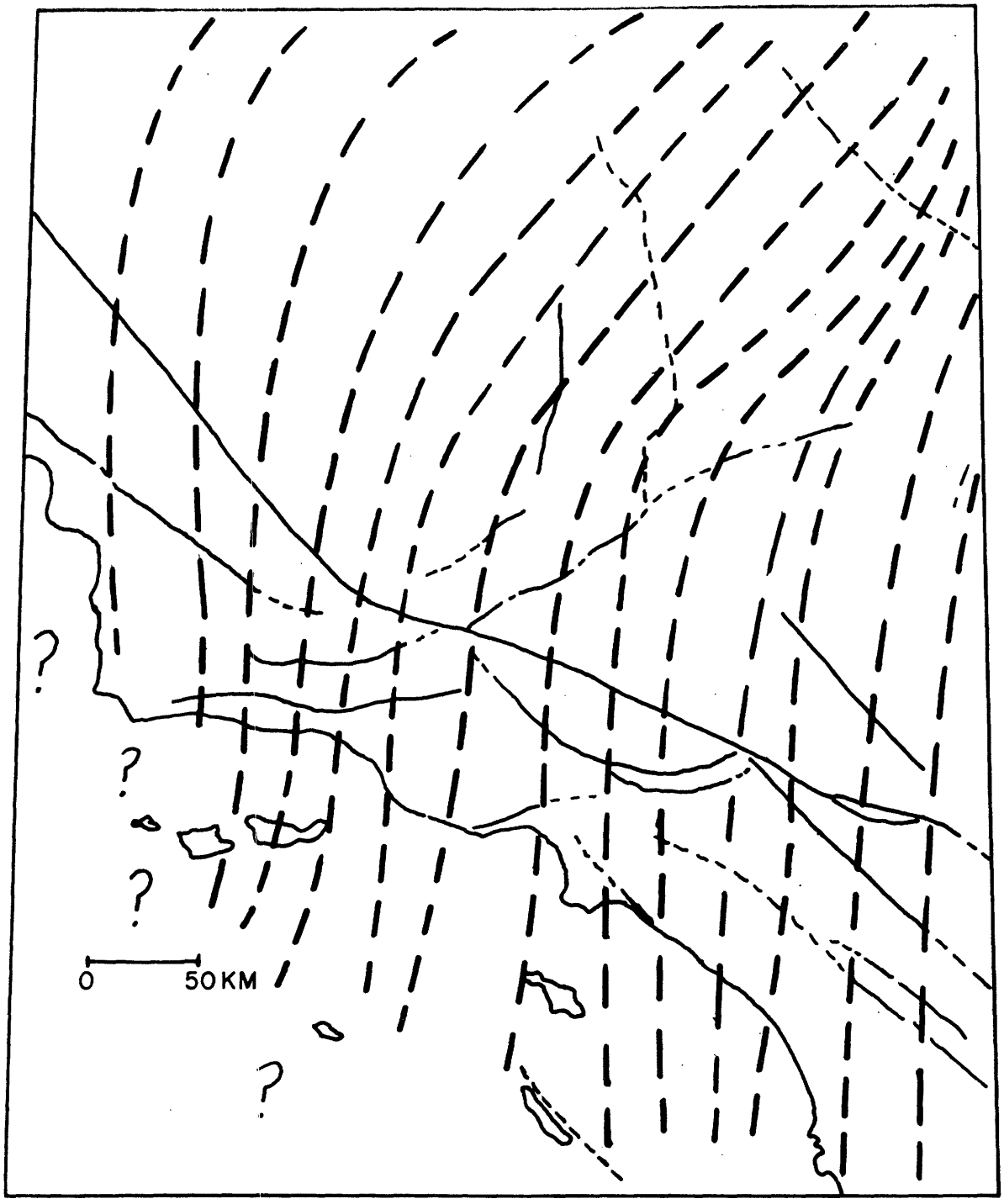

Figure 4.36

Figure 4.37

Schematic view of model Tejon 1. The corners of the dislocation are chosen to follow the profile of the San Andreas in the north and the San Jacinto in the south. Dark areas represent the locked portion of the fault. The corner positions for Tejon 1 are:

Corner	Latitude	Longitude	Depth (km)
1	39.00	124.00	0
2	35.23	119.64	0
3	35.00	119.46	0
4	34.94	119.27	0
5	34.90	119.23	0
6	34.76	118.55	0
7	34.64	118.23	0
8	34.17	117.34	0
9	32.69	11[illegible].00	0
10	32.69	115.00	5
11	34.17	117.34	10
12	34.27	117.45	15
13	34.64	118.23	15
14	34.76	118.55	15
15	34.90	119.23	15
16	34.94	119.27	15

Figure 4.37 (cont'd)

Corner	Latitude	Longitude	Depth (km)
17	35.00	119.46	15
18	35.23	119.64	10
19	35.23	119.64	10
20	35.90	120.40	10
21	35.90	120.40	5
22	39.00	124.00	5.0

$B_r = 1$, $B_\phi = 145°$, $B_z = 0$

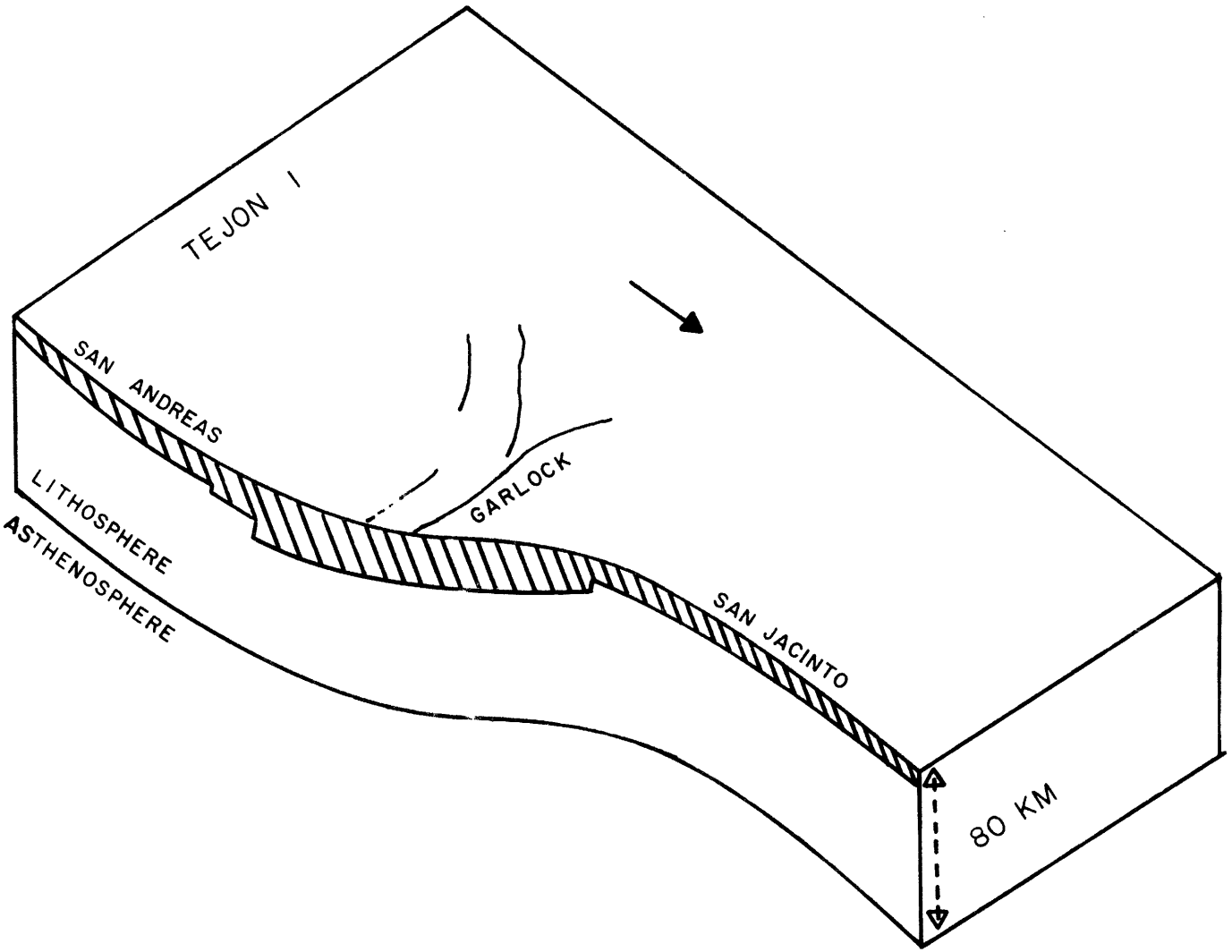
TEJON
SAN ANDREAS
GARLOCK
LITHOSPHERE
ASTHENOSPHERE
SAN JACINTO
80 KM

Figure 4.37

Figures 4.38-4.43

Strains ($X10^{+7}$) stresses (bars), and principal stress directions for model Tejon 1 in figure 4.37. τ_{kk} represents the trace of the stress matrix τ_{ij} (i.e. $\tau_{kk} = \tau_{11} + \tau_{22} + \tau_{33}$).

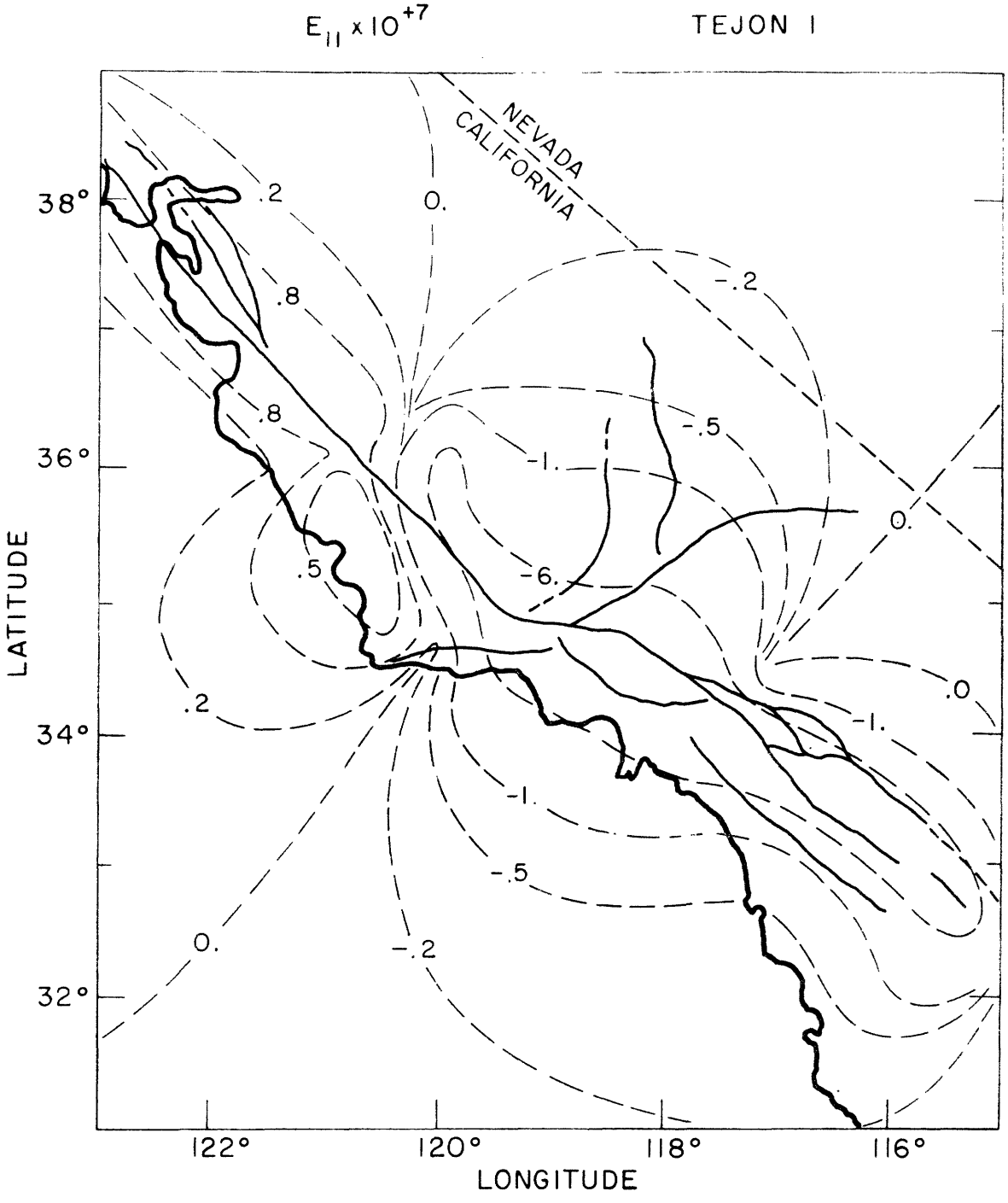
$E_{11} \times 10^{+7}$
TEJON I
NEVADA
CALIFORNIA
38°
36°
34°
32°
LATITUDE
122°
120°
118°
116°
LONGITUDE
.2
0.
.8
.8
-.2
-.5
-1.
-6.
0.
.5
.2
.0
-1.
-1.
-.5
0.
-.2

Figure 4.38

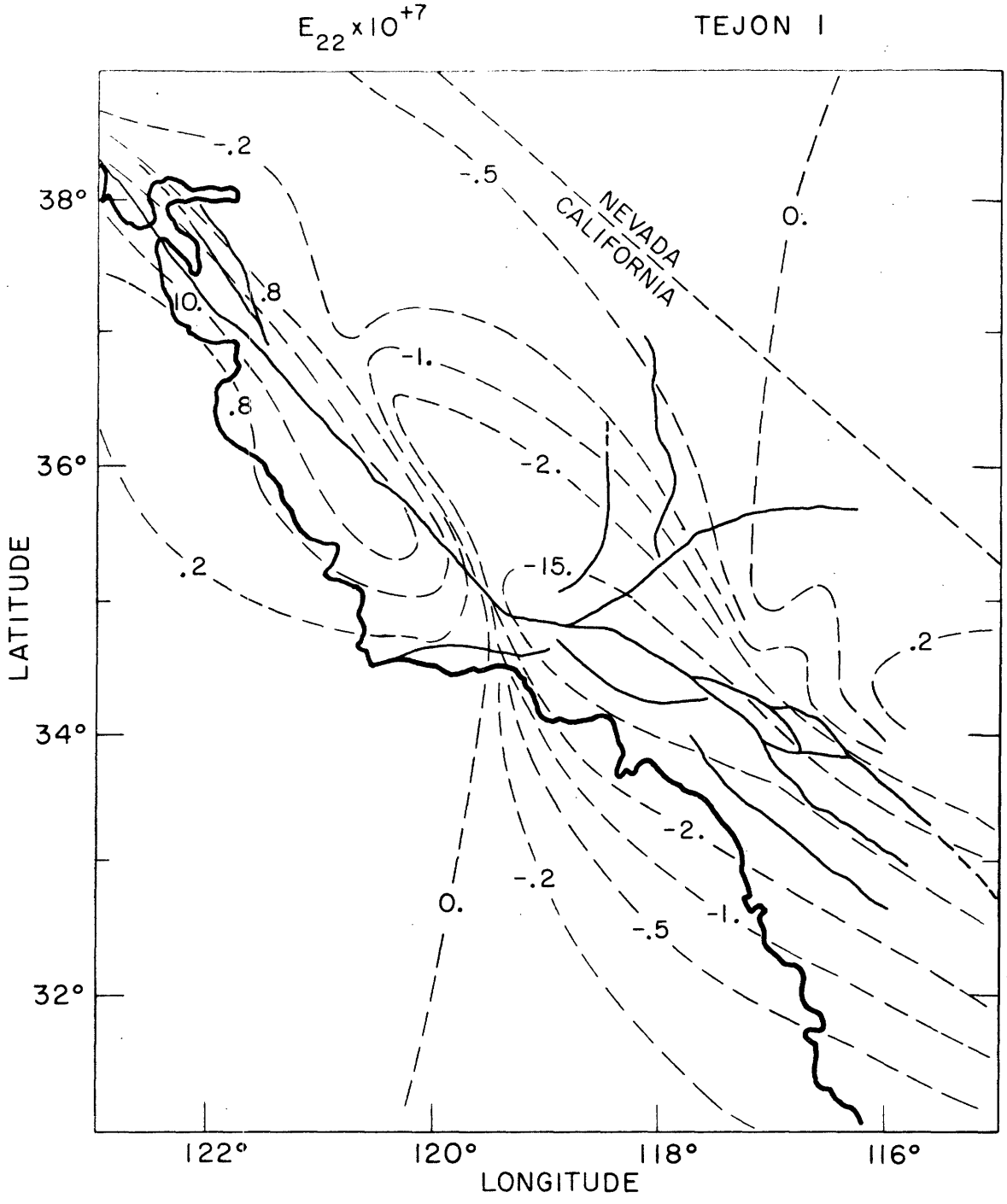
$E_{22} \times 10^{+7}$
TEJON I
NEVADA
CALIFORNIA
-.2
-.5
0.
.8
10.
-1.
-2.
-15.
.2
-.2
-1.
38°
36°
34°
32°
LATITUDE
122°
120°
118°
116°
LONGITUDE

Figure 4.39

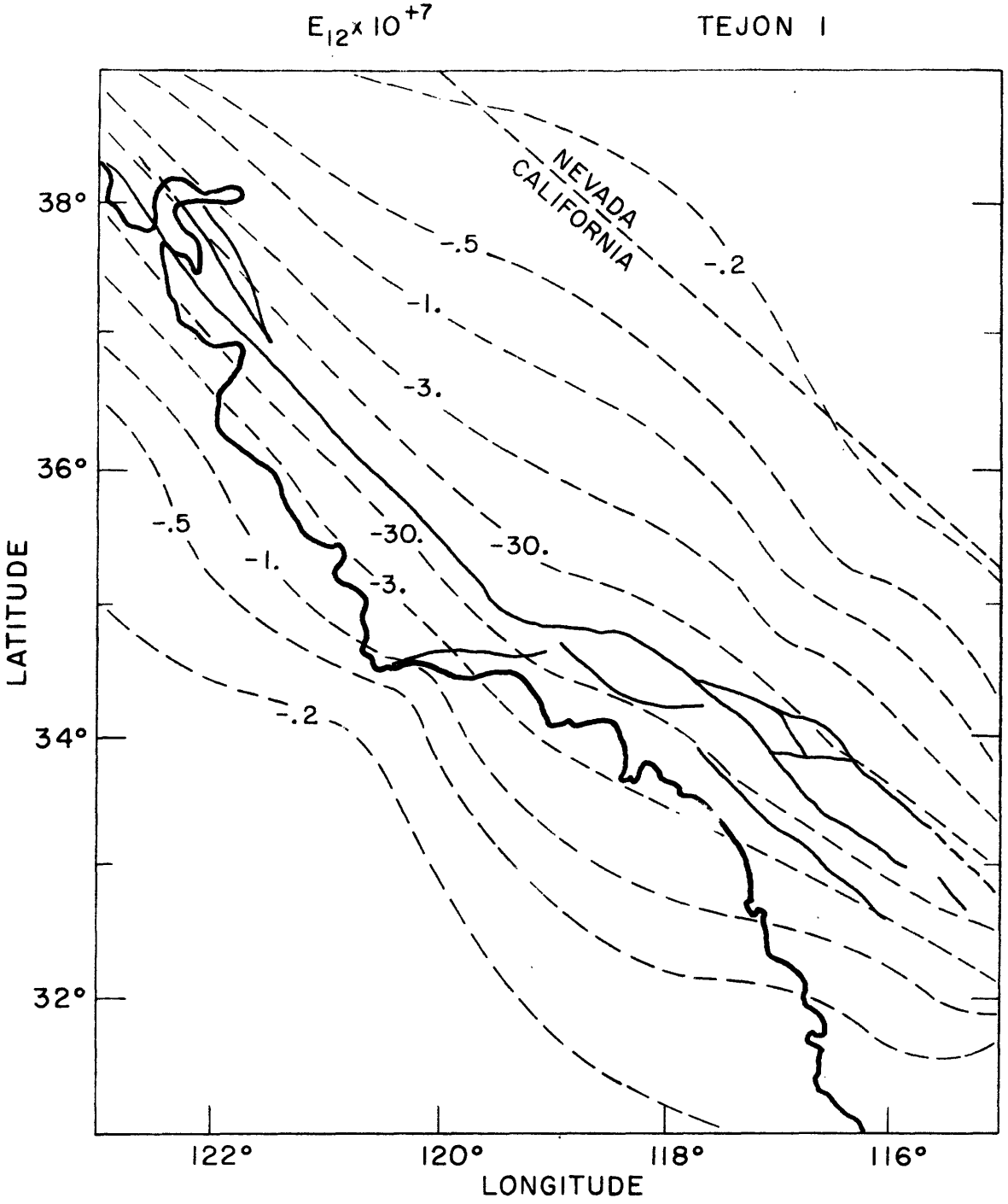
$E_{12} \times 10^{+7}$
TEJON I
NEVADA
CALIFORNIA
-.5
-1.
-3.
-30.
-.2
38°
36°
34°
32°
LATITUDE
122°
120°
118°
116°
LONGITUDE

Figure 4.40

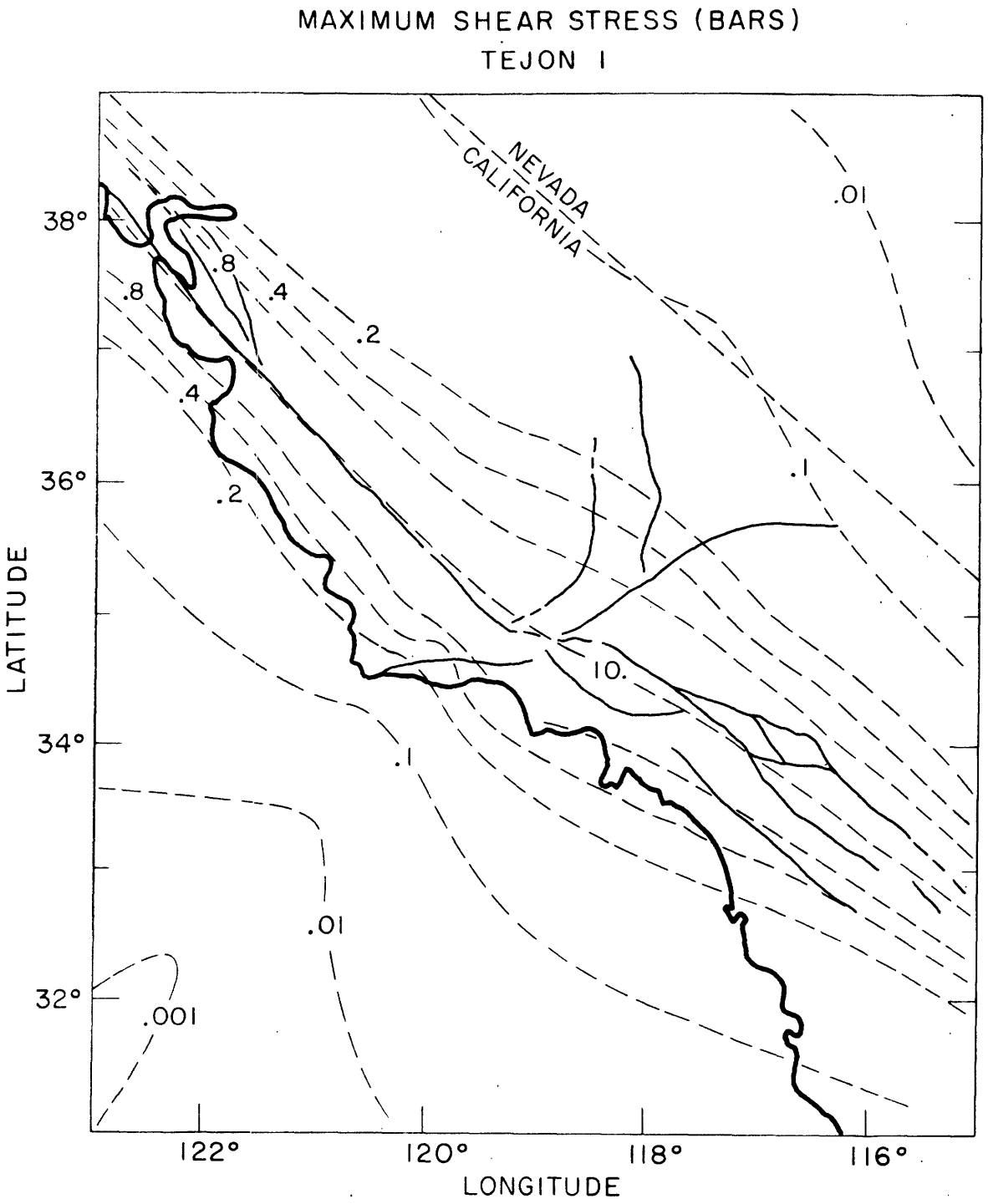
MAXIMUM SHEAR STRESS (BARS)
TEJON I
NEVADA
CALIFORNIA
.01
.8
.8
.4
.2
.4
.2
.1
10.
.1
.01
.001
38°
36°
34°
32°
LATITUDE
122°
120°
118°
116°
LONGITUDE

Figure 4.41

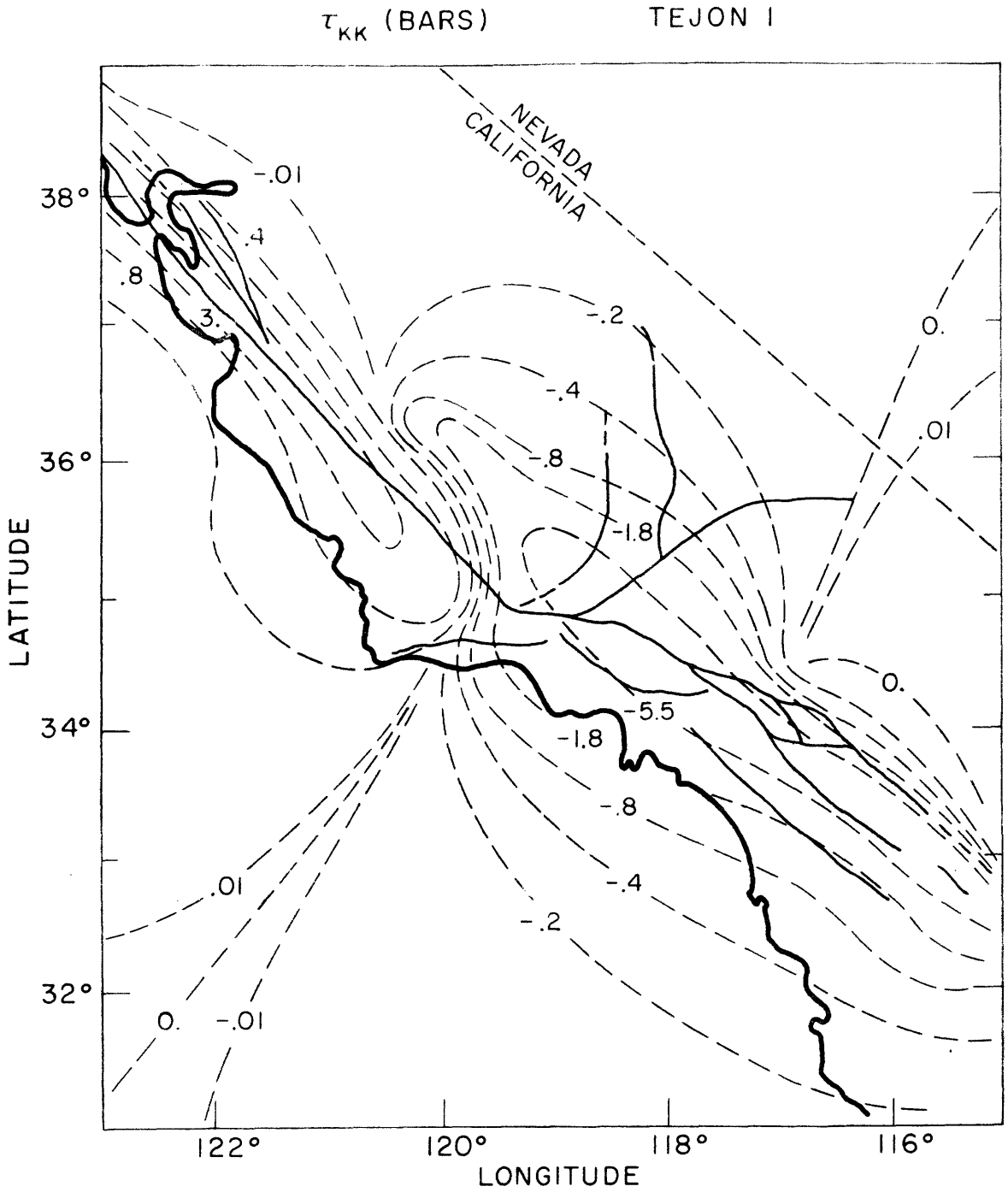
τ_{KK} (BARS)
TEJON I
NEVADA
CALIFORNIA
-.01
.4
.8
3.
-.2
-.4
-.8
-1.8
0.
.01
-5.5
-1.8
-.8
-.4
-.2
.01
0.
-.01
38°
36°
34°
32°
LATITUDE
122°
120°
118°
116°
LONGITUDE

Figure 4.42

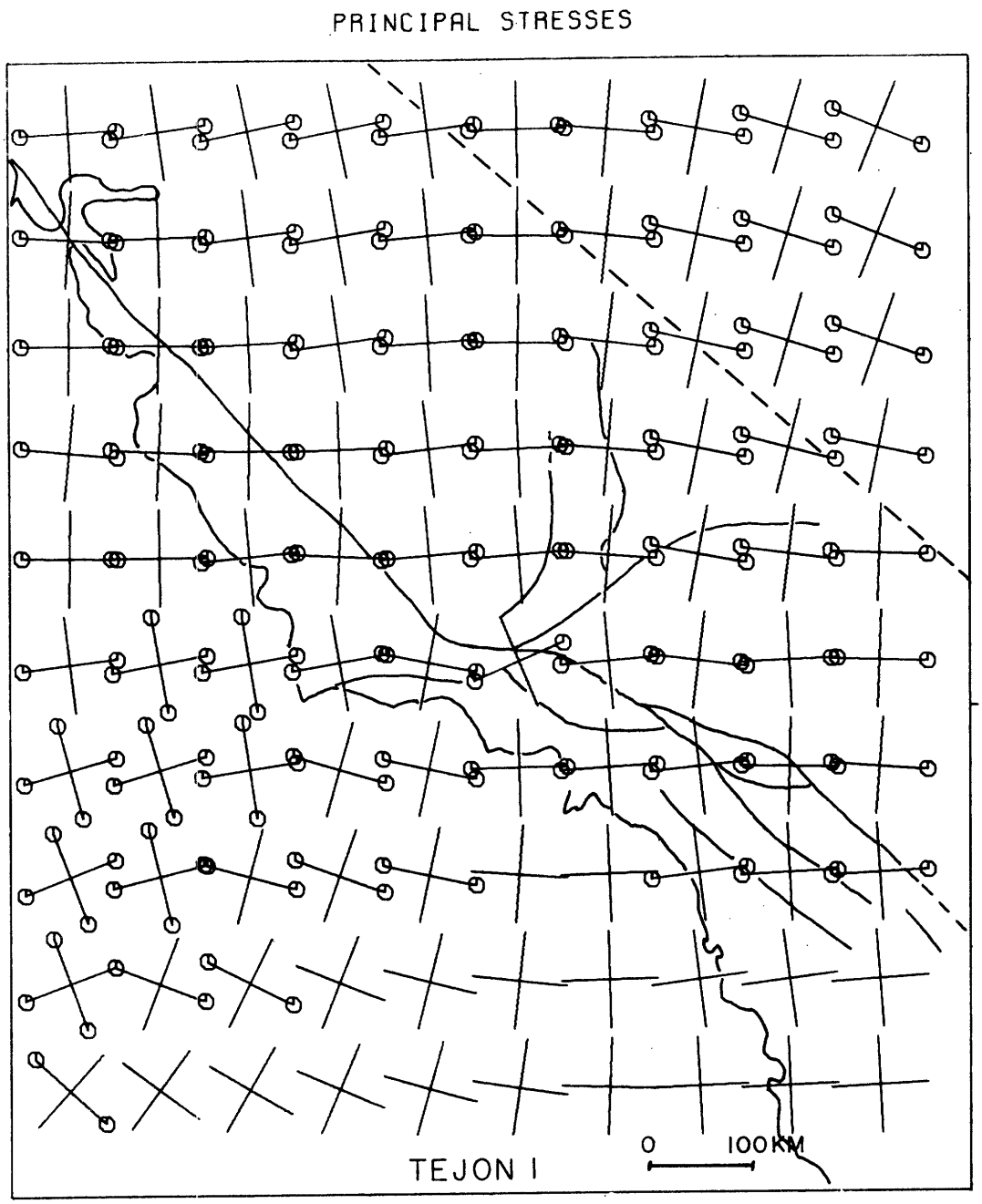

Figure 4.43

Figure 4.44

Schematic diagram of model Tejon 2. This model penetrates the thickness of the plate in the region of the Tejon bend. The first 9 corners of the dislocation model are identical to those for Tejon 1. The rest of the corners for Tejon 2 are:

Corner	Latitude	Longitude	Depth(km)
10	32.69	115.00	10
11	34.17	117.34	25
12	34.27	117.45	80
13	34.64	118.23	80
14	34.76	118.55	80
15	34.90	119.23	80
16	34.91	119.27	80
17	35.00	119.46	80
18	35.23	119.64	40
19	35.23	119.64	20
20	35.90	120.40	20
21	35.90	120.40	10
22	39.00	124.00	5

$B_r = 1$, $B_\phi = 135°$, $B_z = 0$

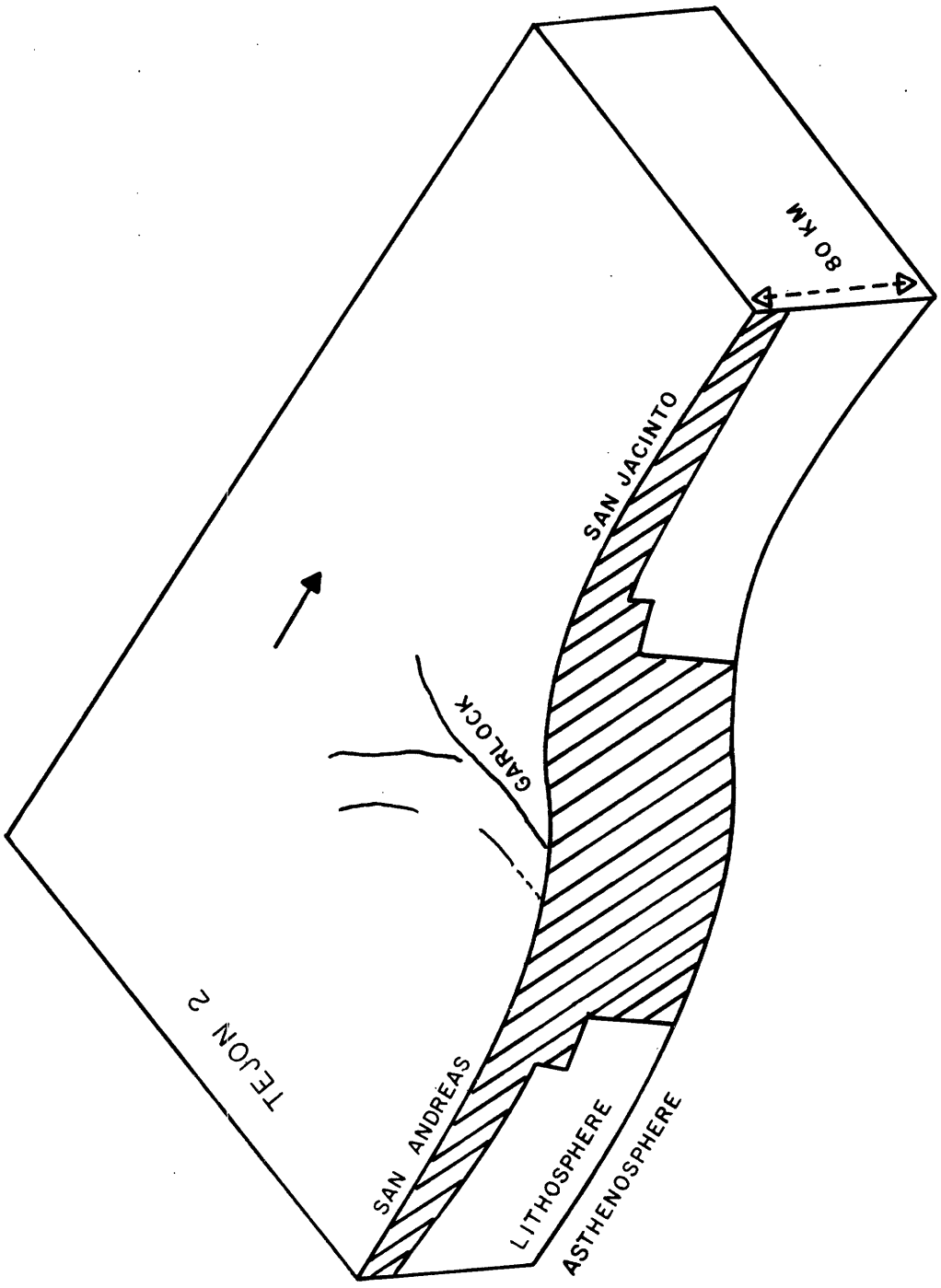
80 KM
SAN JACINTO
GARLOCK
TEJON 2
SAN ANDREAS
LITHOSPHERE
ASTHENOSPHERE

Figure 4.44

Figures 4.45-4.50

Strains ($X10^{+7}$) stresses (bars), and principal stress directions for model Tejon 2 in figure 4.44.

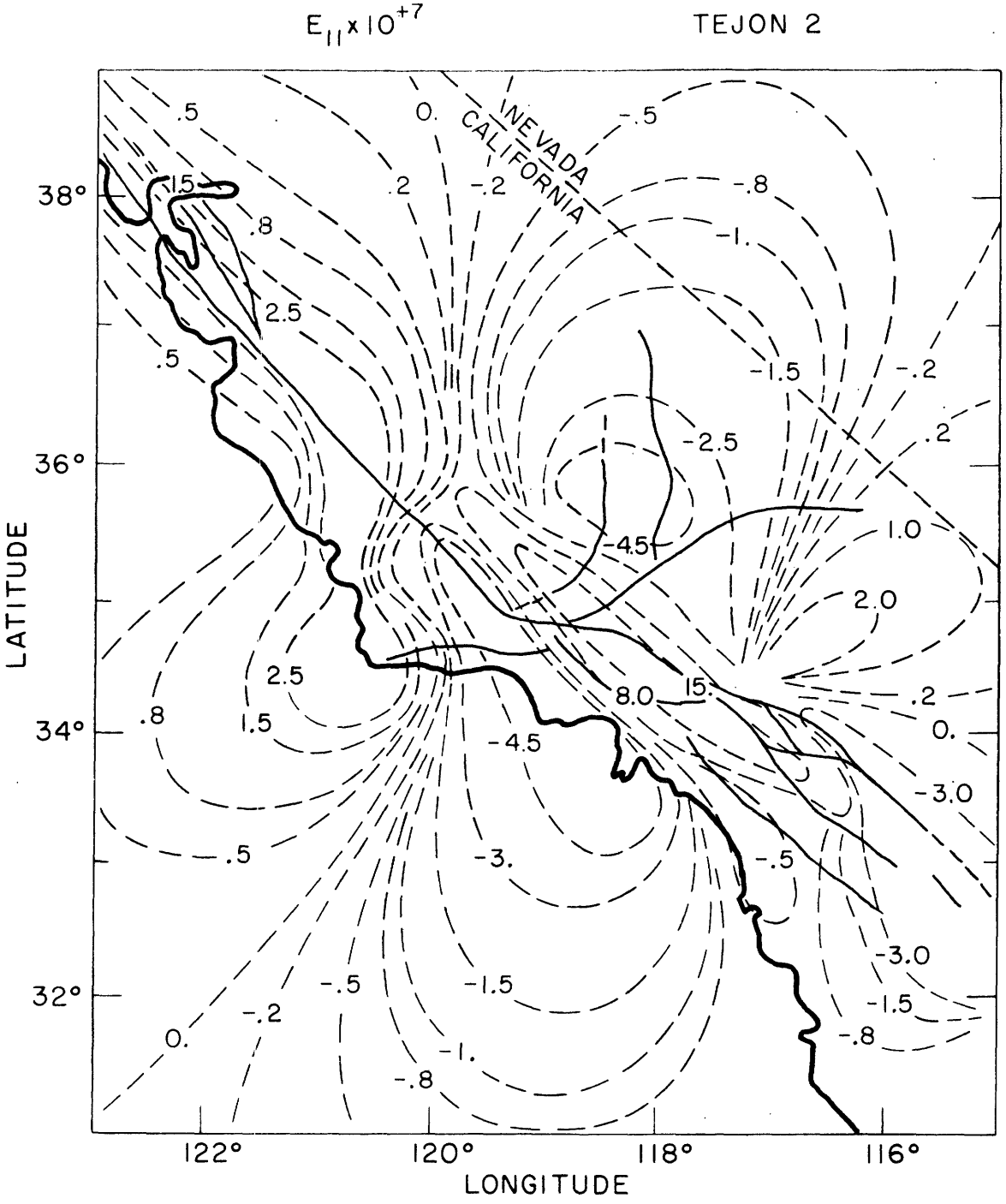
$E_{11} \times 10^{+7}$
TEJON 2
NEVADA
CALIFORNIA
38°
36°
34°
32°
LATITUDE
122°
120°
118°
116°
LONGITUDE
.5
0.
-.5
1.5
.2
-.2
-.8
.8
-1.
2.5
-1.5
-.2
-2.5
.2
1.0
-4.5
2.0
2.5
8.0
15.
.2
.8
1.5
-4.5
0.
-3.0
.5
-3.
-.5
-3.0
-.5
-1.5
-1.5
-.2
0.
-1.
-.8

Figure 4.45

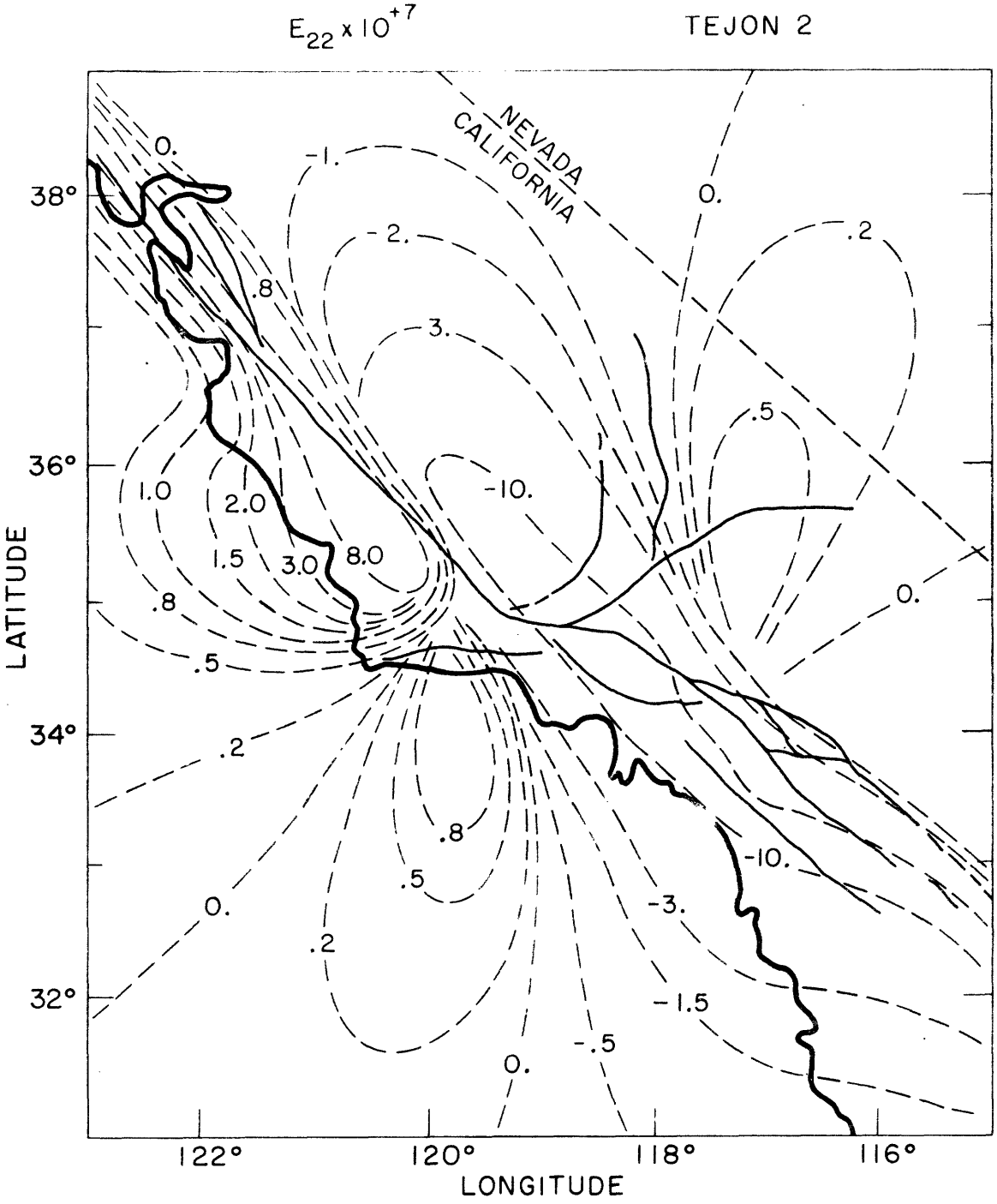
$E_{22} \times 10^{+7}$
TEJON 2
NEVADA
CALIFORNIA
0.
-1.
-2.
3.
.8
.2
0.
.5
1.0
2.0
1.5
3.0
8.0
-10.
.8
.5
.2
0.
.8
.5
-10.
-3.
.2
-1.5
-.5
0.
38°
36°
34°
32°
LATITUDE
122°
120°
118°
116°
LONGITUDE

Figure 4.46

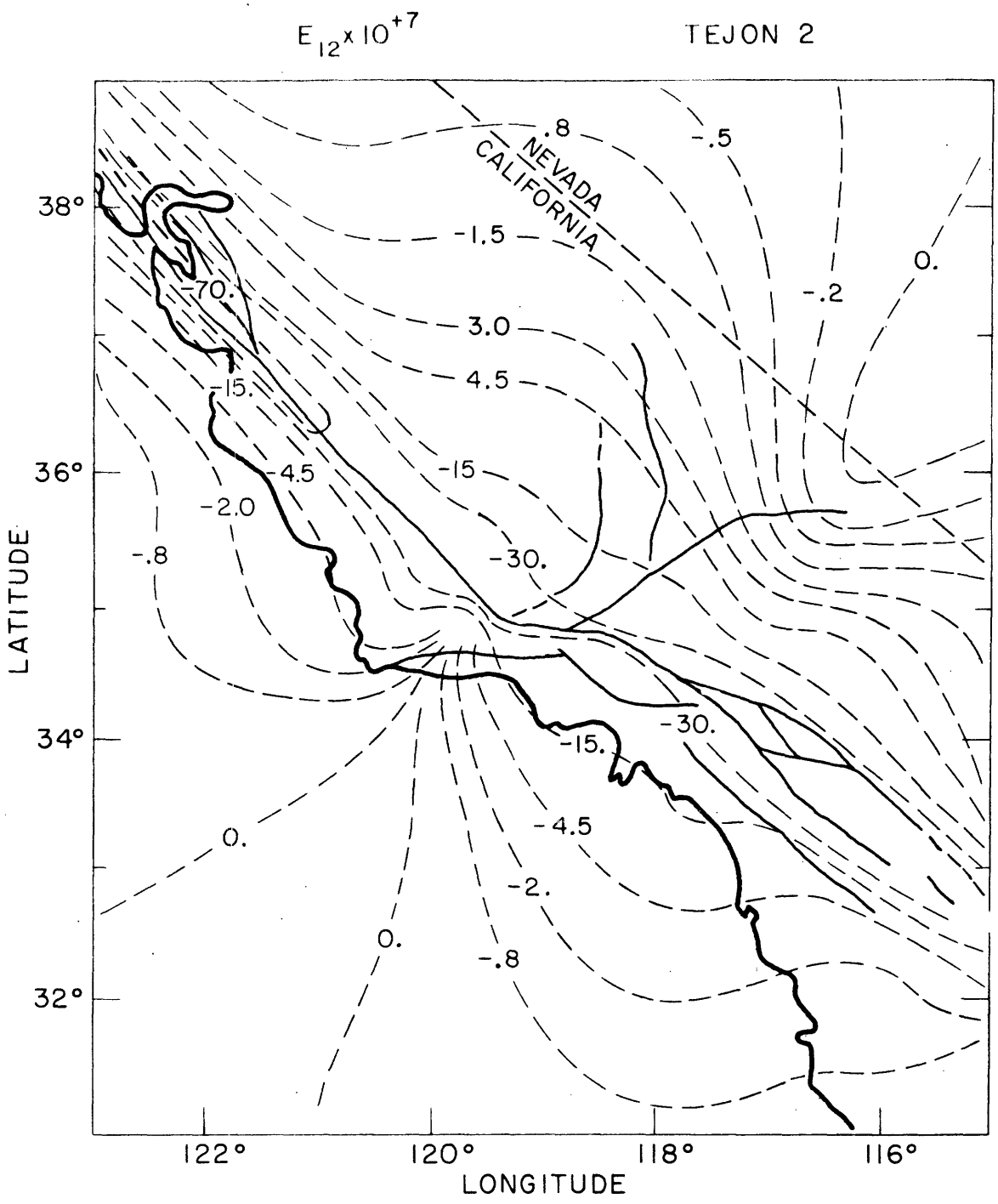
$E_{12} \times 10^{+7}$
TEJON 2
.8
-.5
NEVADA
CALIFORNIA
-1.5
0.
-.2
-70.
3.0
4.5
-15.
-4.5
-15
-2.0
-.8
-30.
-30.
-15.
-4.5
0.
-2.
0.
-.8
38°
36°
34°
32°
LATITUDE
122°
120°
118°
116°
LONGITUDE

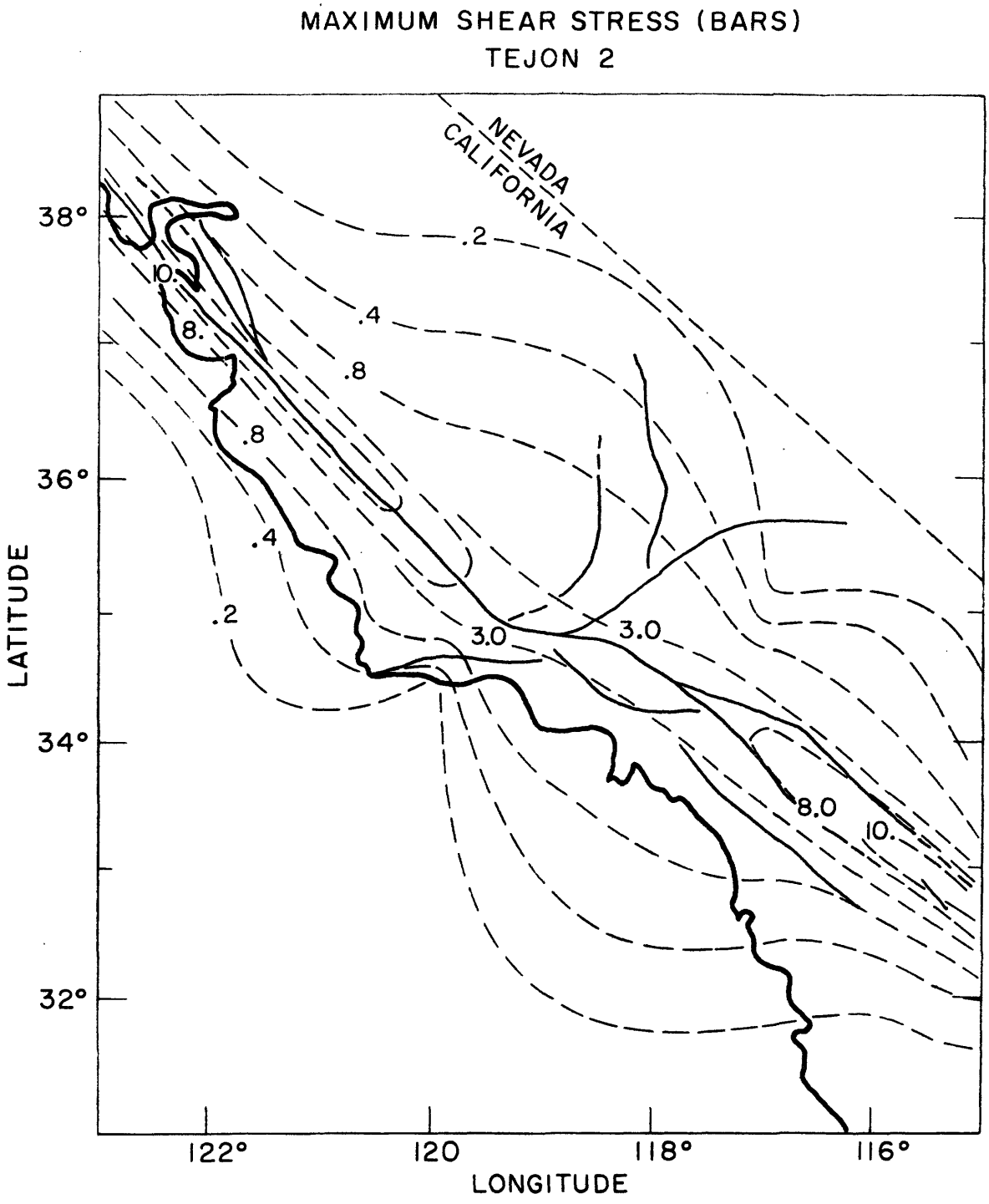
MAXIMUM SHEAR STRESS (BARS)
TEJON 2
NEVADA
CALIFORNIA
.2
.4
.8
.8
.4
.2
10.
8.
3.0
3.0
8.0
10.
38°
36°
34°
32°
LATITUDE
122°
120
118°
116°
LONGITUDE

Figure 4.48

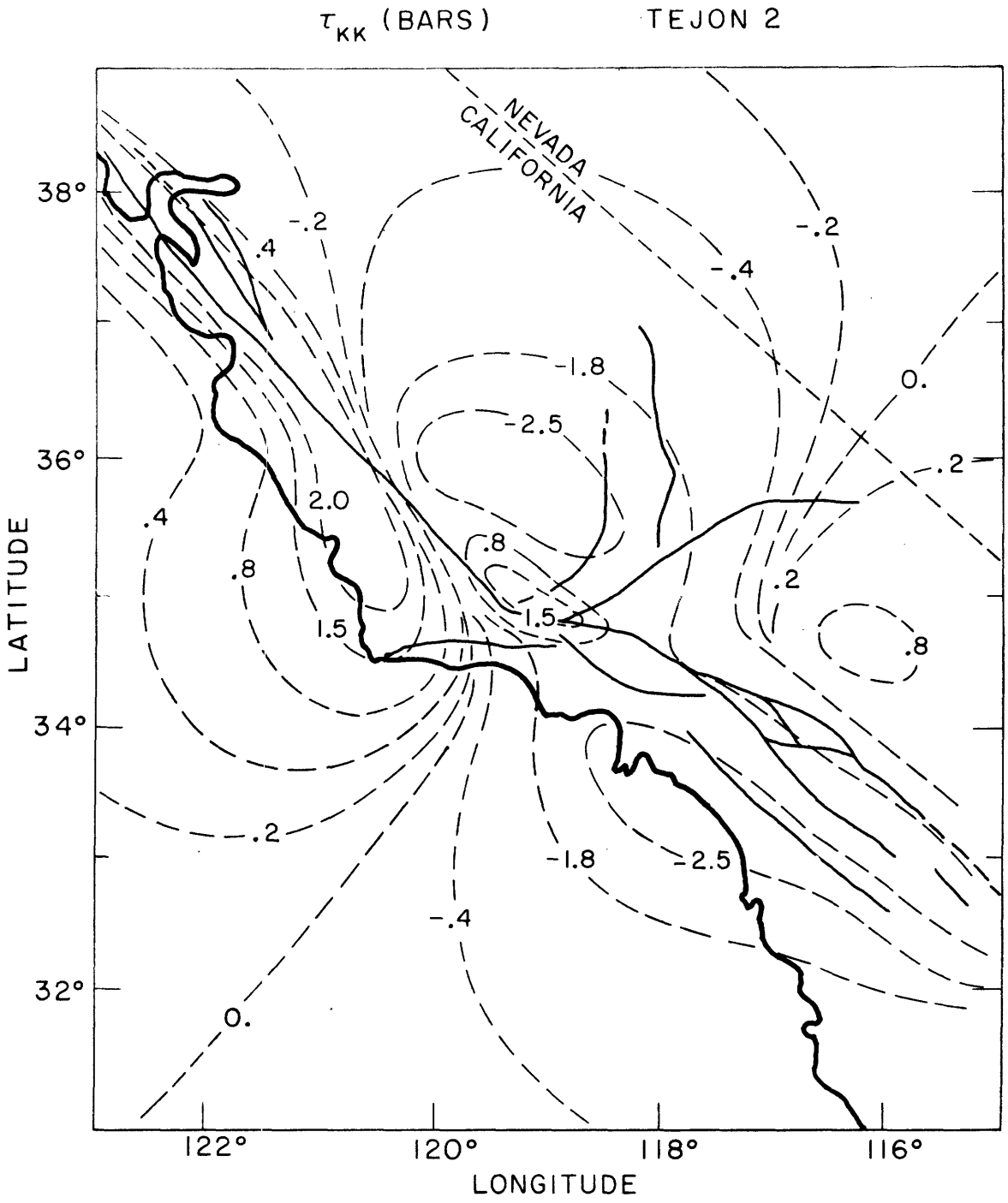
τ_{KK} (BARS)
TEJON 2
NEVADA
CALIFORNIA
38°
36°
34°
32°
LATITUDE
122°
120°
118°
116°
LONGITUDE
-.2
.4
-.4
-1.8
-2.5
0.
.2
2.0
.8
1.5
-1.8
-2.5
-.4
0.

Figure 4.49

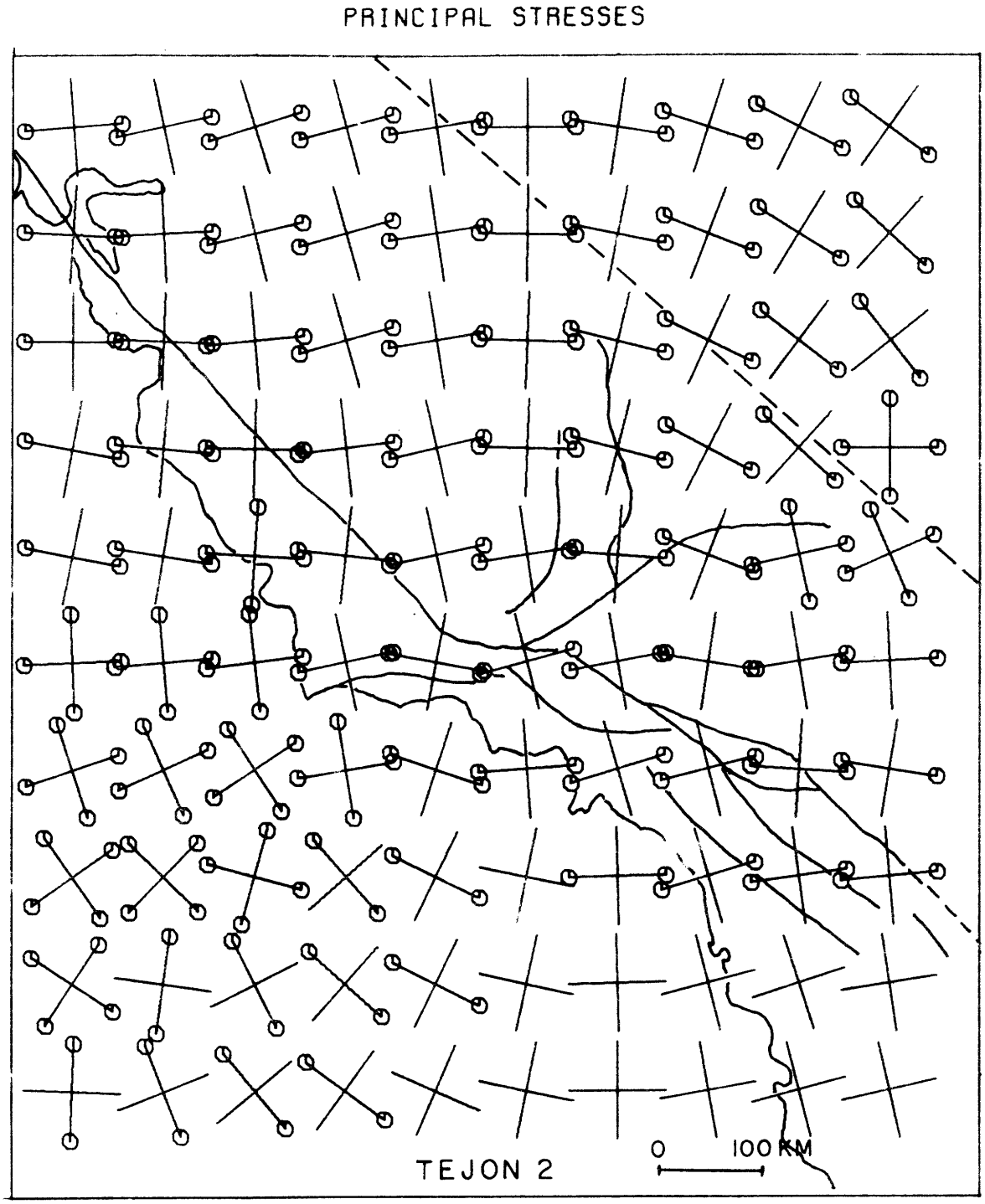

Figure 4.50

Figure 4.51

(a) Schematic diagram of model Tejon 3 and the additional displacement boundary conditions for the "bottom" of the plate. This model is identical to model Tejon 2 except for the two following dislocations on the bottom of the plate.

Corner	Latitude	Longitude	Depth (km)
Bottom A			
1	35.00	119.46	80
2	34.94	119.27	80
3	34.90	119.23	80
4	34.76	118.55	80
5	34.64	118.23	80
6	34.27	117.45	80
7	34.023	118.02	80
8	34.08	118.50	80
Bottom B			
1	35.00	119.46	80
2	35.12	118.89	80
3	35.22	118.16	80
4	34.27	117.45	80
5	34.64	118.23	80
6	34.76	118.55	80
7	34.90	119.23	80
8	34.94	119.27	80

Burgers' vector for all dislocations: $B_r = 1$, $B_\phi = 135°$, $B_z = 0$.

(b) Top view of Tejon 3

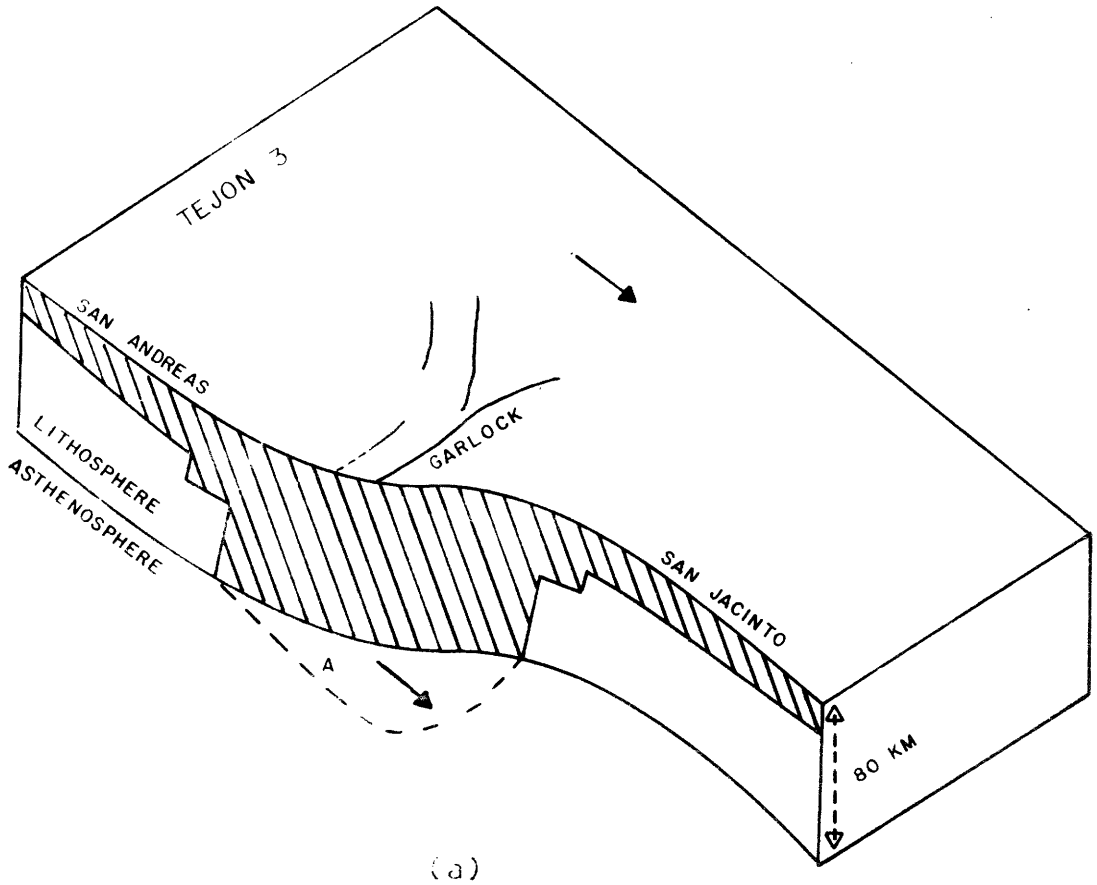
TEJON 3
SAN ANDREAS
LITHOSPHERE
ASTHENOSPHERE
GARLOCK
SAN JACINTO
A
80 KM

(a)

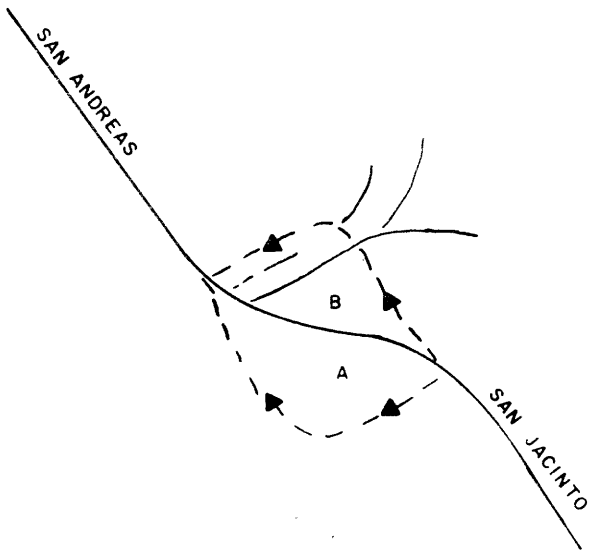
SAN ANDREAS
B
A
SAN JACINTO

Figure 4.5[illegible]

Figure 4.52-4.57

Strains ($X10^{+7}$) and stresses (bars) and principal stress directions for model Tejon 3 shown in figure 4.51.

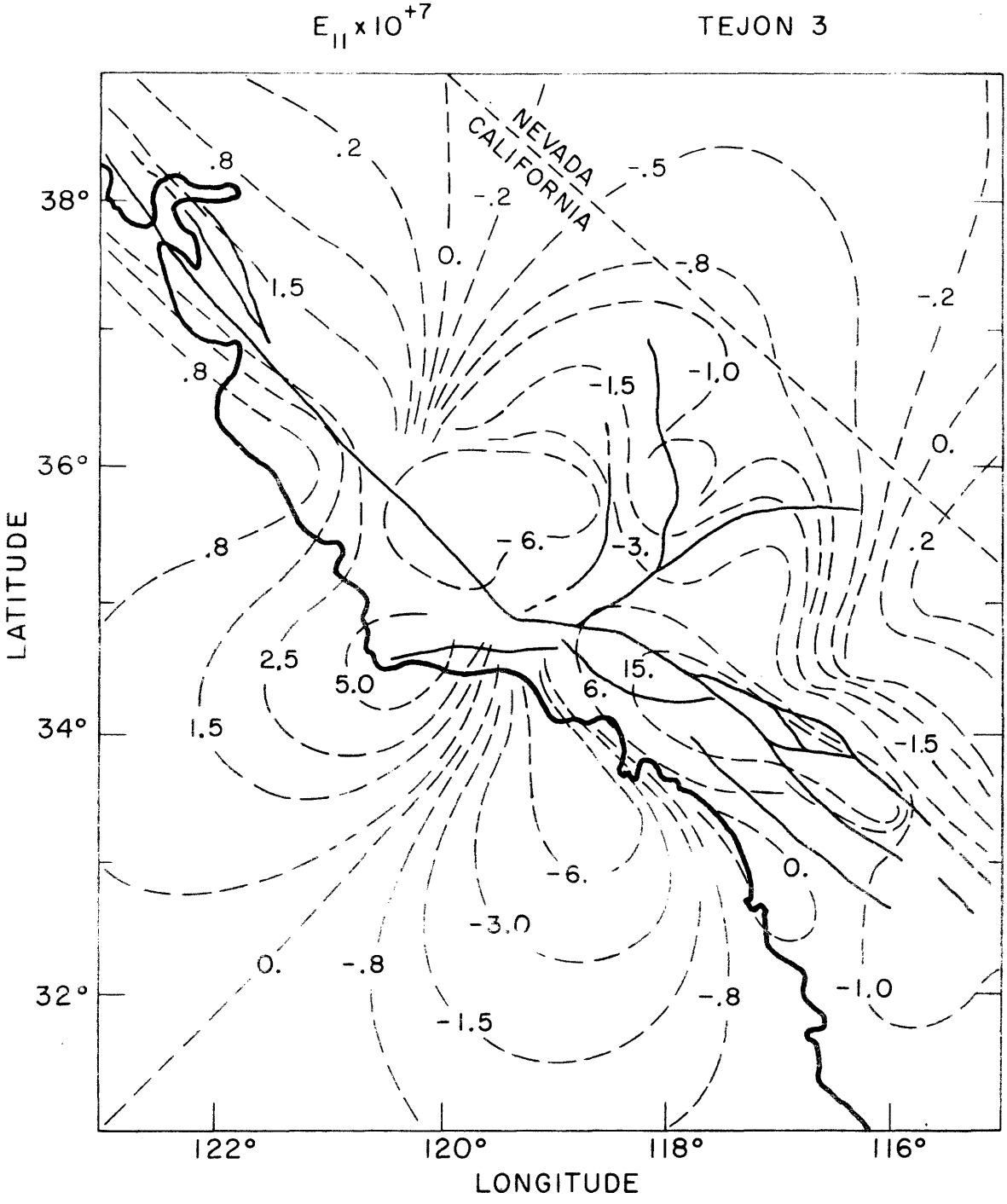
$E_{11} \times 10^{+7}$
TEJON 3
NEVADA
CALIFORNIA
38°
36°
34°
32°
LATITUDE
122°
120°
118°
116°
LONGITUDE
.8
.2
-.2
-.5
0.
1.5
-.8
-.2
-1.5
-1.0
.8
0.
-6.
-3.
.8
.2
2.5
5.0
15.
6.
1.5
-1.5
-6.
0.
-3.0
0.
-.8
-.8
-1.0
-1.5

Figure 4.52

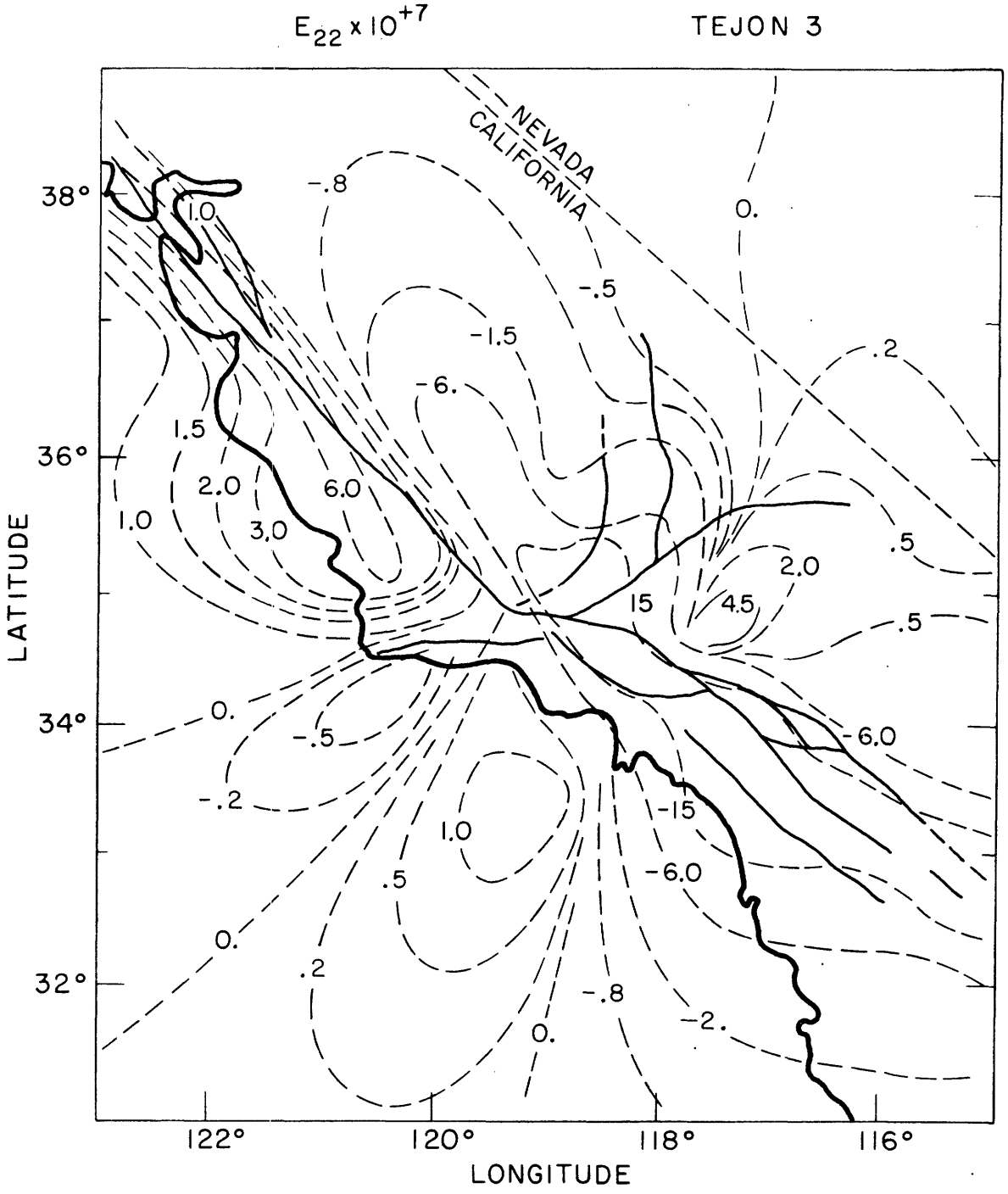
$E_{22} \times 10^{+7}$
TEJON 3
NEVADA
CALIFORNIA
38°
36°
34°
32°
LATITUDE
122°
120°
118°
116°
LONGITUDE
1.0
-.8
0.
-.5
-1.5
-6.
.2
1.5
2.0
6.0
3.0
.5
2.0
15
4.5
.5
-6.0
-.2
1.0
-15
-6.0
.5
.2
-.8
-2.

Figure 4.53

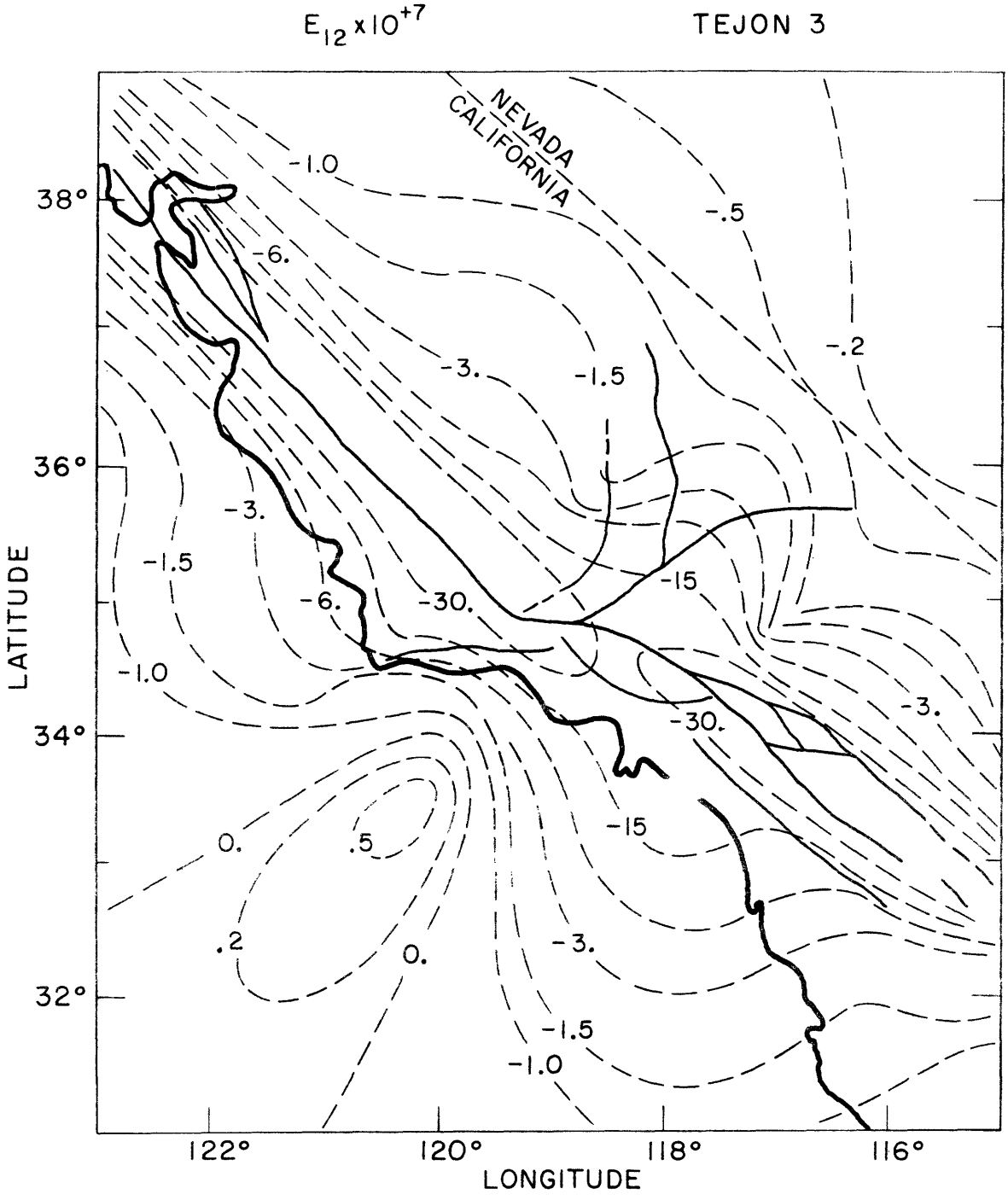
$E_{12} \times 10^{+7}$
TEJON 3
NEVADA
CALIFORNIA
-1.0
-.5
-6.
-.2
-3.
-1.5
-3.
-15
-1.5
-6.
-30.
-1.0
-30.
-3.
-15
0.
.5
.2
0.
-3.
-1.5
-1.0
38°
36°
34°
32°
LATITUDE
122°
120°
118°
116°
LONGITUDE

Figure 4.54

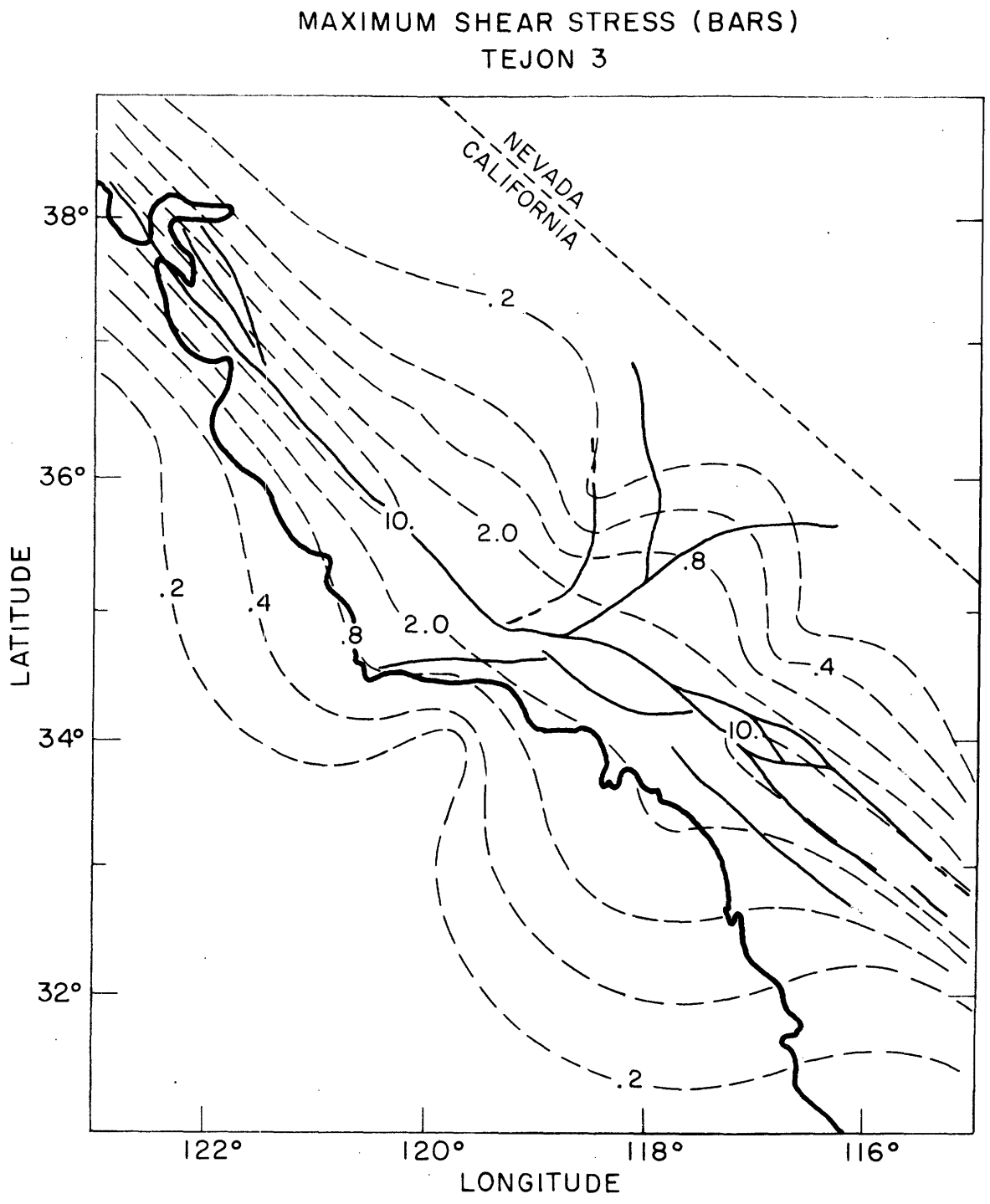
MAXIMUM SHEAR STRESS (BARS)
TEJON 3
NEVADA
CALIFORNIA
38°
36°
34°
32°
LATITUDE
122°
120°
118°
116°
LONGITUDE
.2
.4
.8
2.0
10.

Figure 4.55

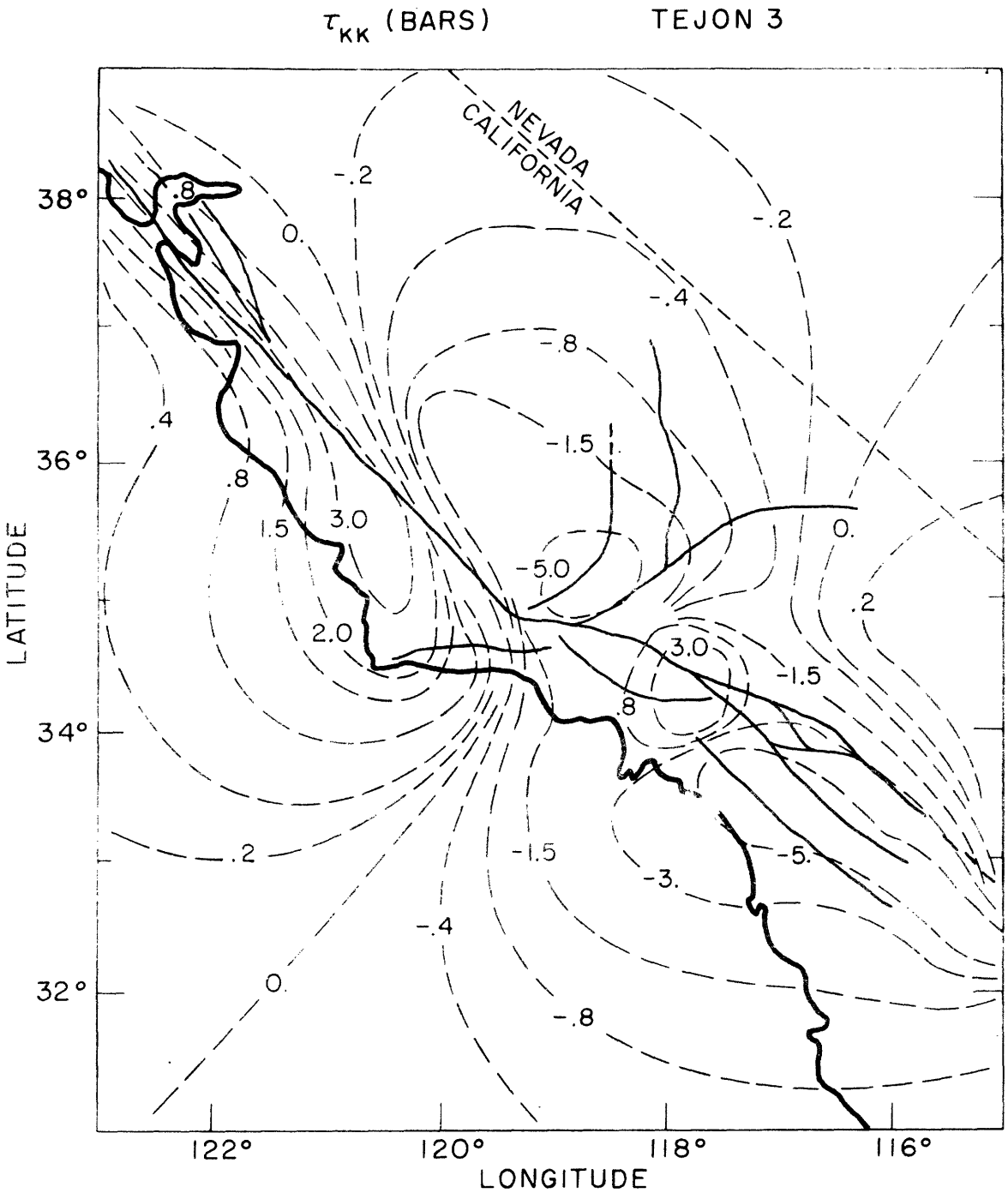
τ_{KK} (BARS)
TEJON 3
NEVADA
CALIFORNIA
38°
36°
34°
32°
LATITUDE
122°
120°
118°
116°
LONGITUDE
.8
0.
-.2
-.2
-.4
-.8
.4
-1.5
.8
1.5
3.0
-5.0
0.
2.0
.2
3.0
-1.5
.8
.2
-1.5
-5.
-3.
-.4
0.
-.8

Figure 4.56

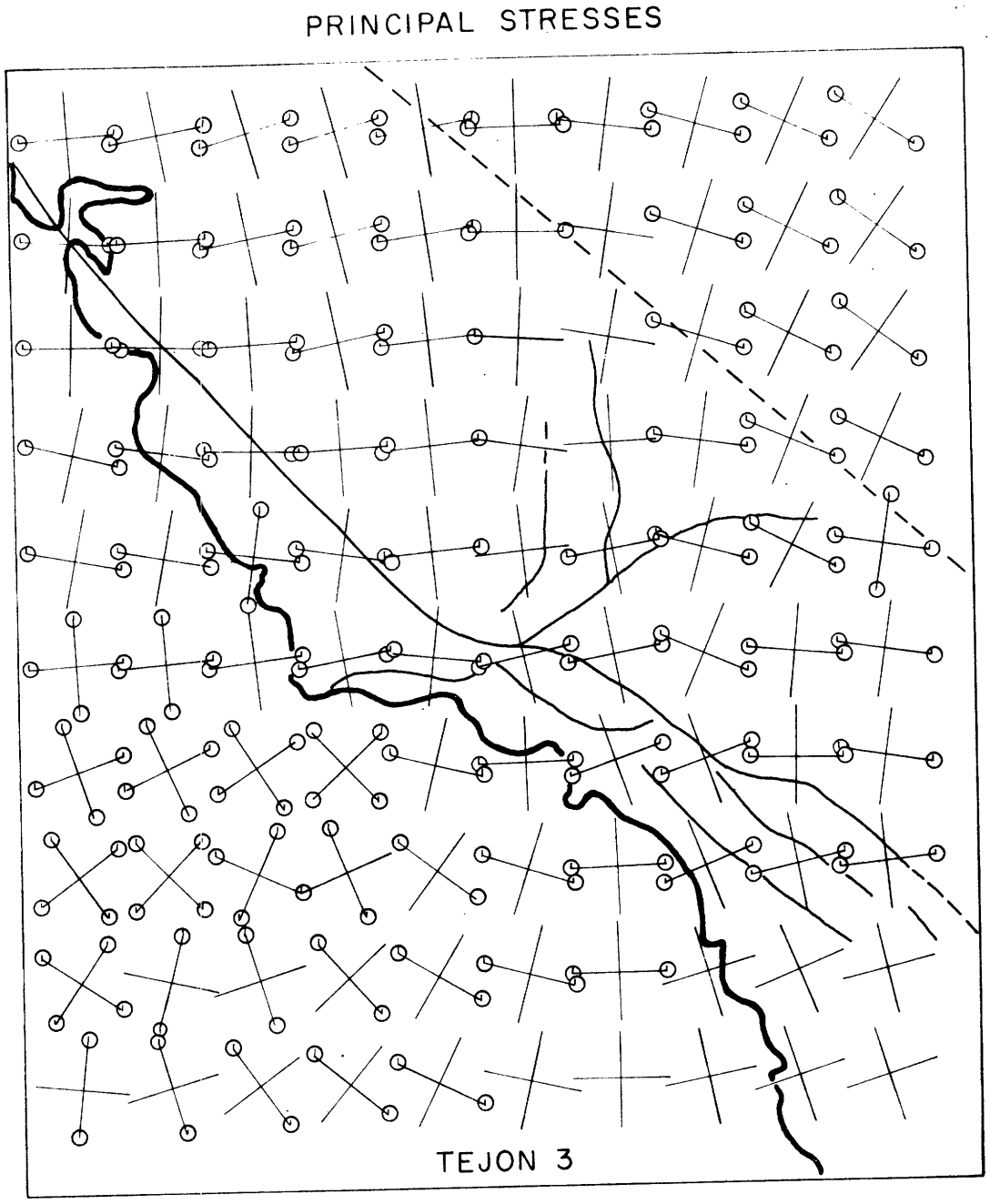

Figure 4.57

CHAPTER V

Models of the Stress History of California

5.1 Introduction

One of the ultimate goals of any program to model the stress distribution in the lithosphere is the prediction of earthquakes. In this chapter we shall use the tectonic modeling discussed in Chapter IV to calculate the stress history of California.

In particular a dislocation model of California will be proposed and discussed in terms of the present day tectonics. The model will be speculative and will not be comprehensive but is intended to account for the major tectonic features observed.

The strain fields from this tectonic model will then be added to the strain release of the large earthquakes that have occurred in California since 1812. The resultant additions allow us to make a study of the strain history of California. A similar study was made for southern California (using a plate model) by Smith and Van De Lindt (1969). Their primary concern was with the interaction of earthquake fields. We are interested in the mutual interaction of the tectonic and earthquake fields.

Because of the uncertainties in initial conditions and model parameters, the deterministic approach to earthquake prediction to be presented does not offer immediate hope for

a self-contained approach to earthquake prediction. However a study such as presented in this chapter offers: (1) a basic understanding of the nature of the strain accumulation and relaxation for our tectonic models, (2) a method which should allow us to point to regions of high strain accumulation that deserve further study, and (3) a method which, when used in conjunction with other approaches to earthquake prediction, could offer a viable system of earthquake prediction.

5.2 Tectonic Model of California

The tectonic model to be used for California will consist of the Tejon 2 model presented in Chapter IV with a few additional features (figure 5.1). The most important change is the introduction of the Great Valley plate. This plate will allow us to account for a proposed differential motion between the northern and southern portions of the San Andreas (Atwater, 1970; Minster et al., 1974), produce a region of more concentrated northwest southeast tension (Smith and Kind, 1972; Gumper and Scholz, 1972) than that predicted by model Tejon 2 and therefore allow our model to be more compatible with the large earthquakes that occur in the California-Nevada tectonic zone, (Ryall et al., 1966). However, the introduction of the Great Valley plate forces us to put a Mojave plate into our model (figure 5.1). Without the Mojave plate it would be necessary to introduce a local rotation of the North American plate with respect to the Great Valley

plate in order to explain the tension along one portion of the interface (Basin and Range province) and compression along another portion (Tehachapi Range). We eliminate this possibility because of the lack of the predicted thrust or normal faulting that would occur on various strike slip portions of the San Andreas.

We shall assume that the Mojave plate is moving slower to the southwest (in a relative sense) than the Great Valley plate. This will introduce compression across the interface between the Mojave desert and Great Valley. In addition, we will assume that the North American plate is moving faster to the southwest than the Great Valley plate, thus producing tension between these two plates and right lateral shear between the eastern portion of the Mojave and the North American plate.

A less important change to our model consists of the introduction of the San Jacinto plate wedged between the San Andreas and San Jacinto faults in the south. This plate is introduced to take account of the geodetic observations of Savage and Burford (1970) and Scholz and Fitch (1969). They find a broad zone of deformation across the San Andreas and San Jacinto faults with most of the strain accumulation being associated with the San Jacinto fault. There is however, a concentration of strain associated with the San Andreas fault which is indicative of slip at depth on this fault. We will

construct our model so that the relative motion between the San Jacinto plate and the North American plate (the San Andreas fault) is small. Therefore, most of the motion between the North American plate and the Pacific plate will be taken up on the San Jacinto fault. The presence of the San Jacinto plate could be related to the existence of proposed spreading centers in southern California (Elders, et al., 1972).

Thus, in our model, the Mojave plate is being squeezed slightly to the east by the San Jacinto and Pacific plates from the south and by the Great Valley plate from the north (Anderson, 1971). The relative motions across the interfaces are determined by the imposed requirement that the Pacific plate move at a rate of 6 cm/year with respect to the North American plate and 5 cm/year with respect to the Great Valley plate (N45°W). Thus, the net movement in our model across the southern portion of the San Andreas will be consistent with that determined in the Gulf of California (Larson et al., 1968). The extra 1 cm/year will be taken up in the Basin and Range region (between the Great Valley and North American plates) (Minster et al., 1974).

In figure 5.2 we have drawn an oblique view of the fault model described above. The model parameters are given in table 5.1. The view is shown with the Pacific plate cut away so that depth of locking on the San Andreas may be shown. Locking is defined here to mean little or no motion with

respect to the slipping portion of the fault (shown in white). Thus the locked sections of the fault shown in figure 5.2 could represent either (a) portions of the fault which are especially resistant to slip or (b) portions of the fault which are at a low stress state (and therefore unable to overcome the local frictional forces). We cannot distinguish between the two possibilities but we speculate that the deeper sections of locked fault under San Francisco and the Tejon bend are related to a low stress state in these areas which resulted from the 1906 and 1857 earthquakes respectively.

The depth of locking in the vicinity of San Francisco is essentially that inferred in Chapter IV. Northwest of Bodega head (near Forth Ross) the high strain rates (Meade, 1971) are indicative of shallow locking (10-20 km). Southwest of San Juan Bautista (between SJB and Cholame) the agreement between fault creep and geodetically determined strain rates indicate very shallow or no locking (0-12 km) (Savage and Burford, 1970; Wesson et al., 1973). This conclusion is supported by the low strain rates observed south of SJB at the Salinas net (Robert Nason, personal communication, 1975). A recent analysis of triangulation arc data in the vicinity of Point Reyes (between Bodega Head and San Francisco) led Thatcher (1975) to conclude that the depth of locking in this region is deeper than that to the northwest of Bodega Head or to the southwest of SJB. This supports our conclusion of deeper locking in the San Francisco area based on the rotation of the pressure axes in this region

and the slower relative motion of geodetic stations across the San Andreas near San Francisco.

South of Cholame we have the depth of locking increase rapidly as we move into the Carrizzo plains area. Based upon the arguments presented in Chapter IV,we estimate the depth of locking in the Carrizzo plains - Tejon bend region to be from 60 to 100 km. We have chosen 80 km as the depth of locking for this region. In fact,all zones of interaction for the Mojave plate are assumed to extend to 80 km. This depth of interaction will extend the range of influence of the Mojave plate but will minimize its effect upon the local fields in the vicinity of the Tejon bend. Southwest of the Tejon bend we assume that both the San Jacinto and San Andreas faults lock to 15 km.

The zone of interaction between the North American plates and the Great Valley plate is assumed to extend to 80 km. Because of the relative motion between the North American plate and the Great Valley this interface represents a region in which the plates are being pulled apart. The interaction extends throughout the thickness of the plates (in this case 80 km) and should result in a broad region of strain accumulation (and therefore earthquake activity).

We wish now to examine two versions of the model described above. The first version (model TCALS) has the Mojave plate moving primarily in a northwest-southeast direction (parallel

to other plate motions). The second model (TCALF) has the Mojave moving toward the east much more rapidly than in model TCALS. The major effect of the faster easterly moving Mojave will be a rotation of the Burgers vector (or relative motion motion vector) across the Tejon bend.

In figures 5.3-5.7 we have contoured the strains and stresses that would accumulate from the model TCALS over a period of 100 years (without earthquakes). The principle stress directions are plotted in figure 5.8. The E_{11} contours in figure 5.3 show that this model puts the Hayward Calaveras fault zone, the offshore region near point Arguello, the San Andreas in the vicinity of the Tejon bend, the eastern edge of the Mojave desert, and the San Jacinto and San Andreas faults in the south under northeast southwest tension. On the other hand,the (1) Monterey Bay, (2) offshore Los Angeles and, (3) Sierra Nevada areas are subjected to northeast southwest compression.

The E_{22} strains contoured in figure 5.4 indicate that the Tejon bend is subjected to northwest-southeast compression while the eastern Mojave, the Sierra-Nevada fault region, the coastal side of the San Andreas between Cholame and Santa Barbara, and the Hayward-Calaveras zones are subjected to northwest-southeast extension. The shear strain and maximum shear stress in figures 5.5 and 5.6 respectively show the highest shear accumulation on the portion of the San Andreas between SJB and Cholame. There is, however, considerable debate over whether

or not this stress is being released by fault creep (see e.g. Scholz and Fitch, 1969; Savage and Burford, 1970). The sum of the stresses $\tau_{kk} = \tau_{11}+\tau_{22}+\tau_{33}$ contoured in figure 5.7 allow us to see the effective lobes of extension (+) and contraction (-) associated with the variable depth of locking along the San Andreas. These lobes are important and their existence should be looked for in future studies of the geodetic data. Data suggestive of the edge effect near Cholame may be found in the papers by Cherry and Savage (1972), Greensfelder and Bennett (1973), and Howard (1968).

The principal stress directions for model TCALS are shown in figure 5.8. As expected (at least by the author), the principal stress directions and signs are essentially those of the Tejon 2 model described in Chapter IV. The two models differ on the northeastern edge of the Mojave plate where model TCALS has tension in both a north-south and east-west direction while model Tejon 2 had compression on the north-south axes in this region.

In figures 5.9-5.11 we show contours of E_{11}, E_{22}, and τ_{kk} for model TCALF in which the Mojave plate is being pushed more rapidly in a N45°E direction. The shear strain and maximum shear stress profiles are not shown for this model since they are essentially the same as those shown for model TCALF. The major difference in the two models for the E_{11} strain occurs on the southern portion of the San Andreas and on

the San Jacinto fault. For model TCALS these faults were under compression in this direction (figure 5.9). In the case of the E_{22} strains the model TCALF broadens the region of northwest-southeast compression which was originally off the coast of Los Angeles and pulls it up to the Santa Barbara channel region. The interesting effect to be noted in the τ_{kk} is the large positive region which includes the areas of the 1857 Tejon earthquake, 1952 Kern County earthquake, and the 1971 San Fernando earthquake (see Table 5.2).

The principle stress directions for model TCALF are shown in figure 5.12. It is interesting to note that the region of extension off the coast (Point Arguello) is now primarily compression in a north south sense with extension in an east-west direction. Thus it appears that one of the most important factors in the tectonics of the offshore area in this region is the direction of relative motion across the Tejon bend. However, in the Santa Barbara channel region model TCALF would predict right lateral motion on the east-west trending faults. This contradicts the observations for the Santa Barbara Channel region (see eg. Ellsworth, 1975). The purely tensional feature on the northeastern portion of the principal stress map for this region does not seem to agree with the observations for this area (Smith and Kind, 1972; Priestly, 1974). If the motion of the Mojave plate is fast enough in a N45°W direction (and it is for model TCALF) then the Mojave plate will be pulling away from the San Jacinto plate in the Banning Mission

Creek area (intersection of San Andreas and San Jacinto faults). Under these circumstances we would expect to see east-west tensional features in this area. Geologically this area is characterized more by a north-south compression (Allen et al., 1965; Sharp, 1967). However recent fault plane solutions for this region indicate normal faulting with an almost north-south strike (David Hadley, personal communication, 1975). However, because this seems to be one of the few desirable features of model TCALF we shall be content with model TCALS for the purposes of this chapter.

5.3 California Earthquakes

Now that we have a model of the mechanism which generates internal stress in California, we wish to examine those mechanisms which allow the strain to be released. We shall categorize them in the following manner: (1) large earthquakes ($M \geq 6$) (2) small earthquakes ($M < 6$) (3) fault creep and (4) diffusion creep. The only strain release mechanism included in our calculation will be that of the large earthquake. Neglect of small earthquakes is justified on the basis of energy considerations (Richter, 1958). As shown in Chapter IV, we are able to model fault creep in terms of dislocations (see eg. Stewart et al., 1973; Nason and Weertman, 1973), but the total amount of fault creep and the contribution it makes to the strain released is uncertain.

However, because of our results in Chapter IV, we believe that fault creep could play a minor role in the release of strain. Diffusion creep in the crust should not effect our calculations as long as we consider time periods on the order of a hundred years. Asthenospheric relaxation could significantly alter our results if the plate is thin or the viscosity is low. In consideration of the results presented in Chapters III and IV we shall assume the effects due to the plate bottom are negligible.

Even restricting our studies to the strain release of large earthquakes does not help us much. This is due to the lack of data on many of the large events being studied. Often, the only data available for past earthquakes are the locations and the observations of the fault. Magnitudes for these historic events are generally assigned from the intensity scale based on the amount of shaking felt by people at various distances from the source (Richter, 1958). We begin accounting for earthquake strain release in the year 1812 and attempt to take account of all large earthquakes that occurred from that year to the present. The magnitudes and locations of many of the events were taken from the book by Gutenberg and Richter (1954). This data was complimented by data on USGS and NOAA tapes.

The magnitudes are then used to calculate the lengths of the earthquakes on the basis of an empirical magnitude-length

relation found by Tocher (1958) and later explained by means of seismic scaling (Aki, 1968). The equation used is

$$L = 10^{.59M-2.24}$$

where M is the earthquake magnitude and L is the length of the earthquake in kilometers. All of the earthquakes were assigned a common width of 15 km and depth of 0 km. This is unreasonable in terms of individual earthquakes but allows us to put a limit on the effective range of earthquakes. The width of 15 km used is consistent with the shallow depth of California earthquakes (Allen, et al.. 1965; Brune, 1968; Richter, 1958; Wyss and Brune, 1968).

In order to choose the net slip for each event we make the assumption that the stress drop for all events is the same (Aki, 1967; Chinnery, 1968; Aki, 1972). The general expression for stress drop is (Aki, 1972)

5.1 $$\Delta\sigma = c\mu \frac{\overline{\Delta\mu}}{\sqrt{S}}$$

where c is a constant dependent upon the fault geometry, μ is the elastic rigidity, $\overline{\Delta\mu}$ is the average slip, and S is the surface area of the fault. C varies from 2.4 (circular crack) to 5. We have chosen c on the assumption that all earthquakes drop 50 bars of stress (Smith and Van De Lindt, 1969) and that

the 1906 San Francisco earthquake is representative of California earthquakes. We thus use L = 435 km and $\overline{\Delta\mu}$ = 5 meters (Chinnery, 1961) for the 1906 earthquake to determine the value of 2.69 for c from equation 5.1($\mu = 3 \times 10^{11}$ dynes/cm^2). With c determined, equation 5.1 may now be used to determine the slip for other California earthquakes. Because our method of choosing lengths, widths, and average slips tends to overestimate the seismic moments, our earthquakes will not obey empirically determined magnitude-moment relations (Brune, 1968). However, it is not clear that the static moment determined seismically gives an accurate representation of the permanent deformation associated with an earthquake (Allen and Wyss, 1967; Thatcher, 1975). The rakes, strikes, and dips of the events were assigned on the basis of geologic and seismic observations (Allen, et al., 1965; Gumper and Scholz, 1971; Richter, 1958; Bolt and Miller, 1968; Bolt et al., 1968; fault map, California division of mines and resources; Hileman et al., 1974). For example, if an earthquake occurred in the northern or southern most portions of the San Andreas it was treated as a vertical strike slip fault with right lateral motion. If on the other hand the earthquake occurred in the Tehachapi Range it was given an almost pure thrust mechanism with a slight left lateral motion. The dip angles used for a region considered to be under predominant compression or tension was 45°. If an earthquake

occurred in an intermediate region, the dislocation parameters were scaled according to the position of the earthquake between the two extreme regions. When other data was available none of the above rules were used (see e.g. Allen et al. 1965; Richter, 1958; Tocher, 1958; Hileman et al., 1972). The dislocation parameters are given in table 5.1. The strike direction (ϕ) is measured positive counterclockwise from north and represents the direction of the Y-axis along which the fault is aligned. The dip direction is toward the positive x-axis. The x and y axes form a right handed coordinate system so that z points out of the earth. Thus, for example, an earthquake with a strike of 45° and a dip of 20° will be dipping toward N45°E with a dip of 20°. Many of the larger events listed in table 5.1 have been plotted in figure 5.13.

5.4 Initial Conditions

One of the most difficult (if not impossible) aspects of our problem is that of choosing the initial conditions with which to start our models of California. We may guess that some fraction of the existing stress field that existed in 1812 (which is the time at which our model will begin) will have originated from the tectonic strain accumulation due to relative plate motion over some period of time. To model this portion of the initial field we have assumed a 100 year accumulation from a modified form of the tectonic

model discussed in the previous section (TCALS). The modification was made on the portion of the San Andreas which extends northward from the Tejon bend. Instead of the variable depth of locking (figure 5.2) we have assumed that this portion locked uniformly to a depth of 40 km. This depth of locking will yield a low prestress associated with the northern leg of the San Andreas. In fact, we shall assume that this smoother tectonic model is in effect until the 1906 earthquake. After 1906, the variable depth of locking shown in figure 5.2 is assumed. Implicit in this assumption is the speculation that the post-seismic slip associated with the 1906 earthquake (Thatcher, 1975) represents the initiation of our model TCALS. Thus, rapid strain accumulation on that portion of the San Andreas between SJB and Cholame is not assumed to have begun until 1906. Any estimates of stress on this portion of the fault will then represent an underestimate since we neglect the possibility of rapid strain accumulation before 1906. On the other hand, our calculations will represent an overestimate since we are neglecting the possibility of fault creep and small earthquakes ($M<6$). The only way to test these assumptions is to compare the predictions of our models with the observations.

The second portion of the initial stress field that existed in 1812 must have been related to the past earthquakes

and their effect upon the tectonic fields. At first glance the assignment of this portion of the initial stress appears impossible since little is known about earthquakes in California before this time. We may, however, make an educated guess at this portion of the field by using our knowledge of events subsequent to 1812. To do this we simply place a dislocation model at the site of a future earthquake with the same parameters as the earthquake which is to occur. However, we put the net slip equal and opposite to that of the future earthquake. If we do this for all the earthquakes which are to occur after 1812, then our model will give us nothing more than the fields due to the tectonic model. On the other hand, if we completely ignore the fact that strain had already accumulated for some earthquakes in 1812, then our initial conditions will not even be approximately correct. We have compromised and used the anti-moments (Andrews, 1975) for the 1812, 1857, 1872, and 1906 earthquakes (figure 5.13). The maximum shear stress and τ_{kk} for the initial conditions described above are shown in figures 5.14 and 5.15 respectively. The future sites of the large earthquakes (1812, 1857, 1872, and 1906) may be easily seen in the maximum shear stress profiles (figure 5.14) but the τ_{kk} do not show any consistent sign relation (at least for strike-slip events) with the site of future events as would be expected from a rock mechanical point of view (Chinnery and

Rogers, 1973). For this reason we shall simply plot the maximum shear stress contour in the following study of the stress history of California.

5.5 Stress History of California

We now wish to turn our model on, so to speak, with the initial conditions shown in figures 5.14 and 5.15. The development of the maximum shear stress from 1812 to the present is of interest to us here and will be shown in the years 1915, 1935, 1954, and 1973. During the first time period the depth of locking on the portion of the San Andreas north of the Tejon bend will be the same as that used in the model for the initial conditions. After 1906, however, model TCALS (figure 5.2) will be used.

In figure 5.17 we have plotted the maximum shear stress contours that result from the addition of (1) the tectonic stress accumulation (1812-1915), (2) the initial conditions (figures 5.14 and 5.15) and, (3) the earthquake strain release (1812-1915). The earthquakes for this time period are plotted in figure 5.16. As expected, the regions where the 1812, 1857, 1872, and 1906 earthquakes occurred are areas of low maximum shear stress at the end of the year 1915. Regions of high shear for the year 1915 are concentrated near the SJB bend and the Parkfield-Chalome region on the portion of the San Andreas north of the Tejon bend.

These high stress regions are probably end effects of the 1906 and 1857 earthquakes. By comparison,the southern portion of the model exhibits a rather uniform distribution of high shear (mostly along the San Jacinto fault) with the highest stresses being in the Borrego Mountain-Superstition Hills fault area (along the San Jacinto fault). However, local highs are associated with the intersection of the San Jacinto and San Gabriel faults and the region between the San Jacinto and San Andreas faults which is just south of the Banning-Mission Creek area.

The high shear region in the southern portion (south of 32°N) of our map (figure 5.17) represents a region in which our model is a failure. This may be seen by comparing figure 5.17 (1915) to figure 5.18 (1935). During the time period 1915-1935 no large earthquakes occurred in this region, yet the shear stress diminished. Thus, the high shear in figure 5.17 represents only the stress release due to earthquakes in this area and does not represent a stress accumulation. From the shear stress map in figure 5.17 we would choose the Sierra-Nevada fault region and the Santa Barbara Channel area as unlikely spots for future activity. This is seen to not be true in figure 5.18 where we have plotted the earthquake activity ($M \geq 5$) for the period 1916-1935. In fact, we may consider the coastal events and the Sierra-Nevada events as a proof of the failure of either our

initial conditions (figures 5.14-5.15) or the tectonic model (figure 5.2). On the other hand, the events on the San Jacinto and near Parkfield occur in regions of high shear predicted by our model.

We now add to the fields described above the strain accumulation due to model TCALS (figure 5.2) over the period 1916-1935 and the strain release for the large earthquakes of this period (table 5.1 and figure 5.18). The resultant shear stress for the end of 1935 is shown in figure 5.19. The high stress region near 32°N, 116.5°W is now diminished from its value for the year 1915. As described earlier this results from the earthquakes releasing more strain than was available from either the initial conditions or the tectonic model. The same argument may be put forth for the offshore high near Point Arguello (1927 M = 7.5 Point Arguello earthquake; Byerly, 1930) and the northernmost high near the Nevada-California border (this high is associated with the 1932 M = 7.3 Cedar Mountain earthquake; Richter, 1958). However, the high shear on the California-Nevada border lasts through the next two time periods and represents what we believe to be a high stress region. This area is about 30-40 km due east of Mono Lake and is probably an end effect of the 1932 event. The stress could be even higher for this region than indicated since we have effectively eliminated the end effects of the 1872 event by our choice of initial

conditions. Just south of this high is another local high which we believe to be the result of the high strain release in this area (concluded from strain contours not shown). The activity in this area is most likely due to an end effect of the 1872 Owens Valley event. A readjustment of initial conditions would probably allow our model to be more compatible with the activity in this region.

The virtual inactivity of the northern portion of the San Andreas during the period 1915-1935 resulted in a general tectonic strain accumulation over this period (figure 5.19). The same is true for the San Jacinto fault in the south even though three M = 6+ events occurred in its vicinity during the 1916-1935 period (figure 5.18).

The earthquakes ($M \geq 4$) for the following time period (1936-1955) are shown in figure 5.20. It is during this time period that activity in the Borrego Valley high shear area appears to increase. This is probably due to increased detection capabilities. However, the local high around the intersection of the San Jacinto and San Andreas faults is still inactive. The high shear region between SJB and Parkfield are also relatively inactive during this period. The same is true for the high shear region west of Mono Lake.

In 1955 (figure 5.21) we have essentially the same high stress regions that were present in 1935. The major difference

is the lower stress near the intersection of the White Wolf fault and the San Andreas. This is due primarily to the 1952 Kern County earthquake (Richter, 1958).

Now, however, the high shear regions represent areas of high future activity ($M \geq 4$) as shown in figure 5.22. The exception seems to be the high shear zone west of Mono Lake which is virtually surrounded by activity but is quiet during the 1956-1973 period. The same is true for a portion of the high shear zone between SJB and Cholame.

Adding the stress accumulation of our tectonic model and the stress release of the earthquakes over the next time period we obtain the present day shear stress contours for our model (figure 5.23). The primary high shear regions are (1) SJB (2) Parkfield-Cholome (3) the area 30-40 km east of Lake Mono (4) Borrego Valley (5) Superstition Mountain and (6) the area where the San Jacinto intersects the San Andreas (Cajon Pass region). These high order areas have existed since at least 1935 (figure 5.19) and represent regions of probable future activity (in terms of our model).

We are, of course, unable to predict that any of the high shear regions listed above will be the site of future large earthquakes. We do believe, however, that these areas deserve further study. This statement is especially true for the SJB-Parkfield and the Borrego Valley-Superstition Mountain regions since they represent the most extensive

high shear areas. Because of its proximity to San Bernadino, however, the high shear region near the intersection of the San Andreas and the San Jacinto faults could be the most potentially dangerous of all the high shear regions. The predicted highs for southern California (especially in the San Bernadino region) were also regions of high strain accumulation in the model presented by Smith and Van De Lindt (1969).

5.6 SJB-Cholame High Shear Zone

One of the major problems with neglecting certain forms of stress release (such as small earthquakes and fault creep) in a calculation aimed toward finding regions of high stress is the possibility that these other mechanisms may indeed release most of the stress in this region. The argument for creep and small earthquakes releasing most of the stress accumulation between SJB and Cholame has been put forth by Savage and Burford (1970) and Wesson et al. (1973). The most convincing piece of evidence in favor of this being the case is the general agreement between the fault creep (measured at the fault trace by alignment arrays) and the relative motion of geodetic stations located several kilometers apart on opposite sides of the fault (see top of figure 5.24). However, the uniqueness of this interpretation is open to question since the geodetic stations are all essentially the same distance away from the fault (about 7 km).

What is needed for this region is a high resolution triangulation arc which is capable of detecting thin zones of locking.

In the bottom of figure 5.24 we have plotted an alternative model to the non-locking model. This model was obtained using the two dimensional equations for a creeping fault which were derived in Chapter IV. Those results allow us to write the relative motion W of two stations a distance X on opposite sides of the fault in the form

$$5.1 \quad \frac{\Delta W}{b_2} = \frac{2}{\pi} \tan^{-1}\left(\frac{X}{d_2}\right) + \frac{\varepsilon}{\pi} \{\pi - 2 \tan^{-1}\left(\frac{X}{d_1}\right)\}$$

where $\varepsilon = b_1/b_2$, b_1 = fault creep, b_2 = relative plate motion at depth below the locked fault, d_1 = depth of the creeping section, and d_2 = depth to the bottom of the locked section. Given the observations ΔW (geodimeter data), b_1 (fault creep measured by alignment array), and the assumption that b_2 = 5 cm/year, we may use equation 5.1 to find a range of d_1 and d_2 which are consistent with the observations. We have chosen instead to find those d_1's and d_2's which are consistent with the creep and geodimeter data and which allow the fault creep to release all of the stress at the surface (on the fault trace). The additional constraint that the stress vanish on the fault at the surface is at least approximately true near Hollister (see figure 4.18) and we propose that it exists all along the creeping section

of the San Andreas from SJB to Cholame. This constraint is equivalent to the assumption that

$$\frac{b_1}{d_1} = \frac{b_2}{d_2} \qquad 5.2$$

The zone of locking obtained in this manner (trial and error solution of 5.1 and 5.2) is shown in the bottom of figure 5.24.

The region of locking just north of Parkfield (area of 1934 Parkfield earthquake) and the area between Parkfield and Cholame (1966 Parkfield earthquake) is very narow and would perhaps be non-existent if we had assumed a slower plate motion than 5 cm/year. On the other hand our model is indicative of at least 5 km of locking in the region extending northward from Bear Valley. South of Cholame the geodimeter data are indicative of a rapid increase in the depth of locking. The reader is reminded at this point that locking is intended to mean little or no motion with respect to the slipping section of the fault.

The pattern of locking described above is in general agreement with the pattern of microearthquake activity for this region (figure 5.25). It is impossible to argue, however, that this agreement of the microearthquake pattern with our pattern of partial locking is in support of our model.

The only two trinagulation arcs in this region of California fall at the northern (Hollister arc) and southern (Cholame arc) ends of the region of interest. The data from the Cholame arc (figures 5.27 and 5.28) is indicative of the edge effect that would be expected from the rapid increase in the depth of locking inferred to occur near Cholame (figure 5.24). Savage and Burford (1970) have suggested that this effect could be due to slip on a large surface associated with the 1934 earthquake (top of figure 5.26). Two alternative models are shown in the center (solid line in figures 5.27 and 5.28) and bottom (dashed line in figures 5.27 and 5.28) of figure 5.26.

The center model represents slip in the region of the 1934 earthquake and 10 km below the region where the 1966 Parkfield earthquake occurred (between Parkfield and Cholame). The bottom model represents a thin (5 km) locked zone (in general agreement with the shallow depth determined by Aki (1967)) with a deep edge south of Cholame.

The point to be made with these models is that (a) the component which is the component indicative of an edge effect, does not allow us to determine whether the edge is north or south of Cholame and (b) the Cholame arc data is consistent with (but not proof of) a rapid increase in the depth of locking south of Cholame, As pointed out earlier, the observations of Cherry and Savage (1972) and Howard (1968) may also be indicative of the edge effect near Cholame.

5.7 Conclusions

In summary, we have made dislocation models which we consider to be representative of at least a portion of the tectonics in California. Although the models presented are plagued by a large number of assumed parameters (and extra plates), the major features will be contributed by the San Andreas-Tejon bend-San Jacinto portion of the tectonic model. The microplates used (Great Valley, Mojave, and San Jacinto plates) are hypothetical and are introduced to explain a portion of the zone of activity extending from the Santa Barbara channel into Nevada and the eastern Mojave desert. It was tempting at this point to include the possible effects of other plates such as a Salinian block (Clark, 1930) that could be used to explain much of the coastal activity (from Point Arguello to San Francisco) which seems to end in the vicinity of San Francisco Bay (Bolt et al., 1968). We have, however, avoided this temptation and have restricted ourselves to a model which represents a minor change from the Tejon model presented in Chapter IV. The point that we have concluded from the models presented, however, is that the direction of relative plate motion in the vicinity of the Tejon bend is an important parameter in determining the tectonics of the offshore region (Santa Barbara channel-Point Arguello area).

In testing our model by adding to it the stress release

of the large earthquakes we find, naturally, that our model is incapable of explaining the offshore activity. We cannot, however, eliminate our model for the interface between the Great Valley and North American plates since the problems we have there may be due to our initial conditions.

Our computation of the stress history of California has predicted several high shear zones which we believe deserve further study. In particular we believe that a high resolution triangulation arc (with elements of 1 km or less) should be established across the San Andreas between the Holister arc and the Cholame arc (see Savage and Burford (1970)). A likely area would be north of Bear Valley and south of SJB (figure 5.24). The establishment of this arc would aid in the resolution of thin zones of locking. The possibility that many of the large events in this region could have been very thin (e.g. the 1906 San Francisco earthquake has been suggested to have been 3 km (Knopoff, 1958) to 5 km (Chinnery, 1961) wide while the 1966 Parkfield earthquake (Aki, 1967) could have been of a similar width) must be taken into account.

In terms of populated areas we believe the San Jacinto-San Andreas intersection could be the dangerous of the high shear regions predicted because of its proximity to the San Bernadino region.

Table 5.1

Tectonic Model of California

Plates		Latitude	Longitude	Depth
Pacific-Great Valley	1	39.00	124.00	0.
	2	37.25	122.08	0.
	3	36.50	121.25	0.
	4	35.25	119.64	0.
	5	35.00	119.46	0.
	6	34.94	119.27	0.
	7	34.90	119.23	0.
	8	34.90	119.23	80.
	9	34.94	119.27	70.
	10	35.00	119.46	60.
	11	35.25	119.64	40.
Cholame	12	35.72	120.26	40.
Cholame	13	35.72	120.26	10.
	14	36.50	121.25	10.
	15	37.25	122.08	20.
	16	37.25	122.08	40.
Bodega Head	17	38.30	123.22	40.
	18	38.30	123.22	15.
	19	39.00	124.00	15.
$B_r = 5.$, $B_\phi = 135°$, $B_z = 0$ (assuming 5 cm/yr for 100 years)				
Great Valley-North America	1	35.74	118.25	0.
	2	40.00	118.86	0.
	3	40.00	118.86	80.
	4	35.74	118.25	80.
$B_r = 1.$, $B_\phi = -45°$, $B_z = 0$ (1 cm/yr for 100 years)				
Pacific-San Jacinto	1	34.17	117.34	0.
	2	31.00	113.70	0.
	3	31.00	113.70	15.
	4	34.17	117.34	15.
$B_r = 4.$, $B_\phi = 135°$, $B_z = 0$ (4 cm/yr for 100 years)				
San Jacinto-North America	1	33.90	116.25	0.
	2	31.00	112.85	0.
	3	31.00	112.85	15.
	4	33.90	116.25	15.
$B_r = 2.$, $B_\phi = 135°$, 0. (2 cm/yr for 100 years)				

Table 5.1 (cont'd)

Great Valley-Mojave	1	34.90	119.23	0.
	2	35.74	118.25	0.
	3	35.74	118.25	80.
	4	34.90	119.23	80.

Model TCALF - B_r = 1.12, B_ϕ = 71°, B_z = 0.
Model TCALS - B_r = .509, B_ϕ = 124°, B_z = 0.

Mojave-North America	1	35.74	118.25	0.
	2	33.90	116.25	0.
	3	33.90	116.25	80.
	4	35.74	118.25	80.

Model TCALF - B_r = 1.80, B_ϕ = 101.3°, B_z = 0.
Model TCALS - B_r = 1.50, B_ϕ = 131°, B_z = 0.

Pacific-Mojave	1	34.90	119.23	0.
	2	34.76	118.55	0.
	3	34.64	118.23	0.
	4	34.17	117.34	0.
	5	34.17	117.34	80.
	6	34.64	118.23	80.
	7	34.76	118.55	80.
	8	34.90	119.23	80.

Model TCALF - B_r = 4.61, B_ϕ = 122.5°, B_z = 0.
Model TCALS - B_r = 4.50, B_ϕ = 134°, B_z = 0.

Mojave-San Jacinto	1	34.17	117.34	0.
	2	33.90	116.25	0.
	3	33.90	116.25	80.
	4	34.17	117.34	80.

Model TCALF - B_r = 1.12, B_ϕ = 71°, B_z = 0.
Model TCALS - B_r = .51, B_ϕ = 124°, B_z = 0.

Table 5.2

California Earthquakes ($M \geq 6$)

Event #	Date	δ(°)	λ(°)	L(km)	$\Delta\bar{\mu}$ (meters)	Latitude	Longitude	ϕ(°)	M
1	1812	45.	-135.	80.	2.15	34.20	120.00	-110.	7.8
2	1836	90.	180.	55.	1.78	37.90	122.30	35.	7.0
3	1838	90.	180.	12.	.83	37.60	122.50	38.	7.5
4	1857	90.	180.	186.	3.27	35.40	119.75	70.	7.8
	1857	90.	180.	111.	2.52	34.50	118.20	45.	
	1861	90.	180.	1.	.24	37.75	121.96	20.	6.0
	1865	90.	180.	10.	.76	37.05	121.80	45.	6.0
5	1868	90.	180.	47.	1.65	37.70	122.10	35.	7.0
6	1872	45.	135.	153.	2.97	36.70	118.30	18.	7.5
	1890	90.	180.	11.	.80	36.90	121.61	50.	6.0
7	1892	90.	180.	100.	2.40	31.40	116.00	78.	7.4
8	1899	80.	190.	100.	2.40	33.60	116.80	45.	7.4
9	1903	90.	180.	100.	2.40	31.50	115.00	78.	7.4
10	1906	90.	180.	435.	5.00	38.00	123.00	35.	8.3
11	1906	90.	180.	39.	1.50	32.50	115.50	45.	6.5
12	1907	70.	200.	20.	1.07	34.20	117.10	60.	6.0
13	1908	45.	100.	39.	1.50	36.00	117.00	135.	6.5
14	1910	90.	180.	20.	1.07	33.70	117.40	45.	6.0
15	1911	90.	180.	45.	1.61	37.20	121.70	34.	6.6
16	1915	90.	180.	29.	1.30	32.80	115.50	35.	6.2
17	1915	90.	180.	29.	1.30	32.80	115.50	35.	6.2
18	1915	90.	180.	65.	1.93	32.00	115.00	40.	7.1
19	1916	45.	-60.	20.	1.07	34.90	118.90	-45.	6.0
20	1918	75.	200.	58.	1.83	33.75	117.00	45.	6.8
21	1922	90.	180.	39.	1.50	35.75	120.25	45.	6.5
22	1923	90.	180.	29.	1.30	34.00	117.25	40.	6.2
23	1925	45.	-135.	30.	1.31	34.30	119.80	-110.	6.3
24	1926	90.	180.	23.	1.15	36.70	122.00	45.	6.1
25	1926	90.	180.	23.	1.15	36.70	122.00	45.	6.1
26	1927	60.	200.	20.	1.07	37.50	118.70	10.	6.0
27	1927	45.	-120.	117	2.60	34.50	121.50	-90.	7.5
28	1932	45.	135.	102	2.42	38.75	118.00	0.	7.2
29	1933	90.	180.	30.	1.31	33.60	118.00	45.	6.3
30	1933	45.	135.	23.	1.15	39.20	119.00	0.	6.1
31	1934	45.	90.	1.5	.29	38.00	118.50	-45.	6.5

Table 5.2 (cont'd)

Event #	Date	δ(°)	λ(°)	L(km)	$\Delta\bar{\mu}$ (meters)	Latitude	Longitude	ϕ(°)	M
32	1934	90.	180.	20.	1.07	35.80	120.40	40.	6.0
33	1934	90.	180.	39.	1.50	32.30	115.50	45.	6.5
34	1934	90.	180.	89.	2.26	32.00	114.70	45.	7.1
35	1935	90.	180.	20.	1.07	33.50	116.50	45.	6.0
36	1940	90.	180.	52.	1.73	32.70	115.50	40.	6.7
37	1941	90.	180.	20.	1.07	31.70	115.10	45.	6.0
38	1941	90.	180.	20.	1.07	37.60	118.70	40.	6.0
39	1942	90.	180.	40.	1.52	33.00	116.00	50.	6.5
40	1946	45.	130.	30.	1.31	35.70	118.10	180.	6.3
41	1947	90.	0.	34.	1.40	35.00	116.60	-75.	6.4
42	1948	90.	180.	39.	1.50	33.90	116.40	45.	6.5
43	1952	45.	-45.	70.	2.00	35.00	119.03	-50.	7.7
44	1952	45.	-45.	23.	1.15	35.10	118.90	-50.	6.0
45	1952	45.	-45.	23.	1.15	35.00	119.00	-50.	6.3
46	1952	45.	-45.	20.	1.07	35.00	118.50	-50.	6.0
47	1952	45.	-45.	39.	1.50	35.00	119.00	-50.	6.5
48	1952	45.	-45.	20.	1.07	35.50	118.50	-10.	6.0
49	1952	90.	180.	20.	1.07	35.80	121.20	55.	6.0
50	1954	90.	180	29.	1.29	33.30	116.20	78.	6.2
51	1954	90.	180.	20.	1.07	31.50	116.00	78.	6.0
52	1954	90.	180.	30.	1.31	31.50	116.00	78.	6.3
53	1956	90.	180.	58.	1.83	31.70	115.90	78.	6.8
54	1956	90.	180.	23.	1.15	31.70	115.90	78.	6.1
55	1956	90.	180.	23.	1.15	31.50	115.50	78.	6.3
56	1956	90.	180.	34.	1.40	31.50	115.50	78.	6.4
57	1959	45.	135.	23.	1.15	39.10	118.80	0.	6.1
58	1959	45.	135.	29.	1.29	39.00	119.00	0.	6.2
59	1968	90.	180.	39.	1.50	33.10	116.10	45.	6.5
60	1971	52.	-45.	14.	.90	34.40	118.40	67.	6.4
61	1973	49.	-70.	20	1.07	34.00	119.00	69.	6.0

Figure 5.1

Microplate structure for tectonic model of California. The primary features of the model are along: (1) the San Andreas fault in the north (2) the San Jacinto fault in the south and (3) the San Andreas in the Tejon bend region. Secondary features used to explain seismicity and/or strain accumulation determined geodetically include (1) the Great Valley plate, (2) the Mojave plate and (3) the San Jacinto plate. The most important variable in this model is the direction of relative motion across the Tejon bend. Two versions of this model will be presented.

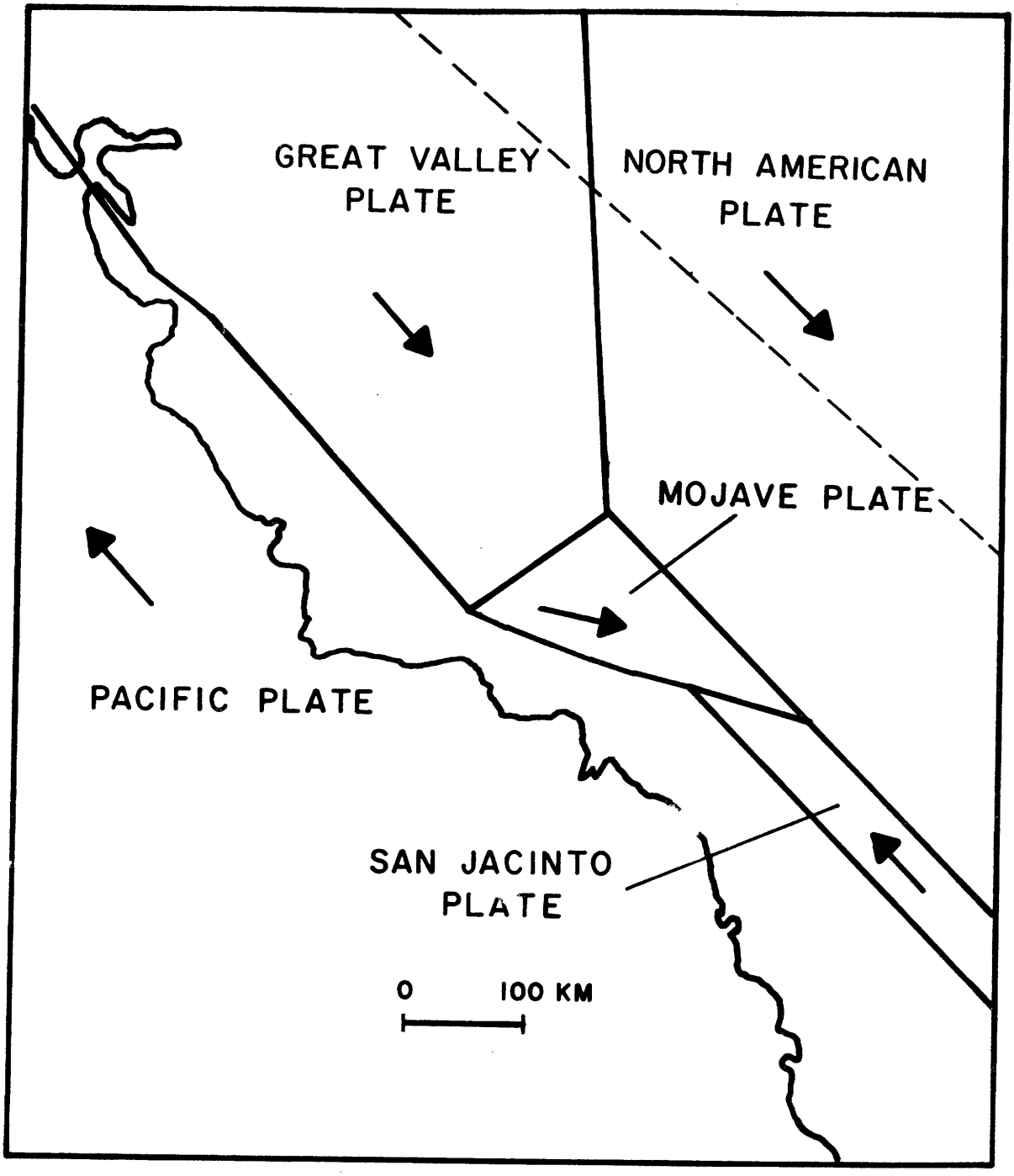
GREAT VALLEY PLATE
NORTH AMERICAN PLATE
MOJAVE PLATE
PACIFIC PLATE
SAN JACINTO PLATE
0
100 KM

Figure 5.1

Figure 5.2

Oblique view of tectonic model of California. Shaded areas are used to represent locking. Two versions of the model are considered in this chapter. Model TCALS represents the case in which the motion of the Mojave plate is primarily in a direction parallel to S45°E. Model TCALF considers the case in which the Mojave plate moves in a more easterly direction.

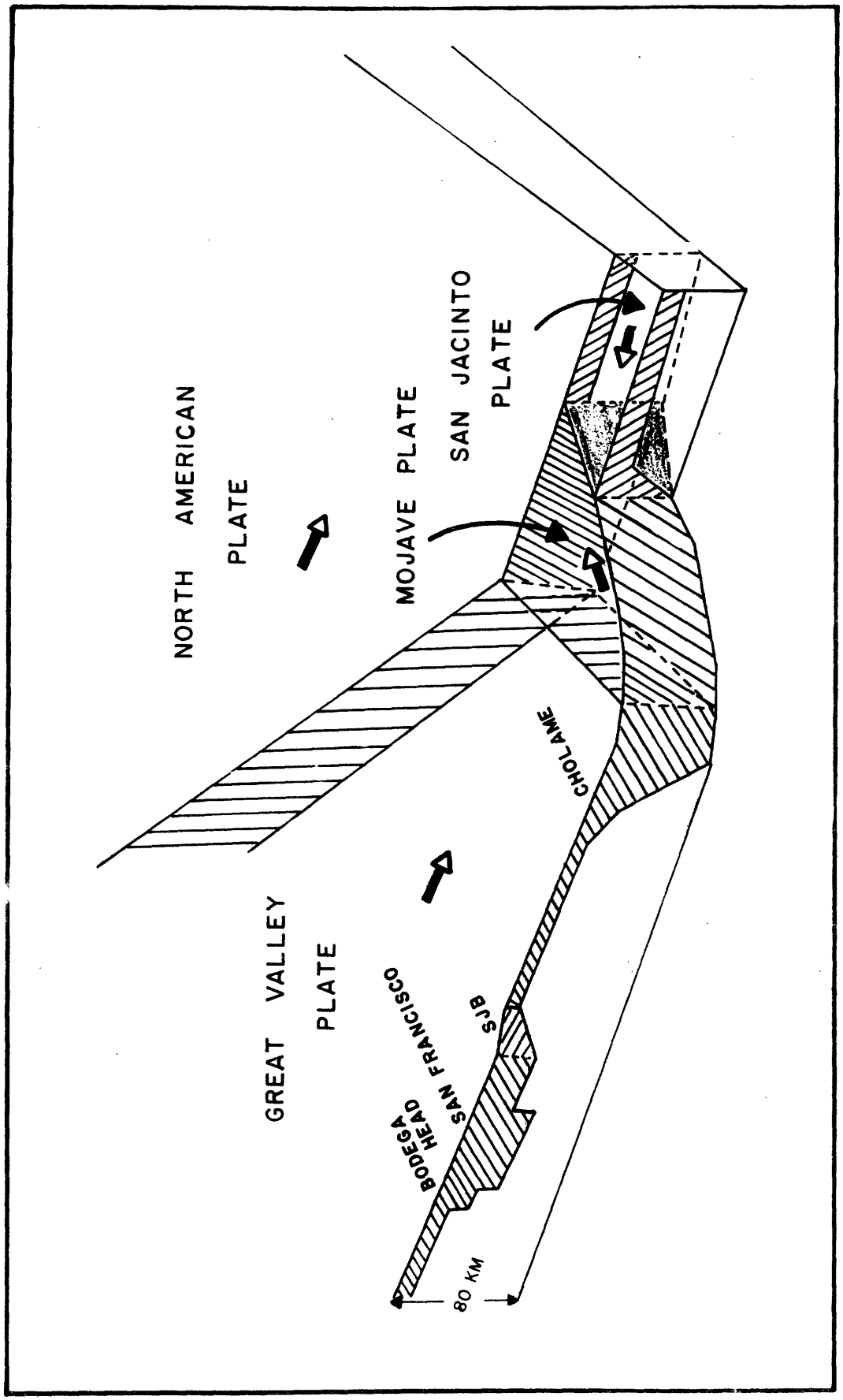
NORTH AMERICAN PLATE
MOJAVE PLATE
SAN JACINTO PLATE
GREAT VALLEY PLATE
CHOLAME
SJB
SAN FRANCISCO
BODEGA HEAD
80 KM

Figure 5.2

Figures 5.3-5.8

Strains, stresses, and principal stress directions for model TCALS (figure 5.2).

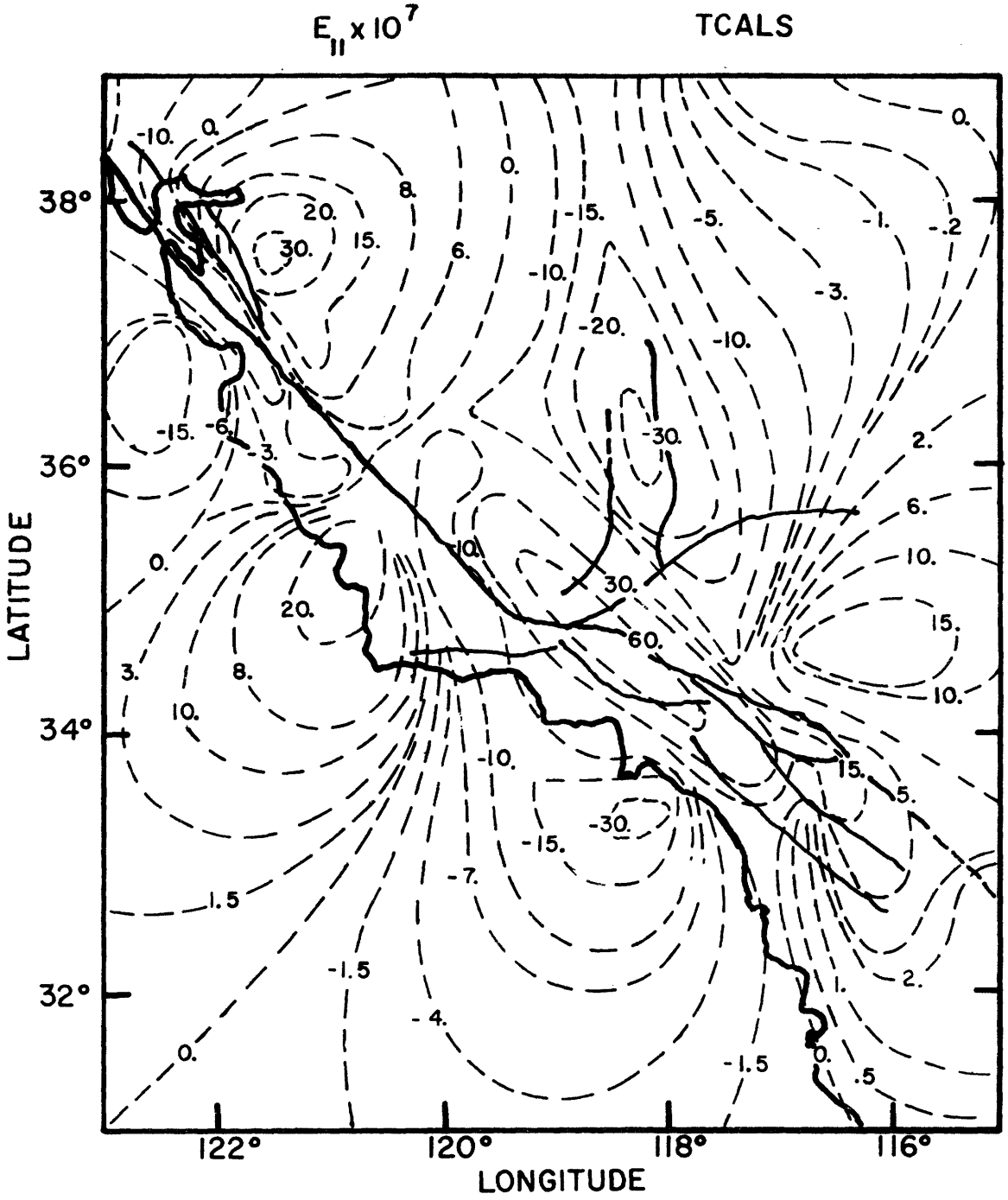
$E_{11} \times 10^7$
TCALS
LATITUDE
LONGITUDE
38°
36°
34°
32°
122°
120°
118°
116°
-10.
0.
8.
20.
30.
15.
6.
0.
-15.
-10.
-20.
-5.
-1.
-.2
-3.
-10.
-15.
-6.
-3.
-30.
2.
6.
10.
0.
20.
10.
30.
60.
15.
3.
8.
10.
10.
-10.
15.
5.
-30.
-15.
-7.
1.5
-1.5
-4.
2.
1.
0.
-1.5
0.
.5

Figure 5.3

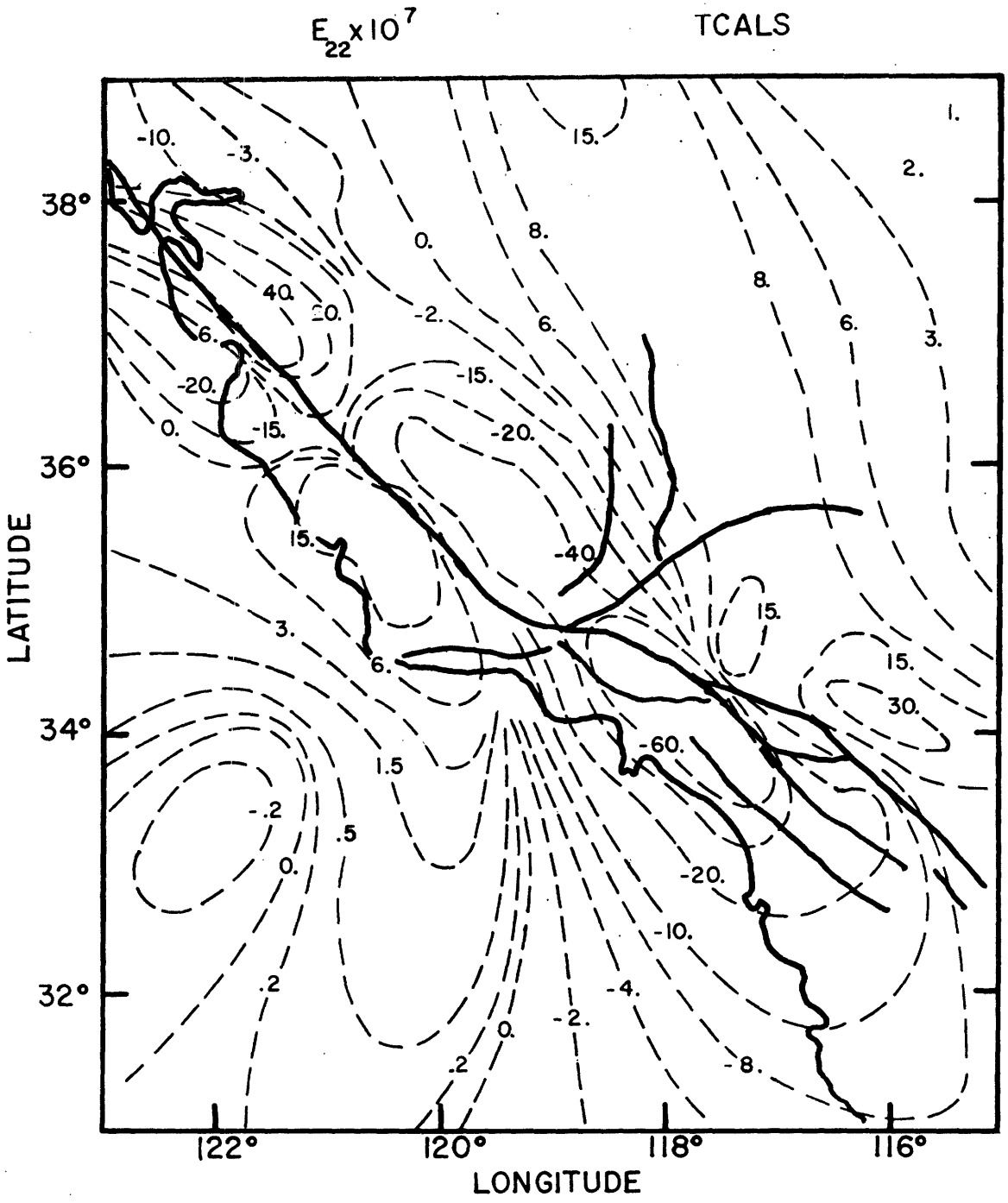
$E_{22} \times 10^7$
TCALS
LATITUDE
LONGITUDE
38°
36°
34°
32°
122°
120°
118°
116°
-10.
-3.
15.
1.
2.
0.
8.
40.
20.
-2.
6.
3.
-20.
-15.
-40.
-60.
30.
.5
1.5
.2
-4.
-8.

Figure 5.4

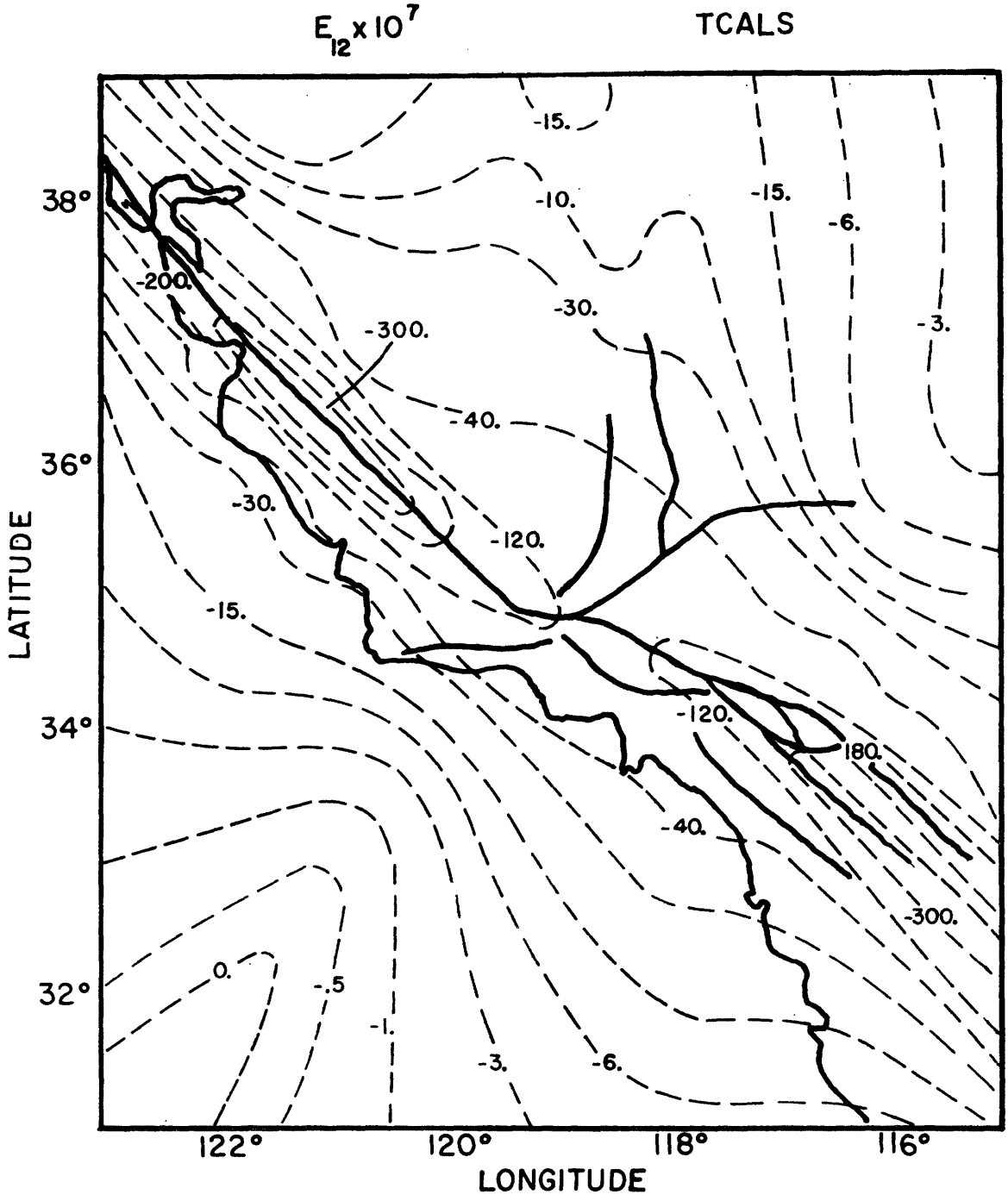
$E_{12} \times 10^7$
TCALS
-15.
-10.
-15.
-6.
-200.
-30.
-3.
-300.
-40.
-30.
-120.
-15.
-120.
180.
-40.
-300.
0.
-.5
-1.
-3.
-6.
38°
36°
34°
32°
LATITUDE
122°
120°
118°
116°
LONGITUDE

Figure 5.5

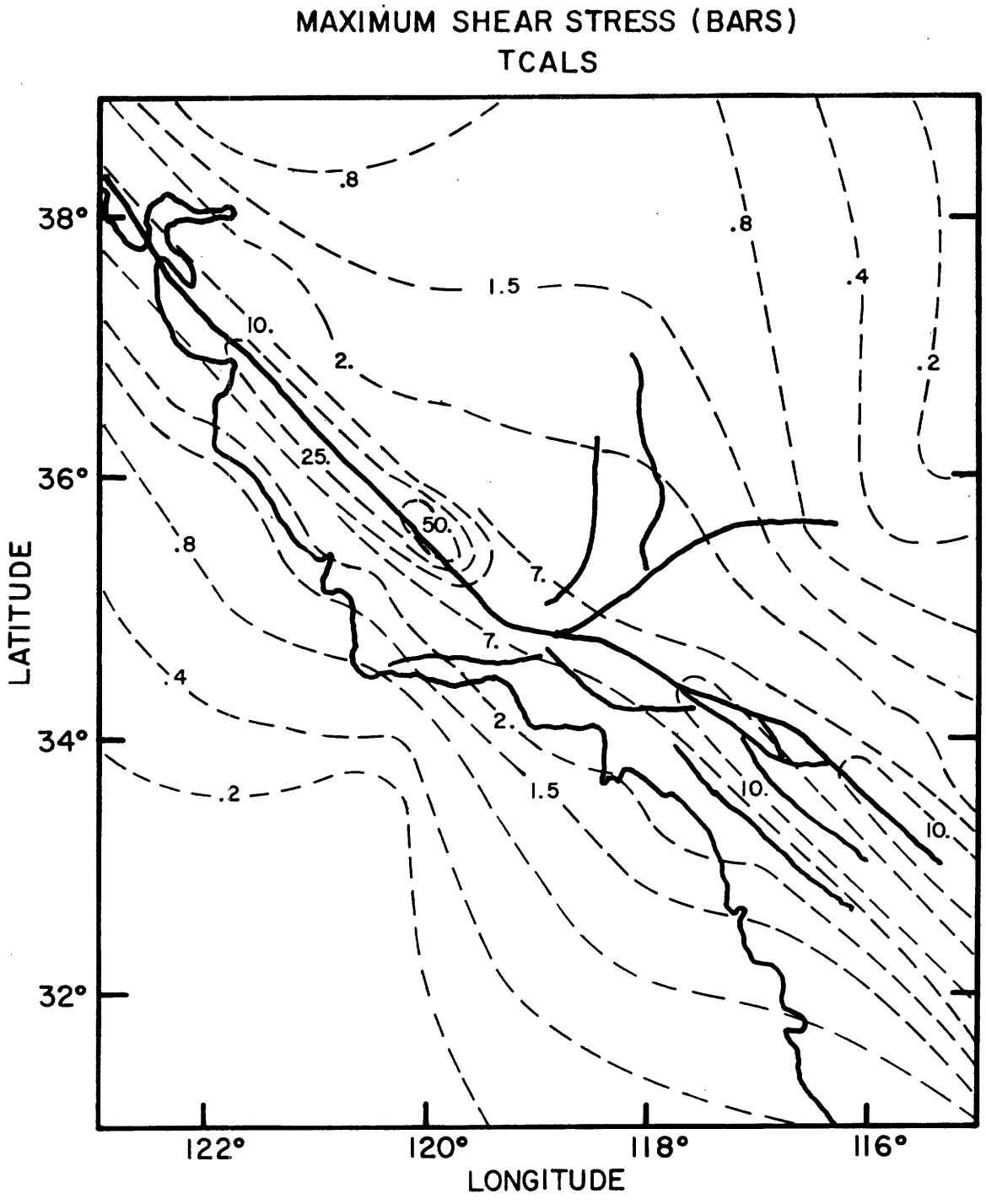
MAXIMUM SHEAR STRESS (BARS)
TCALS
38°
36°
34°
32°
LATITUDE
122°
120°
118°
116°
LONGITUDE
.8
1.5
10.
2.
25.
50.
7.
.4
.2

Figure 5.6

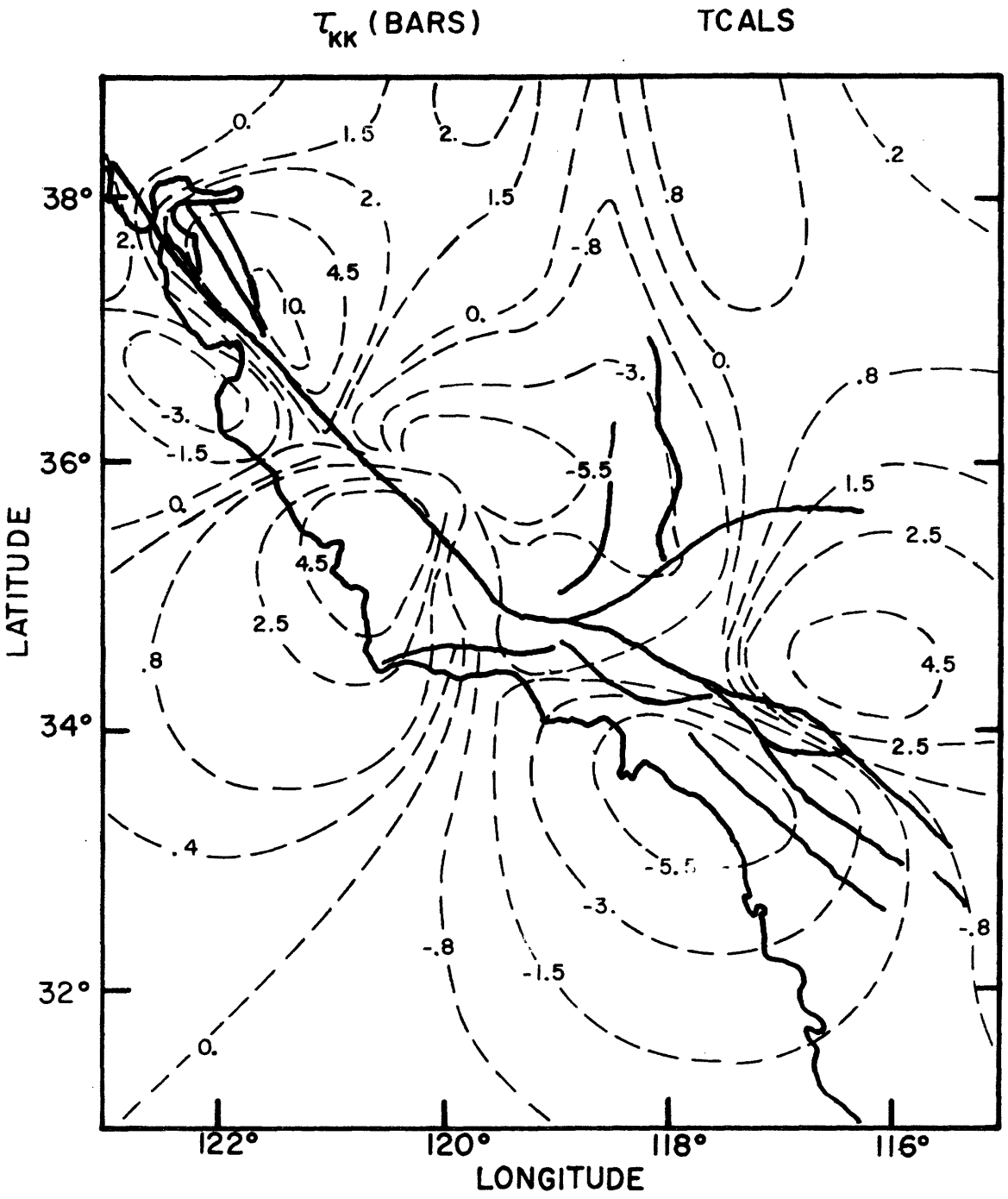
τ_{KK} (BARS)
TCALS
LATITUDE
LONGITUDE
38°
36°
34°
32°
122°
120°
118°
116°
0.
1.5
2.
.2
.8
-.8
4.5
10.
-3.
-1.5
-5.5
2.5
.4
-1.5

Figure 5.7

PRINCIPAL STRESSES

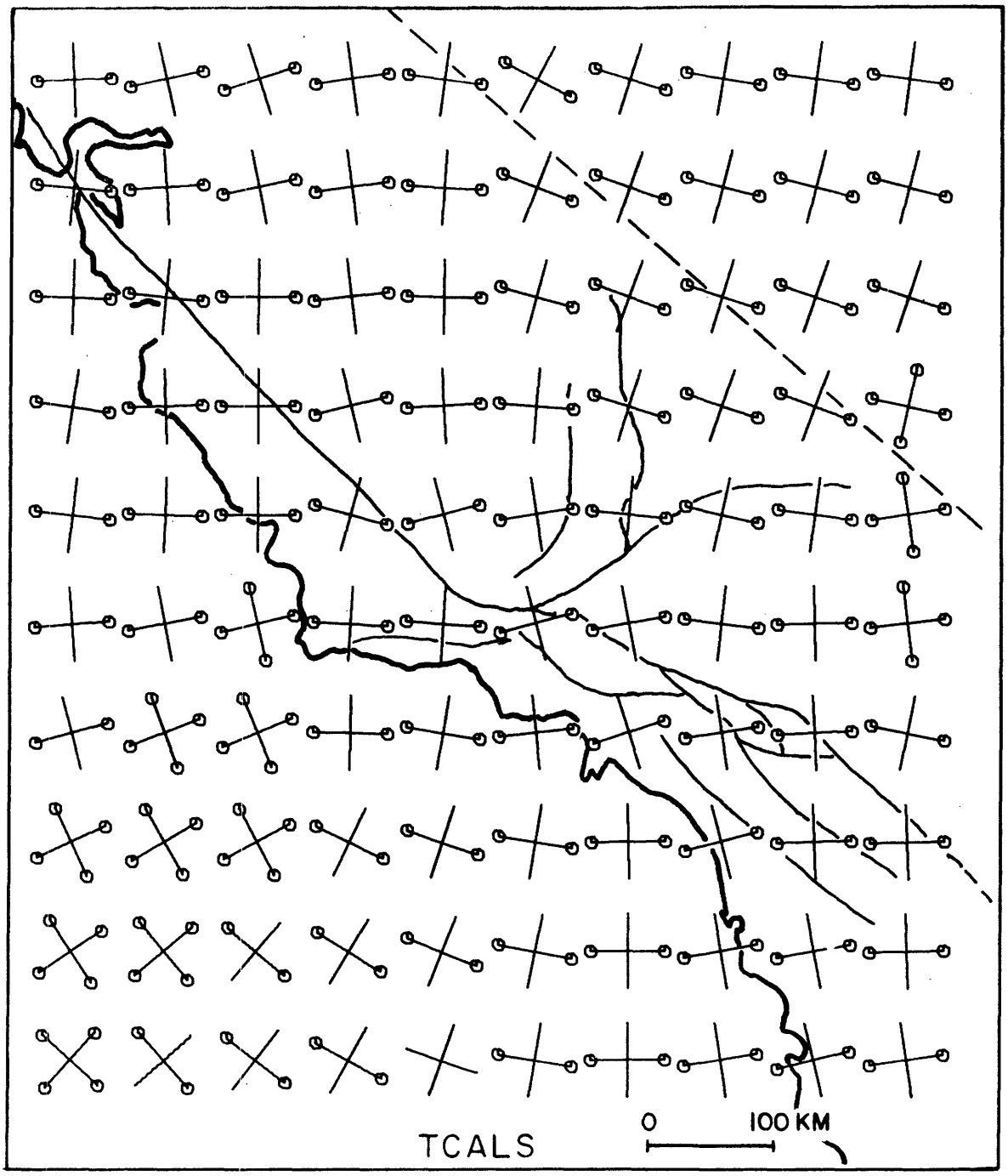

Figure 5.8

Figure 5.9-5.12

Strains (E_{11} and E_{22}), τ_{kk}, and principal stress directions for model TCALF.

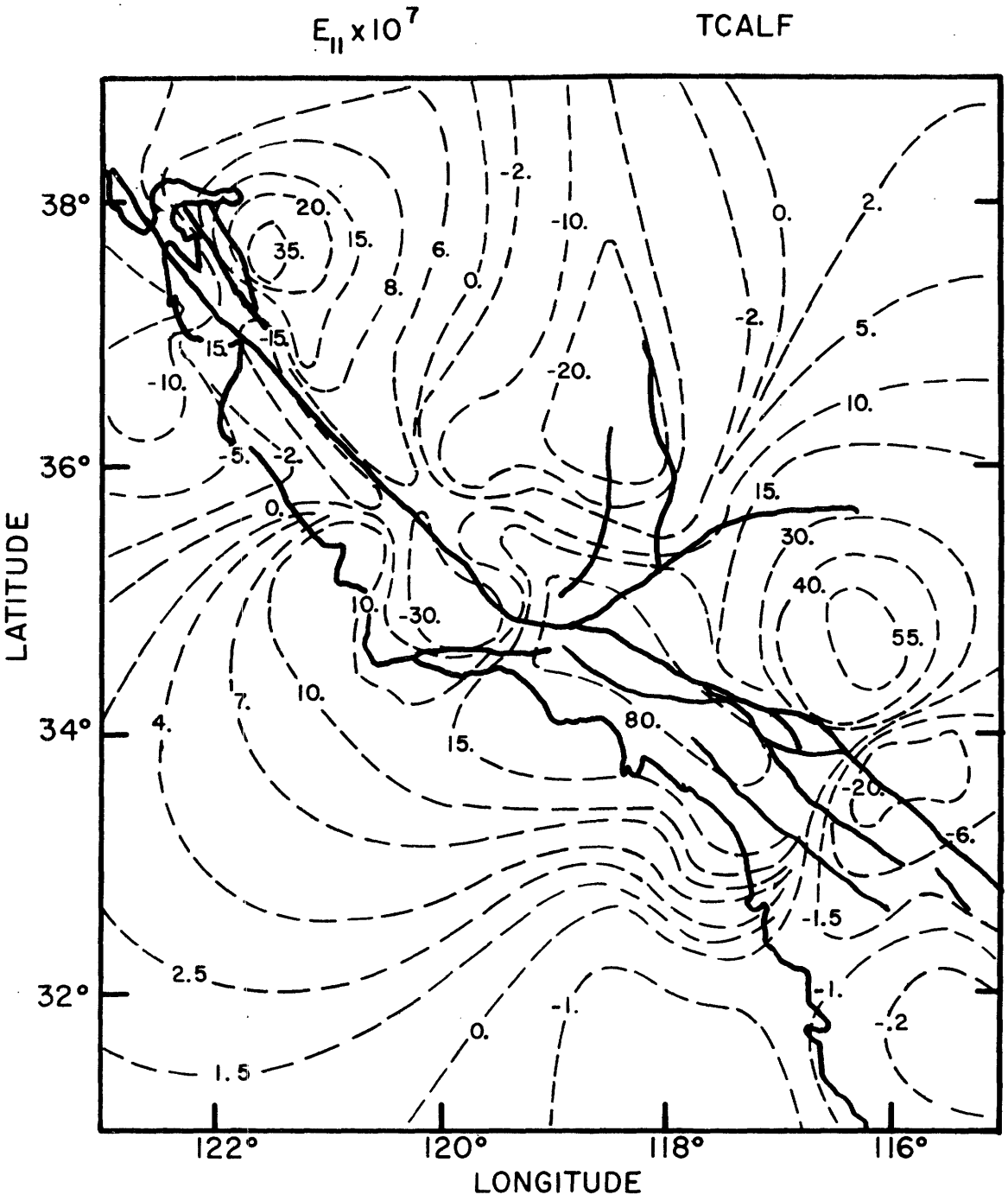
$E_{11} \times 10^7$
TCALF
38°
36°
34°
32°
LATITUDE
122°
120°
118°
116°
LONGITUDE
20.
35.
15.
6.
8.
0.
-2.
-10.
-15.
-5.
-30.
10.
7.
4.
2.5
1.5
-20.
0.
2.
5.
30.
40.
55.
80.
-6.
-1.5
-1.
-.2

Figure 5.9

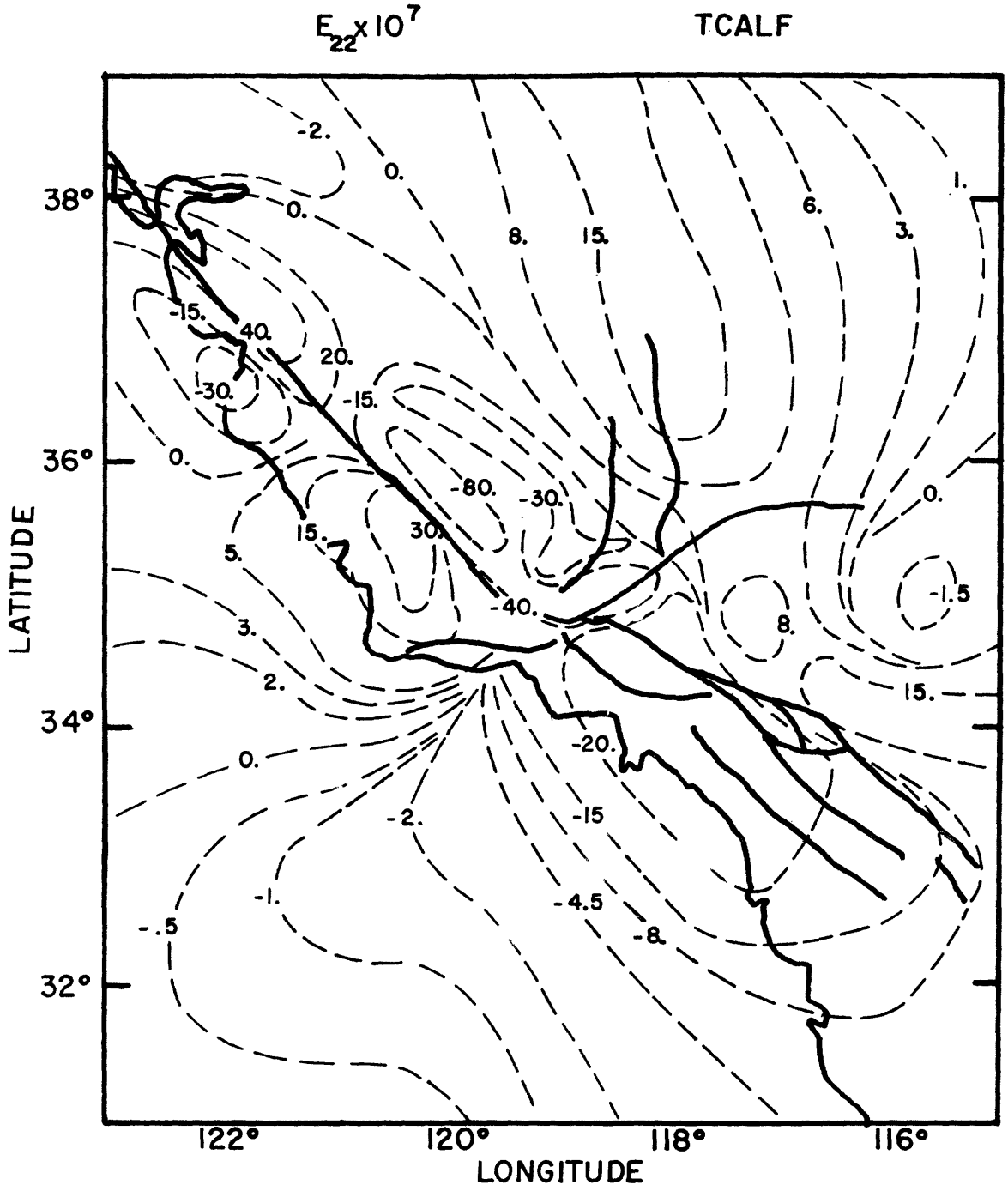
$E_{22} \times 10^7$
TCALF
-2.
0.
0.
8.
15.
6.
3.
1.
38°
-15.
40.
20.
-30.
-15.
36°
0.
-80.
-30.
0.
15.
30.
5.
-40.
-1.5
8.
3.
2.
15.
34°
0.
-20.
-2.
-15
-1.
-4.5
-.5
-8.
32°
LATITUDE
122°
120°
118°
116°
LONGITUDE

Figure 5.10

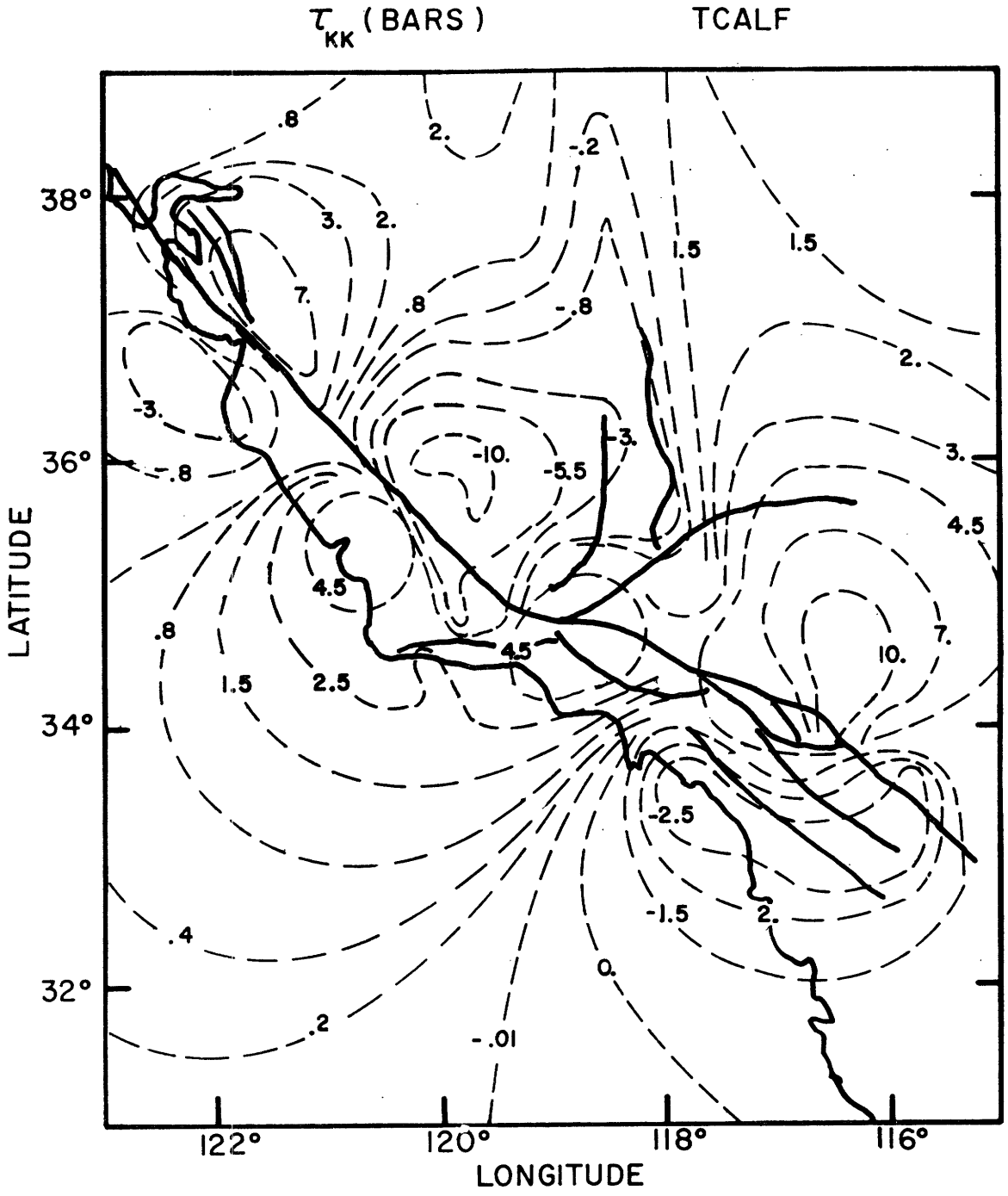
τ_{KK} (BARS)
TCALF
38°
36°
34°
32°
LATITUDE
122°
120°
118°
116°
LONGITUDE
.8
2.
-.2
3.
2.
1.5
1.5
7.
.8
-.8
2.
-3.
-.8
-10.
-5.5
-3.
3.
4.5
4.5
.8
4.5
7.
10.
1.5
2.5
-2.5
-1.5
2.
.4
0.
.2
-.01

Figure 5.11

PRINCIPAL STRESSES

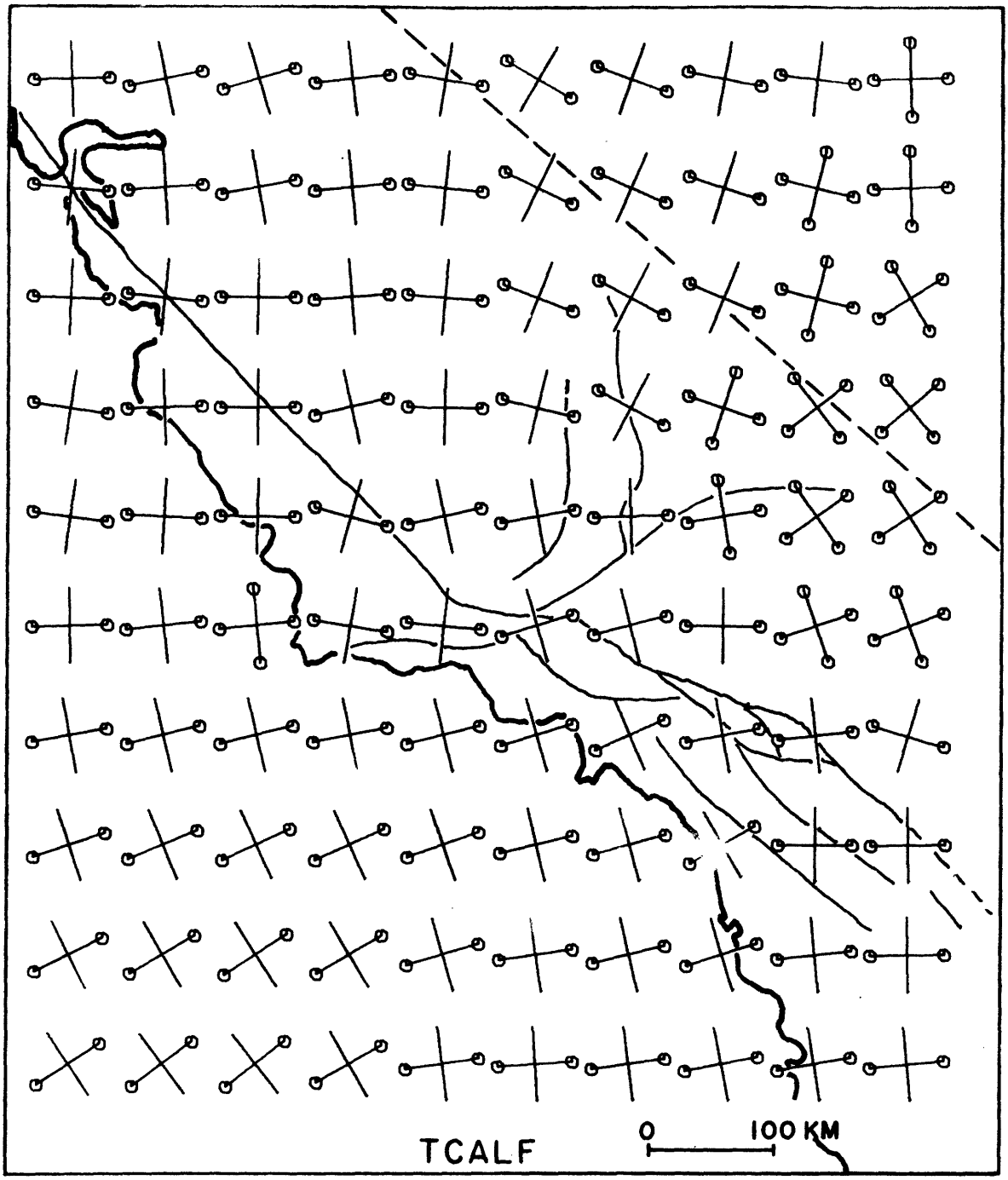

Figure 5.12

Figure 5.13

Plot of many of the large earthquakes since 1812 (see table 5.1 for assigned earthquake parameters and event numbers). Events 1, 4, 8, and 10 are used to set up the initial stresses contoured in figures 5.14 and 5.15.

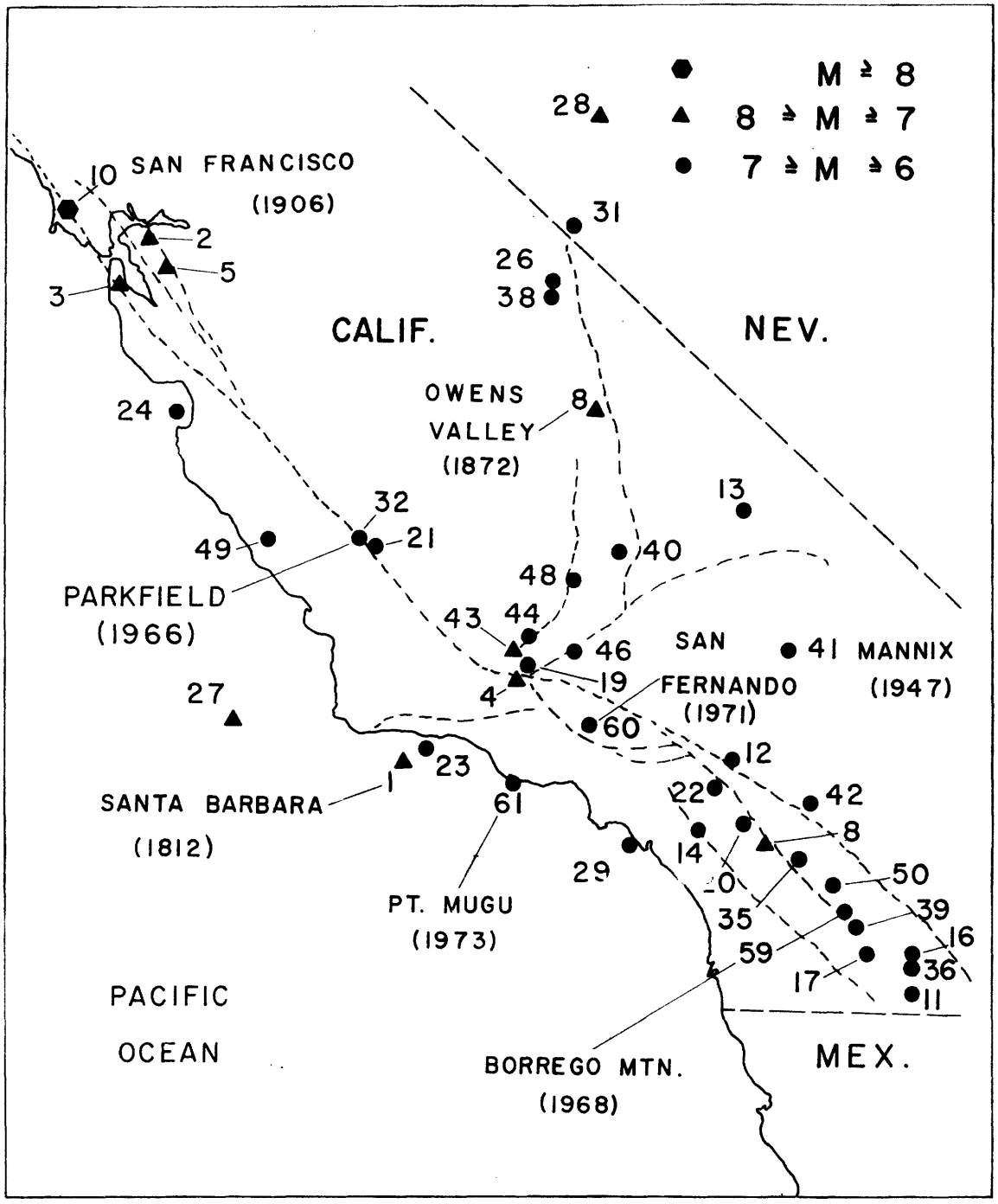
M ≥ 8
8 ≥ M ≥ 7
7 ≥ M ≥ 6
SAN FRANCISCO
(1906)
CALIF.
NEV.
OWENS
VALLEY
(1872)
PARKFIELD
(1966)
SAN
FERNANDO
(1971)
MANNIX
(1947)
SANTA BARBARA
(1812)
PT. MUGU
(1973)
BORREGO MTN.
(1968)
PACIFIC
OCEAN
MEX.

Figure 5.13

Figures 5.14 and 5.15

Maximum shear stress (bars) and τ_{kk} for initial conditions (1812). High shear regions in figure 5.14 are sights of future earthquakes (1812, 1857, 1872, and 1906 events in Table 5.1).

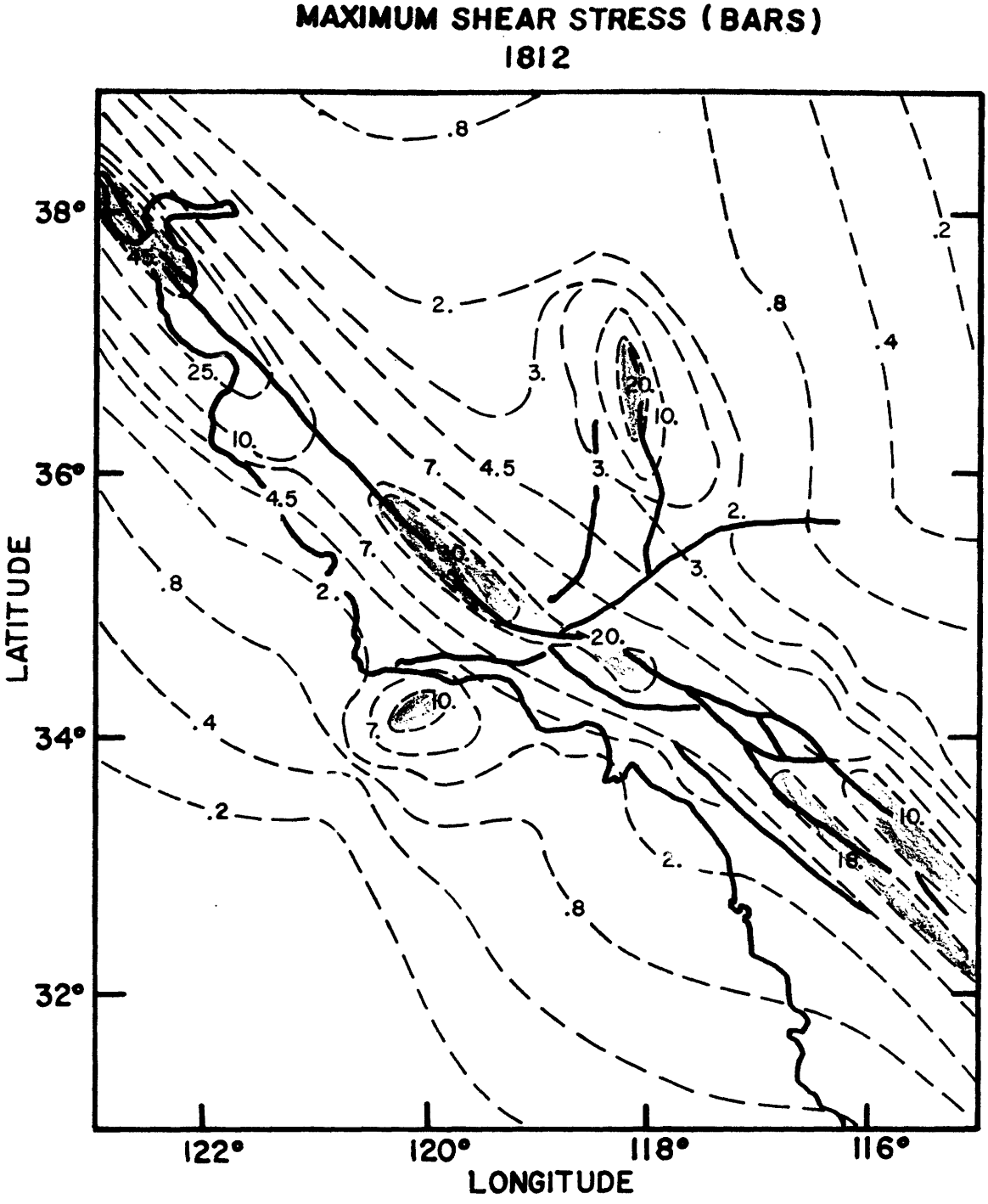
MAXIMUM SHEAR STRESS (BARS)
1812
38°
36°
34°
32°
LATITUDE
122°
120°
118°
116°
LONGITUDE
.8
2.
3.
.2
.4
.8
25.
10.
20.
10.
7.
4.5
4.5
3.
2.
7.
10.
3.
.8
2.
20.
10.
7.
.4
.2
10.
2.
18.
.8

Figure 5.14

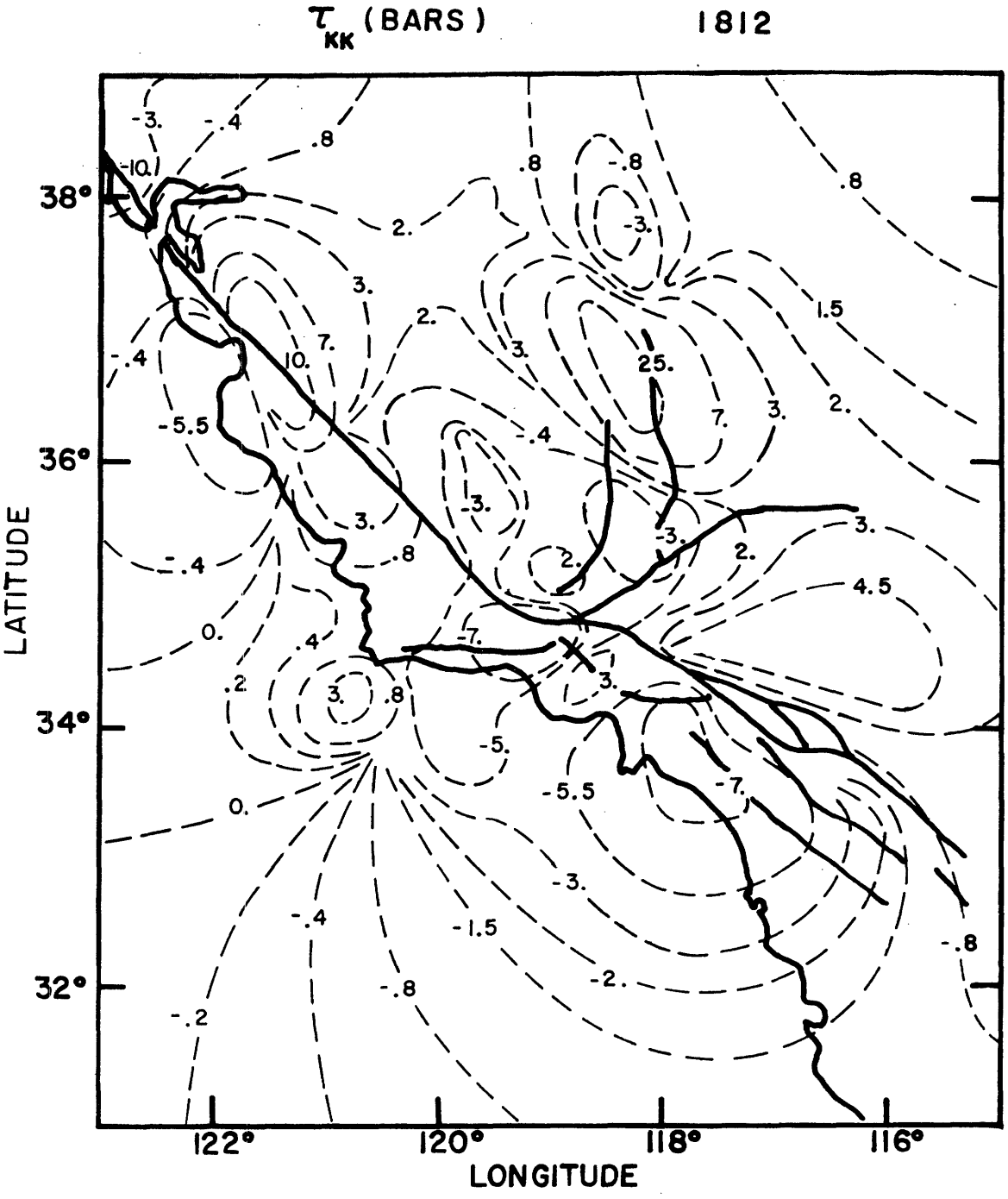
τ_{KK} (BARS) 1812
38°
36°
34°
32°
LATITUDE
122°
120°
118°
116°
LONGITUDE

Figure 5.15

Figure 5.16

Locations of large earthquakes in California during the period 1812-1915. Dark circles represent events of magnitude greater than or equal to 6 and less than 7, triangles represent events of magnitude greater than or equal to 7 and less than 8, and squares are for events of magnitude 8 or greater.

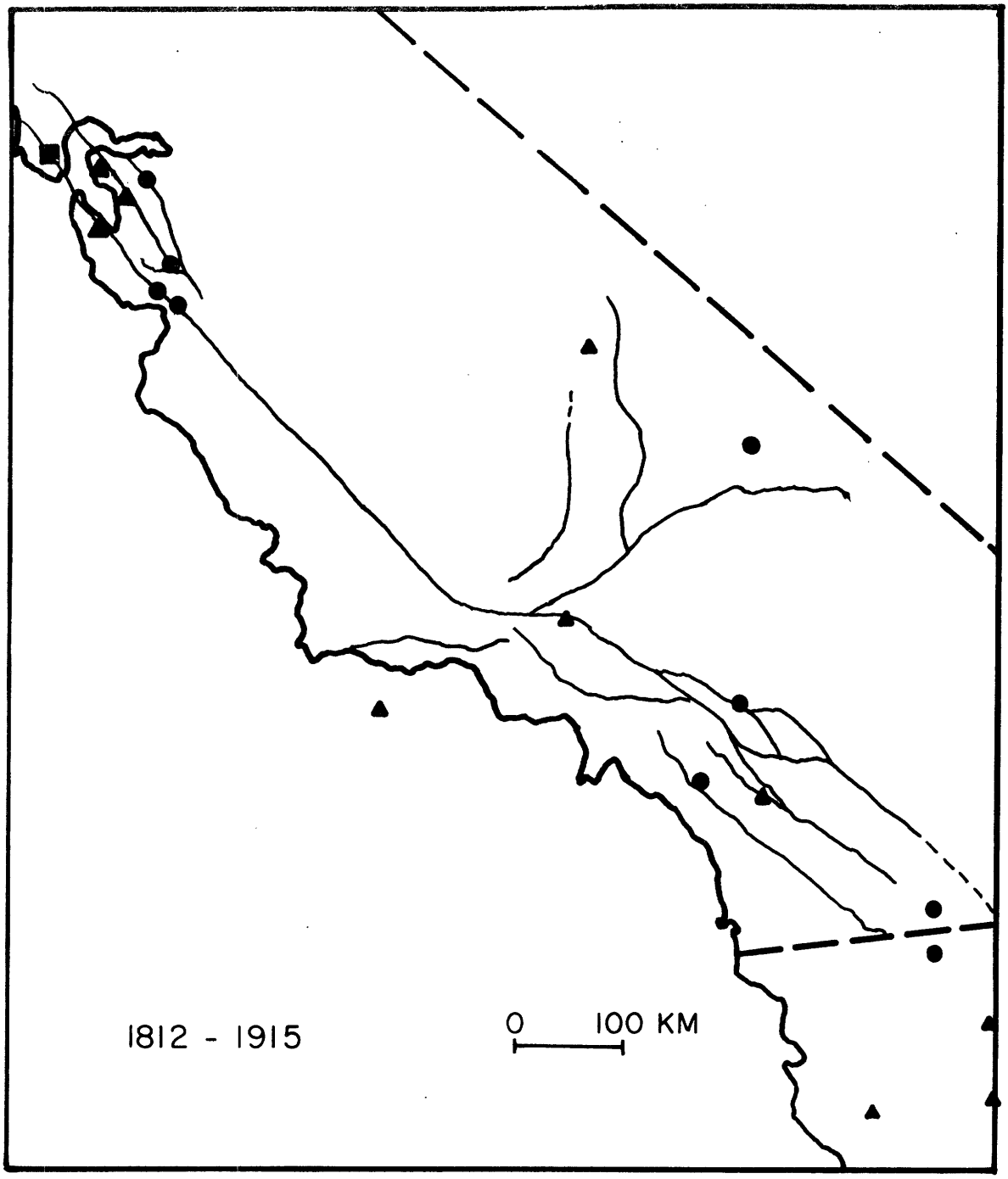

Figure 5.16

Figure 5.17

Maximum shear stress contours for model TCALS + initial conditions + earthquakes (1812-1915). High shear regions near SJB, Parkfield, San Bernadino, Borrego Valley, and Superstition Mountain are areas which survive subsequent earthquake stress release and may be present today.

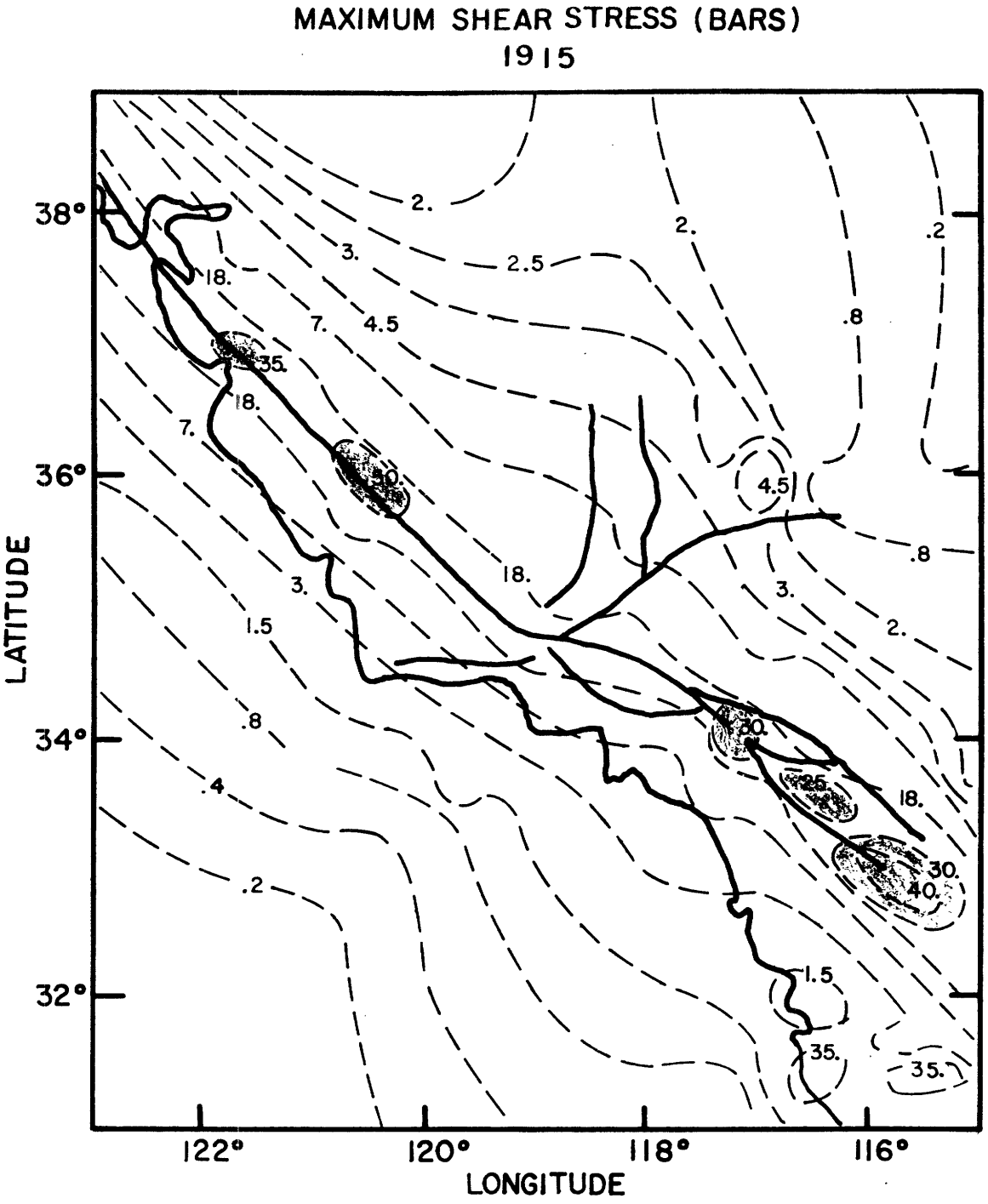
MAXIMUM SHEAR STRESS (BARS)
1915
38°
36°
34°
32°
LATITUDE
122°
120°
118°
116°
LONGITUDE
2.
2.5
3.
4.5
7.
18.
35.
30.
40.
25.
1.5
.8
.4
.2

Figure 5.17

Figure 5.18

Earthquakes during 1916-1935 period. Plus represents an earthquake with magnitude greater than or equal to 5 and less than 6.

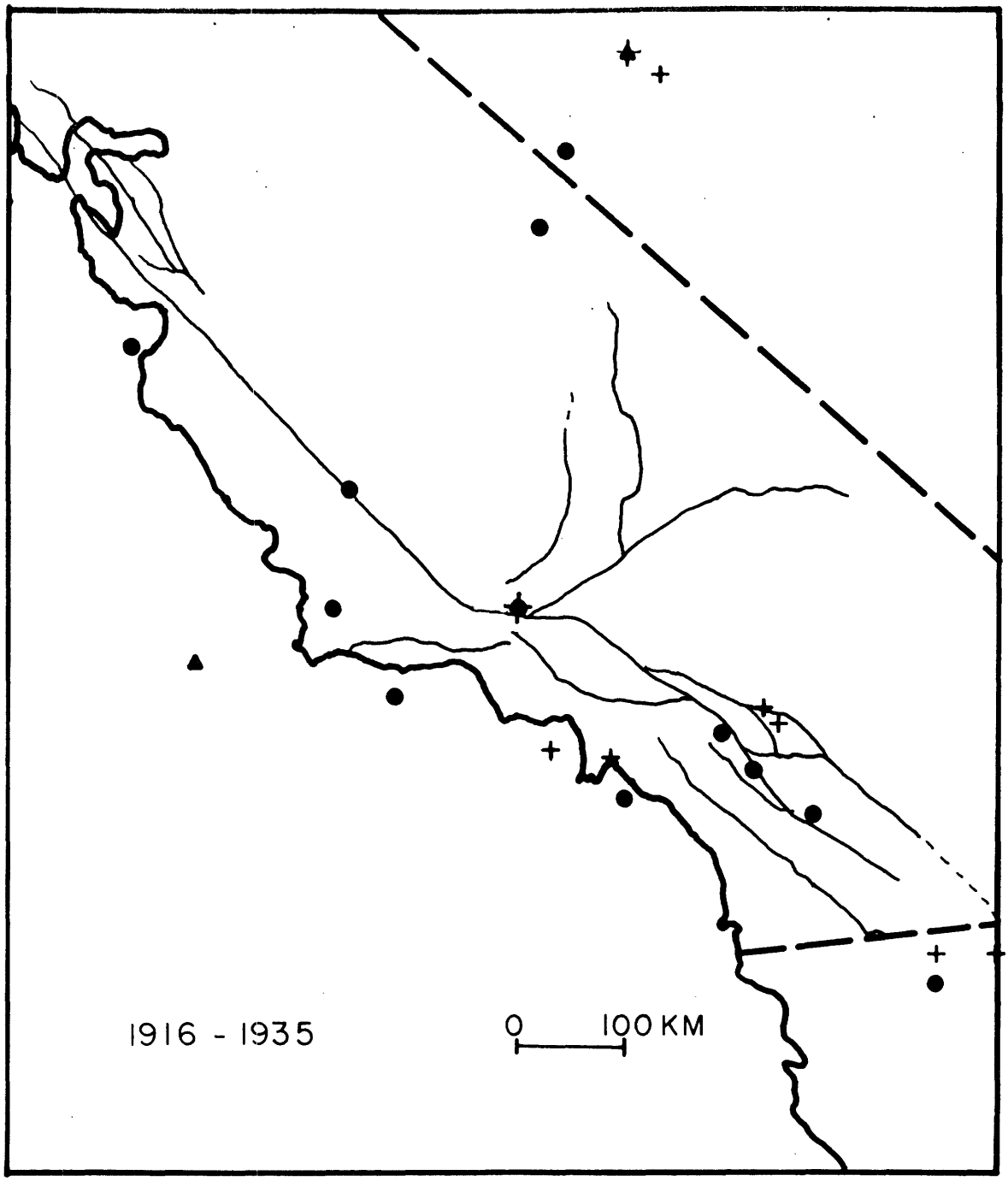

Figure 5.18

Figure 5.19

Maximum shear stress contours computed for the year 1935. Stresses are calculated by adding initial conditions (1812), earthquakes (1812-1935), and 1935-1812=123 years of our tectonic model (TCALS).

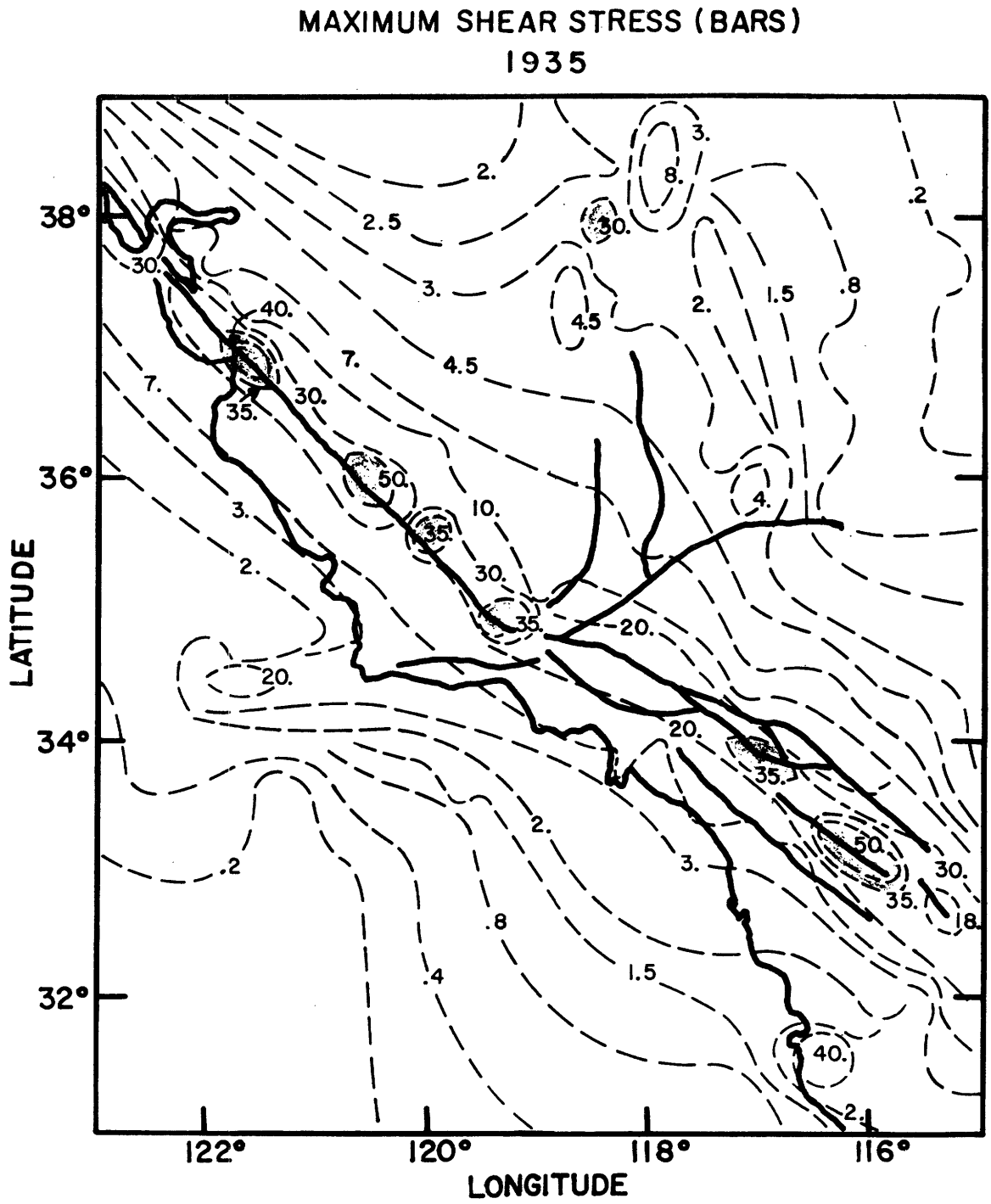
MAXIMUM SHEAR STRESS (BARS)
1935
38°
36°
34°
32°
LATITUDE
122°
120°
118°
116°
LONGITUDE
2.
2.5
3.
7.
4.5
8.
30.
.2
1.5
.8
4.5
40.
35.
50.
10.
4.
20.
.4
1.5
18.

Figure 5.19

Figure 5.20

California earthquakes ($M \geq 4$) during the period 1936-1955. X represents the location of $5 < M \geq 4$ events. The other symbols are defined in figures 5.16 and 5.18.

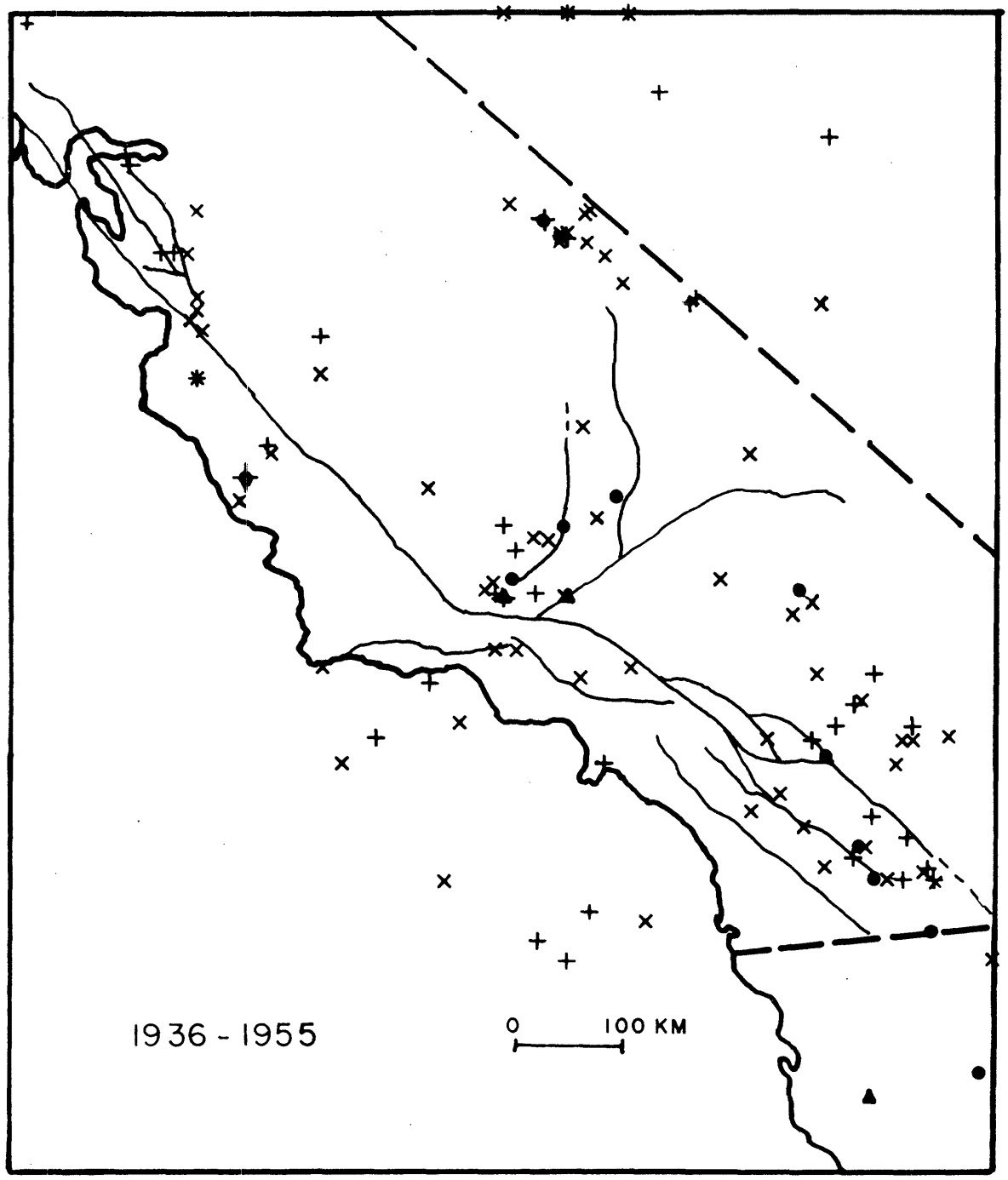

Figure 5.20

Figure 5.21

Maximum shear stress accumulation for the year 1955. Stresses are computed by adding the initial conditions (1812) shown in figures 5.14 and 5.15, the earthquake stress release (1812-1955), and 1955-1812=143 years of our tectonic model (TCALS).

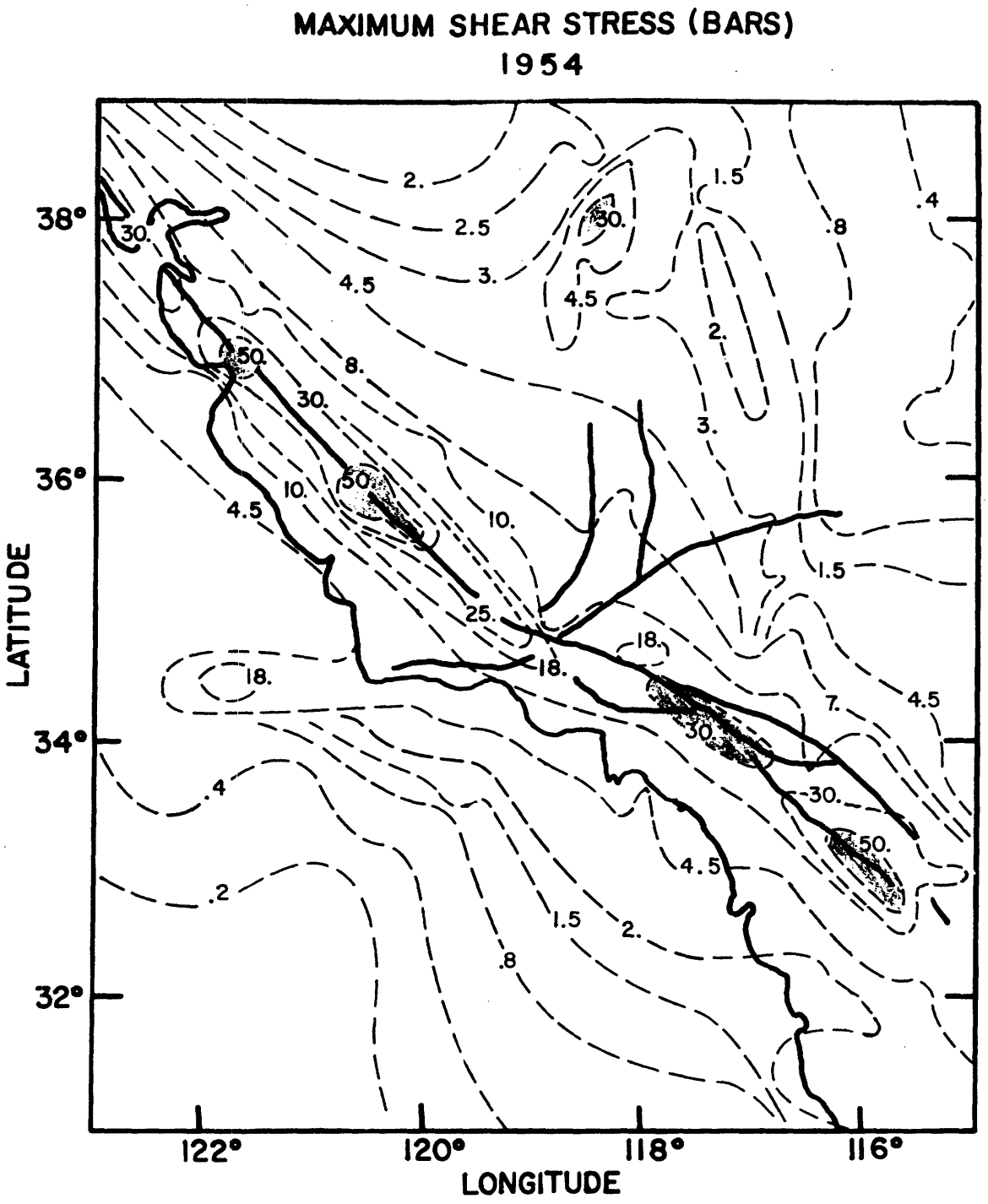
MAXIMUM SHEAR STRESS (BARS)
1954
38°
36°
34°
32°
LATITUDE
122°
120°
118°
116°
LONGITUDE
2.
2.5
3.
4.5
1.5
.8
.4
30.
50.
8.
10.
25.
18.
7.
.2
1.5
2.
3.

Figure 5.21

Figure 5.22

California earthquakes ($M \geq 4$) during the period 1956-1973.

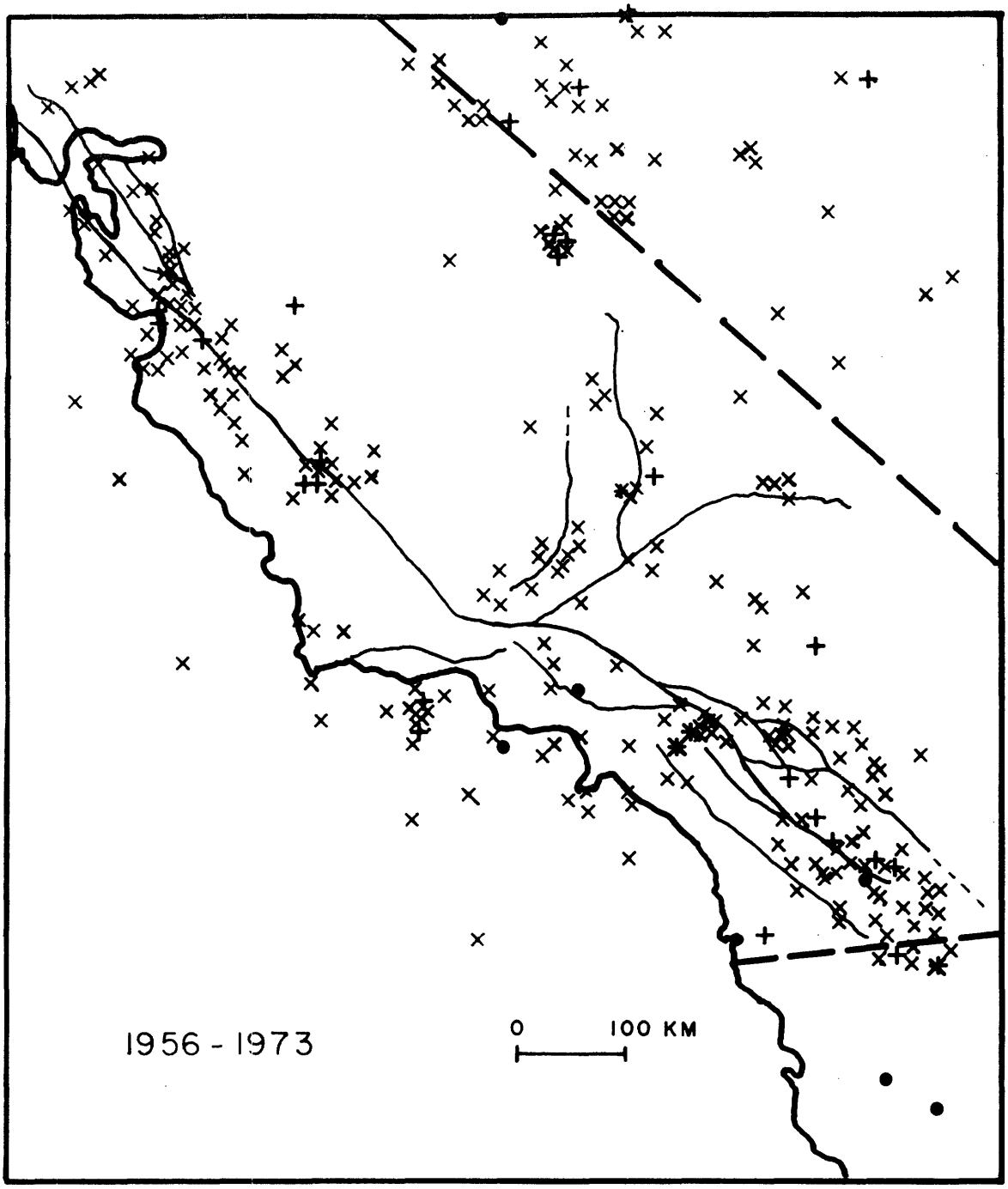

Figure 5.22

Figure 5.23

Maximum shear stress contours for the year 1973. Stresses are computed by adding the initial conditions (1812), earthquakes (1812-1973), and 1973-1812=161 years of our tectonic model (TCALS). High shear regions near SJB, Parkfield, San Bernadino, Borrego Valley, and Superstition Mountain have existed since 1915 (figure 5.17).

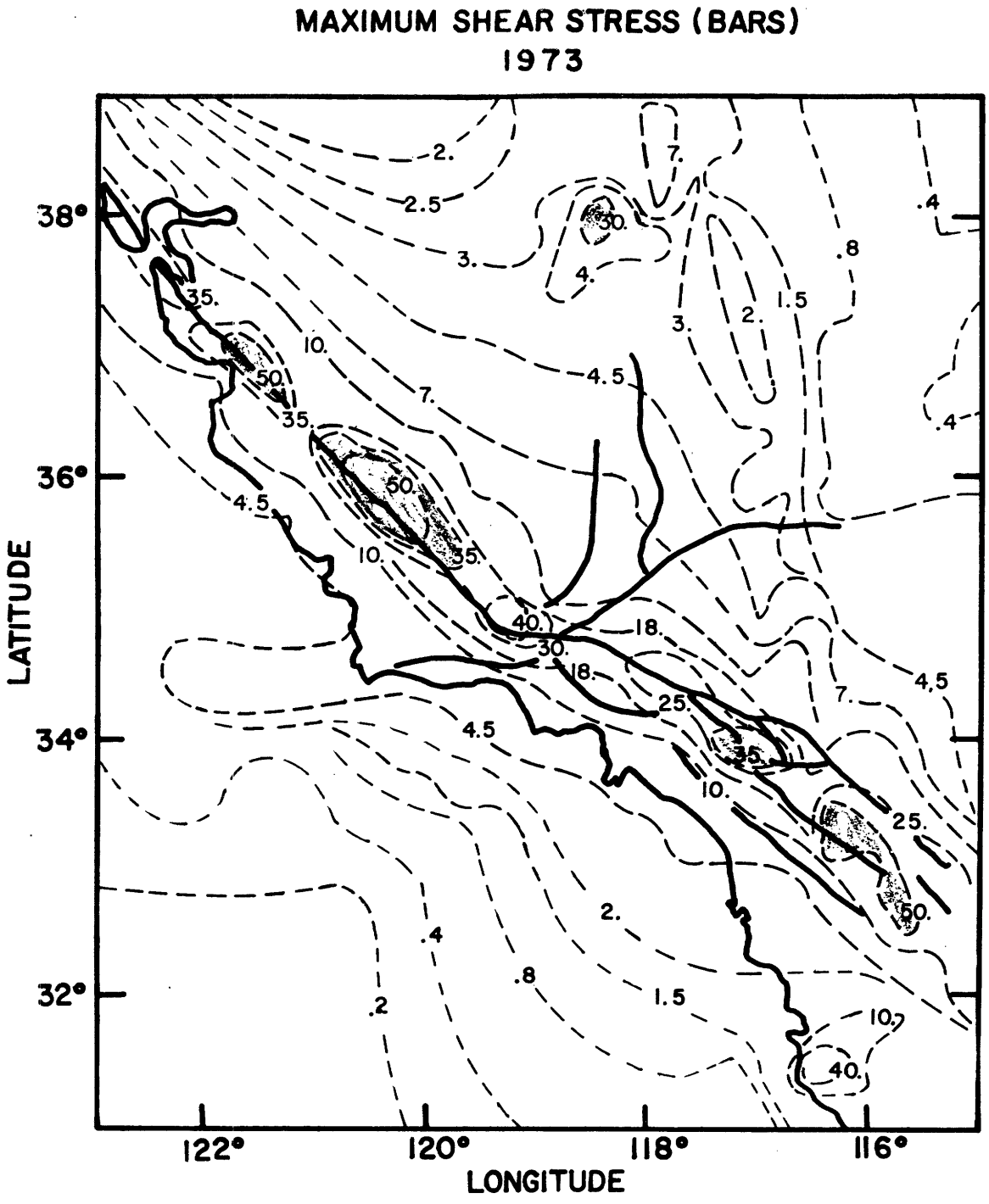
MAXIMUM SHEAR STRESS (BARS)
1973
38°
36°
34°
32°
LATITUDE
122°
120°
118°
116°
LONGITUDE
2.
2.5
3.
4.
7.
30.
.4
.8
1.5
3.
2.
4.5
35.
10.
50.
7.
35.
4.5
50.
10.
35.
40.
18.
30.
18.
25.
4.5
7.
4.5
35.
10.
25.
50.
2.
.4
.8
1.5
10.
.2
40.

Figure 5.23

Figure 5.24

Top-figure compares relative motion (ΔW) of geodetic stations (Geodimeter data) on opposite sides of the fault (stations are approximately 7 km from the fault) to fault creep (alignment array). Geodimeter data for the period 1967-1971 and alignment array data for the period 1968-1971 were taken from Wesson et al. (1973). Geodimeter data for the period 1959-1965 may be found in the report by Hofman (1968).

Bottom-zone of locking inferred from two dimensional model described in text and the data described above. Depths d_1 (distance from surface to bottom of creep zone) and d_2 (distance from surface to bottom of zone of locking) are fixed so that the strain on the fault is zero at the surface (a condition which is approximately true near Hollister - figure 4.19). This additional constraint is equivalent to the requirement that

$$\frac{b_1 \text{ (fault creep)}}{d_2 \text{ (depth of creep)}} = \frac{b_2 \text{ (relative plate motion)}}{d_2 \text{ (depth to bottom of locking)}}$$

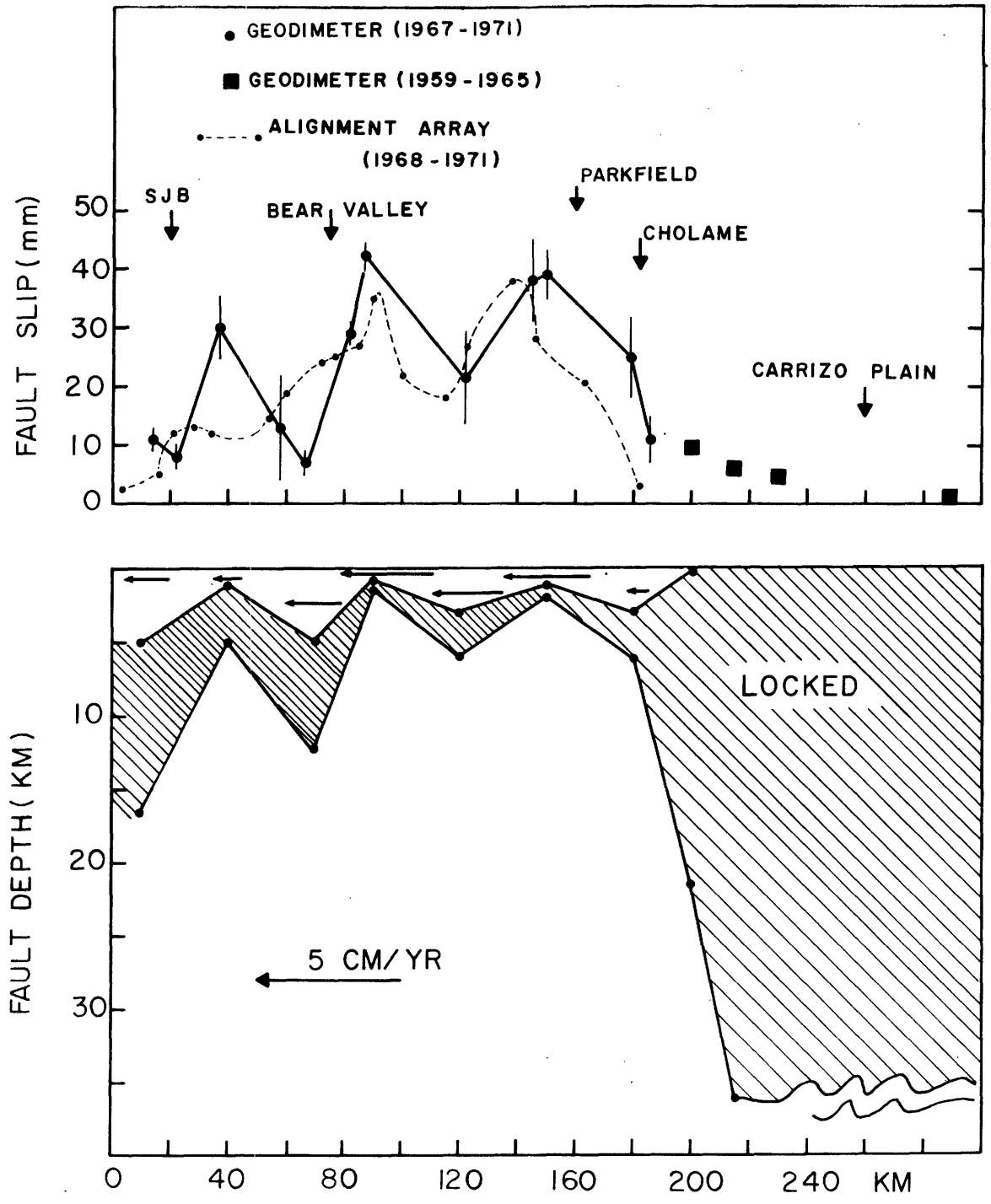
GEODIMETER (1967-1971)
GEODIMETER (1959-1965)
ALIGNMENT ARRAY (1968-1971)
SJB
BEAR VALLEY
PARKFIELD
CHOLAME
CARRIZO PLAIN
FAULT SLIP (mm)
0
10
20
30
40
50
LOCKED
5 CM/YR
FAULT DEPTH (KM)
10
20
30
0
40
80
120
160
200
240
KM

Figure 5.24

Figure 5.25

Depth of small earthquakes along the San Andreas from SJB to Parkfield are indicative of possible locking along this portion of the fault. Figure is from Wesson et al. (1973) and was furnished to the author by W.L. Elsworth.

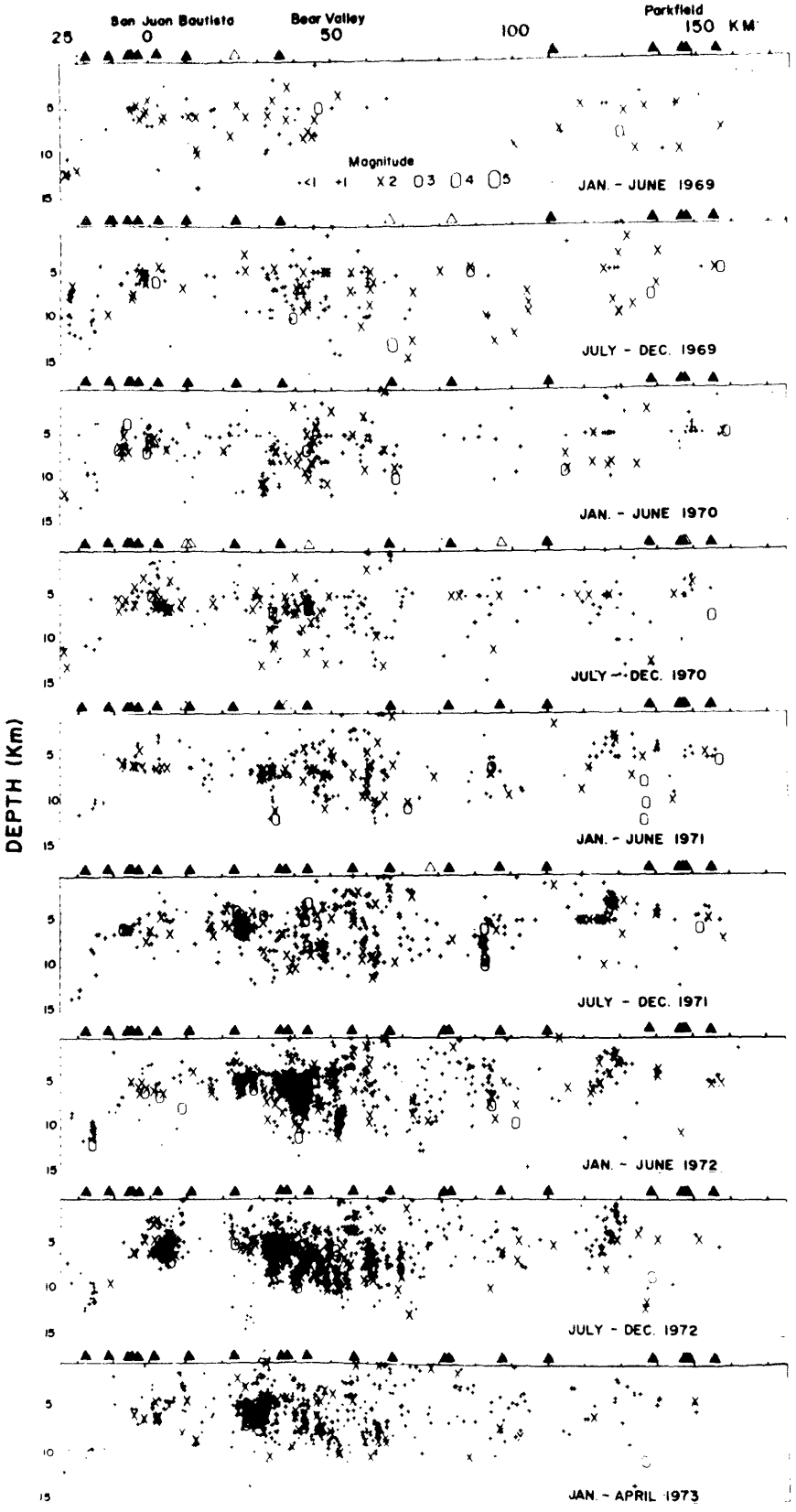
San Juan Bautista
Bear Valley
Parkfield
25
0
50
100
150 KM
Magnitude
<1 +1 X2 03 04 05
JAN. - JUNE 1969
JULY - DEC. 1969
JAN. - JUNE 1970
JULY - DEC. 1970
JAN. - JUNE 1971
JULY - DEC. 1971
JAN. - JUNE 1972
JULY - DEC. 1972
JAN. - APRIL 1973
DEPTH (Km)
5
10
15

Figure 5.25

Figure 5.26

Top-model of slip and locking near Parkfield from 1932-1962 suggested by Savage and Burford (1970). They suggest that the slip was associated with the 1934 Parkfield earthquake.

Center-Model of slip and locking suggested for the period 1932-1962. The zone between Parkfield and Cholame is the eventual site of the 1966 Parkfield earthquake. Slip is assumed to occur at 5 cm/yr. The strain components γ_1 and γ_2 for this model are plotted in figures 5.27 and 5.28 (solid line).

Bottom-alternate model with deep locking to the south of Cholame (dashed line in figures 5.27 and 5.28). Shear strain component (γ_1) falls off too rapidly because of the thin wedge assumed. Slip rate assumed to be 2.5 cm/year.

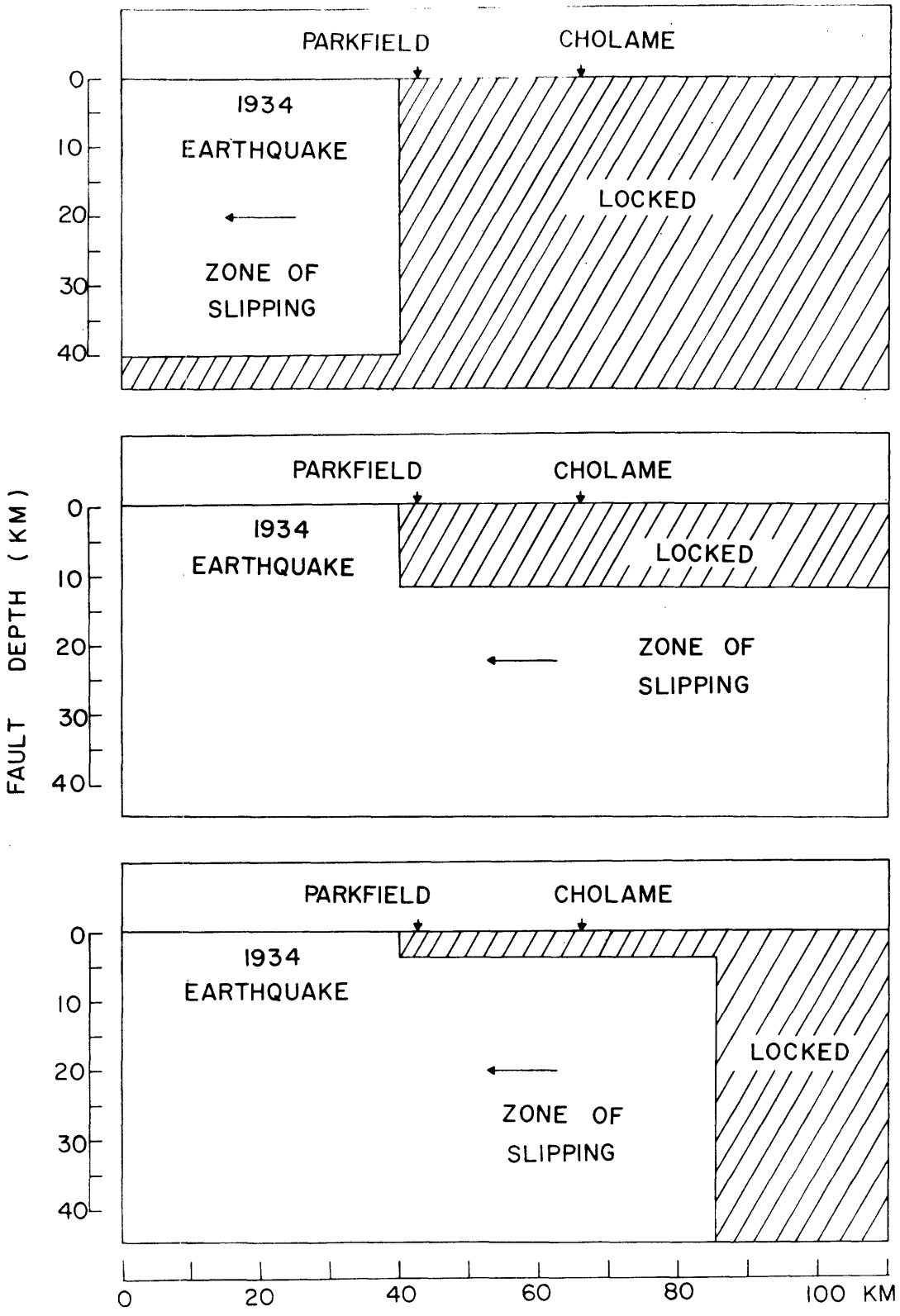
PARKFIELD
CHOLAME
0
10
20
30
40
1934
EARTHQUAKE
LOCKED
ZONE OF
SLIPPING
PARKFIELD
CHOLAME
FAULT DEPTH (KM)
0
10
20
30
40
1934
EARTHQUAKE
LOCKED
ZONE OF
SLIPPING
PARKFIELD
CHOLAME
0
10
20
30
40
1934
EARTHQUAKE
LOCKED
ZONE OF
SLIPPING
0
20
40
60
80
100 KM

Figure 5.26

Figures 5.27 and 5.28

γ_1 and γ_2 strain components for the triangulation arc near Cholame, California (Savage and Burford, 1970). The data represents the period 1932-1962. Solid and dashed lines represent center and bottom models respectively, in figure 5.26.

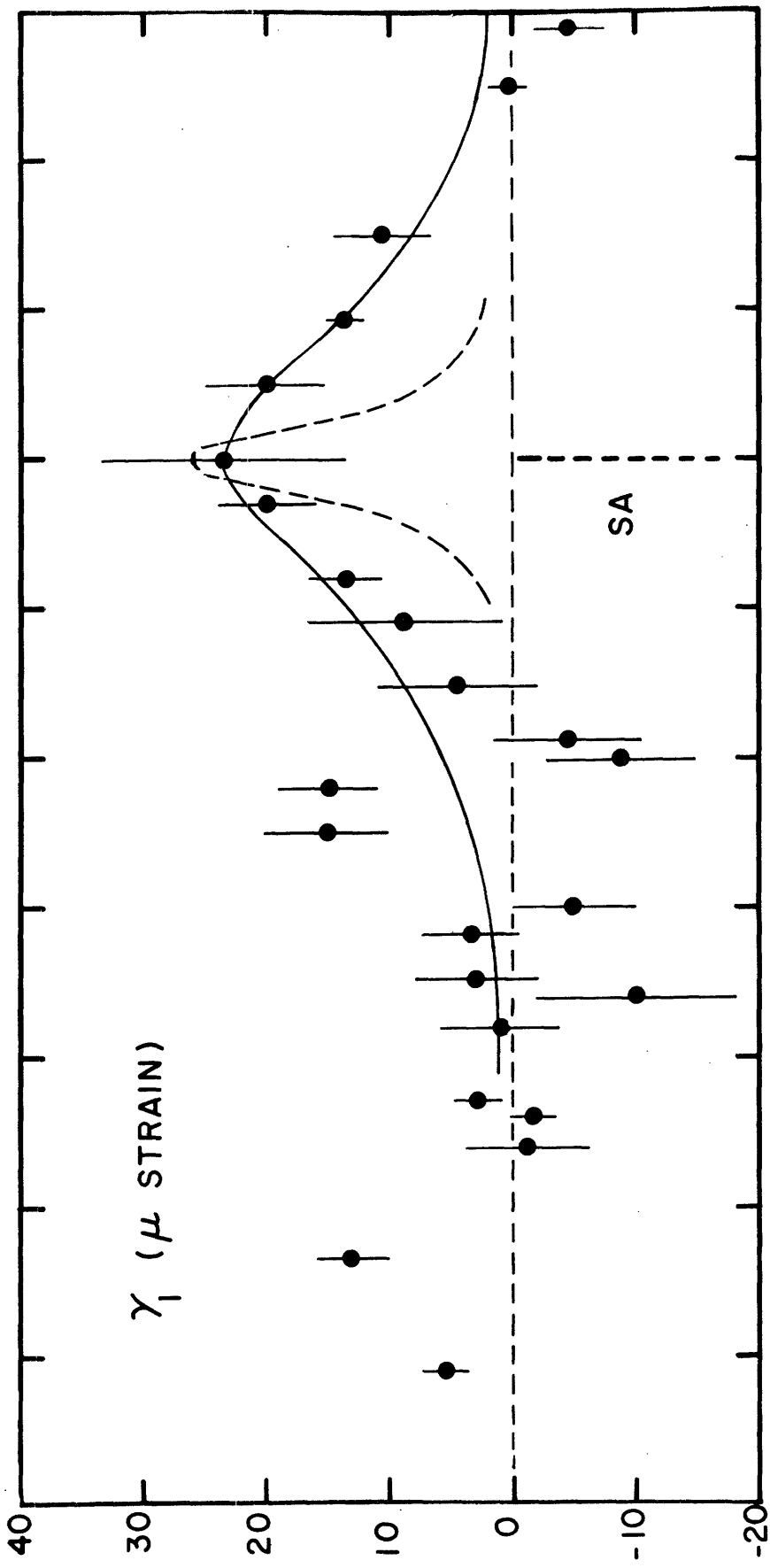
40
30
20
10
0
-10
-20
γ_1 (μ STRAIN)
60
40
20
0
20
SA
DISTANCE FROM SAN ANDREAS (KM)

Figure 5.27

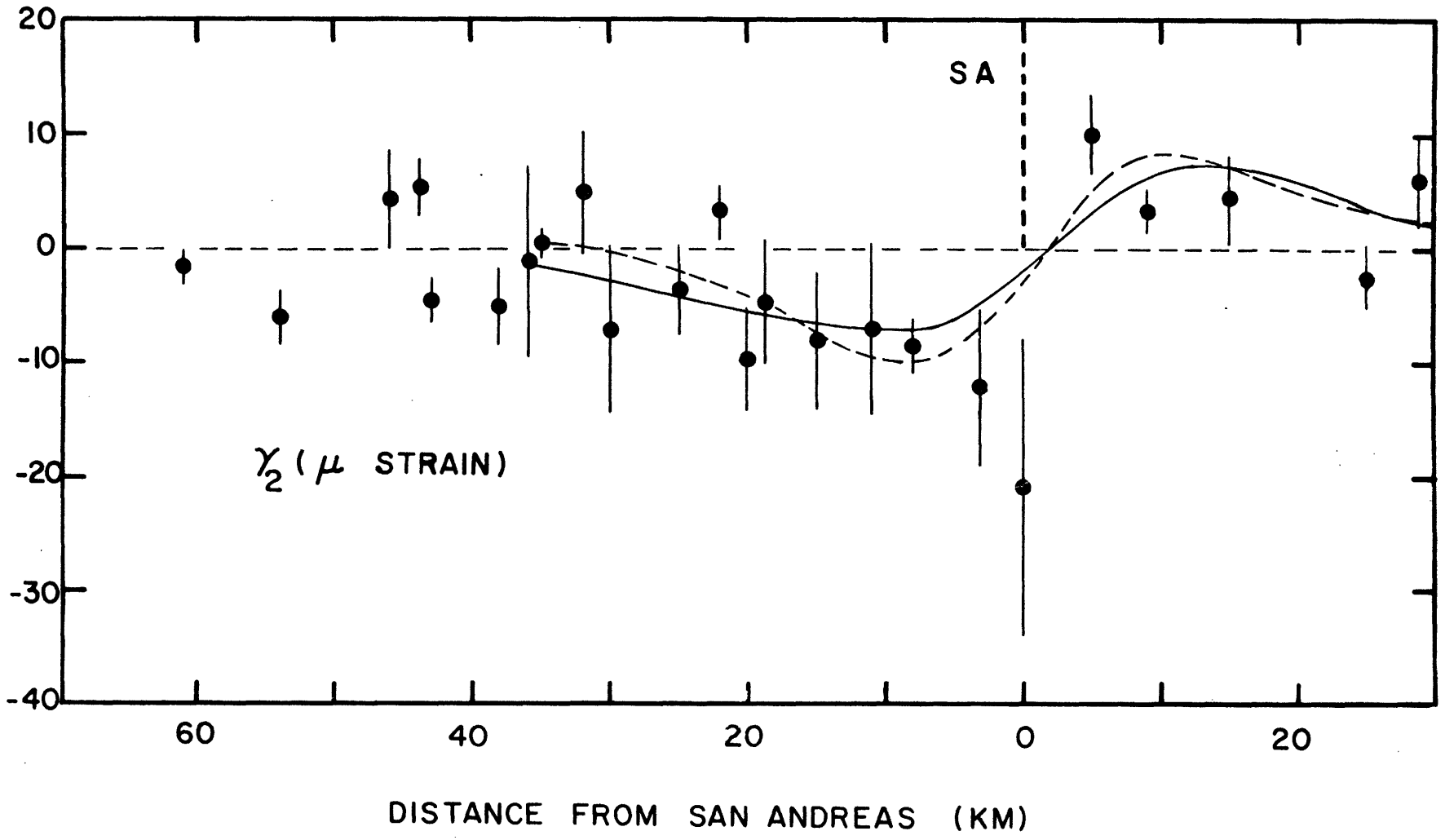
20
10
0
-10
-20
-30
-40
SA
γ_2 (μ STRAIN)
60
40
20
0
20
DISTANCE FROM SAN ANDREAS (KM)

Figure 5.28

CHAPTER VI

Summary of Thesis

The foundations of this thesis are built upon the angular dislocations of Yoffe (1960) and Comninou (1973). In order to apply their solutions to displacement fields we have had to modify the multi-valued terms in their solutions. Angular dislocations allow us to easily compute the solutions for finite angular dislocations.

In Chapter III a numerical method for the solution of a finite dislocation distributed throughout a layered half-space was developed. The Finite Source Method (FSM) is based upon the Fast Fourier Transform (FFT) algorithm (Cooley and Tukey, 1965) and allows for a rapid computation of the fields due to finite sources. In fact, for the same amount of information, more conventional schemes would take 18 to 100 years of computer time! This statement is based upon the assumption of a 5 second (Javanovich et al., 1975) to 11 minute (Ben-Menahem and Gillon, 1970) computation time per point of data per point source. To construct a finite source out of many point sources, integrate a set of integrals for each source, and finally to repeat this process for the displacements, strains, and tilts over a large array (e.g. a 128 x 128 grid) is quite time consuming. The FSM allows all of this to be done at once.

Next, the FSM was applied to a series of particular

problems concerning layered earth models. We found that it is most important to know the properties of the layers in which the source is imbedded (when modeling earthquake displacement fields).

In Chapters IV and V we applied a tectonic modeling scheme (in terms of dislocations) to various sections of the San Andreas fault in California. Our models yielded several important results which deserve further study. First, the depth at which slip is continuously taking place on the San Andreas must extend to greater depths (~40 km) under San Francisco than in surrounding areas. Secondly, we suggest that fault creep serves to obscure locking at depth from surface geodetic measurements and that the SJB-Cholame section of the San Andreas cannot be eliminated as a potential earthquake site.

South of Cholame the apparent depth of locking deepens and probably extends through the thickness of the plate (80 km in model Tejon 2) in the vicinity of the Tejon bend. Our primary support for this model rested upon the agreement of the principal compressive stress directions with the directions inferred by this author from geodetic and seismic data. Our confidence in this model is further enhanced by recent strain measurements near Palmdale, California (Jim Savage, personal communication, 1975).

Finally, by the addition of our tectonic model to the large California earthquakes we have predicted possible high stress regions which deserve further study. The most populated of these areas (San Bernadino) has also been predicted by Smith and Van de Lindt (1969).

Aki, K., Scaling law of seismic spectrum, J. Geophys. Res., 72, 1217-1231, 1967.

Aki, K., Seismic displacements near a fault, J. Geophys. Res., 73, 5359-5376, 1968.

Aki, K., Earthquake mechanism, in The Upper Mantle, edited by A.R. Ritsema, Tectonophysics 13 (1-4), 423-446, 1972.

Aki, K., A. Christofferson, and E. Husebye, Determination of the three dimensional seismic structure of the lithosphere, submitted to the J. Geophys. Res., 1975.

Alewine, R.W. and P.H. Jungels, Applications of stochastic inversion theory and the finite-element method to zero-frequency: the 1964 Alaskan earthquake, submitted to Geophys. J.R. astr. Soc., 1974.

Allen, C.R., and S.W. Smith, Parkfield earthquakes of June 27-29, Monterey and San Luis Obispo counties, California. Pre-earthquake and post-earthquake surficial displacements, Bull. Seism. Soc. Am., 56, 966-967, 1966.

Allen, C.R., P. St. Amand, C.R. Richter, and J.M. Norquist, Relationship between seismicity and geologic structure in the southern California region, Bull. Seism. Soc. Am., 55, 753-798, 1965.

Anderson, D.L., The San Andreas Fault, Scientific American, November, 1971.

Anderson, O.L. and P.C. Perkins, Application of the stress corrosion theory of crack propagation to geophysical problems, EOS, Transactions AGU, 56, 1193, 1974.

Andrews, D.J., From antimoment to moment: plane-strain models of earthquakes that stop, Bull. Seismo. Soc. Am., 65, 163-182, 1975.

Atwater, T., Implications of plate tectonics for the Cenozoic tectonic evolution of western North America, Geol. Soc. Am. Bull., 81, 3513-3536, 1970.

Ben-Menahem, A. and A. Gillon, Crustal deformation by earthquakes and explosions, Bull. Seism. Soc. Am., 60, 193-215, 1970.

Ben-Menahem, A. and S.J. Singh, Multipolar elastic fields in a layered half space, Bull. Seism. Soc. Am., 58, 1519-1572, 1968.

Ben-Menahem, A., S.J. Singh, and F. Solomon, Static deformation of a spherical earth model by internal dislocations, Bull. Seism. Soc. Am., 59, 813-853, 1969.

Bolt, B.A., C. Lomnitz, and T.V. McEvilly, Seismological evidence on the tectonics of central and northern California and the Mendocino Escarpment, Bull. Seism. Soc. Am., 61, 1831-1847, 1968.

Bolt, B.A. and R.D. Miller, Seismicity of northern and central California, 1965-1969, Bull. Seism. Soc. Am., 58, 1725-1767, 1968.

Bonilla, M.G., Deformation of railroad tracks by slippage on the Hayward fault in the Niles district of Fremont, California, Bull. Seism. Soc. Am., 56, 281-289, 1966.

Brace, W.F. and J.D. Byerlee, Stick-slip as a mechanism for earthquakes, Science, 153, 990-992, 1966.

Brace, W.F. and J.D. Byerlee, California earthquakes: why only shallow focus, Science, 168, 1573-1575, 1970.

Braslau, D. and P. Lieber, Three-dimensional fields due to a Volterra dislocation imbedded in a layered half-space: analytic representation of a seismic mechanism, Bull. Seism. Soc. Am., 58, 613-628, 1968.

Brown, R.L., M.N. Toksöz, and N. Canitez, A dislocation approach to earthquake prediction, EOS, Trans. Am. Geophys. Un., 53, 445, 1972.

Brune, J.N., Seismic moment, seismicity, and the rate of slip along major fault zones, J. Geophys. Res., 73, 777-784, 1968.

Burford, R.O. and J.C. Savage, Tectonic evolution of a crustal wedge caught within a transform fault system (abstract), Program with abstracts, 68th Annual Natl. Meeting of the Seism. Soc. of Am., 134, 1972.

Burgers, J.M., Some considerations on the fields of stress connected with dislocations in a regular crystal lattice, Proc. Acad. Sci., Amst. 42, 293-325, 1939.

Burton, C.V., A theory concerning the constitution of matter, Phil. Mag., 33, 191, 1892.

Byerly, P., The California earthquake November 4, 1927, Bull. Seism. Soc. Am., 20, 53-66, 1930.

Byerlee, J.D. and W.F. Brace, Stick-slip stable sliding, and earthquakes - effect of rock type, pressure, strain rate, and stiffness, J. Geophys. Res., 73, 6031-6037, 1968.

Canitez, N. and M.N. Toksöz, Static and dynamic study of earthquake source mechanism: San Fernando earthquake, J. Geophys. Res., 77, 2583-2594, 1972.

Cherry, J.T. and J.C. Savage, Rock dilatancy and strain accumulation near Parkfield, California, Bull. Seism. Soc. Am., 62, 1343-1347, 1972.

Chinnery, M.A., The deformation of the ground around surface faults, Bull. Seism. Soc. Am., 51, 355-372, 1961.

Chinnery, M.A., The stress changes that accompany strike-slip faulting, Bull. Seism. Soc. Am., 53, 921-932, 1963.

Chinnery, M.A., The strength of the earth's crust under horizontal shear stress, J. Geophys. Res., 69, 2085-1089, 1964.

Chinnery, M.A., Secondary faulting I: theoretical aspects, Can. J. Earth Sci., 3, 163-174, 1966a.

Chinnery, M.A., Secondary faulting II: geological aspects, Can. J. Earth Sci., 3, 175-190, 1966b.

Chinnery, M.A., Theoretical fault models, in A Symposium on Processes in the Focal Region, edited by K. Kasahara and A.E. Stevens, Publ. of the Dom. Obs., Ottawa, 211-223, 1969.

Chinnery, M.A., and D.B. Javanovich, The effect of earth layering on earthquake displacement fields, Bull. Seism. Soc. Am., 62, 1629-1639, 1972.

Clark, B.L., Tectonics of the coast ranges of middle California, Geol. Soc. Amer. Bull. 41, 747-828, 1930.

Comninou, M.A., Angular dislocation in a half-space, Ph.D. Thesis, Northwestern University, Evanston, Illinois, 1973.

Converse, G., Nonuniform dislocations on buried, inclined faults, Trans. Amer. Geophys. Un., 55, 352, 1974.

Cooley, J.W. and J.W. Tukey, An algorithm for the machine calculation of complex Fourier series, Math. of Comput., 19, 297-301, 1965.

Cooley, J.W., P.A.W. Lewis and P.D. Welch, Application of the fast Fourier transform to computation of Fourier integrals, Fourier series, and convolution integrals IEEE, Trans. Audio Electroacoust., AU-15, 79, 1967.

Cooley, J.W., P.A.W. Lewis, and P.D. Welch, The fast Fourier transform algorithm: Programming considerations in the calculation of sine, cosine, and Laplace transforms, J. Sound Vib., 12 (3), 315-337, 1970.

Dickinson, W.R., D.S. Cowan, R.A. Schweickert, A test of new global tectonics: discussion, Amer. Assoc. Petrol. Geol., 375-384, 1972.

Droste, S. and R. Teisseyre, The theory of the dislocation processes and its application to the Pacific region,

50, 57-70, 1960.

Eaton, J., Crustal structure from San Francisco, California to Eureka, Nevada, from seismic refraction measurements, J. Geophys. Res., 68, 5789-5806, 1963.

Elders, W.A., R.W. Rex, J. Meidav, P.J. Robinson, and S. Biehler, Crustal spreading in southern California, 178, 15-24, 1972.

Ellsworth, W.L., R.H. Campbell, D.P. Hill, R.A. Page, R.W. Alewine, III, T.C. Hanks, T.H. Heaton, J.A. Hileman, H. Kanamori, B. Minster, and J.H. Whitcomb, Point Mugu, California, earthquake of 21 February 1973 and its aftershocks, Science, 182, 1127-1129, 1973.

Ellsworth, W.L., Bear Valley, California, earthquake sequence of February-March 1972, Bull. Seism. Soc. Am., 65, 483-506, 1975.

Eshelby, J.D., The determination of the elastic field of an ellipsoidal inclusion, and related problems, Proc. Roy. Soc. A241, 376-396, 1957.

Farrington, R.L. and C.W. Myers, A major bend in the San Andreas fault: a possible locking mechanism, Abstracts of papers presented at the conference on tectonic problems of the San Andreas fault system, Stanford Univ., 1973.

Fitch, F.J. and C.H. Scholz, Mechanism of underthrusting in southwest Japan; a model of convergent plate interation, J. Geophys. Res., 76, 7260-7292, 1971.

Fung, Y.C., Foundations of Solid Mechanics, Prentice-Hall, Inc., Englewood Cliffs, New Jersey, 1965.

Gold, B. and C.M. Rader, Digital Processing of Signals, McGraw-Hill, New York, 1965.

Greene, H.G., W.H.K. Lee, D.S. McCulloch and E.E. Brabb, Faults and earthquakes in the Monterey Bay region, California, U.S. Geol. Surv., Misc. field studies, Map MF-518, 1973.

Greensfelder, R.W. and J.H. Bennett, Characteristics of strain variation along the San Andreas fault from geodimeter measurements, Proceedings of Conference on Tectonic Problems of the San Andreas Fault System, edited by R.L. Kovach and A. Nur, 54-63, 1973.

Griffith, A.A., The phenomena of rupture and flow in solids, Phil. Trans. Roy. Soc. A, 221, 163-198, 1921.

Gumper, F.J. and C. Scholz, Microseismicity and tectonics of the Nevada seismic zone, Bull. Seism. Soc. Am., 61, 1413-1432, 1971.

Gutenberg, B. and C.F. Richter, Seismicity of the Earth, Hafner Publishing Co., New York and London, 310 pp., 1965.

Hamilton, R.M., R.F. Yerkes, R.D. Brown, Jr., R.O. Burford, and J.M. De Noyer, Seismicity and associated effects, Santa Barbara region, pt. D of Geology, Petroleum Development and Seismicity of the Santa Barbara Channel region, California, U.S. Geol. Survey Prof. Paper, 629, 47-68, 1969.

Haskell, N.A., Radiation pattern of Rayleigh waves from a fault of arbitrary dip and direction of motion in a homogeneous medium, Bull. Seism. Soc. Am., 53, 619-642, 1963.

Healy, J.H., W.H.K. Lee, L.C. Pakiser, C.B. Raleigh, and M.D. Wood, Prospects for earthquake prediction and control, Tectonophysics, 14 (314), 319-332, 1972.

Herrin, E., A comparative study of upper mantle models: Canadian Shield and Basin and Range Provinces, in The Nature of the Solid Earth, edited by E.C. Robertson, McGraw-Hill, New York, 1972.

Hileman, J.A., C.R. Allen, and J.M. Nordquist, Seismicity of the Southern California Region, Seismological Lab., Calif. Inst. of Tech., Pasadena, Calif., 1973.

Hill, D.M., C. Lao, V.A. Moore, and J.E. Wolfe, Earthquake epicenter and fault map of California, State of California, Dept. of Water Resources, Crustal strain and fault movement investigation, 1969.

Hill, M.L. and T.W. Dibblee, Jr., San Andreas, Garlock, and Big Pine faults, California, Geol. Soc. Am. Bull., 64, 443-458, 1953.

Hofmann, R.B., Geodimeter fault movement investigations in California, Calif. Dept. Water Resources Bull., 116, part 6, 183 pp., 1968.

Hokanson, J.L., Elastic stress field of an angular dislocation, J. Appl. Phys., 34, 2337-2340, 1963.

Honda, H., The mechanism of the earthquakes, Science Reports Tohoku Univ. Ser. 5, Geophys. 9, Suppl., 1-46, Pub. Dominion Obs. Ottawa, 20, 295-340, 1957.

Honda, H. and T. Miura, On the strain produced in a semi-infinite elastic solid by a statical surface force; with some applications to seismology, Geophys. Mag. 9, 61-81, 1935.

Housner, G.W., Properties of strong ground motion earthquakes, Bull. Seism. Soc. Am., 45, 197-218, 1955.

Howard, J.H., Recent deformation of the Cholame and Taft-Maricopa areas, California, Proceedings of Conference on Tectonic Problems of the San Andreas Fault System, edited by W.R. Dickinson and A. Grant, Stanford Univ. Pub., 1968.

Isacks, B., J. Oliver, and L.R. Sykes, Seismology and the new global tectonics, J. Geophys. Res., 73, 5855-5899, 1968.

Johnston, M.J.S. and W.D. Stuart, The form of pre- and post-earthquake crustal deformation for moderate earthquakes on the San Andreas, EOS, Trans. Am. Geophys. Un., 56, 1196, 1974.

Jovanovich, D.B., M.I. Husseini, and M.A. Chinnery, Elastic dislocations in a layered half-space - I. Basic theory and numerical methods, Geophys. J. Roy. astr. Soc., 39, 205-217, 1974a.

Jovanovich, D.B., M.I. Husseini, and M.A. Chinnery, Elastic dislocations in a layered half-space - II. The point source, Geophys. J. Roy. astr. Soc., 39, 219-239, 1974b.

Jungels, P.H., and G.A. Frazier, Finite element analysis of the residual displacements for an earthquake rupture: Source parameters for the San Fernando earthquake, J. Geophys. Res., 78, 5062-5083, 1973.

Kasahara, K., The nature of seismic origins as inferred from seismological and geodetic observations, Bull. Earthquake Res. Inst., 35, 473-532, 1957.

Kasahara, K., Physical conditions of earthquake faults II, Bull. Earthquake Res. Inst., 37, 251-273, 1959.

Kasahara, K., A strike-slip fault buried in a layered medium, Bull. Earthquake Res. Inst., 42, 609-619, 1964.

Keylis-Borok, V.I., 1959, On estimation of the displacement in an earthquake source and of source dimensions, Annali Geofis., 12, 205-214, 1959.

Knopoff, L., Energy release in earthquakes, Geophys. J. Roy. astr. Soc., 1, 44-52, 1958.

Koch, T.W., Analysis and effects of current movement on an active fault in Buena Vista Hills oilfield, Kern County, California, Amer. Assoc. Petroleum Geol. Bull., 17, 694-712, 1933.

Larmor, J., A dynamical theory of the electric and luminiferous medium - Part III Relations with material media, Phil. Roy. Soc. London, A190, 205, 1897.

Larson, R.L., H.W. Menard, and S.M. Smith, Gulf of California: a result of sea-floor spreading and transform faulting, Science, 161, 781-784, 1968.

Lee, W.H.K. and J.G. Vedder, Recent earthquake activity in the Santa Barbara Channel region, Bull. Seism. Soc. Am., 63, 1757-1773, 1973.

Love, A.E.H., A Treatise on the Mathematical Theory of Elasticity, 643 pp., Cambridge University Press, Great Britain, 1927.

Mansinha, L. and D.E. Smylie, The displacement fields of inclined faults, Bull. Seism. Soc. Am., 61, 1433-1440, 1971.

Maruyama, T., Statical elastic dislocations in an infinite and semi-infinite medium, Bull. Earthquake Res. Inst., Tokyo University, 42, 289-368, 1964.

Mayer-Rosa, D., Travel time anomalies and distribution of earthquakes along the Calaveras fault zone, California, Bull. Seism. Soc. Am., 63, 713-729, 1973.

McGarr, A., Stable deformation of rock near deep-level tabular excavations, J. Geophys. Res., 76, 7088-7106, 1971.

McGinley, J.R., Jr., A comparison of observed permanent tilts and strains due to earthquakes with those calculated from displacement dislocations in elastic earth models, Ph.D. Thesis, California Institute of Technology, Pasadena, 1968.

McKenzie, D.P., The relation between fault plane solutions for earthquakes and the directions of the principal stresses, Bull. Seism. Soc. Am., 59, 591-601, 1969.

Meade, B.K., Horizontal movement along the San Andreas fault system, Roy. Soc. N.Y. Bull., 9, 175-179, 1971.

Menard, H.W., Minor lineations in the Pacific Basin, Bull. Geol. Soc. Am., 70, 1491-1496, 1959.

Minster, J.B., T.H. Jordan, P. Molnar, and E. Haines, Numerical modeling of instantaneous plate tectonics, Geophys. J.R. astr. Soc., 36, 541-576, 1974.

Mitchell, J.H., Some elementary distributions of stress in three dimensions, Proc. Math. Soc. London, 32, 23-61, 1900.

Morse, M.M. and H. Feshback, Methods of Theoretical Physics, McGraw-Hill Book Company, New York, 1953.

Mortensen, C.E. and M.J.S. Johnston, Some results from a 14 tiltmeter array along 85 km of the San Andreas fault, EOS, Trans. Am. Geophys. Union, 1196, 1974.

Mura, T., The continuum theory of dislocations, Advances in Materials Research, edited by Herbert Herman, Interscience Publishers (John Wiley and Sons), 1968.

Nabarro, F.R.N., Theory of Crystal Dislocations, 821 pp., Oxford University Press, Great Britain, 1967.

Nason, R.D., Investigation of fault creep slippage in northern and central California, Thesis, Univ. of Calif., San Diego, 1971.

Nason, R.D., Fault creep and earthquakes on the San Andreas fault, Proceedings of Conference on Tectonic Problems of the San Andreas Fault System, 13, Stanford Univ. Pub. Geol. Sci., 275-284, 1973.

Nason, R. and J. Weertman, A dislocation theory analysis of fault creep events, J. Geophys. Res., 78, 7745-7751, 1973.

Nur, A. and Mavko, G., Post-seismic viscoelastic rebound, Science, 183, 204-206, 1974.

Orowan, E., Mechanism of seismic faulting, Geol. Soc. America Mem., 79, 323-345, 1960.

Page, B.M., Sur-Nacimiento fault zone of California: Continental margin tectonics, Geol. Soc. Am. Bull., 81, 667-690, 1970a.

Page, B.M., Time of completion of underthrusting of Franciscan beneath Great Valley rocks west of Salinian Block, California, Geol. Soc. Am. Bull., 81, 2827-2834, 1970b.

Plafker, G. and J.C. Savage, Mechanism of the Chilean earthquakes of May 21 and 22, Bull. Geol. Soc. Am., 81, 1001-1030, 1970.

Prescott, W. and J.C. Savage, A study of possible pre-earthquake anomalies on the central San Andreas fault, EOS, Trans. Am. Geophys. Union, 56, 1196, 1974.

Priestley, K., Earth strain observations in the western Great Basin, Ph.D. thesis, Univ. Nevada, Reno, 1974.

Press, F., Displacements, strains, and tilts at teleseismic distances, J. Geophys. Res., 70, 2395-2412, 1965.

Raleigh, B., J. Healy, and B. Bredehoeft, Faulting and crustal stress at Rangely, Colorado, in Flow and Fracture of Rocks, the Griggs Volume, 1970.

Reid, H.F., California Earthquake of April 18, 1906, Vol. II, Mechanics of the Earthquake, Carnegie Institution of Washington, 1910.

Richter, C.F., Elementary Seismology, W.H. Freeman and Co., San Francisco, 768 pp., 1958.

Richter, C.F., Transversely aligned seismicity and concealed structures, Science, 166, 173-178, 1969.

Richter, C.F. and J.M. Nordquist, Instrumental study of the Mannix earthquakes, Bull. Seism. Soc. Am., 41, 347-358, 1951.

Rochester, M.G., The application of dislocation theory to fracture of the earth's crust, M.A. Thesis, Univ. of Toronto, Canada, 1956.

Rogers, D.A., Deformation stress accumulation and secondary faulting in the vicinity of the Transverse Ranges of southern California, Ph.D. Thesis, Brown Univ., 1975.

Rogers, D.A. and M.A. Chinnery, Stress accumulation in the Transverse Ranges, southern California, in Proceedings of Conference on Tectonic Problems of the San Andreas Fault System, edited by R.L. Kovach and A. Nur, 70-79, 1973.

Rogers, T.H., Active extensional faulting north of Hollister near the Calaveras, Bull. Seism. Soc. Am., 57, 813-816, 1967.

Ryall, A., D. Slemmons, and L. Gedney, Seismicity, tectonism, and surface faulting in the western United Stated during historic times, Bull. Seism. Soc. Am., 56, 1105-1136, 1966.

Rybicki, K., The elastic residual field of a very long strike-slip fault in the presence of a discontinuity, Bull. Seism. Soc. Am., 61, 79-92, 1971.

Saito, M., Excitation of free oscillations and surface waves by a point source in a vertically heterogeneous earth, J. Geophys. Res., 72, 3689-3699, 1967.

Sato, R., Formulations of solutions for earthquake source models and some related problems, J. Phys. Earth, 17, 101-110, 1969.

Sato, R., Crustal deformation due to a dislocation in a multi-layered medium, J. Phys. Earth, 19, 31-46, 1971.

Sato, R., and M. Matsu'ura, Satatic deformation due to the fault spreading over several layers in a multi-layered medium, Part I: displacement, J. Phys. Earth, 21, 227-249, 1973.

Savage, J.C. and R.O. Burford, Accumulation of tectonic strain in California, Bull. Seism. Soc. Am., 60, 1877-1901, 1970.

Savage, J.C. and R.O. Burford, Geodetic determination of relative plate motion in central California, J. Geophys. Res., 78, 832-845, 1973.

Savage, J.C. and L.M. Hastie, Surface deformation associated with dip-slip faulting, J. Geophys. Res. 71, 4897-4904, 1966.

Savage, J.C. and L.M. Hastie, A dislocation model for the Fairview Peak, Nevada, earthquake, Bull. Seism. Soc. Am., 59, 1937-1948, 1969.

Savage, J.C. and M.D. Wood, The relation between apparent stress and stress drop, Bull. Seism. Soc. Am., 61, 1381-1388, 1971.

Scholz, C.H. and T.J. Fitch, Strain accumulation along the San Andreas fault, J. Geophys. Res., 74, 6649-6666, 1969.

Scholz, C.H., M. Wyss, and S.W. Smith, Seismic and aseismic slip on the San Andreas fault, J. Geophys. Res., 74, 2049-2069, 1969.

Scholz, C.H. and T.J. Fitch, Strain and creep in central California, J. Geophys. Res., 75, 4447-4453, 1970.

Scholz, C., P. Molnar, and T. Johnson, Detailed studies of frictional sliding of granite and implications for the earthquake mechanism, J. Geophys. Res., 77, 6392-6406, 1972.

Sezawa, K., The tilting of the surface of a semi-infinite solid due to internal nuclei of strain, Bull. Earthquake Res. Inst., 7, 1-14, 1929.

Sharp, R.V., San Jacinto fault zone in the Peninsula Ranges of southern California, Geol. Soc. Amer. Bull., 78, 705-730, 1967.

Singh, S.J., Static deformation of a multilayered half-space by internal sources, J. Geophys. Res., 75, 3257-3263, 1970.

Sleep, N.H., Stress and flow beneath island arcs, (in press), Geophys. J. Roy. astr. Soc., 1975.

Smith, S.W. and R. Kind, Observations of regional strain variations, J. Geophys. Res., 77, 4976-4980, 1972.

Smith, S.W. and W. Van De Lindt, Strain adjustments associated with earthquakes in southern California, Bull. Seism. Soc. Am., 54, 1569-1589, 1969.

Smylie, D.E. and L. Mansinha, The elasticity theory of dislocations in real earth models and changes in the rotation of the earth, Geophys. J. Roy. astr. Soc., 23, 329-354, 1971.

Sommerfeld, A., Optics, Academic Press, New York and London, 1964.

Spieth, M., J.C. Savage, and W. Prescott, Fault slip in Hollister, California areas, EOS, Trans. Am. Geophys. Un., 56, 1191, 1974.

Steinbrugge, K.V. and E.G. Zacher, Creep on the San Andreas fault-fault creep and property damage, Bull. Seism. Soc. Am., 50, 389-396, 1960.

Starr, A.T., Slip in a crystal and rupture in a solid due to shear, Proc. Camb. Phil. Soc., 24, 489-500, 1928.

Steketee, J.A., On Volterra's dislocations in a semi-infinite medium, Can. J. Phys., 36, 192-205, 1958a.

Steketee, J.A., Some geophysical applications of the elasticity theory of dislocations, Can. J. Phys., 36, 1168-1198, 1958b.

Stewart, R.M., C.G. Bufe, and J.H. Pfluke, Creep-caused strain events at Stone Canyon, California, Proceedings of the Conference on Tectonic Problems of the San Andreas Fault System, 286-293, edited by Robert L. Kovach and Amos Nur, School of Earth Sciences, Stanford University, 1973.

Stuart, W.D. and M.J.S. Johnston, Tectonic implications of anomalous tilt before central California earthquakes, EOS, Trans. Am. Geophys. Un., 56, 1196, 1974.

Taylor, G.I., The mechanism of plastic deformation of crystals, Proc. Roy. Soc., A, 145, 362, 1934.

Thatcher, W., Strain accumulation on the Northern San Andreas fault zone since 1906, submitted to J. Geophys. Res., 1975.

Tocher, D., Earthquake energy and ground breakage, Bull. Seism. Soc. Am., 48, 147-152, 1958.

Tocher, D., Seismographic results from the 1957 San Francisco earthquakes of March 1957, Calif. Div. of Mines, Special Report 57, 1959.

Tocher, D., Creep on the San Andreas fault-creep rate and related measurements at Vineyard, California, Bull. Seism. Soc. Am., 50, 396-404, 1960.

Udias, A., A study of the aftershocks and focal mechanisms of the Salinas-Watsonville earthquakes of August 31 and September 14, 1963, Bull. Seism. Soc. Am., 55, 85-106, 1965.

Volterra, V., Sur l'equilibre des corps elastiques multiplement connexes, Ann. Ec. norm. (Ser. 3), t. 24, 401-517, 1907.

Von Huene, R., Geologic structure between the Murray fracture zone and the Transverse Ranges, Marine Geol., 7, 475-499, 1969.

Vrana, R.S., Seismic activity near the eastern end of the Murray fracture zone, Geol. Soc. Am. Bull., 82, 789-792, 1971.

Vvedenskaya, A.V., The determination of displacement fields by means of dislocation theory, Bull. Acad. Sci. USSR, Geophys. Ser., English Transl., 3, 277-284, 1956.

Walsh, J.G., Mechanics of strike-slip faulting with friction, J. Geophys. Res., 73, 761-766, 1968.

Weertman, J. and J.R. Weertman, Elementary Dislocation Theory, Macmillan Company, London, 1964.

Wesson, R.L., R.O. Burford, and W.L. Ellsworth, Relationship between seismicity, fault creep, and crustal loading along the central San Andreas fault, Proceedings of Conference

on Tectonic Problems of the San Andreas Fault System, 13, Stanford Univ. Pub. Geol. Sci., 303-321, 1973.

Wesson, R.L. and W.L. Ellsworth, Seismicity preceeding moderate earthquakes in California, J. Geophys. Res. 78, 8527-8546, 1973.

Whipple, F.J.W., On the theory of the strain in an elastic solid bounded by a plane where there is a nucleus of strain at an internal point, and on the relation of the theory to seismology, Mon. Nat. Roy. astr. Soc., Geophysics Suppl., 3, 380-389, 1936.

Wideman, C.J., and M.W. Major, Strain steps associated with earthquakes, Bull. Seism. Soc. Am., 57, 1429-1448, 1967.

Wilson, J.T., A new class of faults and their bearing on continental drift, Nature, 207, 343-347, 1965.

Wyss, M. and J.N. Brune, Seismic moment, stress, and source dimensions for earthquakes in the California-Nevada region, J. Geophys. Res., 73, 4681-4694, 1968.

Yoffe, E.H., The angular dislocation, Phil. Mag., 5, 161-175, 1960.

APPENDIX

THE E MATRIX, ITS INVERSE, AND THE E' MATRIX

In solving the problem of a dislocation in a flat layered half-space we have found it convenient to use the matrix approach used by Thompson (1950) and Haskell (1963). The matrix relation between the Fourier coefficients $\underset{\sim}{K}$ and motion-stress vector $\underset{\sim}{Y}$ is:

$$\underset{\sim}{Y} = \underset{\sim}{E}\ (Z)\ \underset{\sim}{K} \tag{A1}$$

where

$$Y = \begin{pmatrix} U_1 \\ U_2 \\ U_3 \\ P_{13} \\ P_{23} \\ P_{33} \end{pmatrix} \tag{A2}$$

and

$$K = \begin{pmatrix} A^+ + A^- \\ A^+ - A^- \\ B^+ + B^- \\ B^+ - B^- \\ C^+ + C^- \\ C^+ - C^- \end{pmatrix} \tag{A3}$$

The resulting $\underset{\sim}{E}(z)$ matrix is obtained from the expressions given in the text for the displacements and strains. The components of $\underset{\sim}{E}(z)$ are:

$$E_{11} = ik_x \cosh(\nu z)$$

$$E_{12} = ik_x \sinh(\nu z)$$

$$E_{13} = ik_y \cosh(\nu z)$$

$$E_{14} = ik_y \sinh(\nu z)$$

$$E_{15} = ik_x [-\cosh(\nu z) - 2\delta\nu z \sinh(\nu z)]$$

$$E_{16} = ik_x [-2\delta\nu z\cosh(\nu z)-\sinh(\nu z)]$$

$$E_{21} = ik_y \cosh(\nu z)$$

$$E_{22} = ik_y \sinh(\nu z)$$

$$E_{23} = -ik_x \cosh(\nu z)$$

$$E_{24} = -ik_x \sinh(\nu z)$$

$$E_{25} = ik_y[-\cosh(\nu z) - 2\delta\nu z \sinh(\nu z)]$$

$$E_{26} = ik_y[-2\delta\nu z \cosh(\nu z) - \sinh(\nu z)]$$

$$E_{31} = \nu \sinh(\nu z)$$

$$E_{32} = \nu \cosh(\nu z)$$

$$E_{33} = 0$$

$$E_{34} = 0$$

$$E_{35} = -2\delta\nu^2 z \cosh(\nu z) + \nu \sinh(\nu z)$$

$$E_{36} = \nu \cosh(\nu z) - 2\delta\nu^2 z \sinh(\nu z)$$

$$E_{41} = 2\mu\nu i k_x \sinh(\nu z)$$

$$E_{42} = 2\mu i k_x \nu \cosh(\nu z)$$

$$E_{43} = i\mu\nu k_y \sinh(\nu z)$$

$$E_{44} = i\mu\nu k_y \cosh(\nu z)$$

$$E_{45} = [-4\mu\nu^2\delta z \cosh(\nu z) - 2\mu\delta\nu \sinh(\nu z)] i k_x$$

$$E_{46} = [-2\mu\delta\nu \cosh(\nu z) - 4\mu\nu^2\delta z \sinh(\nu z)] i k_x$$

$$E_{51} = 2\mu i\nu k_y \sinh(\nu z)$$

$$E_{52} = 2\mu i\nu k_y \cosh(\nu z)$$

$$E_{53} = -i\mu\nu k_x \sinh(\nu z)$$

$$E_{54} = -i\mu\nu k_x \cosh(\nu z)$$

$$E_{55} = [-4\delta\mu\nu^2 z \cosh(\nu z) - 2\delta\mu\nu \sinh(\nu z)] i k_y$$

$$E_{56} = [-2\delta\mu\nu \cosh(\nu z) - 4\delta\mu\nu^2 z \sinh(\nu z)] i k_y$$

$$E_{61} = 2\mu\nu^2 \cosh(\nu z)$$

$$E_{62} = 2\mu\nu^2 \sinh(\nu z)$$

$$E_{63} = 0$$

$$E_{64} = 0$$

$$E_{65} = [2\lambda\nu^2(1-\delta) + 2\mu\nu^2(1-2\delta)] \cosh(\nu z) - 4\mu\nu^3\delta z \sinh(\nu z)$$

$$E_{66} = -4\mu\nu^3\delta z \cosh(\nu z)$$

$$+ 2\lambda\nu^2(1-2\delta) + 2\mu\nu^2(1-2\delta)]\sinh(\nu z)$$

where $\nu = (k_x^2 + k_y^2)^{1/2}$

$\delta = 1/(3-4\sigma)$

and $\sigma = \lambda/2(\lambda+\mu)$

In order to use the above matrix to relate solutions in one layer to those in the next layer it is necessary to evaluate the matrix product

$$A_n = E_n(z_n)E_{n+1}^{-1}(z_{n+1}) \tag{A5}$$

If the origin of our coordinate system is temporarily translated to the z_{n+1} interface, this matrix becomes

$$A_n = E_n(d_n)E_{n+1}^{-1}(0) \tag{A6}$$

where d_n is the thickness of the nth layer. Shifting the origin in this manner simplifies taking the inverse of the 6 x 6 $\underset{\sim}{E}$ matrix. The non-zero components of $B = \underset{\sim}{E}^{-1}(0)$ are:

$$B_{11} = (-\alpha i k_x)/[\nu^2(\alpha + 2\mu)] \tag{A7}$$

$$B_{12} = (-\alpha i k_y)/[\nu^2(\alpha + 2\mu)]$$

$$B_{16} = 1/[(\alpha + 2\mu)\nu^2]$$

$$B_{23} = \delta/\nu(1+\delta)$$

$$B_{24} = k_x/[2\mu i\nu^3(1+\delta)]$$

$$B_{25} = -ik_y/[2\mu\nu^3(1+\delta)]$$

$$B_{31} = -ik_y/\nu^2$$

$$B_{32} = ik_x/\nu^2$$

$$B_{44} = k_y/(i\mu\nu^3)$$

$$B_{45} = ik_x/(\mu\nu^3)$$

$$B_{51} = (2\mu ik_x)/[(\alpha+2\mu)\nu^2]$$

$$B_{52} = (2\mu ik_y)/[(\alpha+2\mu)\nu^2]$$

$$B_{56} = 1/[(\alpha+2\mu)\nu^2]$$

$$B_{63} = +1/[\nu(1+\delta)]$$

$$B_{64} = ik_x/[2\mu\nu^3(1+\delta)]$$

$$B_{65} = ik_y/[2\mu\nu^3(1+\delta)]$$

where $$\alpha = 2[\lambda(1-\delta) + \mu(1-2\delta)] \qquad \text{(A8)}$$

and the other variables are defined in the text.

The $\underset{\sim}{E}(z)$ and $\underset{\sim}{B}$ matrices given above allow us to calculate the layer matrices via equation A6. In the derivation given in the text we found that the $\underset{\sim}{Y}$ vector on the surface $\underset{\sim}{Y}(0)$ could be related to the $E'(z_n)$ matrix where Z_n is the depth to the last

interface.

$$Y(0) = A_1 A_2 A_3 \cdot \cdot \cdot A_{n-1} E'_n(z_n) \qquad \text{(A9)}$$

E'(z) is defined so that

$$Y(z) = E'(z) \begin{pmatrix} A^+ \\ A^- \\ B^+ \\ B^- \\ C^+ \\ C^- \end{pmatrix} \qquad \text{(A10)}$$

The components of E' are:

$$E'_{11} = ik_x e^{\nu z}$$

$$E'_{12} = ik_x e^{-\nu z}$$

$$E'_{13} = ik_y e^{\nu z}$$

$$E'_{14} = ik_y e^{-\nu z}$$

$$E'_{15} = -(1 + 2\delta\nu z)\ ik_x e^{\nu z}$$

$$E'_{16} = -(1 - 2\delta\nu z)\ ik_x e^{-\nu z}$$

$$E'_{21} = ik_y e^{\nu z}$$

$$E'_{22} = ik_y e^{-\nu z}$$

$$E'_{23} = -ik_x e^{\nu z}$$

$$E'_{24} = -ik_x e^{-\nu z}$$

$$E'_{25} = -(1 + 2\delta\nu z)ik_y e^{\nu z}$$

$$E'_{26} = -(1 - 2\delta\nu z)ik_y e^{-\nu z}$$

$$E'_{31} = \nu e^{\nu z}$$

$$E'_{32} = -\nu e^{-\nu z}$$

$$E'_{33} = 0$$

$$E'_{34} = 0$$

$$E'_{35} = (\nu - 2\delta\nu^2 z)e^{\nu z}$$

$$E'_{36} = -(\nu + 2\delta\nu^2 z)e^{-\nu z}$$

$$E'_{41} = 2\mu ik_x \nu e^{\nu z}$$

$$E'_{42} = -2\mu ik_x \nu e^{-\nu z}$$

$$E'_{43} = i\mu\nu k_y e^{\nu z}$$

$$E'_{44} = -i\mu\nu k_y e^{-\nu z}$$

$$E'_{45} = -2\mu\delta\nu[2\nu z+1]ik_x e^{\nu z}$$

$$E'_{46} = -2\mu\delta\nu[2\nu z-1]ik_x e^{-\nu z}$$

$$E'_{51} = -2\mu i\nu k_y e^{\nu z}$$

$$E'_{52} = -2\mu i\nu k_y e^{-\nu z}$$

$$E'_{53} = -i\mu\nu k_x e^{\nu z}$$

$$E'_{54} = i\mu\nu k_x e^{-\nu z}$$

$$E'_{55} = -2\delta\mu\nu[2\nu z+1]ik_y e^{\nu z}$$

$$E'_{56} = -2\delta\mu\nu[2\nu z-1]ik_y e^{-\nu z}$$

$$E'_{61} = 2\mu\nu^2 e^{\nu z}$$

$$E'_{62} = 2\mu\nu^2 e^{-\nu z}$$

$$E'_{63} = 0$$

$$E'_{64} = 0$$

$$E'_{65} = \{2\lambda\nu^2(1-\delta)+2\mu\nu^2(1-2\delta-2\delta\nu z)\}\ e^{\nu z}$$

$$E'_{66} = \{\lambda\nu^2(1-2\delta)+2\mu\nu^2(1-2\delta+2\delta\nu z)\}e^{-\nu z}$$